

A Classical Analogue to the Standard Model and General Relativity

Chapters 4–10

Robert N. C. Pfeifer

10 December 2022

The relationships determined to date between fundamental constants in the $\mathbb{C}^{\wedge 18}$ Classical Analogue to the Standard Model are:

$$\begin{aligned} \frac{m_{e_i}^2}{m_e^2} &= \frac{[k_i^{(e)}(\mathcal{E}_{e_i})]^4 [1 + \Delta_e(m_{e_i}, \mathcal{E}_{e_i})]}{[k_1^{(e)}(\mathcal{E}_{e_i})]^4 [1 + \Delta_e(m_e, \mathcal{E}_{e_i})]} \left[1 + \mathcal{O}_e(m_{e_i}, \mathcal{E}_{e_i}) \right] \quad \left| \quad e_i \in \{e, \mu, \tau\} \text{ for } i \in \{1, 2, 3\} \text{ respectively} \right. \\ \frac{m_W^2}{m_e^2} &= 18N_0^4 \left(1 + \frac{2}{N_0}\right)^{-4} \left(1 + \frac{1}{N_0}\right)^{-4} \frac{\left[1 + \left(64 + \frac{3}{2\pi} - fz\right) \frac{\alpha}{2\pi}\right] \left\{1 + \frac{19}{18[k_1^{(e)}(\mathcal{E}_e) N_0]^4}\right\}}{[1 + \Delta_e(m_e, \mathcal{E}_e)]} [1 + \mathcal{O}_b + \mathcal{O}_e(m_e, \mathcal{E}_e)] \\ \frac{m_W^2}{m_Z^2} &= \frac{3 \left[1 + \left(64 + \frac{3}{2\pi} - fz\right) \frac{\alpha}{2\pi}\right] \left\{1 + \frac{19}{18[k_1^{(e)}(\mathcal{E}_e) N_0]^4}\right\}}{4 \left[1 + \left(\frac{401}{12} + \frac{3}{2\pi}\right) \frac{\alpha}{2\pi}\right] \left\{1 + \frac{23}{18[k_1^{(e)}(\mathcal{E}_e) N_0]^4}\right\}} (1 + \mathcal{O}_b) \quad \frac{m_W^2}{m_c^2} = \frac{1 + \frac{19}{18[k_1^{(e)}(\mathcal{E}_e) N_0]^4}}{1 + \frac{99}{18[k_1^{(e)}(\mathcal{E}_e) N_0]^4}} (1 + \mathcal{O}_b) \\ \frac{m_{W^{cc}}^2}{m_W^2} &= \frac{1 + \frac{100}{18[k_1^{(e)}(\mathcal{E}_e) N_0]^4}}{1 + \frac{19}{18[k_1^{(e)}(\mathcal{E}_e) N_0]^4}} (1 + \mathcal{O}_b) \quad \frac{m_{Z^{cc}}^2}{m_Z^2} = \frac{1 + \frac{104}{18[k_1^{(e)}(\mathcal{E}_e) N_0]^4}}{1 + \frac{23}{18[k_1^{(e)}(\mathcal{E}_e) N_0]^4}} (1 + \mathcal{O}_b) \\ \frac{m_W^2}{m_H^2} &= \frac{9 \left[1 + \left(64 + \frac{3}{2\pi} - fz\right) \frac{\alpha}{2\pi}\right] \left\{1 + \frac{19}{18[k_1^{(e)}(\mathcal{E}_e) N_0]^4}\right\}}{20 \left\{\left(1 - \frac{1}{9N_0}\right)^2 \left[1 + \frac{30\alpha}{9\pi} \left(1 + \frac{1}{9N_0}\right)\right] + \frac{1}{2\pi} \left[1 + \frac{30\alpha}{\pi} \left(1 - \frac{1}{9N_0}\right)\right]\right\} \left\{1 + \frac{7}{18[k_1^{(e)}(\mathcal{E}_e) N_0]^4}\right\}} (1 + \mathcal{O}_b) \\ G_N &= \frac{2\alpha^4 hc [1 + \Delta_e(m_e, \mathcal{E}_e)]^{\frac{1}{2}} \left(1 + \frac{7\alpha}{2\pi} + \frac{229\alpha}{12\pi N_0}\right)}{\pi [k_1^{(e)}(\mathcal{E}_e)]^4 m_e^2 \left(1 + \frac{\alpha}{2\pi} + \left\{\frac{197}{144} + \frac{\pi^2[1-6\ln(2)]}{12} + \frac{3\zeta(3)}{4}\right\} \frac{\alpha^2}{\pi^2}\right)^8} \left[1 + \mathcal{O}_b + \mathcal{O}_e(m_e, \mathcal{E}_e) + \mathcal{O}\left(\frac{\alpha^2 m_e^2}{\pi^2 m_\mu^2}\right)\right] \\ &\quad \times \frac{N_0^6}{\{2[(N_0 + 4)(N_0 + 3)]^4 + [8(N_0 + 3)^4 + 6(N_0 + 2)^4](N_0 + 1)^4\}[(N_0 + 2)(N_0 + 1)^2]^4 (N_0 + \frac{5}{4})^3 (N_0 + 2)} \end{aligned}$$

Taking α , m_e , and m_μ as input, these may be solved for m_W , m_Z , m_H , m_τ , G_N , $m_{W^{cc}}$, $m_{Z^{cc}}$, m_c , and N_0 . Additional symbols appearing in the above expressions are defined as follows:

$$\begin{aligned} \Delta_e(m_{e_i}, \mathcal{E}) &:= \frac{8\alpha}{3N_0(3\alpha + 2\pi)} \left\{1 + \frac{(10\pi + 180\alpha)m_{e_i}^2}{3\pi [m_c^*(\mathcal{E})]^2} + \frac{(5 - 4fz)\alpha m_{e_i}^2}{4\pi m_W^2}\right\} + \frac{90\alpha m_{e_i}^2}{\pi [m_c^*(\mathcal{E})]^2} + \frac{(5 - 4fz)\alpha m_{e_i}^2}{2\pi m_W^2} \\ &\quad + \frac{5m_{e_i}^2}{[m_c^*(\mathcal{E})]^2} \left\{1 + \frac{90\alpha m_{e_i}^2}{\pi [m_c^*(\mathcal{E})]^2} + \frac{(25 - 12fz)\alpha m_{e_i}^2}{6\pi m_W^2}\right\} + \frac{40m_{e_i}^2}{3m_H^2 [k_1^{(e)}(\mathcal{E}_e) N_0]^4} + \mathcal{O}_e(m_{e_i}, \mathcal{E}) \\ \theta_e(\mathcal{E}) &:= -\frac{3\pi}{4} \left(1 - \frac{4\sqrt{\delta_e \{r[\Delta_e(m_\tau, \mathcal{E}) - \Delta_e(m_\mu, \mathcal{E})]\}}}{3\pi}\right) \left(1 + \frac{4}{3\pi} \sqrt{\delta_e \left\{r \left[\frac{1 + \Delta_e(m_e, \mathcal{E})}{1 + \Delta_e(0, \mathcal{E})} - 1\right]\right\}}\right) \\ fz &:= \frac{1}{3} \left(4 - 24 \frac{m_W^2}{m_Z^2} + 16 \frac{m_W^4}{m_Z^4}\right) \quad \delta_e(n) := \sqrt{1 + \frac{\pi^2 n}{8} \left(1 + \frac{\pi^2 n}{32}\right) + \mathcal{O}(n^3)} - 1 \quad r(n) := n \cdot \sqrt{1 - \frac{n}{9}} \\ [m_c^*(\mathcal{E})]^2 &:= m_c^2 \left(1 - \frac{27}{10} \frac{\mathcal{E}^2}{m_c^2 c^4}\right) \quad k_n^{(\ell)}(\mathcal{E}) := 1 + \sqrt{2} \cos \left[\theta_\ell(\mathcal{E}) - \frac{2\pi(n-1)}{3}\right] \quad \mathcal{E}_\ell := m_\ell c^2 \end{aligned}$$

$$\begin{aligned} \mathcal{O}_e(m_{e_i}, \mathcal{E}) &:= \mathcal{O}\left(\frac{\alpha}{\pi N_0^2}\right) + \mathcal{O}\left(\frac{\alpha^2}{\pi^2 N_0}\right) + \mathcal{O}\left[\frac{\alpha m_{e_i}^4}{\pi N_0 [m_c^*(\mathcal{E})]^4}\right] + \mathcal{O}\left\{\frac{\alpha^2 m_{e_i}^2}{\pi^2 [m_c^*(\mathcal{E})]^2}\right\} + \mathcal{O}\left\{\frac{\alpha m_{e_i}^2}{\pi m_H^2 [k_1^{(e)}(\mathcal{E}_e) N_0]^4}\right\} + \mathcal{O}\left\{\frac{m_{e_i}^6}{[m_c^*(\mathcal{E})]^6}\right\} \\ &\quad + \mathcal{O}\left\{\frac{m_{e_i}^2}{m_H^2 [k_1^{(e)}(\mathcal{E}_e)]^4 N_0^5}\right\} + \mathcal{O}\left\{\frac{m_{e_i}^4}{m_H^4 [k_1^{(e)}(\mathcal{E}_e) N_0]^4}\right\} \quad \mathcal{O}_b := \mathcal{O}\left\{\frac{\alpha}{\pi} [k_1^{(e)}(\mathcal{E}_e) N_0]^{-4}\right\} + \mathcal{O}\left(\frac{\alpha^2}{\pi^2}\right). \end{aligned}$$

Software solving these equations numerically may be found at <https://www.academia.edu/65931512>

Alternatively, an easier-to-read MATLAB/Octave function which verifies the main relationships may be found at <https://www.academia.edu/88569427>

Contents

4	Calculation of fermion masses on $\mathbb{C}^{\wedge 18}$	7
4:1	Introduction	7
4:2	Conventions	8
4:3	Fermion masses	8
4:3.1	General considerations	8
4:3.2	Leptons	11
4:3.2.1	A -sector interactions	11
4:3.2.2	C -sector interactions	15
4:3.3	Quarks and preons	23
4:4	Conclusion	23
4:A	Extension of gauge choices to $SU(9)$	24
5	Calculation of boson masses on $\mathbb{C}^{\wedge 18}$	27
5:1	Introduction	27
5:2	Conventions	27
5:3	Boson masses	28
5:3.1	Vector boson masses	28
5:3.1.1	Fig. 5.1(i):	28
5:3.1.2	Fig. 5.1(ii):	28
5:3.1.3	Fig. 5.1(iii):	30
5:3.1.4	Fig. 5.1(iv):	30
5:3.1.5	Fig. 5.1(v):	30
5:3.1.6	Fig. 5.1(vi):	35
5:3.1.7	Exception: The G boson.	36
5:3.2	Boson generations	36
5:3.3	Scalar boson mass	36
5:3.4	Summary of boson masses	43
5:3.4.1	Photon	43
5:3.4.2	W and Z bosons	43
5:3.4.3	Gluons and N boson	44
5:3.4.4	G boson	44
5:3.4.5	a_{μ}^{12} boson	44
5:3.4.6	Scalar boson	44
5:4	Conclusion	44
6	Particle generations and masses on $\mathbb{C}^{\wedge 18}$	46
6:1	Introduction	46
6:2	Conventions	47
6:3	The pseudovacuum	47
6:4	Boson Mass Interactions	49
6:4.1	W mass	49
6:4.1.1	Boson loops—overview	49
6:4.1.2	Gluon loops	55
6:4.1.3	Photon, W , and Z boson loops	59
6:4.1.4	Scalar boson loops	63
6:4.1.5	Net effect of all boson loops	68
6:4.1.6	Species dependence of k_1	68

6:4.1.7	Background photon and scalar interactions	70
6:4.1.8	Universality of loop corrections	71
6:4.2	Z mass	73
6:4.2.1	Boson loops	73
6:4.2.1.a	Gluon loops:	73
6:4.2.1.b	Photon, W , and Z boson loops:	74
6:4.2.1.c	Scalar boson loop:	76
6:4.2.1.d	Net effect of all boson loops:	77
6:4.2.2	Background photon and scalar interactions	77
6:4.2.2.a	Direct coupling:	77
6:4.2.2.b	Indirect (universality) coupling:	77
6:4.2.2.c	Gluon sector:	79
6:4.3	Weak mixing angle	79
6:4.4	Gluon masses	79
6:4.5	Scalar boson mass	81
6:4.5.1	Boson loops	81
6:4.5.1.a	Gluon loops:	81
6:4.5.1.b	Photon, W , and Z boson loops:	82
6:4.5.1.c	Scalar boson loops:	83
6:4.5.1.d	Net effect of all boson loops:	85
6:4.5.2	Background photon and scalar interactions	85
6:4.5.2.a	Direct coupling:	85
6:4.5.2.b	Indirect (universality) coupling:	85
6:4.6	Neutral boson gravitation	85
6:5	Lepton Mass Interaction	86
6:5.1	Leading order	86
6:5.1.1	Action on colour sector	86
6:5.1.2	Mass from photon and gluon components of the pseudovacuum	91
6:5.1.3	Mass from scalar component of the pseudovacuum	93
6:5.1.4	Gluon and scalar field mass deficits	95
6:5.2	Foreground loop corrections	96
6:5.2.1	1-loop EM corrections	96
6:5.2.2	$O(N_0^{-1})$ correction to 1-loop EM corrections	99
6:5.2.2.a	$O(N_0^{-1})$ correction to EM loop correction to background photon coupling:	99
6:5.2.2.b	$O(N_0^{-1})$ correction to EM loop correction to background gluon coupling:	101
6:5.2.3	1-loop gluon corrections	102
6:5.2.3.a	Main correction:	102
6:5.2.3.b	$O(N_0^{-1})$ correction to gluon loop correction to back- ground photon coupling:	104
6:5.2.4	1-loop weak force corrections	105
6:5.2.4.a	Background photon interaction:	105
6:5.2.4.b	Background gluon interactions:	107
6:5.2.4.c	Background scalar boson interaction:	107
6:5.2.4.d	$O(N_0^{-1})$ correction to weak loop corrections to back- ground photon coupling:	108
6:5.2.5	1-loop scalar corrections	108
6:5.2.6	2-loop EM corrections	108

6:5.3	Corrections to the lepton mass angle	109
6:5.3.1	Origin of corrections	109
6:5.3.2	Preamble	110
6:5.3.3	First-order correction to K_ℓ^4 from the tau channel	111
6:5.3.4	Second-order correction to K_ℓ^4 from the tau channel	115
6:5.3.5	Reparameterisation of θ_e	116
6:5.3.6	Corrections to $[K_e(\theta_e)]^4$ from the muon channel	118
6:5.3.7	Local scaling symmetry	119
6:5.3.8	Corrections to $[K_e(\theta_e)]^4$ from the electron channel	121
6:5.3.9	Species and energy dependence of K_ℓ -matrix eigenvalues in boson mass interactions	122
6:5.3.9.a	Species dependence:	122
6:5.3.9.b	Energy dependence:	122
6:6	Predictions of the $\mathbb{C}^{\wedge 18}$ analogue model	123
6:6.1	Mass relationships	123
6:6.2	Results	125
6:6.3	Sources of numerical error	125
6:7	Conclusion	128
6:A	Mass-related loop coefficients	129
6:B	Symmetry factors and photon loops	130
6:C	Solving the particle mass relationships	131
6:D	Evaluation of accessory results	134
6:E	Further notes on the colour sector	135
6:E.1	Gluon masses	135
6:E.2	Separability of A and C charge sectors	136
7	Curved space-times from $\mathbb{C}^{\wedge 18}$	138
7:1	Introduction	138
7:2	Conventions	139
7:2.1	Notation and terminology	139
7:2.2	Quantum/classical correspondence	140
7:3	$\mathbb{C}^{\wedge 18}$ with curved space-time	141
7:3.1	Curvature and choice of gauge	141
7:3.2	Beyond-Standard-Model processes in the photon pair field	142
7:3.2.1	Origin of the photon pair field	142
7:3.2.2	Interactions of the photon pair field	143
7:3.2.3	Principle of equivalence	149
7:3.3	Evaluation of space-time curvature	150
7:3.3.1	Leading-order photon pair decay profile	150
7:3.3.2	Higher-order corrections	158
7:3.3.2.a	The $O(N_0^{-1})$ corrections	158
7:3.3.2.b	The $O(\alpha)$ corrections	160
7:3.3.2.c	The $O(N_0^{-1})$ corrections to the $O(\alpha)$ corrections	161
7:3.3.3	Elimination of GG^\dagger pairs	164
7:3.3.4	Rotating source	165
7:3.4	Beyond the dominant process	165
7:3.4.1	Other spin-2 processes	165
7:3.4.2	The right weak interaction and other spin-1 effects	165
7:4	Results	166

7:4.1	Value of Newton's constant	166
7:4.2	Qualitative implications	169
7:5	Conclusion	169
8	Further Calculations: W mass in CDF II, and Muon $g - 2$	171
9	Leptoquarks and LHCb	172
9:1	Introduction	172
9:2	$B^+ \rightarrow K^+$ decay in the CASM	173
9:2.1	Fermions in $B^+ \rightarrow K^+$ decay	173
9:2.2	Leptoquark processes in $B^+ \rightarrow K^+$ decay	174
9:3	Conclusion	177
10	Additional Brief Notes	179
10:1	Higher-generation weak bosons in the CASM	179
10:1.1	Brief comments	179
10:1.1.1	Meaning of boson generation	179
10:1.1.2	Beyond the preon scale	179
10:1.2	Calculating the heavy weak boson masses	180
10:2	Neutrino masses	181
10:2.1	No seesaw mechanism	181
10:2.2	Neutrino masses	181

Chapter 4

Calculation of fermion masses on \mathbb{C}^{18}

Abstract

The \mathbb{C}^{18} model is an analogue model capable of emulating the complete particle spectrum of the Standard Model, including interactions, using only free scalar fields on a manifold with anticommuting co-ordinates. Solitonic excitations in a pseudovacuum state behave as coloured preons, forming triplets which behave as emergent fermions and pairs which behave as emergent bosons. This chapter demonstrates how the emergent fermions acquire mass through interaction with the pseudovacuum, with particle generations arising from diagonalisation of colour interactions within the triplet.

4:1 Introduction

Analogue models are one of the most powerful concepts in modern physics. At their most abstract, they may be summarised by the observation that two systems described by the same mathematical systems will exhibit equivalent behaviours. This equivalence may be exact, as in the application of Onsager’s exact solution to the 1-D quantum Ising chain [1, 2], or approximate and valid only in appropriate regimes, with examples including the effective field theories of quasiparticles [3–6]. These analogies are bidirectional, such that the microscopic model emulates the behaviour of quasiparticles, and the quasiparticle model provides an effective description of the microscopic system in the appropriate regime. Copious examples of analogue systems abound in nature, in models, and in the laboratory [7–23].

One may argue that the value of an analogue model is determined by its utility in performing calculations or in granting qualitative insight into the behaviour of a physical system. While the mapping of the \mathbb{C}^{18} model to the low-energy regime of a quantum field theory resembling the Standard Model in Chapter 3 provides qualitative insight into the behaviour of the \mathbb{C}^{18} model, of far greater interest is whether the \mathbb{C}^{18} model can enable the calculation of observable quantities in the Standard Model, especially if it exhibits relationships which the quantum field theory does not. Such calculations are indeed possible, but to perform them it is first necessary to elucidate the mass mechanisms of the \mathbb{C}^{18} model. Thus the fermionic mass mechanism is presented to tree level in the present chapter, and the bosonic mass mechanism is presented in Chapter 5. Of particular note in the present chapter is the mechanism giving rise to particle generations, which is found to have resemblance to earlier work by Koide [24]. Koide’s work is remarkable for proposing an approximate relationship between the masses of the different

generations of leptons [25], and this similarity in structure yields particle generations from the mass matrix on $\mathbb{C}^{\wedge 18}$.

4:2 Conventions

This chapter follows the same conventions as Chapters 1–3. Units are chosen such that $c = 1$, $\hbar = 1$. When equations and lemmas from Chapters 1–3 are referenced, they take the forms (1.1), (2.1), etc.

Symmetry factors arising from Feynman diagrams are typically denoted n_{sym} whereas those arising from the Fundamental Scalar Fields (FSFs) are typically denoted n_{φ} .

Regarding terminology around Feynman diagrams and symmetry factors:

- Where there exist multiple ways to connect up sources, vertices, and sinks to obtain equivalent diagrams up to interchange of non-distinguishable co-ordinates, the same term is obtained from the generator \mathcal{Z} in multiple different ways and thus the diagram acquires a multiplicative factor. This is referred to in the present volume as a *symmetry factor*.
- Where integration over the parameters of a diagram (for example, over source/sink co-ordinates) yields the same diagram multiple times up to interchange of labels on these parameters, this represents a double- (or multiple-)counting of physical processes. It is then necessary to eliminate this multiple-counting by dividing by the appropriate symmetry factor. This is referred to in the present volume as *diagrammatic redundancy* or *double-(multiple-)counting*.

4:3 Fermion masses

4:3.1 General considerations

For any species of fermion, mass terms may arise from interactions between its constituent preons and the vector or complex scalar boson fields of the pseudovacuum, which correspond to specific gradients of the fundamental scalar fields. In order for their expectation values (1.167, 1.172) to be nonvanishing, the boson fields in such an interaction must appear as conjugate pairs. The relevant interactions between a fermion and a vector boson are shown in Fig. 4.1; couplings to the scalar boson are analogous but much weaker (Sec. 3:3.5.5 and Fig. 3.6), so are ignored.

The preon lines in these diagrams correspond, in theory, to the whole preon field, and in principle any particle (foreground or background/pseudovacuum) may acquire mass from this mechanism. However, the normalisation of the generating functional adopted in Sec. 1:3.8.6 factors out interactions involving background particles only, with the result that this interaction only takes place when a foreground field is present. Preons obey the Pauli exclusion principle, and field excitations satisfying the long-range correlation properties of a foreground field excitation cannot also be pseudovacuum excitations, and thus in effect only foreground preons participate in mass interactions.

A foreground fermion propagates over a distance or time large compared to \mathcal{L}_0 in the isotropy frame of the pseudovacuum, with the fermion source and sink in Fig. 4.1 separated by distance or time large compared to \mathcal{L}_0 . However, if these diagrams are to be non-vanishing then the pseudovacuum fields at the two boson sources must be correlated. They must therefore constitute a conjugate or self-conjugate pair, and it is convenient to adopt the approximation of Eq. (1.169) such that they are separated by a distance of $\mathcal{O}(\mathcal{L}_0)$ or less. The interactions of the boson pair may either be both with the same preon, as in Fig. 4.1(i), or with different preons as in Fig. 4.1(ii).

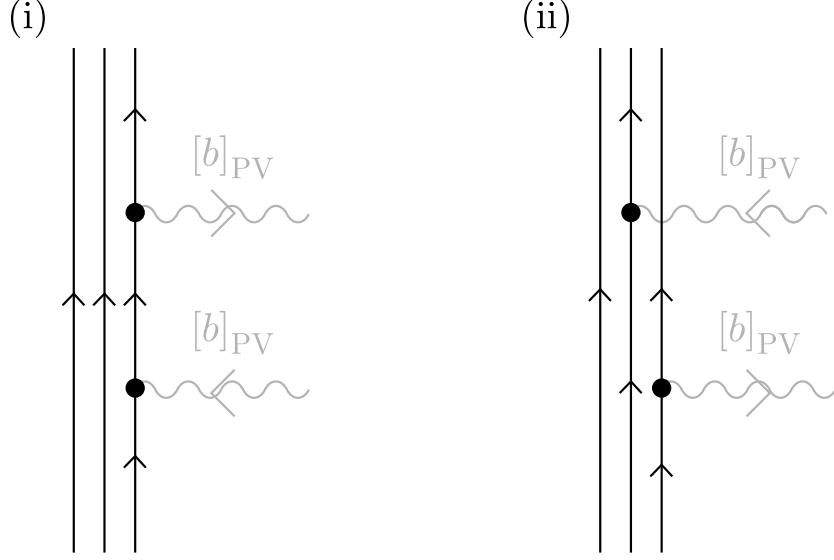


Figure 4.1: Interactions between preons in an arbitrary foreground fermion and a pseudovacuum (PV) vector boson field b . Each of the bosons may interact with any of the three preons, and in any order, with two example configurations shown here. Arrows are present on the boson lines for interactions with complex vector bosons such as $W_\mu^{(\dagger)}$.

The preons are bound into a triplet by the exchange of gluons over length and timescales \mathcal{L}_ψ , which is anticipated to be small compared with the characteristic length of the pseudovacuum, \mathcal{L}_0 . Given this, it follows that both Fig. 4.1(i) and (ii) will contribute to the lepton mass, with preon-preon interactions within the fermion (not shown) distributing any transferred momentum evenly among the three component preons.

Considering that a bosonic background field has units of L^{-1} , a non-vanishing conjugate pair of interactions with the pseudovacuum may in general be expected to yield terms contributing to the square of the particle mass. The tree-level couplings with the pseudovacuum may be viewed as analogous to the mass vertices, and any higher-order corrections to these diagrams will either yield corrections intrinsic to the mass vertex, or contributions to the diagrams of the proper self-energy (PSE). In the present chapter diagrams are only evaluated to tree level and thus no examples of these corrections are shown, though these are discussed at length in Chapter 6. For the moment, it suffices to note that if a 1-particle-irreducible (1-PI) foreground field correction could equally well be applied either to a pseudovacuum interaction mass vertex or to a conventional mass vertex arising from a Lagrangian term such as $m_e \bar{e}_R e_L$ in the Standard Model, it belongs in the PSE and not in the definition of the mass vertex itself. Terms not meeting this criterion are instead accounted part of the expression for the mass vertex, and in consequence, the structures of the PSE terms are identical in the $\mathbb{C}^{\wedge 18}$ model and the Standard Model.

Now note that, in general, the two interaction vertices illustrated in either diagram of Fig. 4.1 may appear anywhere in the series expansion of the fermion propagator, and since the fermion line between these two interactions is foreground, there will typically be other 1-PI vertices intercalated in between. To allow for this, let the propagator linking the two vertices be the dressed propagator, incorporating additional mass vertices equivalent to those presently being computed. To represent this, treat the propagator as that of a massive fermion, and solve by

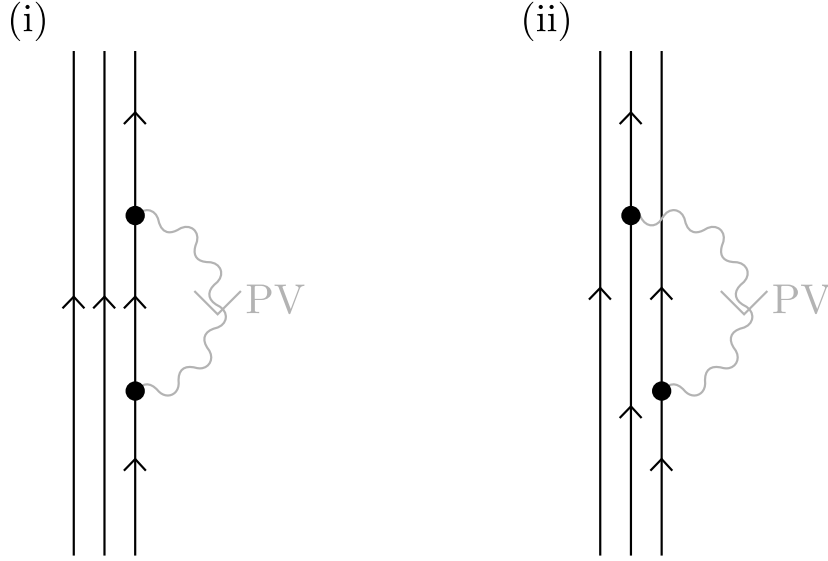


Figure 4.2: Interactions with the pseudovacuum (PV) may be thought of as the mean-field term in a perturbation expansion of a loop correction to the particle propagator. These diagrams reproduce Fig. 4.1 with the pseudovacuum interactions redrawn as loops. The boson propagator in grey is replaced by the mean field expansion of the pseudovacuum.

requiring consistency.

Returning to Fig. 4.1, note that the two vertices (whose locations will be denoted x and y) are separated on all axes by less than $O(\mathcal{L}_0)$ in the isotropy frame of the pseudovacuum, and momentum of the foreground fermion and the pseudovacuum need not be separately conserved over this interval. Indeed, although the pseudovacuum field is evaluated as a mean field value at points x and y , the fermion field in the loop must propagate across the intervening distance, and can surrender momentum to the pseudovacuum at x and recover it at y , or vice versa. This ability for a propagating particle to surrender momentum to and recover momentum from the pseudovacuum is responsible for the 4-momentum fluctuations described in Sec. 1:3.8.5, and is directly equivalent to the emission and absorption of a boson in a loop correction (Fig. 4.2). Provided the magnitude of the 4-momentum transferred to the pseudovacuum loop is sufficiently small compared with \mathcal{E}_Ω , evaluation of these diagrams is essentially unchanged and continues to be dominated by the pseudovacuum mean field term. Since there are no background fields in the Standard Model, these interactions are associated to the mass vertices, and not the PSE, even when written in the form of a background field loop. Meanwhile, by construction, the PSE terms of the two models remain largely equivalent.

Discussion of PSE terms leads naturally to considerations of renormalisation. The $\mathbb{C}^{\wedge 18}$ model emulates renormalisation through the existence of a real UV cutoff $\Lambda := \frac{1}{2}\mathcal{E}_\Omega$, with this emulation being good in a regime where the error introduced on taking $\Lambda \rightarrow \infty$ is negligible.¹ However, all physical predictions of QFTs are independent of renormalisation methods used, and thus the $\mathbb{C}^{\wedge 18}$ model equivalently emulates a QFT subject to either UV cutoff or $\overline{\text{MS}}$ renormalisation. To achieve a practical realisation of $\overline{\text{MS}}$ renormalisation, the portions of all PSE diagrams which are finite in the limit $\Lambda \rightarrow \infty$ may be absorbed into the definition of the mass vertex such that

¹The factor of $\frac{1}{2}$ is discussed in Sec. 1:3.6.4 and Chapter 8.

the bare mass vertex factor for a particle corresponds to the observable mass of that particle. Further to this, however, note that there are also loop corrections to the mass interactions which have no counterpart in the Standard Model. These diagrams necessarily contribute to the bare mass vertex, and a number of them are evaluated in Chapter 6. Given the ability to change renormalisation scheme, it is convenient to evaluate these higher-order corrections to the bare mass vertices in the UV cutoff scheme for which Fig. 4.1 maps to a pair of simple vertices. Having evaluated these corrections to whatever order is desired, and reduced them to numerical multipliers on the vertices of Fig. 4.1, the PSE diagrams may then be reintroduced, being corrections to these vertices which are common to $\mathbb{C}^{\wedge 18}$ and the Standard Model. A further choice of emulated renormalisation scheme may then be made, determining whether the numerical multipliers from the PSE terms are absorbed into a further redefinition of the bare mass vertices. Next, recognise that with both the PSE terms and the obligate bare mass vertex terms reducing to numerical multipliers on Fig. 4.1, the order of this process may be inverted. Thus the net effect of the PSE terms may be evaluated first, and reduced to a numerical multiplier of the bare vertices, with the higher-order non-PSE terms then correcting bare vertices corresponding to the PSE rescaling of Fig. 4.1. This approach is frequently the most convenient, and permits the correction of Fig. 4.1 by higher-order non-PSE terms to be identified with the physical mass of the participating fermion. A similar treatment applies to bosons, which are discussed in Chapters 5–6.

It is also worth noting that when a calculation yields a diagram which corresponds to a PSE loop on a massive propagator which does not enclose an explicit mass vertex, regardless of the renormalisation scheme being emulated that diagram may be discarded as a redundant representation of terms already incorporated into the mass vertices and loop corrections which are implicitly associated with the massive propagator.

Finally, to determine which pseudovacuum bosons make a contribution to fermion mass, recognise that the preons making up a fermion in $\Psi^{ag\alpha}$ (3.37) carry charges with respect to both $SU(3)_A$ and $SU(3)_C$, and thus interact with vector bosons from both the electroweak and the gluon sector (counting N_μ as a ninth gluon). Contributions to particle mass may then be separated according to sector of origin, and by the requirement that the species in Eq. (1.167) be conjugate, any pairwise term such as that shown in Fig. 4.1 receives contributions only from one sector. Further, since the propagators in Fig. 4.1 are taken to be dressed propagators in which only one pair of pseudovacuum interactions has been made explicit, there is no need to explicitly evaluate terms of higher order in the pseudovacuum fields.

4:3.2 Leptons

4:3.2.1 A-sector interactions

In evaluating Fig. 4.1, initially treat particle generation as an *ad hoc* concept, and specialise to a single generation of leptons. For now also ignore the contribution of coloured and scalar pseudovacuum bosons (these may be written as small corrections to the photon term, and will be reintroduced in Chapter 6), so that for any given generation g the amplitudes associated with Fig. 4.1 may simply be written down in terms of Ψ , the vector of composite leptons $\Psi^{ag\alpha}$. Since the interacting bosons are of type $a_{\mu}^{\bar{a}}$, the colour of the interacting preon remains unchanged. Each boson may interact with any of the three components, giving nine distinct diagrams, but the corresponding factor of nine is cancelled by factors from Eq. (3.31) and this cancellation is incorporated into the resulting boson/fermion coupling in Eq. (3.39) and Sec. 3:3.5.8. Taking

into account these factors, the total amplitude is therefore

$$n_\varphi n_{\text{sym}} f^2 \int \int d^4x d^4y [\bar{\Psi}(x) \lambda_a^A \bar{\sigma}^\mu \Psi(x)]_{\text{fg}} a_\mu^{\tilde{a}}(x) \times [\bar{\Psi}(y) \lambda_b^A \bar{\sigma}^\nu \Psi(y)]_{\text{fg}} a_\nu^{\tilde{b}}(y) \quad (4.1)$$

where $a_\mu^{\tilde{a}}(x)$ and $a_\nu^{\tilde{b}}(y)$ represent the total boson fields, i.e. not just background or foreground, at x and y respectively. Factor n_{sym} is a diagrammatic symmetry factor comprising

- the number of choices for which vertex the fermion source should be connected to (2 if the boson species is self-dual, 1 if not),
- the number of different ways to connect the photon sources to the interaction vertices (2),
- and a diagrammatic redundancy factor of $\frac{1}{2}$ as the photon exchange factor is redundant, leading to double counting,

and factor n_φ contains symmetry factors of $O(N_0)$ arising from FSF exchange similar to that described in Sec. 3:3.5.

Over length scales of order \mathcal{L}_0 or greater, expression (4.1) is dominated by boson contributions from the pseudovacuum, and thus it will ultimately be helpful to take a form of mean field approximation and replace the fields $a_\mu^{\tilde{a}}(x)$ with $[a_\mu^{\tilde{a}}(x)]_{\text{bg}}$. However, with x and y being separated on all axes by less than $O(\mathcal{L}_0)$ in the isotropy frame of the pseudovacuum, first note that the background fields may be rewritten as a loop, as per Sec. 4:3.1 and Fig. 4.2. Provided the magnitude of the 4-momentum transferred to the pseudovacuum loop is sufficiently small compared with \mathcal{E}_0 , evaluation of these diagrams continues to be unambiguously dominated by the pseudovacuum mean field term.

Furthermore, note that both limbs of the loop are potentially massive. The fermion remains a foreground particle and thus may undertake an arbitrary excursion *en route* between x and y —it need not remain within the region of characteristic dimension $O(\mathcal{L}_0)$ —and may engage in additional mass interactions while doing so. If it has surrendered momentum to the boson field, it does so with a 4-momentum deficit. The surrendered momentum is carried in the indicated boson channel, is necessarily also foreground in character, and the ends of the loop are separated by up to \mathcal{L}_0 in the isotropy frame of the pseudovacuum. This allows the boson excitation associated with the surrendered 4-momentum to also engage in additional mass interactions not explicitly shown. The excitation of the boson channel corresponding to the surrendered momentum therefore acquires mass interactions appropriate to the boson species.

For a lepton ℓ the factor associated with such a loop, accounting for the transient fermion momentum surfeit or deficit, may be written

$$n_\varphi n_{\text{sym}} \frac{\Xi f^2}{4\pi} \mathbf{f}\left(\frac{m_\ell^2}{m_a^2}\right) \quad (4.2)$$

where

$$\mathbf{f}\left(\frac{m_\ell^2}{m_b^2}\right) \rightarrow \begin{cases} 1 & \text{if } m_b^2 = 0 \\ O\left(\frac{m_\ell^2}{m_b^2}\right) & \text{if } m_b^2 \gg m_\ell^2. \end{cases} \quad (4.3)$$

Ξ is a structure factor equal to 2 for the photon, 10/3 for the $W^{(\dagger)}$ boson, etc. [26], and n_φ and n_{sym} are symmetry factors. Anticipating a mean field substitution for the boson fields yields

$$n_\varphi n_{\text{sym}} f^2 \int \int d^4x d^4y [\bar{\Psi}(x) \lambda_a^A \bar{\sigma}^\mu \Psi(x)]_{\text{fg}} [a_\mu^{\tilde{a}}(x)]_{\text{bg}} \times [\bar{\Psi}(y) \lambda_b^A \bar{\sigma}^\nu \Psi(y)]_{\text{fg}} [a_\nu^{\tilde{b}}(y)]_{\text{bg}}, \quad (4.4)$$

which is exactly equal to Eq. (4.1) in the absence of foreground bosons. To incorporate the loop factors (4.2), recognise that the vertex couplings and symmetry factors are already present in Eq. (4.4), and that for consistency the factor of $(4\pi)^{-1}$ and the structure factor must be absorbed into the mean field value associated with the pseudovacuum.² Introducing the remaining factor $\mathbf{f}(\cdot)$ yields

$$n_\varphi n_{\text{sym}} f^2 \mathbf{f}\left(\frac{m_\ell^2}{m_{a\tilde{a}}^2}\right) \iint d^4x d^4y [\bar{\Psi}(x) \lambda_a^A \bar{\sigma}^\mu \Psi(x)]_{\text{fg}} [a_\mu^{\tilde{a}}(x)]_{\text{bg}} \times [\bar{\Psi}(y) \lambda_b^A \bar{\sigma}^\nu \Psi(y)]_{\text{fg}} [a_\nu^{\tilde{b}}(y)]_{\text{bg}}. \quad (4.5)$$

In the absence of external foreground bosons, by gauge choices (3.55–3.58) this expression (4.5) may be non-vanishing only for $\tilde{a} = \tilde{b} = 3$ on the A sector, corresponding to interactions with the pseudovacuum photon field $[A_\mu]_{\text{bg}}$. The electrons and quarks may acquire mass as a result of this interaction (for the quarks this will be a bare mass), but the neutrino does not as it does not couple to this species of boson. To proceed with a definite example, specialise to the electron fields to obtain

$$n_\varphi f^2 \iint d^4x d^4y \sum_{e \in \{e_L, \bar{e}_R\}} \prod_{z \in \{x, y\}} \{[\bar{e}(z) \bar{\sigma}^\mu e(z)]_{\text{fg}} [A_\mu(z)]_{\text{bg}}\}. \quad (4.6)$$

Using spinor and sigma matrix identities this may be rewritten

$$-\frac{n_\varphi f^2}{2} \iint d^4x d^4y \sum_{e \in \{e_L, \bar{e}_R\}} [\bar{e}(x) \bar{e}(y) e(x) e(y)]_{\text{fg}} [A^\mu(x) A_\mu(y)]_{\text{bg}}. \quad (4.7)$$

Provided the two vertices are sufficiently close, i.e. $\delta_{\mathcal{L}_0}^{(4)}(x^\mu - y^\mu)$ is non-vanishing in the rest frame of the pseudovacuum, this admits the per-excitation mean field substitution

$$[A^\mu(x) A_\mu(y)]_{\text{bg}} \rightarrow -\omega_0^2 \quad (4.8)$$

where ω_0 is the mean energy per FSF gradient, as in Eq. (1.230). In contrast with Eq. (1.167), but in keeping with the approach of Sec. 3:3.5, symmetry factors from FSF exchange are evaluated separately and represented by n_φ . These factors are shown in Fig. 4.3.

To appreciate the origin of these factors, first recall that the fermion is foreground, and thus an extra FSF is recruited for both the inbound and outbound legs of each vertex. This reflects that after the first interaction the intermediate fermion segment may propagate and interact outside of the locally correlated area before returning, and regardless of whether it does so or not, the foreground nature of the correlations it carries—which are in addition to the correlations of the background field—necessitate the introduction of additional FSFs. (At its simplest this may be a single additional FSF capable of hosting both a holomorphic and an antiholomorphic derivative with foreground correlations, which may bridge between the lower and the upper vertices.) Note that since a nonvanishing correlator requires that vertex co-ordinates x and y lie within the same correlation region, all additional FSFs are accessible to both vertices. Evaluating the FSF symmetry factors for the preon lines within the fermion (and recalling that factors associated with the noninteracting lines are subsumed into the fermion definition as per Secs. 3:3.2 and 3:3.5.1), the presence of these additional correlated FSFs yields factors of $(N_0 + 2)$ twice and $(N_0 + 1)$ twice. This may be compared with the factors on the emission vertex in Fig. 3.3.

²In actuality the factor of $(4\pi)^{-1}$ vanishes when the loop field is background, as is discussed in Appendix 6: A. However, this distinction has no impact on the present calculation.

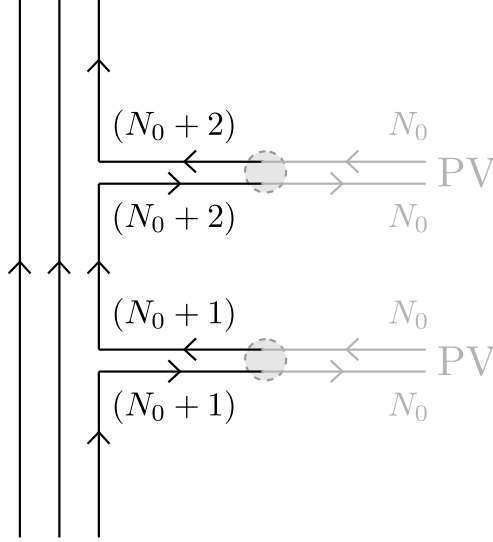


Figure 4.3: Symmetry factors arising from the exchange of fundamental scalar fields (FSFs). One factor attaches to each field operator appearing on a vertex. The net FSF symmetry factor for this diagram is $(N_0 + 2)^2(N_0 + 1)^2N_0^4$. [Each vertex also attracts a factor of $\frac{1}{3}$ from the normalisation of Eq. (3.28) but this is offset as each photon may couple to any of the three preons.]

Next, consider the preons in the background photons, which must come from the background fields. Considering the upper vertex first, the holomorphic and antiholomorphic preons at the upper vertex each attract factors of N_0 . Recalling that preons in photons may carry labels $a = 1$ or $a = 2$, if the preons of the lower vertex do not match those of the upper vertex then they also attract a factor of N_0 apiece. However, if they do match then each attracts a factor of $N_0 - 1$ from the background fields, plus a further factor of one as the inbound preon on the upper vertex may also be understood as an outbound antipreon, and the inbound antipreon as an outbound preon, giving one additional source apiece, replacing the effective free background preons which were consumed and once again returning a total FSF symmetry factor of N_0^2 for the background fields associated with the vertex. The net FSF symmetry factor for this diagram is thus

$$n_\varphi = (N_0 + 2)^2(N_0 + 1)^2N_0^4 \quad (4.9)$$

$$= N_0^8 [1 + 6N_0^{-1} + 13N_0^{-2} + \mathcal{O}(N_0^{-3})] \quad (4.10)$$

$$=: N_0^8 S_{6,13},$$

where $S_{6,13}$ is a convenient notation for this power series in N_0^{-1} introduced in Eq. (3.79).

By the choice of gauge described in Sec. 3:3.3.6, Eq. (4.5) is the only non-vanishing colourless boson correlator for the pseudovacuum at x and y : The $a^{12(\dagger)}$ bosons have been eliminated, the $G^{(\dagger)}$ pseudovacuum correlator always vanishes, the N boson has in this context been restricted to the colour sector, and the pseudovacuum correlators for $W^{(\dagger)}$ and Z boson fields vanish in the absence of a foreground particle of the same type.

Defining

$$m_e := \sqrt{\frac{n_\varphi}{2}} f \omega_0, \quad (4.11)$$

Eq. (4.7) becomes

$$\iint d^4x d^4y \sum_{e \in \{e_L, \bar{e}_R\}} [\bar{e}(x)\bar{e}(y)]_{\text{fg}} m_e [e(x)e(y)]_{\text{fg}} m_e. \quad (4.12)$$

When working at energy scales $\mathcal{E} \ll \mathcal{E}_0$ or over probe scales $\mathcal{L}_p \gg \mathcal{L}_0$ this will be indistinguishable from

$$\iint d^4x d^4y [\bar{e}_L(x)e_R(x)]_{\text{fg}} m_e [\bar{e}_R(y)e_L(y)]_{\text{fg}} m_e \quad (4.13)$$

due to the expression being non-vanishing only when co-ordinates x and y satisfy the window function constraint

$$\delta_{\mathcal{L}_0}^{(4)}(x^\mu - y^\mu) \neq 0 \quad (4.14)$$

arising from Eq. (1.169), and due to the intermediate lepton state between the two mass vertices not being accessible at probe scales large compared to \mathcal{L}_0 . Note that symmetry factors arising from different ways to connect the $\mathbb{C}^{\wedge 18}$ mass diagram have already been accounted for in constructing Eq. (4.1), and there are no further factors arising from Eq. (4.13), so identifying Eqs. (4.7), (4.12), and (4.13) with one another corresponds directly to equating the electron mass m_e in Eq. (4.12) with the leading order expression given in Eq. (4.11).

Expression (4.13) is exactly the Standard Model term for electron mass, applied twice to the left-handed electron and written in terms of Weyl spinors:

$$\iint d^4x d^4y \bar{e}_L(x)e_R(x)m_e \bar{e}_R(y)e_L(y)m_e. \quad (4.15)$$

In both instances the electron spinors pass through an intermediate state which is not observed, in which their helicities reverse. In the present model this is only an approximation introduced on going from Eq. (4.12) to Eq. (4.13), whereas in the Standard Model observation of this state is prohibited by imposing conservation of spin as a superselection criterion. Note that

- (i) a similar argument may be followed for the right-handed electron, and
- (ii) in the present model it is the window constraint (4.14) which requires close proximity of the interaction vertices, making the details of the mass mechanism undetectable at probe scales $\mathcal{L}_p \gg \mathcal{L}_0$ in the rest frame of the pseudovacuum.

Taking all of this into account, including the discussion of probe scales in Sec. 1:3.6.5, interaction with the background photon field $[A_\mu]_{\text{bg}}$ is anticipated to give rise to electron mass terms structurally equivalent to those of the Standard Model in current experimentally accessed regimes.

4:3.2.2 C-sector interactions

Now consider the role of the colour charge on interacting preons. First, note that the preon propagator lines in Fig. 4.1 have been oversimplified, ignoring both unpaired interactions with pseudovacuum photons, and a multitude of colour-mediated interactions between a preon and (i) its neighbours and (ii) the coloured bosons of the background field (Fig. 4.4).

Thus far, only interactions with pairs of colourless bosons separated by at most \mathcal{L}_0 have been considered. However, by definition of the pseudovacuum, interactions with unpaired bosons of any sort (or paired and separated by more than \mathcal{L}_0) must leave the pseudovacuum unchanged over length and timescales large compared with \mathcal{L}_0 , and thus unpaired bosons may impart no net mass or momentum to the propagating preon triplet.

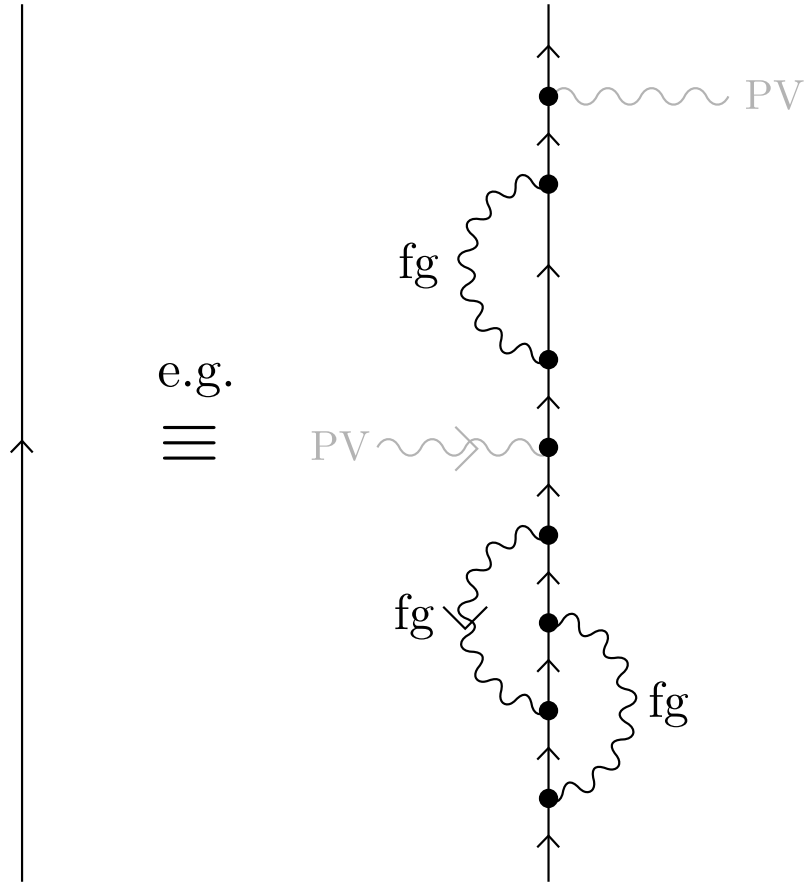


Figure 4.4: To represent the preon propagator as a single fermion line, even over length scales of $O(\mathcal{L}_0)$, is a major oversimplification neglecting the multiple interactions taking place between the preon, its neighbours, and the background field which may potentially change preon colour.

(i)	<table><tr><th>c_1</th><th>c_2</th><th>c_3</th></tr><tr><td>r</td><td>g</td><td>b</td></tr><tr><td>g</td><td>b</td><td>r</td></tr><tr><td>b</td><td>r</td><td>g</td></tr></table>	c_1	c_2	c_3	r	g	b	g	b	r	b	r	g	(ii)	<table><tr><th>c_1</th><th>c_2</th><th>c_3</th></tr><tr><td>r</td><td>b</td><td>g</td></tr><tr><td>b</td><td>g</td><td>r</td></tr><tr><td>g</td><td>r</td><td>b</td></tr></table>	c_1	c_2	c_3	r	b	g	b	g	r	g	r	b
c_1	c_2	c_3																									
r	g	b																									
g	b	r																									
b	r	g																									
c_1	c_2	c_3																									
r	b	g																									
b	g	r																									
g	r	b																									

Table 4.1: Colour configurations forming a basis on the colour sector for a colour-neutral preon triplet. Configurations (ii) are obtained by any pairwise column exchange of configurations (i).

The only remaining interactions to consider are thus paired coloured bosons engaging in the interactions shown in Fig. 4.2, and colour transfer to and from the pseudovacuum fields (which approaches negligible over scales large compared with \mathcal{L}_0 , and is guaranteed to vanish by a process described below). Since the gluons are seen in Chapter 5 to have masses on order of m_W at this length/energy scale, Eq. (4.5) implies that their direct contribution to particle mass may reasonably be ignored at leading order as it is small compared with that arising from the photon. However, each interaction between a preon and a coloured boson may change the colour of that preon, and this effect is distinct from that direct mass contribution and must still be accounted for. There are nine gluon-type bosons (three diagonal, six off-diagonal), and all are of equal mass. Although over the totality of the preon propagator they all appear in conjugate pairs, these may be overlapping and intercalated. Once again this is represented by allowing the fermion propagator between the two vertices to be massive.

Now note that the decomposition of $GL(9, \mathbb{R})$ to yield $SU(3)_A$ and $SU(3)_C$ in Eq. (3.7) is associated with the covariant derivative (3.19) in which the vector bosons of $su(3)_A$ and $su(3)_C$ act independently and with equal weight. This suggests that for each application of the (totality of the) $SU(3)_A$ sector's contribution to fermion mass, there is on average also one application of the (totality of the) $SU(3)_C$ sector's contribution. [This argument is made more formal in Appendix 4: A on examining the extension of the gauge choices of Sec. 3:3.3 to $SU(9)$ and its consequences for the construction of A -sector bosons.] Only the photon makes a meaningful contribution to the A sector's mass interaction and thus this is accompanied by application of the entire C sector.

To evaluate the $SU(3)_C$ sector's action on a preon triplet, introduce the vector notation

$$\psi^{a\alpha} = \begin{pmatrix} \psi^{ar\alpha} \\ \psi^{ag\alpha} \\ \psi^{ab\alpha} \end{pmatrix} \quad (4.16)$$

for an interacting preon, and recognise that on the colour sector the N boson acts as an additional, ninth gluon associated with the representation matrix

$$\lambda_9^C = \frac{1}{\sqrt{3}} \begin{pmatrix} 1 & 0 & 0 \\ 0 & 1 & 0 \\ 0 & 0 & 1 \end{pmatrix}. \quad (4.17)$$

Triplet (4.16) is therefore acted on by both the trivial and non-trivial (dimension-8) matrix representations of $su(3)_C$, collectively $\{\lambda_i^C | i \in 1, \dots, 9\}$. This symmetry is unbroken in the low-energy limit ($\mathcal{E}_p \ll \mathcal{E}_0$).

Now recognise that for a colour-neutral triplet of three preons at $\{x_i | i \in \{1, 2, 3\}\}$, a basis on the colour sector for a preon triplet is given by the six configurations of Table 4.1. However, in the low-energy limit the position of individual preons is not precisely determined, and must be integrated over a region of characteristic length at least \mathcal{L}_ψ . Where two preons have identical

A -charges, exchange of colour is equivalent to exchange of position, and is therefore seen to be a double-counting. Since all fermions not eliminated by gauge contain at least one pair of preons with identical A -charge, in the low-energy limit it therefore suffices to consider only Table 4.1(i). Putting preon 1 into a superposition of colour states then corresponds to a superposition of cyclic spatial rearrangements of the members of the triplet, with colours $c_1 = r$, $c_1 = g$, and $c_1 = b$ corresponding to colour assignments *with respect to preon spatial co-ordinates* of rgb , gbr , and brg respectively. It is then incidentally clear that for leptons at least, colour superselection is not violated in the low-energy regime, with any superposition of colour states on the constituent preons mapping into a superposition of preon spatial configurations.³

Next, consider the action of the bosons of both representations of $\text{su}(3)_C$ on a single preon in a fermion triplet. On average this preon will interact with background bosons of all such species with equal frequency, and each boson will act the associated representation matrix on the preon's colour state (4.16). Bosons in the non-trivial representation which have off-diagonal elements change the colour of the preon on which they act, breaking colour neutrality of the preon triplet.

On average any such colour change is reverted over a length scale of $O(\mathcal{L}_0)$. However, over any finite timescale there are only a finite number of such interactions, and measurement of the net colour charge of the preon triplet will interrupt some number of vertex pairs. As the number of interactions thus interrupted is finite, there is no guarantee that the net colour shift will vanish and hence colour measurements may be inconsistent even over macroscopic length and time scales. Since the macroscopic theory must be expressible without reference to the presence of the pseudovacuum, it is necessary to restore colour neutrality. Let a preon triplet with vanishing net foreground gluon interaction over macroscopic length scales *define* colour neutrality, and for each pair of interactions with conjugate bosons (Fig. 4.2) perform a local change of co-ordinates on a patch of space-time enveloping the non-interacting preons such that the triplet as a whole continues at all times to be colour-neutral.

As an aside, note that although measurements performed on a fermion may interrupt conjugate pairs of interactions with off-diagonal background gluons, these colour-unpaired interactions must nevertheless still occur in even numbers on any given subsystem. This is necessary in order that the background gluon correlator (3.70) which arises from these interactions does not vanish. This is automatically satisfied in the current scenario, as the colour interactions under consideration occur pairwise as per Fig. 4.2.

Returning to the effects on preon colour, for any given off-diagonal colour mapping, for example from g to r , contributions are received from two representation matrices which must be weighted with equal magnitude by non-violation of $\text{SU}(3)_C$ symmetry. Associating

$$r \equiv 1, \quad g \equiv 2, \quad b \equiv 3, \quad (4.18)$$

transformation of a preon from green to red is enacted by the representation matrices λ_1^C and λ_2^C , and these may be combined according to

$$\frac{1}{\sqrt{2}}(\pm\lambda_1^C \pm \lambda_2^C). \quad (4.19)$$

A preon being transformed from green to red therefore attracts a factor of

$$A = \pm \frac{1 \pm i}{2} \quad (4.20)$$

³The same argument cannot be applied directly to the preons in quarks due to inhomogeneity of A -charge, but may be applied in a more general form: Any superposition of states involving different colour configurations on one or more preons must have equal total charge across the whole state, and will admit interpretation as the result of colour-redistributing procedures and/or co-ordinate transformations—which for leptons may be reinterpreted as particle position exchange.

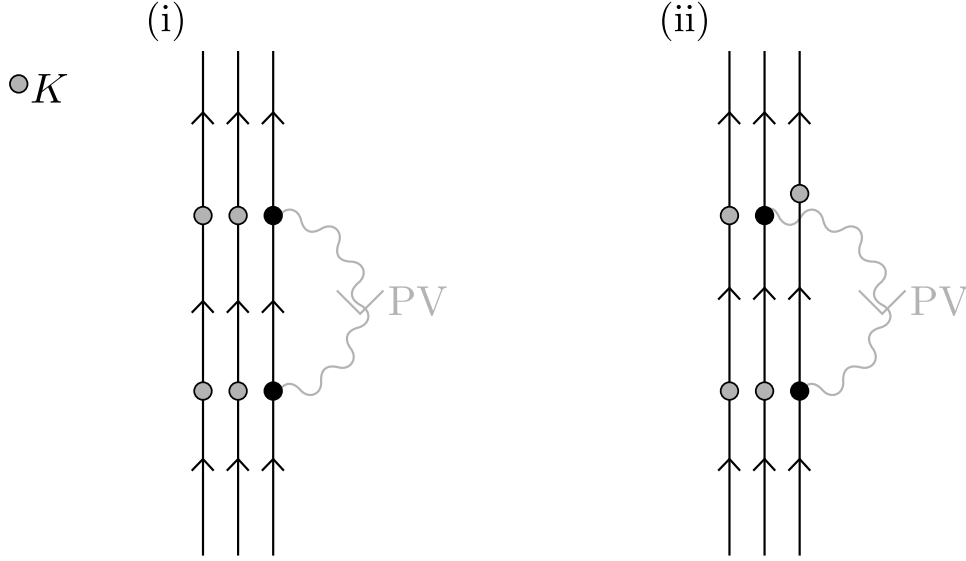


Figure 4.5: The gluon contributions to fermion mass, represented as a single $\text{GL}(3, \mathbb{R})$ -valued boson loop. The K -matrices act on all preons not coupling to the boson, and this is simultaneous with the boson interaction in the isotropy frame of the pseudovacuum. The K matrix is slightly offset in diagram (ii) for clarity.

with the net transformation corresponding to matrix $A e_{rg}$. Likewise, one being transformed from red to green attracts the conjugate transformation $A^* e_{gr}$. Other off-diagonal coefficients follow from colour cycle invariance. These coefficients may be collected into a matrix K ,

$$K = \begin{pmatrix} 1 & A & A^* \\ A^* & 1 & A \\ A & A^* & 1 \end{pmatrix}, \quad A = \pm \frac{1 \pm i}{2}, \quad (4.21)$$

with the diagonal elements being 1 as couplings which leave colour unchanged do not induce any co-ordinate transformation. For any given gluon acting at a lower vertex in Fig. 4.2, colour cycle invariance implies this is associated with the action of $K^{i+1, j+1} e_{i+1, j+1}$ and $K^{i+2, j+2} e_{i+2, j+2}$ on the other two preons of the triplet to maintain colour neutrality. The upper vertex is then acted on by the conjugate gluon and attracts the conjugate factors

$$K^{j+1, i+1} e_{j+1, i+1} = (K^{i+1, j+1} e_{i+1, j+1})^\dagger \quad (4.22)$$

$$K^{j+2, i+2} e_{j+2, i+2} = (K^{i+2, j+2} e_{i+2, j+2})^\dagger. \quad (4.23)$$

Collectively the nine gluon-type bosons may be summed to yield a single $\text{gl}(3, \mathbb{R})_C$ -valued boson

$$c_\mu^{ij} e_{ij} := c_\mu^{\tilde{c}} \lambda_{\tilde{c}}^C, \quad (4.24)$$

with concomittant summing of the co-ordinate transformations yielding a copy of matrix K acting on the colour space of each non-interacting preon simultaneous with the boson interaction (as determined in the isotropy frame of the pseudovacuum), as shown in Fig. 4.5. To collect

these effects together, define an operator

$$\begin{aligned}\hat{\mathcal{K}}_\mu = & c_\mu^{ij} e_{ij} \otimes K \otimes K \\ & + K \otimes c_\mu^{ij} e_{ij} \otimes K \\ & + K \otimes K \otimes c_\mu^{ij} e_{ij}.\end{aligned}\tag{4.25}$$

As each preon of the propagating fermion triplet undergoes a near-arbitrarily large number of such interactions over the course of any macroscopic propagator, it follows that the fermion triplet as a whole must be an eigenstate of pairwise applications of operator $[\hat{\mathcal{K}}_\mu]_{\text{bg}}$ (constructed using bosons $[c_\mu^{ij}]_{\text{bg}}$). For leptons, it further follows from colour-cycle invariance that each individual preon must be an eigenstate of matrix $K = K^{ij} e_{ij}$, and that that eigenstate must be the same for each member of the triplet. For leptons, it is therefore convenient to define an operator $\hat{K}^{(\ell)}$ which acts on a lepton $\Psi^{ag\alpha}$ to yield $k_g \Psi^{ag\alpha}$ (no sum over g) where $k_g|_{g \in \{1,2,3\}}$ is an eigenvalue of matrix K . Note that g is a label, not an index, so the choice of upper or lower position is not meaningful.

To complete the determination of matrix K , note that while the sign on i is free to be chosen by convention, the overall sign on A is fixed by requiring that a full cyclic permutation of colours ($r \rightarrow g \rightarrow b \rightarrow r$ and similar), which is in K^3 , must leave the sign of an eigenstate of K unchanged in accordance with the colour cycle invariance of the unbroken $\text{GL}(3, \mathbb{R})_C$ symmetry. The eigenvalues of K must therefore be non-negative, which requires that

$$A = -\frac{1 \pm i}{2}.\tag{4.26}$$

It is useful to write the mixing matrix K as a function of an angle θ_f . In the notation of Ref. [24]:

$$K = a_f E - b_f S(\theta_f)\tag{4.27}$$

$$E = \frac{1}{\sqrt{3}} \mathbb{I}_3\tag{4.28}$$

$$S(\theta_f) = \frac{1}{\sqrt{6}} \begin{pmatrix} 0 & e^{i\theta_f} & e^{-i\theta_f} \\ e^{-i\theta_f} & 0 & e^{i\theta_f} \\ e^{i\theta_f} & e^{-i\theta_f} & 0 \end{pmatrix}\tag{4.29}$$

$$a_f = b_f = \sqrt{3} \quad \theta_f = \frac{\pi}{4}.\tag{4.30}$$

Now recognise that when operator $\hat{\mathcal{K}}_\mu$ acts on a preon, implicitly representing a gluon/preon coupling, this occurs at an energy scale $\mathcal{E}_0 \ll \mathcal{E}_\psi$ and consequently this interaction is necessarily a gluon/fermion coupling. All preons in the fermion are involved in the vertex, and thus all preons attract FSF symmetry factors when they connect to a K matrix as in Fig. 4.5. In order to maintain normalisation of the nonparticipatory preons, these factors are accompanied by compensatory factors of N_0^{-2} per K matrix such that the norm of a free preon propagating in the presence of the pseudovacuum is maintained. Each preon in the triplet is of unique colour, and thus the symmetry factor n_φ is corrected to

$$\begin{aligned}n_\varphi &= (N_0 + 2)^6 (N_0 + 1)^6 N_0^4 \cdot N_0^{-8} \\ &= N_0^8 (1 + 18N_0^{-1} + 147N_0^{-2} + \dots)\end{aligned}\tag{4.31}$$

$$=: N_0^8 S_{18,147}\tag{4.32}$$

where the name $S_{18,147}$ has been assigned to this power series in N_0^{-1} .

Next, return to considering the mass interaction as a whole. The pseudovacuum photon interaction is summed over all choices of preon coupling, and since there are no foreground W or Z bosons in Fig. 4.1, this sum corresponds to the totality of the A -sector acting on all preons. This interaction is accompanied by the action of the totality of the C sector on all preons (including the preon(s) being acted on by the photon). The pseudovacuum photon interaction is capable of coupling any of the three preons to any of the three preons, while each gluon can couple one specific preon to one specific preon; as noted before, the direct contribution to particle mass arising from interactions between a fermion and the pseudovacuum gluon fields is small compared to the contribution from the photon field, and it is therefore convenient to treat each gluon contribution as a multiplicative correction to the corresponding photon contribution. As per Eq. (4.25), whenever gluons act on a preon, the corresponding co-ordinate transform from K acts on the other two preons of the triplet, and thus each photon (plus implicit gluon correction) is accompanied by a pair of K -matrices (Fig. 4.5).

Writing the gluon contribution as a multiplicative correction of order $[1 + \mathcal{O}(m_\ell^2/m_c^2)]$, it thus suffices to approximate each lepton/pseudovacuum interaction vertex by

$$\frac{f}{\sqrt{2}} \bar{\psi}^{\dot{a}} \hat{K}^{(\ell)\dagger} \bar{\sigma}^\mu \hat{K}^{(\ell)} \psi^a [a_\mu]_{\text{bg}} (\lambda_{\dot{a}}^A)_{aa} \left[1 + \mathcal{O}\left(\frac{m_\ell^2}{m_c^2}\right) \right] \Big|_{\dot{a}=3}. \quad (4.33)$$

Denoting the eigenvalues of matrix K as k_g , $g \in \{1, 2, 3\}$, the resulting leading-order expressions for the electron, muon, and tau masses are thus

$$m_{e_g} := \sqrt{\frac{n_\varphi}{2}} k_g^2 f \omega_0 \quad (4.34)$$

$$m_{e_1} \equiv m_e, \quad m_{e_2} \equiv m_\mu, \quad m_{e_3} \equiv m_\tau,$$

justifying the earlier introduction of index g in Eq. (3.31).

On computing the lepton masses as per Eq. (4.34) above, m_μ and m_τ are non-zero but m_e is found to vanish. However, a non-vanishing τ mass and non-vanishing gluon, W , and Z boson masses (see Chapter 5) imply the existence of non-vanishing electroweak loop corrections to Figs. 4.2(i)-(ii). Taking into account the evaluation of the weak interaction strength as per Sec. 3:3.5.3, the lowest-order correction is of $\mathcal{O}(m_\tau^2/m_W^2)$. Noting that

$$1 + \frac{m_\tau^2}{m_W^2} = \left(1 + i \frac{m_\tau}{m_W}\right) \left(1 - i \frac{m_\tau}{m_W}\right) \quad (4.35)$$

it is reasonable to speculate that this generation-dependent correction may be approximated by a correction to θ_f of order $\mathcal{O}(m_\tau/m_W)$. The dependency of K on preon species is not fully explored in the present chapter, but for now it suffices to note that higher-order diagrams do indeed give rise to corrections to θ_f which are dependent on fermion mass, and which result in a nonvanishing mass for the electron in Chapter 6.

With angle θ_f depending on fermion mass, and fermion mass in turn depending on preon charge, it follows that matrix K will in general depend on the species of preon to which it is applied. In the quarks, the dependency of the eigenvalues of K on preon type then selectively favours or disfavors interactions with the unique preon compared with the others, perhaps yielding an effective overall colour charge in addition to the dipole effect discussed in Secs. 3:3.2.1 and 3:3.4.2, again corresponding to the colour (or anti-colour) of the unique preon (or its inverse).

With regard to the construction presented in this Section, and in particular with the reduction of electroweak corrections to a shift in θ_f , it is worth noting several important points:

1. Mass matrices derived from Eq. (4.27) are known not to be capable of reproducing the observed lepton masses precisely [24].

2. However, the generation-dependent electroweak loop corrections to Fig. 4.2 also represents a deviation from form (4.27).
3. The best fit to observed values of the lepton masses obtainable using form (4.27) is given by setting [24]

$$\frac{b_f}{a_f} = \left[3 \frac{m_e + m_\mu + m_\tau}{(\sqrt{m_e} + \sqrt{m_\mu} + \sqrt{m_\tau})^2} - 1 \right]^{\frac{1}{2}} \quad (4.36)$$

$$\theta_f = \tan^{-1} \left(\sqrt{3} \frac{\sqrt{m_\tau} - \sqrt{m_\mu}}{\sqrt{m_\tau} + \sqrt{m_\mu} - 2\sqrt{m_e}} \right) \quad (4.37)$$

in K , yielding

$$\frac{b_f}{a_f} = 0.999991(10) \quad \theta_f = 0.8249679(83) \text{ radians}. \quad (4.38)$$

4. This best-fit value of θ_f corresponds to

$$\frac{\pi}{4} \left[1 + 2.27904(61) \frac{m_\tau}{m_W} \right] \text{ radians}, \quad (4.39)$$

so the correction to θ_f which yields the best possible fit is therefore of similar magnitude to both the the gluon contributions to particle mass, and the electroweak loop corrections required to Fig. 4.2.

It must be emphasised that the gluon and electroweak connections do *not* in fact take the form of a pure correction to θ_f , and this is just a convenient estimate allowing confirmation that the electroweak loop correction is of the correct order of magnitude to yield the observed lepton mass ratios. These corrections are addressed in detail in Chapter 6. [Note that purely electromagnetic loop corrections to Fig. 4.2(i)-(ii) also apply, but are independent of lepton mass so may be factored out into a generation-independent correction to Eq. (4.34) and thus do not appear in the estimated mass ratio.]

Also note that neutrinos acquire no mass through the photon term of this mechanism. However, the colour mixing matrix still admits the same eigenvectors, with three distinct eigenvalues, and terms in the mass process which are subleading for the photon are capable of giving rise to mass for the neutrinos. Further exploration is required to determine whether these masses are consistent with experimental constraints from neutrino mixing.

Finally, two observations with regards to the local change of co-ordinates which permits lepton triplets to remain colour-neutral. First, note that this change of co-ordinates is not a choice of gauge. It is therefore worth asking whether this transformation may be rewritten as the introduction of additional boson species. However, by construction these bosons are very tightly constrained, appearing only in conjunction with the K -matrices, acquiring no 4-momentum at their interaction vertices, and having no interactions other than to perform the desired preon colour changes. By the scale of the fermionic mass interaction, their effects vanish when integrated over regions larger than $O(\mathcal{L}_0)$. To represent these colour-transformations as bosons is therefore not productive. (This may be contrasted with the *energy-dependent* co-ordinate transforms of Sec. 6:5.3.3, where the boson description is very useful indeed.) Second, recognise that unpaired interactions with the background gluon field may also impart random shifts in preon colour. These too may be eliminated by adjusting the local $SU(3)_C$ co-ordinate transformations, but these random shifts do not yield any systematic contribution to the K matrix and thus over length scales large compared with \mathcal{L}_0 they have no effect on the eigenvalues of operator $\hat{\mathcal{K}}$. This observation is necessary for the earlier assertion that all intercalated interactions may be represented by making the intermediate fermions of Fig. 4.2 massive.

4:3.3 Quarks and preons

As commented on briefly above, a calculation similar to that for leptons also applies for quarks. However, the varying A -charges within the quark triplets imply that colour cycle invariance is only respected across superpositions of colour combinations for the triplet as a whole, and is anticipated to result in a quark colour mixing matrix K_q which is A -charge-dependent. If the colour of the unique quark is taken to provide a reference point in colour space, then this dependency breaks colour cycle invariance, which may have a role in the residual colour charge on the quarks. Further, it is also likely that this A -charge dependency will permit calculation of this model's counterpart to the CKM matrix. It is interesting to speculate that this difference between lepton and quark eigenvectors may facilitate neutrino generation mixing during interactions with baryonic matter, though this idea is not explored further here.

It is also noted that:

- Individual foreground preons may acquire mass through interactions with the background fields in the same way as foreground fermions, and that for preons with A -charge $a = 1$ or $a = 2$ this effect will be dominated by interaction with the background photon field, giving these preons non-zero rest masses. It follows that summed preon pairs $\psi^{1c_1\alpha}\psi^{2c_2\alpha}$ will not in general vanish, in conflict with the choices of gauge on $SU(3)_C$ discussed in Sec. 3:3.3.6, with the outcome that species incorporating such pairs have no valid foreground on-shell excitations as noted in Sec. 3:3.3.7.
- K -matrices are only associated with all-species interaction vertices in which the gluon sector is viewed as a small but nonvanishing correction to the photon sector, and is dominated by its background field term. This is because K -matrices arise in response to the colour transformations mediated by the gluons of the background field, being co-ordinate transformations induced on the other preons present on allowing the preon triplet to define colour neutrality. As discussed in Sec. 4:3.2.2, these gluon vertices are in 1:1 correspondence with A -sector interactions and risk proceed unremarked when the interacting species are collectively colourless. It is therefore crucial to recognise all-species processes as distinct from situations involving only a specific boson. For example:
 - Interaction of a fermion with the background boson fields over length scales of $O(\mathcal{L}_0)$ is an all-species interaction as per Sec. 4:3.2 above.
 - The electroweak interaction of Sec. 3:3.5 is a single-species interaction. Only one photon interaction takes place at emission and one at absorption, and thus there is likewise only one associated colour interaction. To be nonvanishing these interactions must form a conjugate pair, but over foreground length- and timescales they are uncorrelated. Thus this is a single-species interaction with no associated K factors.
 - Further examples will be encountered in Chapters 5 and 7.

4:4 Conclusion

This chapter has introduced the mass mechanism for fermions in the \mathbb{C}^{18} model, as illustrated by a tree-level calculation of the lepton masses. An interesting feature of this model is its ability to approximately reproduce the Koide relationship between the charged lepton masses, and a preliminary calculation indicates that higher-order corrections to the mass process are of the correct magnitude to potentially improve upon this approximation.

The next chapter presents an equivalent calculation for bosons, following which the evaluation of higher-order corrections to both of these calculations in Chapter 6 yields the first predictive calculations of the $\mathbb{C}^{\wedge 18}$ analogue model.

Appendices

4: A Extension of gauge choices to SU(9)

It is frequently convenient to decompose the local $SU(9) \otimes GL(1, \mathbb{R})$ symmetry of the $\mathbb{C}^{\wedge 18}$ model as $[SU(3)_A \oplus GL(1, \mathbb{R})_A] \otimes [SU(3)_C \oplus GL(1, \mathbb{R})_C]$, as is done through much of the present paper. However, in the corresponding quantum field theory the bosons associated with $su(9)$ may carry charges in both the A and the C sector on a single quantum whereas those of $su(3)_A$ or $su(3)_C$ are restricted to the A sector or the C sector respectively. The situation is further complicated by the representations of $gl(1, \mathbb{R})_A$ and $gl(1, \mathbb{R})_C$ being accidentally degenerate.

To extend the gauge choices of Sec. 3:3.3 to the full $SU(9)$ symmetry, recognise as follows:

- A choice of gauge involving a boson $b_\mu^{\tilde{a}}$ in $su(3)_A$ may be understood as generalising to the nine bosons carrying the same A -sector charge in $su(3)_A \otimes [su(3)_C \oplus gl(1, \mathbb{R})_C]$.
- A choice of gauge involving a boson $b_\mu^{\tilde{c}}$ in $su(3)_C$ may be understood as generalising to the nine bosons carrying the same C -sector charge in $[su(3)_A \oplus gl(1, \mathbb{R})_A] \otimes su(3)_C$.
- Due to accidental degeneracy, the gauge choices associated with $gl(1, \mathbb{R})_A$ and $gl(1, \mathbb{R})_C$ are mediated by a single boson N_μ which may be viewed as a representation of either $gl(1, \mathbb{R})_A$ or $gl(1, \mathbb{R})_C$. When there is only a single gauge boson present, the generalisations of these choices of gauge consequently apply to all of $gl(1, \mathbb{R})_A \otimes gl(1, \mathbb{R})_C$, $gl(1, \mathbb{R})_A \otimes su(3)_C$, and $su(3)_A \otimes gl(1, \mathbb{R})_C$. When multiple boson fields overlap, gauge choices (3.43–3.44) apply to the sum of all bosons involving a trivial representation on one or both sectors.
- However, note that the choices involving $gl(1, \mathbb{R})_A$ and/or $gl(1, \mathbb{R})_C$ act at the level of composite fermions as per Eqs. (3.43–3.44). They consequently place no constraints on interactions at the level of individual preons.

Now revisit the construction of single-sector bosons, and begin with the bosons of the C sector. Recognise that all leptons, even quarks, are colour-neutral sums over preon triplets as per Sec. 3:3.4 (with the apparent quark colour residual arising from a difference in spatial distribution of the constituent preons in conjunction with colour shielding). Each of the nine gluons is only able to interact with one preon out of a colour-neutral triplet, and thus gluon interactions are always gluon/preon interactions, not gluon/fermion interactions. Couplings involving the $gl(1, \mathbb{R})_B$ symmetry groups are therefore permitted. The nine bosons of the C sector are then readily constructed as representations of $gl(1, \mathbb{R})_A \otimes su(3)_C$.

For the A sector, a different approach is required. A -sector bosons interact with the totality of a fermion; for leptons this is immediately apparent as the three preons share a common A -charge, while for quarks it is enforced as described in Sec. 3:3.5.4 where choices of co-ordinate frame ensure that any A -sector interaction is consistent with the fermionic A -charges. For whole-fermion interactions, the construction of bosons involving $gl(1, \mathbb{R})_C$ is prohibited by gauge choices (3.43) and (3.44). Instead, to construct a colour-neutral A -sector boson, recognise that colour charges always appear in the context of a sum over all possible input and output colours, and write

$$b_\mu^{\tilde{a}} \propto \sum_{\tilde{c}} \bar{\psi}^{\dot{a}\tilde{c}} \bar{\sigma}_\mu \psi^{ac} [\lambda^{A\tilde{a}}]_{\tilde{a}\tilde{a}} [\lambda_{\tilde{c}}^C]_{\tilde{c}c}, \quad (4.40)$$

for example

$$W_\mu \propto \sum_{\tilde{c}} \bar{\psi}^{3\tilde{c}} \bar{\sigma}_\mu \psi^{2c} [\lambda_{\tilde{c}}^C]_{\tilde{c}c}, \quad (4.41)$$

where $\lambda_{\tilde{c}}^C$ are the rescaled Gell-Mann matrices including $\lambda_9^C := \frac{1}{\sqrt{3}}\mathbb{I}_3$. At the level of an individual preon, the action of this sum on the colour sector incorporates all nine bosons of $\text{su}(3)_C \oplus \text{gl}(1, \mathbb{R})_C$ and corresponds to an application of the matrix K discussed in Sec. 4:3.2.2 (noting that the eigenvectors of K are also eigenvectors of the traceless diagonal matrices λ_3 and λ_8 with eigenvalue zero, so the absence of any contributions to K from λ_3 and λ_8 is unimportant). The eigenvectors of this matrix correspond to the different generations of fermion, while the eigenvalues of K are absorbed by choosing differing normalisations for the associated fermion fields. For example, a vertex $\frac{g}{2} A \bar{e}_L e_L$ contains an implicit factor of k_1 arising from the photon, and simultaneously redefining

$$A_\mu \rightarrow A_\mu K^{-1} \quad (4.42)$$

$$[e_L]_i \rightarrow [e_L]_i k_i^{\frac{1}{2}} \quad (4.43)$$

etc.

yields fermion fields which interact with the A -bosons via an effective K -matrix having the form \mathbb{I}_3 . It is consequently acceptable to assume the rescaled fermion fields, omit the K -matrix in the treatment of the A -sector interactions in Sec. 3:3.5, and to act the K -matrix only on the non-interacting preons in the mass calculation of Sec. 4:3.2.2. Further, on evaluating the net coupling of a boson of form (4.40) to the colour-homogenised pseudovacuum, it follows from Eqs. (4.21) and (4.26) that the elements of a row of the K -matrix sum to zero and hence these species acquire no mass from the gluon components of the pseudovacuum, as is expected for a species of no net C -sector charge.

Note that the redefinition of the fermion fields has no impact on the gluon coupling constants, as gluons act at the level of individual preons, not fermions.

Now consider the far field of the preon triplet, in which A -sector interactions behave as fermion/boson interactions. The A -sector bosons continue to take the form of Eq. (4.40) but in this regime the net coupling of the various preons to the $[\text{su}(3)_A \oplus \text{gl}(1, \mathbb{R})_A] \otimes \text{gl}(1, \mathbb{R})_C$ sector vanish by gauge choices (3.43–3.44). For a given A -charge, an effective A -sector boson in the far field of an emitting lepton is therefore a superposition on the C -sector over the eight elements of $\text{su}(3)_C$.⁴

Following this treatment, boson exchange is observed to behave largely as if the A and C sectors are separable, as assumed in this document—with two notable exceptions. First, in few-particle experiments it may be necessary to explicitly consider the bosons of $\text{su}(9)$ in certain regimes, most notably collisions in particle accelerators at energies

$$1.79 \text{ GeV} < E < 3.09 \text{ TeV} \quad (4.44)$$

as per Appendix 6:E.2 and Chapter 8, and second, there are some subtleties relating to particle generations and the $W \bar{e}_L \nu_e$ vertex which are discussed in Sec. 10:2.

⁴An A -sector boson emitted by another boson may hypothetically comprise a superposition over all nine elements of $\text{su}(3)_C \oplus \text{GL}(1, \mathbb{R})_C$. However, the only experiment yet performed which is anticipated to be sensitive to the construction of the C -neutral A -sector bosons is the Fermilab Muon $g-2$ experiment, in which interactions predominantly feature a lepton source. This experiment yields results primarily indicative of eight-component C -neutral A -sector bosons, with a small correction arising from the use of nine-component C -neutral A -sector bosons in a higher-order term. See Chapter 8 and Ref. [27].

Acknowledgements

This research was supported in part by the Perimeter Institute for Theoretical Physics. Research at the Perimeter Institute is supported by the Government of Canada through Industry Canada and by the Province of Ontario through the Ministry of Research and Innovation. The author thanks the Ontario Ministry of Research and Innovation Early Researcher Awards (ER09-06-073) for financial support. This project was supported in part through the Macquarie University Research Fellowship scheme. This research was supported in part by the ARC Centre of Excellence in Engineered Quantum Systems (EQuS), Project No. CE110001013.

Chapter 5

Calculation of boson masses on $\mathbb{C}^{\wedge 18}$

Abstract

The $\mathbb{C}^{\wedge 18}$ model is an analogue model capable of emulating the complete particle spectrum of the Standard Model, including interactions, using only free scalar fields on a manifold with anticommuting co-ordinates. Solitonic excitations in a pseudovacuum state behave as coloured preons, forming triplets which behave as emergent fermions and pairs which behave as emergent bosons. This chapter demonstrates how the emergent bosons acquire mass through interaction with the pseudovacuum. The existence of higher-generation massive bosons is cautiously predicted (subject to limitations of the $\mathbb{C}^{\wedge 18}$ analogue model), with the lightest being the second-generation W boson at $16.61730(47) \text{ TeV}/c^2$.

5:1 Introduction

The $\mathbb{C}^{\wedge 18}$ model introduced in Chapter 3 is a classical analogue model [7–9] remarkable for the behaviour of its quasiparticle description in the low-energy limit, which qualitatively resembles the quantum field theory of the Standard Model. The value of an analogue model comes from its ability to grant physical or numerical insight into the system being described, prompting the evaluation of observable quantities in the $\mathbb{C}^{\wedge 18}$ model such as particle mass. Tree-level evaluation of fermion masses in Chapter 4 is remarkable for hinting at an approximately Koide-like [24, 25] relationship between the masses of different generations of leptons. This chapter continues the calculation of tree-level mass interactions in the $\mathbb{C}^{\wedge 18}$ model, this time for the vector and scalar boson fields, with higher-order corrections following in Chapter 6. The $\mathbb{C}^{\wedge 18}$ model is seen to predict the existence of higher generations of massive bosons, though care is required as the masses of these bosons are above the threshold below which the $\mathbb{C}^{\wedge 18}$ model behaves as a good analogue to a quantum field theory.

5:2 Conventions

This chapter follows the same conventions as Chapters 1–4. Units are chosen such that $c = 1$, $\hbar = 1$. When equations and lemmas from Chapters 1–4 are referenced, they take the forms (1.1), (2.1), etc.

In particular, regarding terminology around Feynman diagrams and symmetry factors:

- Where there exist multiple ways to connect up sources, vertices, and sinks to obtain equivalent diagrams up to interchange of non-distinguishable co-ordinates, the same term is obtained from the generator \mathcal{Z} in multiple different ways and thus the diagram acquires a multiplicative factor. This is referred to in the present volume as a *symmetry factor*.
- Where integration over the parameters of a diagram (for example, over source/sink co-ordinates) yields the same diagram multiple times up to interchange of labels on these parameters, this represents a double- (or multiple-)counting of physical processes. It is then necessary to eliminate this multiple-counting by dividing by the appropriate symmetry factor. This is referred to in the present volume as *diagrammatic redundancy* or *double- (multiple-)counting*.

5:3 Boson masses

5:3.1 Vector boson masses

For vector bosons, multiple candidates for mass terms arise from interactions between the propagating boson and both the background preon and boson fields as shown in Fig. 5.1. To address each in turn for a general vector boson $V_\mu^{(\dagger)}$:

5:3.1.1 Fig. 5.1(i):

The $O(f^2)$ four-boson vertex with two background fields yields the background (pseudovacuum) photon term

$$-\frac{n_\varphi f^2}{2} \iint d^4x d^4y [V_\mu^\dagger(x) V^\mu(x)]_{\text{fg}} [A_\nu(x) A^\nu(x)]_{\text{bg}}, \quad (5.1)$$

and similar for background gluons and dilatons. The boson may interact with any of the three preons in the fermion pair, but this cancels with factors of $1/\sqrt{3}$ from Eq. (3.28) (see also Sec. 3:3.5.8 and Fig. 4.3). It vanishes when V^μ is a photon due to the absence of colour or self-coupling, and for the Z boson as it has no charge. In the $SU(3)_A$ sector this diagram therefore contributes mass only to the $W^{(\dagger)}$ and $G^{(\dagger)}$ bosons. By comparison with Eq. (4.34) its contribution is of $O(k_1^{-4} m_e^2)$, and is unlikely to exceed $O(m_\tau^2)$. (This is confirmed in Chapter 6.) There exists a similar contribution to the gluon mass m_c , but this arises instead from the bosons of $\text{gl}(3, \mathbb{R})_C$.

Note that in contrast to the two-photon interactions of Fig. 4.1, there is no foreground propagator separating the two pseudovacuum interaction vertices. This diagram therefore does not attract a factor of $\mathbf{f}(\cdot)$ (4.2) even when the background boson is a gluon.

5:3.1.2 Fig. 5.1(ii):

This diagram yields background photon terms of the form

$$\begin{aligned} & -\frac{n_\varphi f^2}{4} \iint d^4x d^4y \\ & \{ (\delta^{\mu\rho} \delta^{\nu\sigma} + \delta^{\nu\rho} \delta^{\mu\sigma}) [A_\mu(x)]_{\text{bg}} [V_\nu^\dagger(x) \partial_\rho V_\sigma'(x)]_{\text{fg}} \\ & \quad + (\delta^{\mu\rho} \delta^{\nu\sigma} + \delta^{\nu\rho} \delta^{\mu\sigma}) [\partial_\mu A_\nu(x)]_{\text{bg}} [V_\rho^\dagger(x) V_\sigma'(x)]_{\text{fg}} \} \\ & \times \{ (\delta^{\lambda\pi} \delta^{\kappa\tau} + \delta^{\kappa\pi} \delta^{\lambda\tau}) [A_\lambda(y)]_{\text{bg}} [V_\kappa'^\dagger(y) \partial_\pi V_\tau(y)]_{\text{fg}} \\ & \quad + (\delta^{\lambda\pi} \delta^{\kappa\tau} + \delta^{\kappa\pi} \delta^{\lambda\tau}) [\partial_\lambda A_\kappa(y)]_{\text{bg}} [V_\pi'^\dagger(y) V_\tau(y)]_{\text{fg}} \} \end{aligned} \quad (5.2)$$

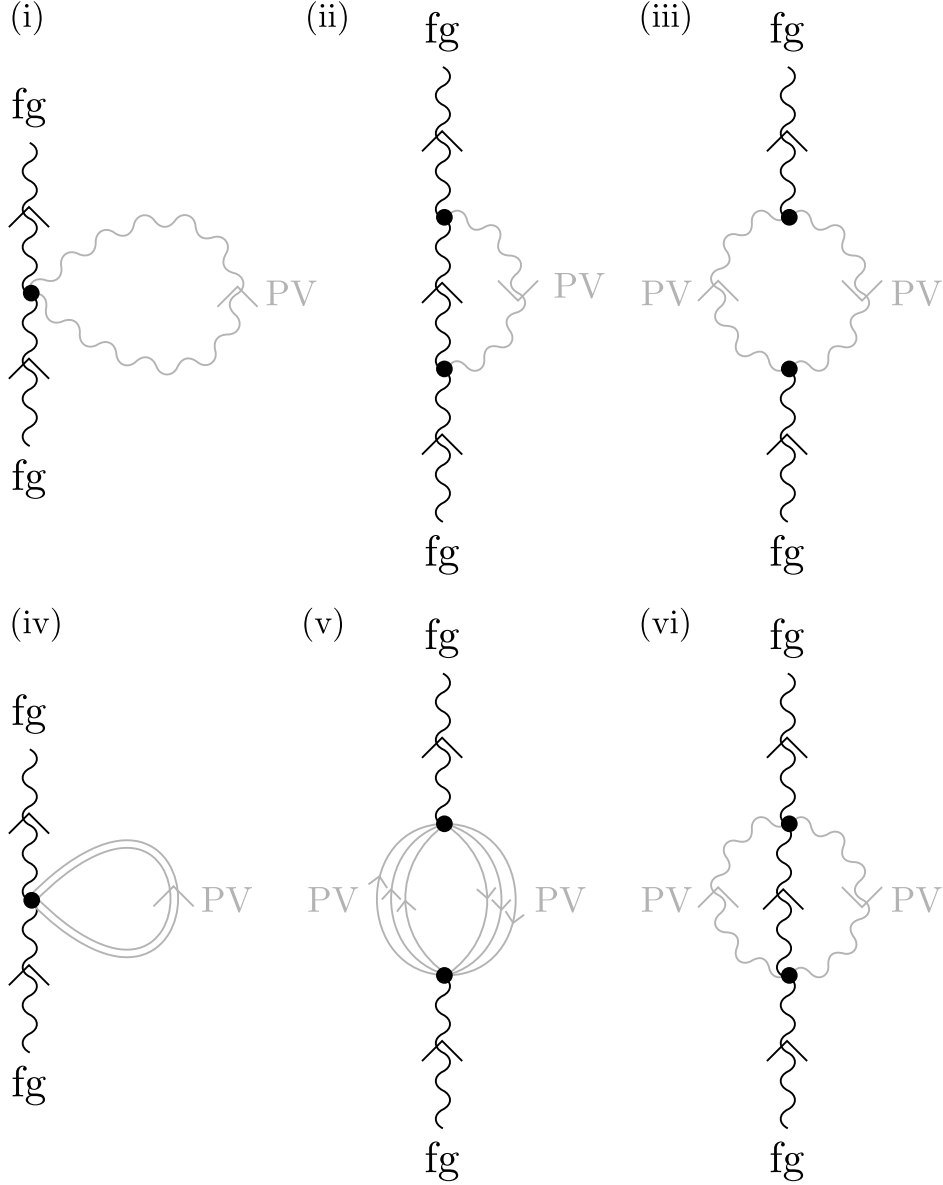


Figure 5.1: Graph types for interactions between a foreground vector boson and the pseudovacuum (PV) vector boson, scalar boson (double line), and fermion fields. (i) $O(f^2)$ interaction with two PV bosons. (ii) Two consecutive $O(f)$ interactions with single PV bosons. (iii) Two disjoint $O(f)$ interactions, each with two PV bosons. (iv) $O(f^2)$ interaction with two PV scalar bosons. This diagram is the scalar counterpart to diagram (i); scalar counterparts to diagrams (ii) and (iii) are also discussed in the text. (v) Two disjoint $O(f)$ interactions, each with six PV preons. Further diagrams can be constructed, e.g. (vi), but reduce to composites of diagrams already discussed. For example, if the central boson in diagram (vi) is foreground (as shown), this corresponds to two copies of the interaction of diagram (ii). If the central boson is background, this corresponds to compounding diagrams (ii) and (iii).

and similar for pseudovacuum gluons up to $\mathbf{f}(\cdot)$. In the electron mass interaction of Eq. (4.5), spinor identities allowed two spatially separated one-boson interactions to be rewritten as an absolute square. In this diagram there is no equivalent identity, so instead the properties of the pseudovacuum may be used to contract the two vertices, replacing

$$\langle [A_\mu(x)A_\nu(y)]_{\text{bg}} \rangle = -\frac{1}{4}\mathbf{f}(x-y)N_0^4\omega_0^2\eta_{\mu\nu}. \quad (5.3)$$

The resulting contraction of the two vertices yields an expression equivalent to an all-foreground loop diagram weighted by a mass coefficient. Comparing with Sec. 5:3.1.1, this expression corresponds to one of the diagrams obtained on expanding the $W^{(\dagger)}$ propagators with Proper Self Energy terms. It is therefore not necessary to count this diagram separately. The same argument applies if the background vector boson is replaced by a background scalar boson.

5:3.1.3 Fig. 5.1(iii):

This diagram is very similar to Fig. 5.1(ii), and with good reason, as both are obtained from mean field theory expansion of the same original figure. This diagram is the lowest-order in foreground fields, and the foreground momentum is understood to travel from the lower to the upper vertex as perturbations about this mean field term. If the interaction vertices are not collocated, a basis (not necessarily spatial) may always be chosen such that all foreground momentum is transferred in a single limb of the loop, recovering Fig. 5.1(ii). Alternatively, if the vertices are collocated, the diagram reduces to the duplication of Fig. 5.1(i). Either way, it is redundant.

5:3.1.4 Fig. 5.1(iv):

This diagram is similar in structure to Fig. 5.1(i), but with the composite scalar boson in place of a vector boson. Mapping $\partial^\mu\partial_\mu$ to $\partial\partial\bar{\partial}\bar{\partial}$ attracts a factor of -2 , but this is offset by a factor of $-\frac{1}{2}$ on evaluating $\langle [\bar{\psi}\psi\psi\psi]_{\text{bg}} \rangle$ using Eq. (3.92). Unusually for a scalar boson the vertex factor is augmented by a FSF symmetry multiplier $N_0^8[1 + \mathcal{O}(N_0^{-1})]$ —this is not reduced by N_0^2 as the composite scalar bosons are emitted at a single vertex and are therefore immediately mapped to their local mean field values without first requiring propagation (see discussion in Sec. 3:3.5.5). Overall this term again evaluates to $\mathcal{O}(k_1^{-4}m_e^2) \lesssim \mathcal{O}(m_\tau^2)$ so contributes only a relatively small amount to m_W^2 .

5:3.1.5 Fig. 5.1(v):

The main contribution to vector boson masses comes from diagrams of the form of Fig. 5.1(v). This diagram is non-vanishing if the preon sources and sinks are all separated by a distance of $\mathcal{O}(\mathcal{L}_0)$ or less, and thus appear collocated to a probe with energy $\mathcal{E}_p \ll \mathcal{E}_0$ or timescale $\mathcal{L} \gg \mathcal{L}_0$ (essentially all probes—see Sec. 1:3.6.5). That is, the two vertices are effectively collocated as discussed in the context of Fig. 5.1(iii), though this time the resulting figure has not previously been accounted for.

Regarding the preon lines in this diagram, note that

- A composite boson necessarily has energy small compared with \mathcal{E}_ψ in the isotropy frame of the pseudovacuum. Since \mathcal{E}_ψ is also anticipated to exceed the energy scale of the pseudovacuum, \mathcal{E}_0 , the preons making up the composite particles in Fig. 5.1(v) appear as bound triplets.
- In the presence of the background fields, the dominant contribution to the average value of Fig. 5.1(v) is given by replacing the fields of the loop with the mean-field value for the

pseudovacuum contribution. Consequently these fields do not give rise to a loop factor $\mathbf{f}(\cdot)$, as there is no foreground propagator between the two interaction vertices in this mean-field term.

- Nevertheless, foreground momentum must be transferred between the lower and the upper vertex and this takes place through perturbations about this mean-field value. These may be viewed as equivalent to foreground fields.
- As discussed in Sec. 4:3.2.2, whenever a fermion engages in an A -sector boson interaction (such as the W interaction discussed here), this may be associated with a set of co-occurring C -sector interactions, corresponding in this case to couplings to the background gluon fields at the upper and lower vertices of the loop. For the background component of the fermion loop the normalisation convention of Sec. 1:3.8.6 ensures that these interactions make no direct contribution to the W boson mass vertex. However, the freedom to pair non-conjugate gluons as per Eq. (3.70) indicates that nonvanishing colour perturbations may take place in these interactions, and following Sec. 4:3.2.2 it is convenient to evaluate the impact of these couplings by associating them with the dominant A -sector interaction. Since $SU(3)_C$ symmetry is preserved, these couplings place the background fermion into eigenstates of matrix K as before.
- In contrast with Sec. 4:3.2.2, however, these C -sector couplings are optional. In Sec. 4:3.2.2 a sum over all propagation processes comprised terms involving fermion/photon coupling and terms involving fermion/gluon coupling, with each vertex appearing in equal numbers, such that each photon interactions was on average accompanied by nine gluon interactions and thus by matrices K . In the present context, the sum over all propagation processes includes the W boson in every diagram, but the preons of the loop may interact either as two background fermions, which accrue K matrices, or as three background bosons, which do not accrue K matrices, in an alternative process discussed further in Sec. 6:4.1.8. (The background preons must always arise from composite background particles, as the background energy scale \mathcal{L}_0 is assumed small compared with \mathcal{L}_ψ .) Consequently there *may* be K matrices associated with the W /preon triplet vertices, and summation over all propagation processes includes diagrams both with and without these matrices present. However, only diagrams with K matrices are considered in the present chapter, as the value of the diagram is much reduced when the K matrices are absent.
- Given the presence of K matrices, it is convenient to work in the generations basis for fermions. At tree level this corresponds to eigenvectors of the colour mixing matrix K given in Eq. (4.27). The vertices may admit triplets from any generation.
- Symmetry factors are computed as normal, as they arise through the extraction of interaction vertices from the generating functional and are independent of the manner by which the propagators are evaluated (e.g. Green's function vs. mean field theory), though care must be taken not to double-count any symmetry factors already present in the mean field expressions. For this reason, as in Eq. (4.8), evaluation in terms of ω_0 (1.230) is preferred over \mathcal{E}_0 (1.166).

It is convenient to represent preon triplets of any generation by the symbols of their associated fermions. The K matrices implicit in the vertices of Fig. 5.1(v) similarly imply a generation structure for massive bosons where (to tree level) the lightest second-generation boson is a W boson with a first approximation to its mass satisfying

$$m_{W_2} \approx \frac{m_{W_1} m_\mu}{m_e} \approx 17 \text{ TeV}/c^2. \quad (5.4)$$

Since only one generation of $W^{(\dagger)}$ bosons has yet been observed, for now restrict attention to generation 1 and see also the discussion in Sec. 5:3.2.

Taking the $W^{(\dagger)}$ boson as the first example of a vector boson acquiring mass from Fig. 5.1(v), and deferring calculation of FSF symmetry factors, the lepton channel is

$$-36f^2k_1^4 \iint d^4x d^4y [W_\mu^\dagger(x)W_\nu(y)]_{\text{fg}} \times [\bar{\nu}_e(x)\bar{\sigma}^\mu e_L(x)\bar{e}_L(y)\bar{\sigma}^\nu \nu_e(y)]_{\text{bg}} \quad (5.5)$$

where the factor of 36 arises as there are $3!$ ways to order the electron propagators on the left (with the exchange of two lines corresponding to the exchange of two spinor operators on the upper vertex and two on the lower vertex for a net factor of $+1$) and $3!$ ways to order the neutrino propagators on the right. The quark channel is similarly

$$-36f^2k_1^4 \iint d^4x d^4y [W_\mu^\dagger(x)W_\nu(y)]_{\text{fg}} \times [\bar{u}_L(x)\bar{\sigma}^\mu d_L(x)\bar{d}_L(y)\bar{\sigma}^\nu u_L(y)]_{\text{bg}} \quad (5.6)$$

where the factors for reordering of identical propagators are now $2! \times 2!$, but each triplet also acquires a factor of 3 corresponding to the three different choices as to the colour of the unique preon, once again giving a net total symmetry factor of 36.

Expanding the fermions and bosons as preons and calculating the FSF symmetry factors proceeds very similarly to Fig. 4.3, only now the foreground preons are in the boson part of the diagram, not the fermion part. These factors are shown in Fig. 5.2. As before, background fields contribute symmetry factors of N_0 per preon and thus the overall FSF symmetry factor is

$$n_{\varphi,W} = (N_0 + 2)^2(N_0 + 1)^2N_0^{12} = N_0^{16}S_{6,13} \quad (5.7)$$

where

$$S_{6,13} := N_0^{-4}(N_0 + 2)^2(N_0 + 1)^2 \approx (1 + 6N_0^{-1} + 13N_0^{-2} + \dots) \quad (5.8)$$

as in Eq. (3.79). From $n_{\varphi,W}$, a factor of N_0^4 is customarily absorbed into the definition of the fermion so that the factors associated with the noninteracting preons can be suppressed. However, to eliminate the noninteracting preons entirely it is more convenient to leave the FSF factors explicit and integrate over d^4y . The fermions therefore take the form of Eq. (3.28). The paired background preons thus take the form

$$f^2 \left\langle \bar{\psi}^{\dot{a}\dot{c}} \bar{\psi}^{\dot{a}\dot{d}} \psi^{ac} \psi^{ad} \right\rangle_{\dot{a}=a, \dot{c}=c, \dot{d}=d} \quad (5.9)$$

which evaluates as

$$-\frac{f^2}{2} \left\langle \left\| \bar{\psi}^{\dot{a}\dot{c}} \bar{\sigma}_\mu \psi^{ad} \right\|^2 \right\rangle_{\dot{a}=a} = -\frac{1}{2} \left\langle \left\| \varphi_\mu^{\dot{a}a\dot{c}d} \right\|^2 \right\rangle = \frac{1}{2} N_0^2 \omega_0^2 \quad (5.10)$$

with integral with respect to y of

$$\int d^4y \left[f^2 \left\langle \bar{\psi}^{\dot{a}\dot{c}} \bar{\psi}^{\dot{a}\dot{d}} \psi^{ac} \psi^{ad} \right\rangle_{\dot{a}=a, \dot{c}=c, \dot{d}=d} \right]^2 = \frac{1}{4}. \quad (5.11)$$

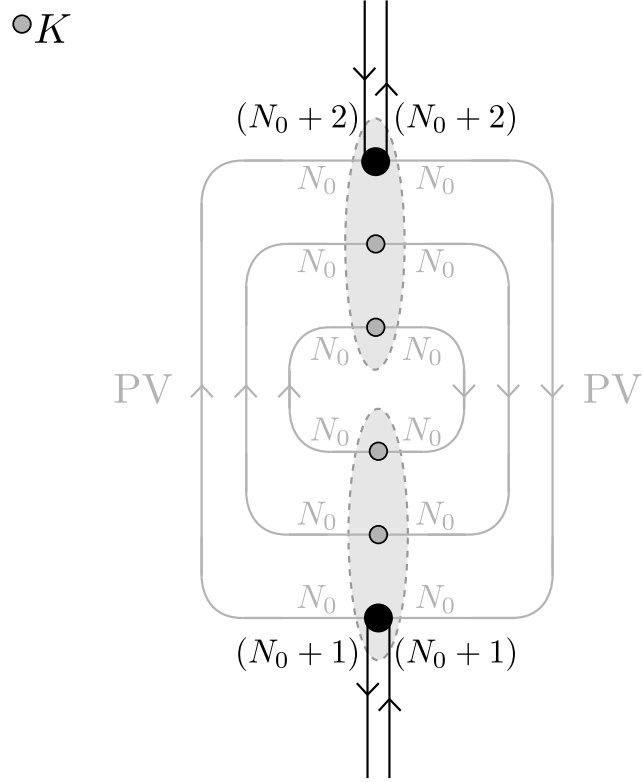


Figure 5.2: Fundamental scalar field symmetry factors in the W boson/background fermions mass interaction. One factor attaches to each field operator appearing on a vertex (grey ellipse). Within the fermion-boson interaction, K -matrices are shown as grey dots, and preon-boson interactions as black dots. [Each vertex also attracts a factor of $\frac{1}{3}$ from the normalisation of Eq. (3.28) but this is offset as each boson may couple to any of the three preons—see also Sec. 3:3.5.8.]

The sum of Eqs. (5.5) and (5.6) thus reduces to

$$9f^2 k_1^4 \omega_0^2 N_0^{12} \int d^4 x W_\mu^\dagger(x) W^\mu(x) [1 + O(N_0^{-1})], \quad (5.12)$$

corresponding to

$$\begin{aligned} m_W^2 &= 9f^2 k_1^4 \omega_0^2 N_0^{12} [1 + O(N_0^{-1})] \\ &= 18m_e^2 N_0^4 [1 + O(N_0^{-1})] \end{aligned} \quad (5.13)$$

at tree level by Eq. (4.34). Higher-order corrections to Fig. 5.1(v) amend this to

$$m_W^2 = 9f^2 k_1^4 \omega_0^2 N_0^{12} [1 + O(N_0^{-1}) + O(\alpha)] \quad (5.14)$$

and are evaluated in Chapter 6.

Interestingly, the higher-order corrections to the FSF symmetry factor $n_{\varphi, W}$ for the W boson are given by series $S_{6,13}$ which also appears when evaluating electron mass (4.10). For the electron this factor subsequently attracts further corrections (4.32), so the two do not cancel exactly. Nevertheless, Eqs. (5.13–5.14) permit the value of N_0 , the mean number of fundamental scalar field centres per hypervolume \mathcal{L}_0^4 , to be evaluated up to corrections of $O(\alpha)$ and $O(N_0^{-1})$ as

$$\begin{aligned} N_0 &= \sqrt{\frac{m_W}{3\sqrt{2}m_e}} [1 + O(N_0^{-1}) + O(\alpha)] \\ &\approx 193. \end{aligned} \quad (5.15)$$

Proceeding similarly for the photon yields the pre-FSF vertex expression

$$-36f^2 k_1^4 \iint d^4 x d^4 y [A_\mu(x) A_\nu(y)]_{\text{fg}} [X_A^\mu(x) X_A^\nu(y)]_{\text{bg}} \quad (5.16)$$

where $X_A^\mu(x)$ is the net vertex interaction on summing over all background fields,

$$\begin{aligned} X_A^\mu(x) &= \left\{ [e_R(x) \bar{\sigma}^\mu \bar{e}_R(x)]_{\text{bg}} - [\bar{e}_L(x) \bar{\sigma}^\mu e_L(x)]_{\text{bg}} \right. \\ &\quad + \frac{1}{3} [d_R(x) \bar{\sigma}^\mu \bar{d}_R(x)]_{\text{bg}} - \frac{1}{3} [\bar{d}_L(x) \bar{\sigma}^\mu d_L(x)]_{\text{bg}} \\ &\quad \left. - \frac{2}{3} [u_R(x) \bar{\sigma}^\mu \bar{u}_R(x)]_{\text{bg}} + \frac{2}{3} [\bar{u}_L(x) \bar{\sigma}^\mu u_L(x)]_{\text{bg}} \right\}. \end{aligned} \quad (5.17)$$

In Eq. (5.16), f^2 has been replaced by $f^2/2$ due to the weaker coupling at the photon vertex, but a compensatory factor of 2 is acquired from exchange symmetry of the two identical interaction vertices. Any diagrams containing “tadpole” fermions (fermion lines whose source and sink are on the same vertex) must vanish, so the per-diagram symmetry factor for the persisting terms is once again $3! \times 3! = 36$, and cross terms (where the fermion species interacting with the two vertices differ) disappear.

As per Sec. 3:3.3.6, gauge choice (3.60) is chosen such that Eq. (5.16) vanishes—up to a small correction. More precisely it is not Eq. (5.16) which is chosen to vanish, but rather the sum of Eq. (5.16) (plus FSF factors and higher-order corrections) and the smaller terms arising from Figs. 5.1(i) and (iv) (plus FSF factors and higher-order corrections). As previously noted in Sec. 3:3.3.7, at any given point x the values of each of these terms may be positive or negative

and the action of the gauge transform is to selectively eliminate the dominant contributions, bringing the net mass to zero. With Figs. 5.1(i) and (iv) having symmetry factors smaller than Fig. 5.1(v) by a factor of N_0^4 , they pose no obstacle to ensuring the mean vanishing of photon mass to probes of scale $\mathcal{L}_p \gg \mathcal{L}_0$ (essentially, all probes—see Sec. 1:3.6.5).

For the Z boson, the corresponding pre-FSF expressions are

$$-72f^2k_1^4 \iint d^4x d^4y [Z_\mu(x)Z_\nu(y)]_{\text{fg}} [X_Z^\mu(x)X_Z^\nu(y)]_{\text{bg}} \quad (5.18)$$

$$\begin{aligned} X_Z^\mu(x) = \frac{2}{\sqrt{6}} \bigg\{ & \frac{1}{2} [e_R(x)\bar{\sigma}^\mu \bar{e}_R(x)]_{\text{bg}} + \frac{1}{2} [\bar{e}_L(x)\bar{\sigma}^\mu e_L(x)]_{\text{bg}} \\ & - \frac{1}{2} [d_R(x)\bar{\sigma}^\mu \bar{d}_R(x)]_{\text{bg}} - \frac{1}{2} [\bar{d}_L(x)\bar{\sigma}^\mu d_L(x)]_{\text{bg}} \\ & - [\bar{\nu}_e(x)\bar{\sigma}^\mu \nu_e(x)]_{\text{bg}} \bigg\}, \end{aligned} \quad (5.19)$$

where the factor of 72 in Eq. (5.18) is made up of 36 from preon exchange symmetries and 2 from interchange of source and sink. (The two vertices may also be interchanged, but when source, sink, and both vertices are exchanged, the original diagram is recovered, reflecting that these are equivalent descriptions of a single twofold symmetry.) Incidentally, note that the factor of two is also present in the Standard Model, where it multiplies the Lagrangian term $\frac{1}{2}m_Z^2 Z^\mu Z_\mu$ to yield a mass vertex $m_Z^2 Z^\mu Z_\mu$.

On evaluating Eq. (5.18), the resulting leading-order expression for the Z boson mass is

$$\begin{aligned} m_Z^2 &= 12f^2k_1^4\omega_0^2 N_0^{12} [1 + \mathcal{O}(N_0^{-1}) + \mathcal{O}(\alpha)] \\ &\approx \frac{4m_W^2}{3}. \end{aligned} \quad (5.20)$$

Finally, the nine gluons $c_\mu^{\tilde{c}}$ also acquire a mass m_c through interaction with the pseudovacuum, primarily also through coupling to the preon fields. This is due to coupling of gluons to the colour charges on preons in the pseudovacuum. By maximal entropy of the pseudovacuum, and the absence of symmetry-breaking gauge choices on the bosonic sector of the $\text{SU}(3)_C$ symmetry, the resulting mass contribution imparted to any gluon is equal to that acquired by the W boson from the pseudovacuum fermion fields,

$$m_c^2 \approx m_W^2. \quad (5.21)$$

Interaction with background gluons and scalar bosons then contributes additional terms, corresponding to the other diagrams of Fig. 5.1, correcting the gluon mass by

$$m_c^2 \longrightarrow m_c^2 \left[1 + \mathcal{O}\left(\frac{m_\tau^2}{m_W^2}\right) \right]. \quad (5.22)$$

In practice this mass is observed only indirectly and in a limited number of circumstances, as the typical gluon lifetime is of $\mathcal{O}(\mathcal{L}_\psi)$ which is much smaller than the scale of the mass interaction, \mathcal{L}_0 . Consequently gluons typically appear massless, except as discussed in Appendix 6:E.1.

5:3.1.6 Fig. 5.1(vi):

A small number of additional two-vertex diagrams may be constructed by making use of the g^2 vertices, but (as noted in the caption to Fig. 5.1) these may all be equated to sums over diagrams already eliminated and so add nothing further to the vector boson mass term.

5:3.1.7 Exception: The G boson.

At first glance the G boson appears to play a very similar role to the W boson, but instead of coupling the electron neutrino and the left-handed electron (or higher-generation equivalents) it couples the electron antineutrino and the right-handed electron. However, gauge choice (3.56) imposes that the magnitude of the background G field vanishes, and this condition is nonsingular so is valid everywhere. This has an interesting collateral effect: If the G boson has a nonvanishing interaction with the pseudovacuum, then the inability to consistently distinguish foreground and background fields over scales small compared with \mathcal{L}_0 implies that the background fields may generate $GG^{(\dagger)}$ pairs. These pairs are then necessarily of background character, with nonvanishing field magnitudes, in violation of the choice of gauge. Thus the G boson may not couple to the background fields, and hence is necessarily massless.

5:3.2 Boson generations

A curious feature of Sec. 5:3.1 is the prediction of second- and third-generation W and Z bosons, with the lightest being W_2 with a mass of approximately $16.6 \text{ TeV}/c^2$. However, as per Sec. 1:3.6.3 the energy scale at which $\mathbb{C}^{\wedge 18}$ ceases to behave as a good analogue to a QFT is

$$\mathcal{E}_\Omega := nN_0(N_0 - \tfrac{1}{2})\omega_0 \quad | \quad n = 9, \quad (5.23)$$

which is seen in Appendix 6:D to take a value of approximately 6.2 TeV. In Chapter 8 it is discussed that the pseudovacuum energy scale \mathcal{E}_Ω corresponds to a particle energy of $E_\Omega = \tfrac{1}{2}\mathcal{E}_\Omega$, which is substantially less than the mass of the W_2 boson. In the $\mathbb{C}^{\wedge 18}$ model the value of E_Ω corresponds to a real UV cutoff, with the consequence that virtual $W_2^{(\dagger)}$ bosons are frozen out of all processes having energy less than about 13.5 TeV in the isotropy frame of the pseudovacuum. Even above this threshold, behaviour is atypical as formation of a virtual $W_2^{(\dagger)}$ boson requires the obligate loan of 13.5 TeV of energy from the foreground particles. However, real $W_2^{(\dagger)}$ bosons in the $\mathbb{C}^{\wedge 18}$ model will still be generated as consistent collision energies and momenta permit.

For further details of the higher-generation weak bosons and their masses, see Sec. 10:1.

5:3.3 Scalar boson mass

The scalar boson is also capable of interacting with both the background vector boson and background preon fields. These interactions are shown in Fig. 5.3, and once again the multiple-preon pseudovacuum interactions of diagrams (ii)-(iii) dominate. These contribute a mass on the order of the electroweak scale (consistent with the Higgs boson of the Standard Model) while the pseudovacuum scalar boson interaction of diagram (i) provides a correction of $\mathcal{O}(m_\tau^2)$.

To evaluate the scalar boson mass to leading order, first consider the preon fields at the interaction vertices in Fig. 5.3(ii), and ignore Fig. 5.3(iii). In diagram (ii) the scalar boson \mathbf{H} interacts with two preons and four anti-preons, rather than three and three as in Fig. 5.1(v). However, this may still be understood as an interaction with the background fermion fields. A pair of fermion operators in the background field is typically written $[\bar{\Psi}(x)\Psi(x)]_{\text{bg}}$ for some x . However, background fields exhibit correlations over length scales of $\mathcal{O}(\mathcal{L}_0)$ and in practice the preons in the particles associated this expression may be detected at disparate locations within a local correlation region. If the two vertices are at x and y , within a common local correlation region, then the preon fields of Fig. 5.3 may therefore be understood as fermion fields nominally written $[\bar{\Psi}(x)\Psi(x)]_{\text{bg}}$ and $[\bar{\Psi}(y)\Psi(y)]_{\text{bg}}$, but with one preon operator from the former being evaluated at y , and one antipreon operator from the latter being evaluated at x . The fermion

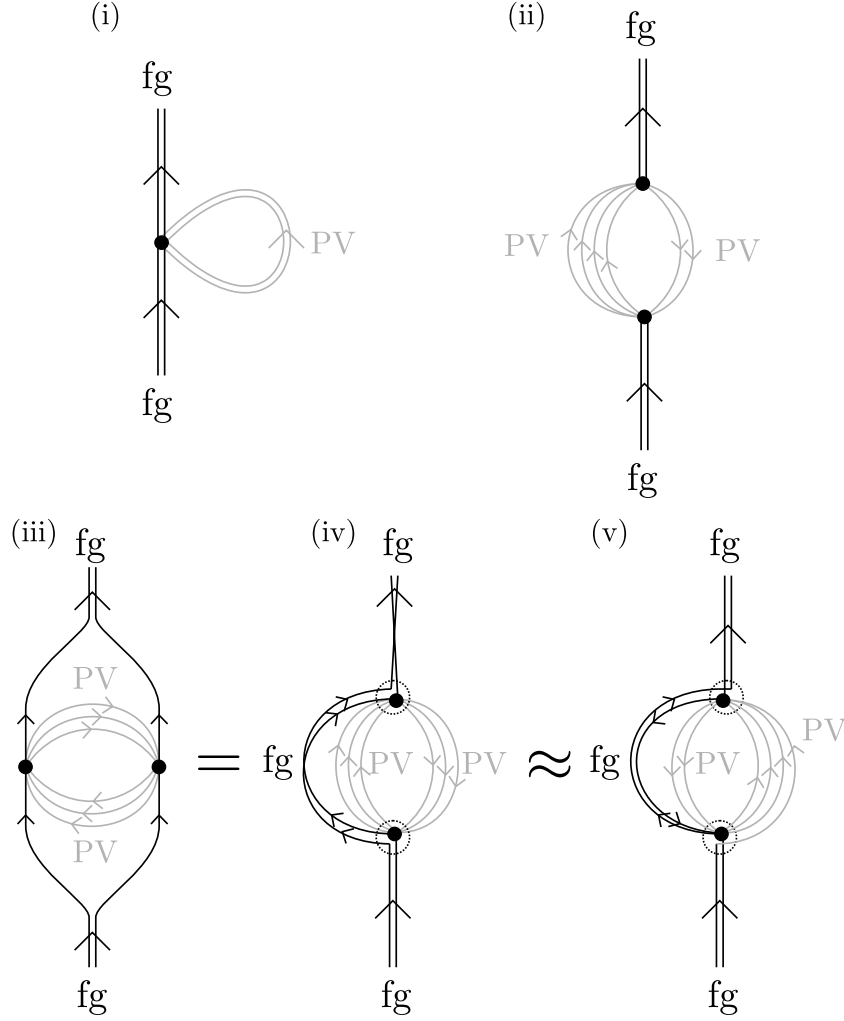


Figure 5.3: Interactions between a foreground scalar boson and (i) the bosons and (ii)-(iii) the preons of the pseudovacuum. Diagram (iii) is drawn in a relatively intuitive form, whereas in diagram (iv), this interaction has been rearranged using diagrammatic isotopy. Dotted circles represent effective net interactions at the upper and lower vertices. In diagram (v) this identification of effective interaction vertices permits a different choice of fields to be replaced with pseudovacuum mean field terms. Several lines have also been taken over from the left side to the right and vice versa to highlight the similarity to diagram (ii). Looking inside the effective vertices of diagram (v), some foreground and pseudovacuum fields are seen to exchange roles; this is permissible due to the quasiparticle nature of the foreground fields, which implies that the foreground momentum is in fact a collective property of all $(N_0 + 2)$ locally correlated FSFs, with the net contribution of N_0 of these being undetectable over length scales $\mathcal{L} \gg \mathcal{L}_0$. Evaluation of diagram (v) is therefore equivalent to evaluation of diagram (iv) up to the presence of a vector boson loop, and a small difference in the FSF symmetry factors of the background fields discussed in the main text. Note also that, as is readily seen from diagram (iii), the scalar boson preons in diagrams (iii)-(v) are confined at all times to be separated by no more than \mathcal{L}_ψ , and this is entirely compatible with the mass interaction illustrated, as the vertices of this interaction must be separated by no more than \mathcal{L}_0 which is larger than \mathcal{L}_ψ .

operators continue to represent sources or sinks for fermions at a point (up to confinement scale \mathcal{L}_ψ), but subject to detection at a distance via their correlations.

This effective redistribution, with four preons and two antipreons (or vice versa) at each vertex, does however impact the FSF symmetry factor of diagram (ii) as the detection operations being performed at the vertices are now grouped as four preon operators and two antipreon operators or vice versa. If the preon/antipreon pairs at a vertex are labelled first, each attracts a factor of N_0^2 and maintains the number of available source/sinks as discussed in Sec. 4:3.2.1. However, the final two background operators on each vertex are either two preons or two antipreons. Recognise that evaluation of the background mean fields occurs essentially pointwise at each interaction vertex, and thus for background fields, symmetry factors must be evaluated independently at each vertex. In practice, the composite nature of the fermion requires that “pointwise” be approximated as “on a region characterised by length scale \mathcal{L}_ψ ”, but for \mathcal{L}_ψ assumed much smaller than \mathcal{L}_0 the symmetry factors on the vertices effectively continue to be evaluated independently.

The factor for a pair of preons or antipreons then depends on whether or not they are of the same species. As noted in Sec. 4:3.2.1, such competition for sources is mitigated by the propensity for preons to change charge (on both A and C sectors) as they interact with the background fields, even within a context such as Fig. 5.3(ii) where the excursions of the background preons are restricted to a region characterised by dimension \mathcal{L}_ψ . If these preons are of identical A - and C -charges as they are considered for application to a contested source/sink then the resulting factor is $N_0(N_0 - 1) = N_0^2(1 - N_0^{-1})$, whereas if they are of different charges then the factor is N_0^2 . As there are nine different charge combinations on each preon, the resulting mean factor may be written $N_0^2[1 - (9N_0)^{-1}]$ and the full labelling of FSF symmetry factors is shown in Fig. 5.4. The resulting FSF symmetry factor for Fig. 5.3(ii) may thus be written

$$\begin{aligned} n_{\varphi, \mathbf{H}} &= n_{\varphi, W} \left(1 - \frac{1}{9N_0}\right)^2 \\ &= N_0^{12} \left(1 + \frac{52}{9}N_0^{-1} + \frac{946}{81}N_0^{-2} + \dots\right). \end{aligned} \quad (5.24)$$

Note that this factor applies only to Fig. 5.3(ii)—there is no factor of $[1 - (9N_0)^{-1}]$ attached to Fig. 5.3(iii) as the number of preon and antipreon fields from the pseudovacuum is equal. The FSF symmetry factor for diagram (iii) is thus simply given by Eq. (5.7) and is the same as for Fig. 5.1(v). This must be kept in mind when relating diagram (iii) to diagram (ii) as shown in Fig. 5.3(iv)-(v).

Proceeding with the evaluation of Fig. 5.3(ii), it is next necessary to count the diagrammatic symmetry factors associated with the different fermions of the background fields. To do so, recognise that all preon configurations which may validly be grouped on the same vertex as the \mathbf{H} operator may be obtained by iterating over all generationless 1 fermion/anti-fermion pairs and considering all ways to replace one preon with an antipreon. For example, briefly ignoring summations on spinor and colour indices, the channel indexed by $e_L \equiv \psi^2\psi^2\psi^2$ has associated vertices resembling

$$\psi^2\psi^2\psi^2\psi^2\psi^2\psi^2\mathbf{H} \quad (5.25)$$

and hermitian conjugate. As with the W boson, integration over one of the spatial degrees of freedom permits elimination of two preons and two antipreons from each vertex. The resultant expression is nonvanishing only where the preon pair and the antipreon pair remaining on the vertices of Fig. 5.3 are conjugate. For the lepton channels this is trivially satisfied, whereas for the quark-labelled channels it is satisfied only when the preon which is replaced by an antipreon (or vice versa) is the unique species in the triplet (e.g. $\psi^{3c\alpha}$ in u_L).

For the resulting diagrams, the symmetry factors associated with the preon connections may then be evaluated at:

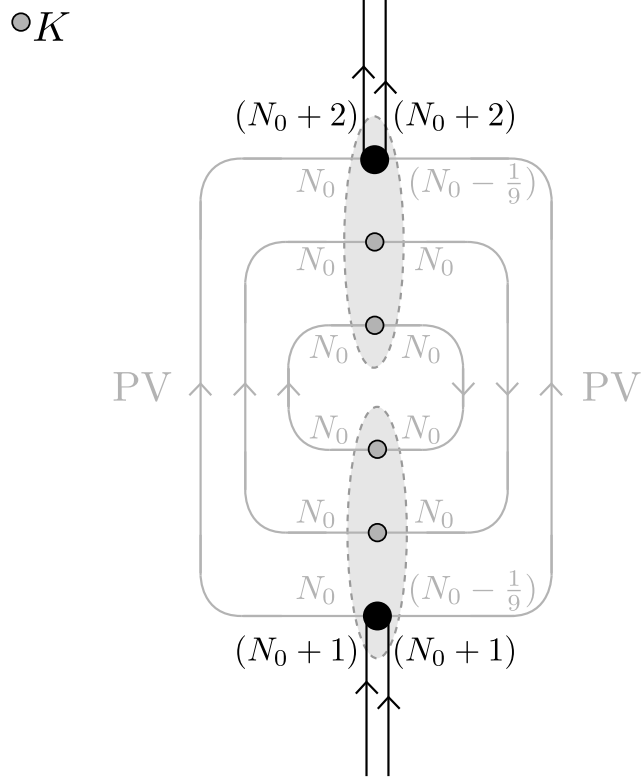


Figure 5.4: Fundamental scalar field symmetry factors in the complex scalar boson/background fermions mass interaction. Note that one orientation arrow is reversed on the pseudovacuum fields compared with Fig. 5.2, causing two factors of N_0 to be replaced with $(N_0 - 1)$ one time in nine. [Each vertex also attracts a factor of $\frac{1}{3}$ from the normalisation of Eq. (3.28) but this is offset as each boson may couple to any of the three preons.]

- 48 for each of the three first-generation lepton channel diagrams ($e_R \bar{\sigma}^\mu \bar{e}_R$, $\bar{e}_L \bar{\sigma}^\mu e_L$, $\bar{\nu}_e \bar{\sigma}^\mu \nu_e$), for a total of 144, comprising $4! \times 2!$ for the reordering of the preon lines and antipreon lines, and
- 144 for each of the four first-generation quark channel diagrams ($\bar{u}_L \bar{\sigma}^\mu u_L$, $u_R \bar{\sigma}^\mu \bar{u}_R$, $\bar{d}_L \bar{\sigma}^\mu d_L$, and $d_R \bar{\sigma}^\mu d_R$), for a total of 576, comprising:
 - $2! \times 2!$ for reordering of the lines in the preon summed pair and antipreon summed pair.
 - 3×3 for the choice of colour of the unpaired species on each side of the interaction vertices, recalling that the boson coupling vertex is implicitly a sum over photon and gluon terms so may change the colour.
 - Noting that reversing the orientation of the unique antipreon line yields another matched preon pair, $2!$ for exchange of the lines in this pair.
 - $2!$ for exchanging the two preon pairs—the summed pair, and the pair arising from the unique preon and antipreon on exchange of orientation of the antipreon.

Where labels match, an exchange corresponds to the associated symmetry factor. Where they do not match, it is a sum over diagrams corresponding to rearrangements of these labels.

Then, for additional factors common to both leptons and quarks:

- Recognise that the scalar boson $\mathbf{H} = f\psi\psi$ contains an internal R -index summation, so is made up of nine terms, which may be thought of as internal channels enumerated by the R -index. A single scalar boson excitation will on average excite only one of these channels. The inbound and outbound R -channels are required to coincide, with a net outcome that each diagram attracts a factor of $n^{-1} = \frac{1}{9}$.
- As described in Sec. 3:3.5.5, the \mathbf{H} and \mathbf{H}^* bosons on the inbound and outbound legs of the diagram are represented in the context of a propagator, and so are far field bosons attracting substantially reduced FSF symmetry factors. Expressed relative to the corresponding vector boson diagrams, these lend the diagrams of Fig. 5.3 a factor of $4[k_1 N_0]^{-4} [1 + O(N_0^{-1})]$ apiece.
- As the background preons correspond to fermion triplets, interaction with the scalar boson may be accompanied by pairs of K matrices as shown in Fig. 5.5. Although diagrams may be constructed with and without K matrices, it turns out that only diagrams involving K matrices contribute to the leading terms in scalar boson mass. Diagrams without K matrices are discussed in Sec. 6:4.1.8.

For vector bosons the Lagrangian yields vertex pairs such as

$$\begin{aligned}
 & -n_{\varphi,W} f^2 k_1^4 \iint d^4x d^4y [W_\mu^\dagger(x) W_\nu(y)]_{\text{fg}} \\
 & \quad \times [\bar{\nu}_e(x) \bar{\sigma}^\mu e_L(x) \bar{e}_L(y) \bar{\sigma}^\nu \nu_e(y)]_{\text{bg}} \\
 & = \frac{n_{\varphi,W} f^2 k_1^4}{2} \iint d^4x d^4y [W_\mu^\dagger(x) W^\mu(y)]_{\text{fg}} \\
 & \quad \times [\bar{\nu}_e(x) \bar{e}_L(y) e_L(x) \nu_e(y)]_{\text{bg}},
 \end{aligned} \tag{5.26}$$

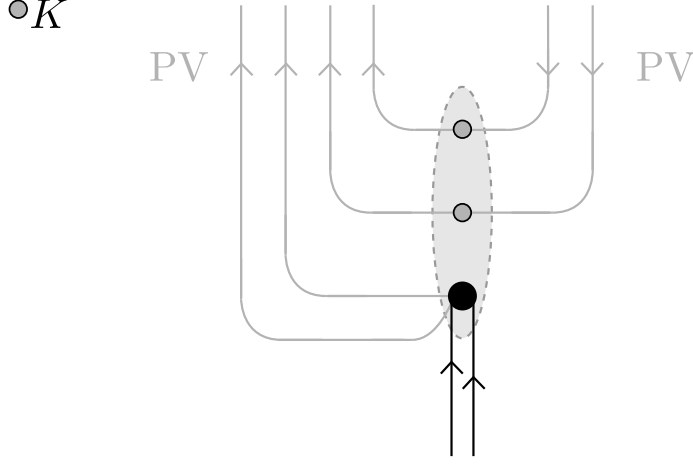


Figure 5.5: Detail of K matrices in a \mathbf{H} /preon triplet interaction vertex, with preons and antipreons grouped as in Fig. 5.3(ii).

with this example, before diagrammatic symmetry factors, yielding $1/72$ of the contribution to the leading-order value of m_W^2 . If the W boson is replaced by an equivalent hypothetical boson diagonal on $SU(3)_A$ and taken to couple only to e_L ,¹ and vector boson factors are written in terms of spinor derivatives acting on φ , then the application of spinor identities and integration by parts yields one of the nine internal channels of the scalar boson, not including the preon pair's foreground FSF exchange symmetry factor. The equivalent term involving the same components of the background fields therefore imparts mass to the scalar boson as a whole according to

$$\begin{aligned}
& \frac{n_{\varphi, W} f^2 k_1^4}{2} \iint d^4 x d^4 y [W_\mu^\dagger(x) W^\mu(y)]_{\text{fg}} \\
& \quad \times [\bar{\nu}_e(x) \bar{e}_L(y) e_L(x) \nu_e(y)]_{\text{bg}} \\
& \quad \downarrow \\
& - \frac{2n_{\varphi, \mathbf{H}} f^2 k_1^4}{9[k_1 N_0]^4} [1 + \mathcal{O}(N_0^{-1})] \iint d^4 x d^4 y \\
& \quad \times [\mathbf{H}^*(x) \mathbf{H}(y)]_{\text{fg}} [\bar{e}_L(x) \bar{e}_L(y) e_L(x) e_L(y)]_{\text{bg}}.
\end{aligned} \tag{5.27}$$

Summing across channels and symmetry factors for the W boson yields a factor of $36 + 36 = 72$ on Eq. (5.5), for a total mass-squared of m_W^2 . An equivalent summing for Fig. 5.3(ii) yields $144 + 576 = 720$, for an apparent mass-squared of

$$- \frac{40m_W^2}{9[k_1 N_0]^4} \frac{n_{\varphi, \mathbf{H}}}{n_{\varphi, W}} [1 + \mathcal{O}(N_0^{-1})]. \tag{5.28}$$

This plays a role similar to m_W^2 in the Lagrangian, and thus appears in a term with *positive* overall sign (whereas m_W^2 appears preceded by a negative sign). However, the propagator term

¹This field may be constructed explicitly from A_μ , Z_μ , and N_μ , as the latter acts trivially on both $SU(3)_A$ and $SU(3)_C$, so may be considered to act as a trivial representation of either group.

for the complex scalar boson similarly takes the form

$$-2[k_1 N_0]^{-4} [1 + \mathcal{O}(N_0^{-1})] \mathbf{H}^* \square \mathbf{H} \quad (3.95)$$

with the same higher-order terms in $[k_1 N_0]^{-1}$ as the mass interaction, and the Lagrangian for the free massive complex scalar boson is consequently

$$\begin{aligned} \mathcal{L}_{\mathbf{H}, m_{\mathbf{H}}} = & -\frac{2}{[k_1 N_0]^4} \left(\mathbf{H}^* \square \mathbf{H} - \frac{20m_W^2}{9} \frac{n_{\varphi, \mathbf{H}}}{n_{\varphi, W}} \mathbf{H}^* \mathbf{H} \right) \\ & \times [1 + \mathcal{O}(N_0^{-1})], \end{aligned} \quad (5.29)$$

yielding [at least, for m_W^2 and $m_{\mathbf{H}}^2$ evaluated to leading order, and ignoring Fig. 5.3(iii)]

$$m_{\mathbf{H}}^2 = \frac{20m_W^2}{9}. \quad (5.30)$$

Recognising that the factor of $-2[k_1 N_0]^{-4} [1 + \mathcal{O}(N_0^{-1})]$ in Eq. (5.29) is a common factor to both terms and can be divided out of $\mathcal{L}_{\mathbf{H}, m_{\mathbf{H}}}$ with no effect on the dynamics of \mathbf{H} , it is then worthwhile to revisit the difference between FSF symmetry factors for the W and \mathbf{H} bosons. Equations (5.7) and (5.24) differ by a factor of $[1 - (9N_0)^{-1}]^2$, correcting only the mass term in $\mathcal{L}_{\mathbf{H}, m_{\mathbf{H}}}$ to yield

$$m_{\mathbf{H}}^2 = \frac{20m_W^2}{9} \left(1 - \frac{1}{9N_0} \right)^2. \quad (5.31)$$

Taking $m_W = 80.377(12)$ GeV [28] and substituting the value of N_0 from Eq. (5.15) gives a first approximation to the leading-order value of $m_{\mathbf{H}}^2$ of $119.75(2)$ GeV/ c^2 (ignoring the unquantified uncertainty from higher-order terms in N_0).

Now consider Fig. 5.3(iii). To evaluate this figure it is useful to employ a technique known as diagrammatic isotopy [29, 30]. When the preons are viewed as intrinsically massless particles, they may be understood as a representation of a conformal field theory (CFT). Their self-consistent exchange relationships imply that this is a braided CFT, and up to the symmetry factors absorbed into the definition of the fermion its vertices also satisfy requirements for unitarity. The modular S -matrix (S_{ab}) is trivial, ensuring that when restricted to the surface of a torus the CFT is also modular. Provided the number of fermion vertices is held constant, the preon model is consequently a unitary, braided, modular conformal field theory. All particle representations are of dimension 1 and thus Feynman diagrams are automatically normalised in the diagrammatic isotopy convention (up to the factors associated with the definition of fermions). Preon lines may therefore be freely deformed so long as the topology of the diagram remains intact in the sense employed in Refs. [29, 30], and the fermion count is left unchanged or appropriate compensatory factors are introduced.

As indicated in the caption to Fig. 5.3, diagrammatic isotopy and braiding permit diagram (iii) to be redrawn as shown in diagram (v), resembling Fig. 5.3(ii) supplemented by an foreground additional loop correction of dimension L^{-1} . The value of diagram (iii) is therefore the value of Fig. 5.3(ii) modified by the factor arising from the presence of the loop in diagram (v)—and also without the reduction in FSF symmetry factors discussed in Fig. 5.4. The correct FSF symmetry factors are yielded by diagram (iv) of Fig. 5.3, and it is also convenient to evaluate the loop factor on this diagram.

Before doing so, consider diagram (iii) once more. The constituent preons of the complex scalar boson in diagram (iii) form a bound pair and thus are separated by a distance of $\mathcal{O}(\mathcal{L}_\psi)$. This distance is much smaller than scale \mathcal{L}_0 associated with mass interactions, and thus when

the preons making up the loop corrections in diagrams (iv) and (v) traverse this length scale, they may do so as massless particles. Further, diagram (iii) represents a mass vertex and thus is implicitly truncated. It is convenient to reintroduce short line segments on the foreground preons to assist in evaluation using diagrammatic isotopy, but these line segments must not engage in any further couplings, including mass vertices. For this reason the loop boson in diagrams (iv)-(v) must be massless.

Since the aim of diagrams (iii)-(v) is to write Fig. 5.3(iii) as a correction to Fig. 5.3(ii), and in the latter the vertex factors are the same as those associated with the composite vertices in Fig. 5.3(v) but arise entirely from the eight-preon vertices marked by a solid dot \bullet , these vertex factors must be recovered after integration out of the loop correction in Fig. 5.3(iv). The presence of the loop correction does not affect the reduction of the pseudovacuum lines to a numerical coefficient, and evaluation of this loop correction is therefore performed independently of that reduction, with vertex factors of 1. Given a specific labelling of the inbound and outbound preons, the foreground loop is one of nine terms arising from a complex scalar boson loop. The boson mass is zero as discussed above, and with no sum over nine different terms the scalar boson loop correction is thus equivalent to a photon loop up to the following relative factors:

- Coupling coefficients yield 1, not α , for a relative factor of α^{-1} .
- The asymmetry of background preons in diagram (v) (four preons and two antipreons at once vertex, and the opposite at the other) is taken to be associated with the \mathbf{H} /preon vertices, leaving the \mathbf{H} /vector boson loop symmetric under exchange of source and sink vertices, like the photon. Relative symmetry factor of 1.

The loop therefore yields a net factor of $1/(2\pi)$. Recalling that also, in contrast with Fig. 5.3(ii), diagram (iii) does not attract a factor of $[1 - (9N_0)^{-1}]^2$, Eq. (5.31) is therefore corrected to

$$m_{\mathbf{H}}^2 = \frac{20m_W^2}{9} \left[\left(1 - \frac{1}{9N_0}\right)^2 + \frac{1}{2\pi} \right] \quad (5.32)$$

giving the leading-order value

$$m_{\mathbf{H}} = 128.94(2) \text{ GeV}/c^2 \quad (5.33)$$

(again ignoring the unquantified uncertainty from higher-order terms in N_0). This will be further improved upon by higher-order corrections performed in Chapter 6.

5:3.4 Summary of boson masses

5:3.4.1 Photon

The photon, A , attracts no mass to all orders by construction of gauge choice (3.60).

5:3.4.2 W and Z bosons

The W and Z bosons attract the majority of their mass from Fig. 5.1(v). In contrast to the photon, this is nonvanishing for the Z boson due to symmetry breaking in the quark sector (Sec. 3:3.3.6). The resulting leading-order expressions are

$$m_W^2 = 9f^2 k_1^4 N_0^{12} \omega_0^2 \quad (5.14a)$$

$$m_Z^2 = 12f^2 k_1^4 N_0^{12} \omega_0^2 \quad (5.20a)$$

yielding

$$\sin^2 \theta_W = 1 - m_W^2/m_Z^2 = 0.25. \quad (5.34)$$

This only very crudely approximates the observed figure of 0.22290(30) [31], but higher-order corrections are calculated in Chapter 6 and yield better agreement with observation.

5:3.4.3 Gluons and N boson

In principle the gluons in $\mathbb{C}^{\wedge 18}$ (including the N boson, which predominantly behaves like a ninth gluon) participate in a mass interaction, acquiring mass through the same mechanisms as the W boson. To leading order their masses satisfy $m_c^2 \sim m_W^2$. However, it is questionable whether this mass can be observed for any but the N boson, as the other eight gluons are confined on an energy scale \mathcal{E}_ψ which is believed large compared with the scale of the mass interactions, \mathcal{E}_0 .

5:3.4.4 G boson

At the present stage of exposition of the $\mathbb{C}^{\wedge 18}$ model (with flat emergent spacetime) the G boson is a massless particle. In principle it could acquire mass through the same mechanisms as the W boson, but the choice of gauge which zeros the magnitude of background $G^{(\dagger)}$ fields also necessarily prevents $G^{(\dagger)}$ bosons from acquiring mass through coupling to the background fields. The $G^{(\dagger)}$ bosons therefore appear to constitute a novel right-handed weak interaction, but are subsequently eliminated in Sec. 7:3.4.2.

5:3.4.5 a_μ^{12} boson

Like the G boson, the magnitude of the background a_μ^{12} boson field vanishes everywhere, and consequently any a_μ^{12} bosons must necessarily likewise be massless. However, this point is moot as the foreground $[a_\mu^{12}]_{\text{fg}}$ bosons are in effect comprehensively eliminated from the effective theory of the foreground fields by the $\text{SU}(3)_C$ gauge choices of Sec. 3:3.3.6.

5:3.4.6 Scalar boson

The scalar boson \mathbf{H} is a massive particle, with mass given approximately by

$$m_{\mathbf{H}}^2 = \frac{20m_W^2}{9} \left[\left(1 - \frac{1}{9N_0} \right)^2 + \frac{1}{2\pi} \right] \quad (5.32)$$

$$N_0 = \sqrt{\frac{m_W}{3\sqrt{2}m_e}} [1 + \mathcal{O}(N_0^{-1}) + \mathcal{O}(\alpha)]. \quad (5.15)$$

5:4 Conclusion

This chapter has introduced the mass mechanisms for bosons in the $\mathbb{C}^{\wedge 18}$ model, and illustrated this with a tree-level calculation of the leading terms in W , Z , and complex scalar boson (\mathbf{H}) masses. An interesting consequence of these calculations is the ability to relate the ratios of the lepton and electroweak boson scales to the number of fundamental scalar fields within a locally correlated region of the pseudovacuum. When calculated to tree level, the electroweak mass ratios m_W^2/m_Z^2 and $m_W^2/m_{\mathbf{H}}^2$ are in crude qualitative agreement with those of the Standard Model.

In the $\mathbb{C}^{\wedge 18}$ model the electroweak bosons are predicted to exhibit generations, with the lightest second-generation boson being a heavy W boson with mass of 16.61730(47) TeV/ c^2 .

However, this energy scale exceeds the limit at which the \mathbb{C}^{18} model behaves as an analogue to a quantum field theory, and the second-generation W boson is *less* able to appear as a virtual particle in the \mathbb{C}^{18} model than would be anticipated from quantum field theory. With divergence of the \mathbb{C}^{18} model and the Standard Model, caution must be exhibited in this regime.

Acknowledgements

This research was supported in part by the Perimeter Institute for Theoretical Physics. Research at the Perimeter Institute is supported by the Government of Canada through Industry Canada and by the Province of Ontario through the Ministry of Research and Innovation. The author thanks the Ontario Ministry of Research and Innovation Early Researcher Awards (ER09-06-073) for financial support. This project was supported in part through the Macquarie University Research Fellowship scheme. This research was supported in part by the ARC Centre of Excellence in Engineered Quantum Systems (EQuS), Project No. CE110001013.

Chapter 6

Particle generations and masses on \mathbb{C}^{18}

Abstract

The \mathbb{C}^{18} analogue model contains counterparts to the full particle spectrum and interactions of the Standard Model, but has only three tunable parameters. As the structure of this model is highly constrained, predictive relationships between its counterparts to the constants of the Standard Model may be obtained. In this chapter, the model values for the masses of the tau, the W and Z bosons, and a Higgs-like scalar boson are calculated as functions of α , m_e , and m_μ , with no free fitting parameters. They are shown to be $1776.867393(45)$ MeV/ c^2 , $80.3785(22)$ GeV/ c^2 , $91.1877(35)$ GeV/ c^2 , and $125.2501(49)$ GeV/ c^2 respectively. All are within 0.1σ or better of the corresponding observed values of $1776.86(12)$ MeV/ c^2 , $80.377(12)$ GeV/ c^2 , $91.1876(21)$ GeV/ c^2 , and $125.25(17)$ GeV/ c^2 respectively. These results are suggestive of the existence of a unifying relationship between lepton generations and the electroweak mass scale, which is proposed to arise from preon interactions mediated by the strong nuclear force.

6:1 Introduction

Introduced in Chapters 1–5, the \mathbb{C}^{18} model is a classical analogue model [7–9] which comprises free scalar fields (Fundamental Scalar Fields, FSFs) on a manifold with 18 anticommuting complex co-ordinates denoted \mathbb{C}^{18} . When the FSFs are in a highly disordered and hence (from a coarse-grained perspective) a highly homogeneous state, the product of these fields on a $\mathbb{R}^{1,3}$ submanifold admits a description as a pseudovacuum state on which exist soliton waves. These soliton waves, in turn, behave as interacting quasiparticles governed by the low-energy regime of a quantum field theory with a gaugeable local symmetry. The emergent quasiparticles behave as coloured fermionic preons, and they in turn condense into fermions, quarks, and a scalar boson, with choices of gauge yielding a particle spectrum closely resembling that of the Standard Model, supplemented only by

- a ninth gluon, with mass on the electroweak scale, weakly interacting, and with action diagonal in colour,
- higher generations of electroweak bosons, with the lightest being W_2 at $16.61730(47)$ TeV, and

- two low-mass WIMPs denoted G and G^\dagger which may be eliminated as described in Sec. 7:3.4.2.

Anticipating the weakness of the residual effects demonstrated in Chapter 7, the species $G^{(\dagger)}$ may be ignored in the current chapter without introducing significant error.

Previously, Chapters 4 and 5 have introduced the boson and lepton mass interactions of the $\mathbb{C}^{\wedge 18}$ model at tree level, in which the emergent composite bosons and leptons acquire mass through coupling to the high-entropy pseudovacuum. At tree level, the mass ratios m_W/m_Z and $m_W/m_{\mathbf{H}}$ of the electroweak bosons have been shown to be in rough qualitative agreement with the Standard Model. A similar calculation at tree level for leptons is not possible due to vanishing of the tree-level electron mass, but order-of-magnitude estimates for higher-order corrections suggest that the electron gains mass once the 1-loop electroweak corrections are taken into account, and that the model is then not conspicuously inconsistent with the observed mass ratios m_μ/m_e and m_τ/m_e . In the present chapter the boson and lepton mass calculations are performed to higher order, and relationships between the sectors are identified which permit the three input parameters of $\mathbb{C}^{\wedge 18}$ to be taken as α , m_e , and m_μ . The calculated values of m_W , m_Z , $m_{\mathbf{H}}$, and m_τ are then seen to be in exceptional agreement with observation.

6:2 Conventions

This chapter follows the same conventions as Chapters 1–5. Units are chosen such that $c = 1$, $\hbar = 1$. When equations and lemmas from Chapters 1–5 are referenced, they take the forms (1.1), (2.1), etc.

When referring to uncertainty in results, experimental uncertainties will be denoted σ_{exp} , and uncertainties in the theoretical calculation will be denoted σ_{th} .

In this chapter, it is generally assumed that any particle under study is at rest or near-rest with respect to the isotropy frame of the pseudovacuum.

Regarding terminology around Feynman diagrams and symmetry factors:

- Where there exist multiple ways to connect up sources, vertices, and sinks to obtain equivalent diagrams up to interchange of non-distinguishable co-ordinates, the same term is obtained from the generator \mathcal{Z} in multiple different ways and thus the diagram acquires a multiplicative factor. This is referred to in the present volume as a *symmetry factor*.
- Where integration over the parameters of a diagram (for example, over source/sink co-ordinates) yields the same diagram multiple times up to interchange of labels on these parameters, this represents a double- (or multiple-)counting of physical processes. It is then necessary to eliminate this multiple-counting by dividing by the appropriate symmetry factor. This is referred to in the present volume as *diagrammatic redundancy* or *double-(multiple-)counting*.

6:3 The pseudovacuum

The FSFs are defined on manifold $\mathbb{C}^{\wedge 18}$ and denoted φ_q . Defining a submanifold $M \subset \mathbb{C}^{\wedge 18}$ such that $M \cong \mathbb{R}^{1,3}$, the mapping of the FSFs to $\mathbb{R}^{1,3}$ is denoted $\varphi_q(x)$. Since $\mathbb{R}^{1,3}$ (but not M) may support fields of arbitrary power in x , the product field $\varphi(x)$ is defined on $\mathbb{R}^{1,3}$ as

$$\varphi(x) := \prod_q \varphi_q(x). \quad (1.133)$$

The observed quasiparticles are then constructed from the gradients of the product field with respect to translations of the $\mathbb{R}^{1,3}$ submanifold within $\mathbb{C}^{\wedge 18}$. The pseudovacuum is characterised by an energy scale \mathcal{E}_0 , a mean expectation value

$$f^{-1} := \langle \varphi \rangle, \quad (6.1)$$

and a particle number N_0 being the number of FSFs having a point of inflection within a hypervolume

$$\mathcal{L}_0^4 := \mathcal{E}_0^{-4}. \quad (6.2)$$

Each FSF has at most one point of inflection. Introducing an energy per FSF,

$$\omega_0 := \frac{\mathcal{E}_0}{N_0}, \quad (6.3)$$

the macroscopic properties of the pseudovacuum may be parameterised in terms of (f, N_0, ω_0) of which f and N_0 are unitless.

On $\mathbb{R}^{1,3}$, the pseudovacuum may conveniently be described in terms of its non-vanishing expectation values. In the notation of Chapters 1–5 the non-vanishing bosonic components are

$$\langle [A^\mu(x) A_\mu(y)]_{\text{bg}} \rangle = -\mathbf{f}(x-y) \mathcal{E}_0^2 \quad (6.4)$$

$$\langle [\tilde{c}^\mu(x) c_\mu^\dagger(y)]_{\text{bg}} \rangle = -\mathbf{f}(x-y) \mathcal{E}_0^2 \quad (6.5)$$

where $\mathbf{f}(x)$ is a Gaussian satisfying

$$\int d^4x \mathcal{E}_0^4 \mathbf{f}(x-y) = 1 \quad \forall \quad y. \quad (1.168)$$

As noted in Sec. 3:3.3.7, the $\text{SU}(3) \otimes \text{GL}(1, \mathbb{R})$ invariance of the C sector implies that the background fields in Eq. (6.5) need not form a conjugate pair to have nonvanishing pseudovacuum expectation values.

The leptons are made up of three differently-coloured preons, generically

$$\begin{aligned} \Psi^{ag\alpha}(x) &\propto (\varepsilon^{\alpha\beta} \varepsilon^{\gamma\delta} - \varepsilon^{\alpha\gamma} \varepsilon^{\beta\delta} + \varepsilon^{\alpha\delta} \varepsilon^{\beta\gamma}) \\ &\times \mathcal{C}_{c_1 c_2 c_3}^g \psi_\beta^{ac_1}(x_1) \psi_\gamma^{ac_2}(x_2) \psi_\delta^{ac_3}(x_3) \end{aligned} \quad (6.6)$$

following Eq. (3.31). In this, g is the generation index, and the coefficients $\mathcal{C}_{c_1 c_2 c_3}^g$ are constrained by requiring that particle $\Psi^{a\alpha}$ be both colourless and an eigenstate of the mass-generating interaction with the pseudovacuum. The preon expectation values satisfy

$$\begin{aligned} &\langle [\bar{\psi}^{\dot{m}}(x) \bar{\psi}^{\dot{n}}(y) \psi^m(x) \psi(y)^n]_{\text{bg}} \rangle \\ &= \langle [\bar{\psi}^{\dot{m}}(x) \bar{\psi}^{\dot{n}}(y) \psi^m(y) \psi(y)^n]_{\text{bg}} \rangle \\ &= \frac{1}{2f^2} \delta_{\dot{m}n} \delta_{\dot{n}m} \mathbf{f}(x-y) \mathcal{E}_0^2 \end{aligned} \quad (6.7)$$

where m (or \dot{m}) and n (or \dot{n}) range from 1 to 9 and enumerate pairs of index values a (or \dot{a}) $\in \{1, 2, 3\}$, c (or \dot{c}) $\in \{r, g, b\}$. The scalar boson is a sum over nine terms,

$$\mathbf{H} := f \psi^m \psi_m, \quad (6.8)$$

and thus satisfies

$$\langle [\mathbf{H}(x) \mathbf{H}^*(y)]_{\text{bg}} \rangle = \frac{9}{2} \mathbf{f}(x-y) \mathcal{E}_0^2. \quad (6.9)$$

The field A_μ corresponds to the photon, and c_μ^c corresponds to gluons associated with the Gell-Mann basis of $SU(3)_C$ plus an additional diagonal species, as enumerated in Eqs. (2.39–2.40). The construction of the pseudovacuum introduces a preferred rest frame, but this is essentially undetectable at energy scales small compared with

$$\frac{1}{2}\mathcal{E}_\Omega := \frac{n}{2}N_0(N_0 - \frac{1}{2})\omega_0 \quad | \quad n = 9, \quad (5.23)$$

which is seen to be approximately 3.1 TeV (6.167). To leading order the value of N_0 is

$$N_0 = \sqrt{\frac{m_W}{3\sqrt{2}m_e}} [1 + O(N_0^{-1}) + O(\alpha)] \approx 193. \quad (5.15)$$

6:4 Boson Mass Interactions

6:4.1 W mass

In Sec. 5:3.1, a first-order expression for the W boson mass was obtained in terms of the free parameters of the $\mathbb{C}^{\wedge 18}$ model, f , N_0 , and ω_0 :

$$\begin{aligned} m_W^2 &= 9f^2 k_1^4 \omega_0^2 N_0^{12} [1 + O(N_0^{-1})] \\ &= 18m_e^2 N_0^4 [1 + O(N_0^{-1})]. \end{aligned} \quad (5.13)$$

To obtain the high-precision numerical results presented in the present chapter, it is necessary to evaluate some higher-order corrections to this expression.

6:4.1.1 Boson loops—overview

The leading contribution to the mass of the W boson arises from interactions between the W boson and the fermion components of the pseudovacuum. This interaction is corrected by numerous boson loops, with the candidate structures being illustrated in Fig. 6.1. Many of these diagrams may rapidly be dismissed. To contribute a loop correction to Fig. 6.1(i), a diagram must contain a loop which may be contracted down onto one of the vertices of Fig. 6.1(i). Diagram (ii) meets this criterion, but diagram (iii) does not as the loop contracts down onto an arbitrary point on the preon line. Diagram (iii) is therefore a correction to the preon propagator, so is already accounted for in the mean-field expansion of the pseudovacuum in diagram (i). Diagram (iv) also looks like it could contain a loop which could contract onto the upper vertex, but is better understood as a diagram *involving* the mass vertex rather than a *correction to* the mass vertex. This distinction is discussed further in the context of diagram (vi).

Diagram (v) requires a little more attention as it contains a loop which can be contracted onto the upper or lower vertex. It is expanded in terms of preons in Fig. 6.2(i). Two of the preons connecting with the loop boson must be expanded about the pseudovacuum term, and where these are both on the same vertex as in, for example, Fig. 6.2(ii), the average over many such interactions reduces to constant factors. The foreground momenta coupling to the loop boson then constitute a tadpole diagram which vanishes. When the pseudovacuum terms are on different vertices as in Fig. 6.2(iii), recognise that the mean background field term is only the first in a perturbative series describing fluctuations in the pseudovacuum. Some foreground momentum may therefore be transferred along pseudovacuum lines in the form of these fluctuations, but this transfer again constructs a tadpole so such contributions to foreground momentum transport

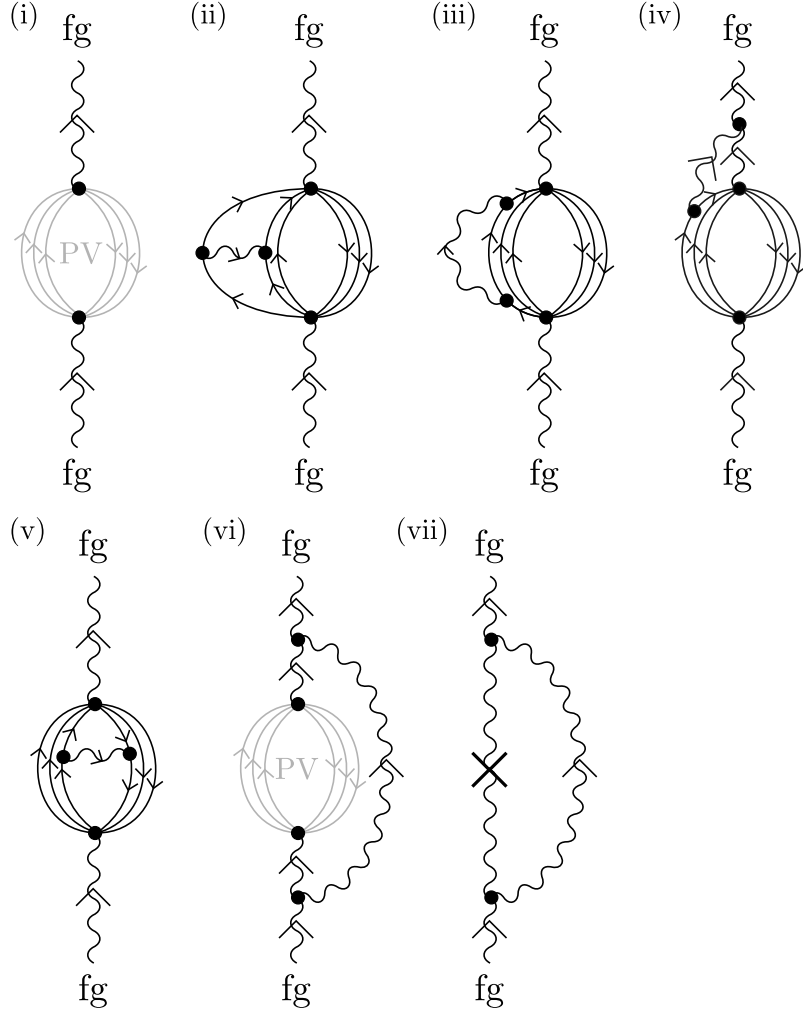


Figure 6.1: (i) Leading-order contribution to the W boson mass. External legs are truncated. (ii)-(v) Candidate structures for vector boson loop corrections to diagram (i). Note that loop diagrams may (ii)-(v) modify the W boson mass-squared interaction, or (vii) merely involve it. They must continue to include six background preons, but on diagrams (ii)-(v) there are now more than six preon/antipreon lines so there are choices as to which are expanded using the mean background field approximation. These choices are not shown here, so it is not specified which preons are foreground and which are background in these diagrams. In diagrams (i) and (vi), PV indicates pseudovacuum. To consider in turn the structures shown: The loop in diagram (ii) may be contracted onto either the upper or lower vertex, and thus this constitutes a loop correction to diagram (i). The loop in diagram (iii) does not contract onto a vertex and thus constitutes part of the preon propagator. It does not contribute to loop corrections, and is already implicit in the mean-field substitution of diagram (i). Diagram (iv) looks like a correction to diagram (i) but is more properly understood as involving rather than contributing to the mass vertex. Diagram (v) looks like it could yield corrections to diagram (i) but on expanding in terms of preons as per Fig. 6.2(i) it may be shown to contain implicit preon tadpoles and therefore vanishes. Diagram (vi) involves but does not contribute to the vertex, and its Standard Model counterpart is shown in diagram (vii). All diagrams are discussed further in the text.

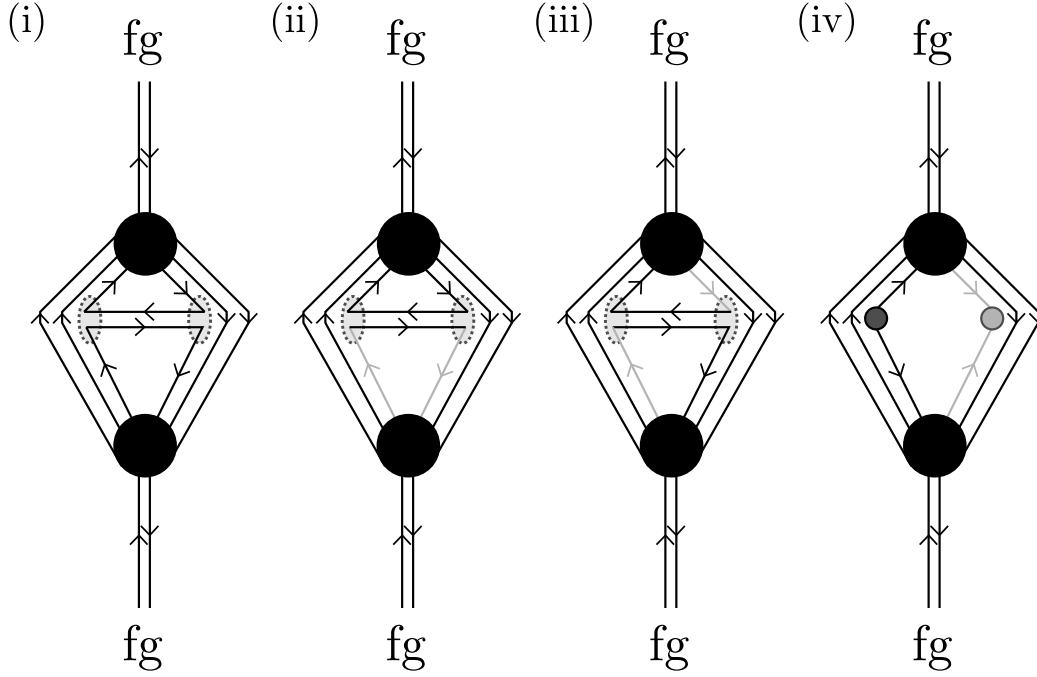


Figure 6.2: (i) Preon expansion of Fig. 6.1(v). (ii) When both lower or both upper preon lines connecting to the loop boson are background, on averaging over many interactions the foreground field lines behave as a tadpole diagram. (iii) When one upper and one lower preon line are background, perturbations about the mean background value cannot transport foreground momentum as this would once again result in an upper or lower tadpole for the momentum transported. This implies that the momenta associated with the background preons at their vertices with the loop boson are not independent, permitting diagram (iii) to be redrawn as diagram (iv). The grey dots are orientation-reversing (and perhaps colour-changing) vertices. The colour transforms they perform are correlated, but they do not exchange momenta. They may be absorbed into the lower vertex, effectively reducing the number of background field lines by one.

Table 6.1: List of labellings of preon lines in Fig. 6.3(i). Labellings which connect the upper and lower vertices with a foreground preon are described as “connected” and may be discounted.

Option	Background	Foreground	Status
1	1,2,3	4,5	Connected
2	1,2,4	3,5	Connected
3	1,2,5	3,4	Valid
4	1,3,4	2,5	Connected
5	1,3,5	2,4	Valid
6	1,4,5	2,3	Connected
7	2,3,4	1,5	Connected
8	2,3,5	1,4	Connected
9	2,4,5	1,3	Valid
10	3,4,5	1,2	Equivalent to option 3

necessarily vanish. The foreground and background momenta therefore propagate independently, equivalent to Fig. 6.2(iv). As the two vertices where the background field contacts the loop boson are not capable of independently borrowing or lending momentum to the foreground fields, the effective number of interface vertices between the foreground and background fields is reduced by two. This diagram therefore does not mediate a coupling between the W boson and the background fermion fields (which require six preon and six antipreon operators), and thus is not part of the mass series for W .

Finally, diagram (vi) again does not contribute as it requires non-truncated external legs. In fact, diagrams (iv) and (vi) are better understood as processes *involving* rather than *correcting* diagram (i). This is readily seen for diagram (vi) when the leading-order interaction of Fig. 6.1(i) is associated with a simple mass vertex $m_W^2 W^\dagger W$. In both the $\mathbb{C}^{\wedge 18}$ model and the Standard Model, expansion of the propagator yields higher-order corrections to the mass vertex as shown in diagram (vii). In the Standard Model a renormalisation scheme such as $\overline{\text{MS}}$ may be chosen to eliminate these terms, such that the coefficient on the simple mass vertex corresponds to the true mass of the W boson. This also holds for the $\mathbb{C}^{\wedge 18}$ model in the regime in which it is a good analogue to the QFT. The correction given in diagram (vi) is therefore a Proper Self Energy (PSE) term extraneous to the simple mass vertex in both the Standard Model and the $\mathbb{C}^{\wedge 18}$ model. For diagram (iv) the situation is similar: For a gluon, the net colourlessness of the W boson causes this diagram to vanish, whereas for A -sector bosons, on summing over all possible locations for the lower vertex to couple to a preon or antipreon, conservation of charges and momenta ensures that equivalency is recovered to a situation where a loop boson couples two separate locations in the propagator of the W boson.

Having eliminated the other candidate diagrams, the only corrections remaining to be evaluated are those having the form of Fig. 6.1(ii). Since these diagrams constitute couplings to background fermions, they must contain couplings between the W boson, three background preon lines, and three background antipreon lines. Numbering the preon lines as per Fig. 6.3(i) there are ten candidate terms in the mean background field expansion, listed in Table 6.1.

Examining option 1, in this diagram only one foreground preon (line 4) connects with the loop boson. The background fields proceeding from the loop boson to the upper vertex (lines 1 and 3) may transport foreground momentum as fluctuations around the background mean field state, but the parameter space of this connection corresponds to two preons, and is therefore over-large for transmitting the momentum of a single foreground preon. Performing a unitary

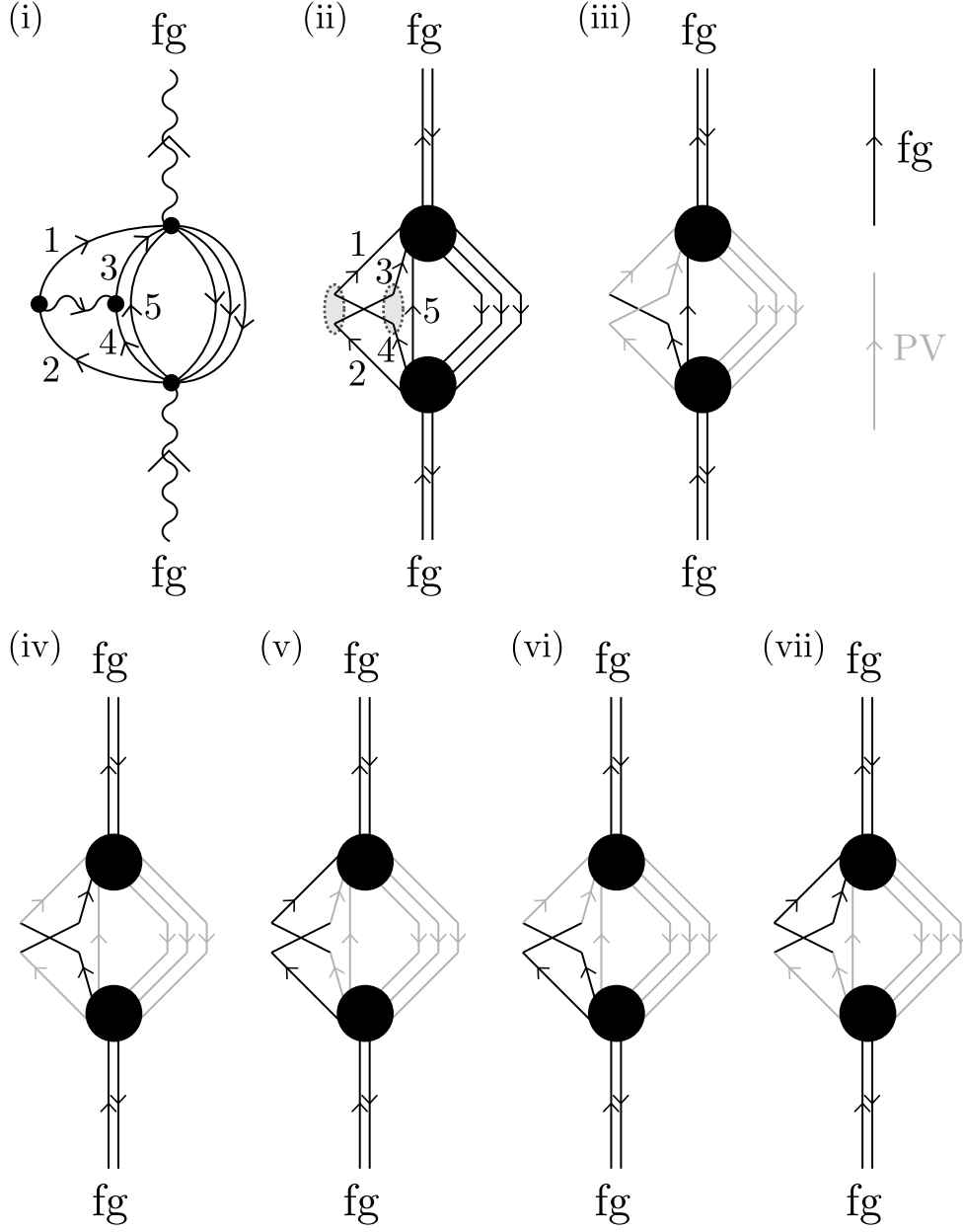


Figure 6.3: (i) Taking the specific diagram shown in Fig. 6.1(ii), label the preon lines as shown. (ii) Preon form of diagram (i). (iii) Option 1 in Table 6.1 has an effective foreground connection between upper and lower vertices, discussed further in the text, and thus only five background preon lines. It is not a valid W boson mass term. Options 2, 4, 6, 7, and 8 may be discarded similarly. Options 3 and 10 are shown in diagrams (iv) and (v) and are seen to be equivalent up to two braids and a cycling in colour labels, so only one need be retained. The other valid diagrams are options 5 and 9, shown in diagrams (vi) and (vii) respectively. In diagrams (iii)-(vii), foreground preons are drawn in black and pseudovacuum preons in grey.

mixing of these two background preons, there exists a (generally nonlocal) basis in which fluctuations about the background mean field value are transmitted along only one of the two upper left background preon lines. Also, fluctuations are on average not transmitted along the lower background field line (line 2) as this creates a tadpole as discussed for Fig. 6.2(ii). Consequently, as with Fig. 6.2(iii), the lower background preon (line 2) and the uninvolved degrees of freedom obtained from lines 1 and 3 may be mapped to a single, connected background field extending from the lower to the upper vertex as was done in Fig. 6.2(iv) (though this time no reversal of orientation is required). This diagram therefore also has the incorrect number of independent background preon operators to mediate an interaction between the W boson and background fermion fields. The same argument applies to options 2, 4, and 7, and a similar argument separating the foreground and background degrees of freedom applies to options 6 and 8.

Further, option 10 is equivalent to option 3 up to a cycling in colour labels. Other diagrams having the same structure as Fig. 6.1(ii) correspond to precisely these cyclings of the colour labels, and are included in a summation over diagrams below, so option 10 is redundant. Therefore only options 3, 5, and 9 remain. It is worth noting that interactions between preons within the loop boson of option 3 [Fig. 6.3(iv)] may also in theory cause construction of foreground momentum loops with both termini connected to the upper or lower vertex—however, these tadpoles vanish and thus the only admissible mixing processes are those which preserve the diagrammatic form shown. These mixing processes may consequently be ignored.

Having identified the valid choices as to which preons participate in the mean background field expansion, now recognise that Fig. 6.1(ii) is one of six diagrams having equivalent structures. On the left of the figure there are three choices of pairs of preons which may be linked by a boson, and on the right side of the figure there are three choices of pairs of antipreons which may similarly be pairwise linked to yield equivalent factors. It suffices to evaluate one of these diagrams, and multiply by six.

In evaluating these corrections, note that the preons which are evaluated using the pseudovacuum mean field values no longer have all field operators on the same vertices. For these preons to remain correlated with their counterparts, such that the diagram's contribution to m_W^2 does not vanish, the pseudovacuum sources and sinks must continue to be within $O(\mathcal{L}_0)$ of one another, and the loop correction must not introduce any correlations with particles outside the local region (both spatial and temporal) within which the pseudovacuum is self-correlated. This region has dimensions of order \mathcal{L}_0 , and is termed the autocorrelation region, or local correlation region. This is similar to the treatment of the scalar boson mass diagram having four preon and two antipreon lines [Fig. 5.3(ii)].

Further recognise that in Fig. 6.1(ii) the loop spans between two components of a composite fermion. These are necessarily separated, on average, by a distance of $O(\mathcal{L}_\psi)$ in the rest frame of the fermion, which is the maximum separation of the preon components of a fermion triplet. As this length scale is much smaller than \mathcal{L}_0 , which is the characteristic length scale of mass interactions, the loop boson may propagate on-shell across this distance as a massless particle. It may also engage in lengthier excursions characterised by scales such as $O(\mathcal{L}_0)$, on which it will acquire a nonzero mass, but over a net distance of $O(\mathcal{L}_\psi)$ from one preon to another, such excursions will inevitably be far off shell and may be disregarded. As noted in Sec. 5:3.1, the underlying vertex diagram is restricted to a region characterised by \mathcal{L}_ψ and thus the added vertices on any loop corrections must also lie within such a region. By the same argument as for Fig. 6.1(ii), the particles participating in these loops are likewise massless. (This argument also applies to corrections arising from the complex scalar boson.)

Having thus established

- the diagrams which need to be evaluated to compute vector boson loop corrections to Fig. 6.1(i), and

- that all bosons in these loops are effectively massless over the length scales involved,

these loop corrections may be evaluated as follows.

6: 4.1.2 Gluon loops

It is convenient to work in the e_{ij} basis of $\mathfrak{gl}(3, \mathbb{R})$, noting the caveat of Sec. 3: 3.3.7 regarding counting of FSF symmetry factors. As noted above, there are six topologically distinct diagrams having the general form of Fig. 6.1(ii) where a gluon propagates either from one preon to another, or from one antipreon to another. Each of these six diagrams admits multiple colour labellings. By $SU(3)_C$ symmetry, all six choices as to which preons engage in gluon exchange, and all valid choices of colour labels, make equal contributions to m_W^2 . Interaction with the pseudovacuum is with randomly chosen background fermion fields compatible with a given diagram, granting colour neutrality to the preon triplet and to the antipreon triplet, and the colour symmetry of the pseudovacuum implies a summing over possible colour configurations. Since the colours of the three members of the triplet are unique, the factor associated with this sum may be equivalently represented either by explicitly summing over all colour labellings, or by suppressing these labellings and instead counting the exchange symmetry of the preon lines. (This works even when the A -charges are not homogeneous, as a sum is then also made over the position of the mismatched A -charge.)

Given one specific choice of diagram with one specific colour labelling, the gluon vertices are each associated with a factor of f , and FSF symmetries yield a factor of $N_0^3 [1 + \frac{33}{8} N_0^{-1} + O(N_0^{-2})]$ with counting being the same as for the photon (3.82) (recalling that for the purpose of counting FSF symmetry factors, the W boson and gluons must be written in terms of their real hermitian components). Comparing with Eq. (3.83) the product of the gluon vertex factors is therefore equal to¹

$$2\alpha[1 + O(\alpha)]. \quad (6.10)$$

Further, taking an approach similar to Sec. 3: 3.5.8, consider a specific one of the six topologically distinct diagrams [e.g. gluon links preon 1 to preon 2, as shown in Fig. 6.1(ii)] but let this diagram be averaged over all colour labellings. For conciseness, include FSF symmetry factors in the vertex coefficients ($f \rightarrow \tilde{f}_A$). Choosing one gluon vertex to nominally be the emission vertex, it attracts factors as follows:

- One (spatial) choice of which preon to interact with.
- Three choices of colour on that preon prior to interaction.
- Interaction strength \tilde{f}_A .

Similarly, for the nominal absorption vertex:

- One (spatial) choice of which preon to interact with.
- Two choices of colour on that preon prior to interaction (which must differ to the preon at the emission vertex prior to interaction).
- Interaction strength \tilde{f}_A .

For the gluon:

- There are nine different species of gluons.

¹Corrections of $O(\alpha^n)$ are implicitly of $O[(\alpha/\pi)^n]$, with factors of π being omitted in Chs. 6 and 7 for brevity.

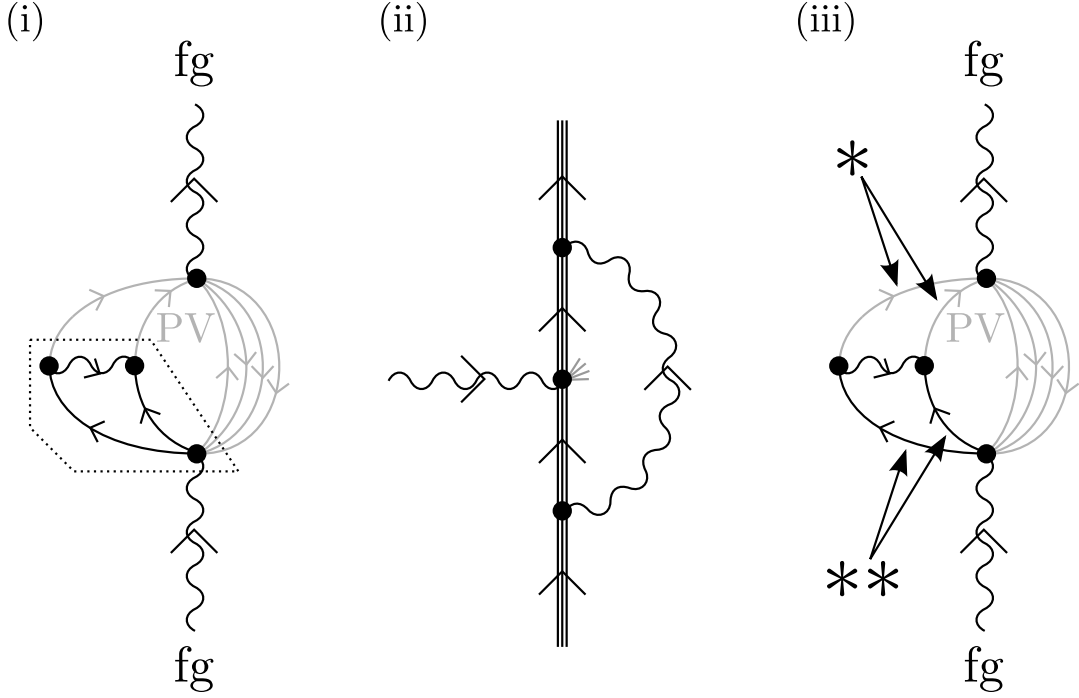


Figure 6.4: Applying diagrammatic isotopy permits (i) gluon exchange to be rewritten as (ii) a gluon-mediated loop correction to W boson emission via either of the processes illustrated in Fig. 6.5. [The other four preons at the vertex are uninvolved, and are shown as truncated stubs in diagram (ii).] This gives numerical equivalence between the vertex loop correction of diagram (ii) and the correction generated by the indicated region of diagram (i), up to a sign due to the crossing in Figs. 6.5(ii) and (vi) and a factor of 2 for the symmetry which interchanges the two different ways this reduction can be achieved. This symmetry is illustrated in diagram (iii), where simultaneous exchange of the two preon lines marked $*$ and the two preon lines marked $**$ leaves the figure unchanged up to a permutation of colour indices, and interchanges Figs. 6.5(i) and (v).

- However, only one in three is compatible with the preon colour at the emission vertex.
- Similarly, only one in three of those remaining is compatible with the preon colour at the absorption vertex.

Finally, to go from a sum to an average over colour labellings on the preon lines, introduce a further factor of $\frac{1}{6}$. After evaluating all colour labellings in this way, the net product of vertex factors for a given position of the loop is $\tilde{f}_A^2 = 2\alpha[1 + O(\alpha)]$.

Next, recognise that each interaction between a preon and a gluon takes place in the presence of two other preons, with the three preons arising from a background fermion. This is a single-boson-species interaction so K matrices are not required (Sec. 4:3.3). For purposes of evaluation it is useful next to consider the choice of diagram and pseudovacuum expansion shown in Fig. 6.4(i) and map the indicated subdiagram into a loop diagram involving fermions. To do so, recognise that a subset of the preon lines in Fig. 6.3(i)-(ii) may be identified with a boson loop correction to $W^{(\dagger)}$ emission, up to an additional crossing. A suitable subset is shown in Fig. 6.5(i)-(ii), with an alternative choice being shown in Fig. 6.5(v)-(vi). An isotopy transfor-

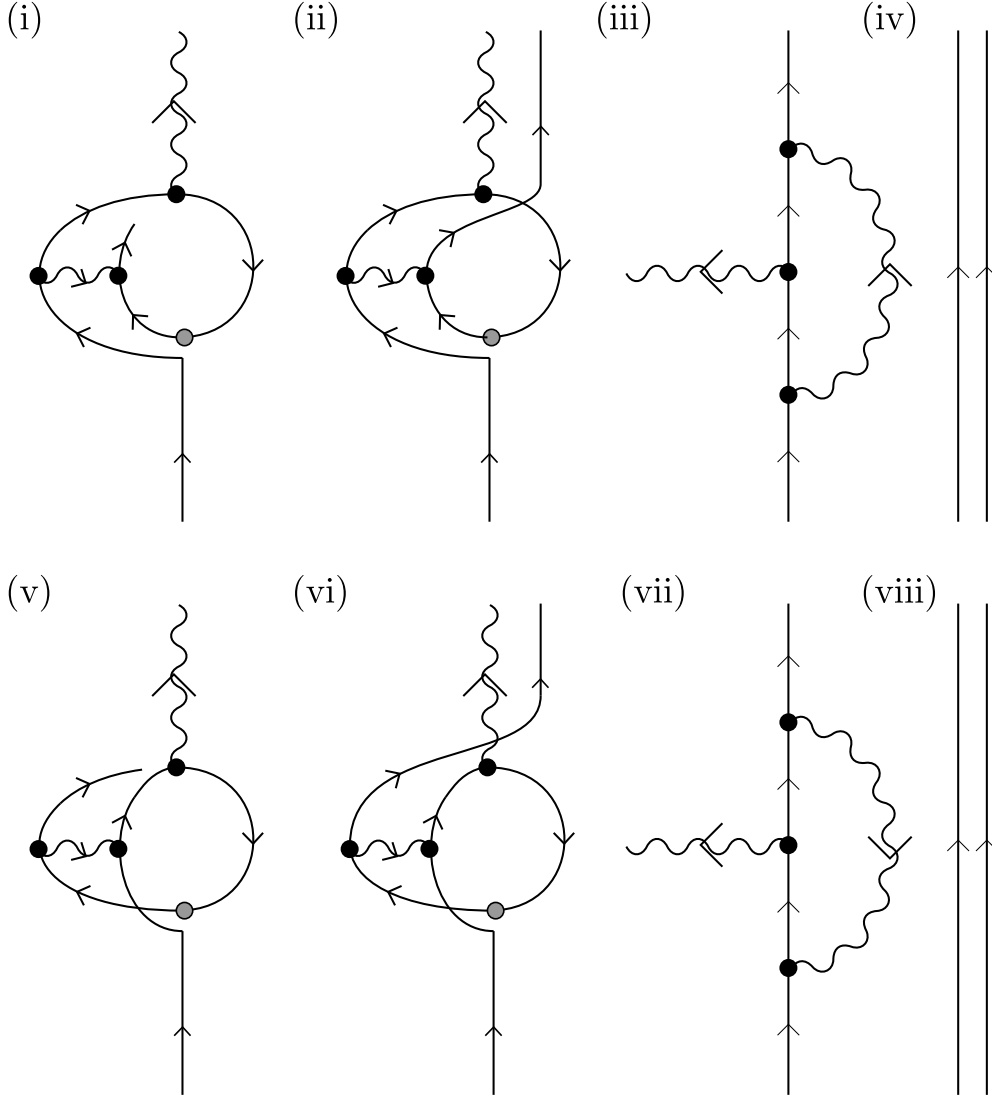


Figure 6.5: (i) A subset of the preon lines in Fig. 6.3(i)-(ii), chosen for consistency of colour, construct an off-diagonal boson loop correction to W boson emission at the upper vertex. The grey dot denotes a change in A -sector charge with no consequence for the colour interaction. If the free preon is taken to the far field as shown in diagram (ii), this is then equivalent to the loop correction shown in diagram (iii) up to a crossing, which yields a factor of -1 . Adding further preons (iv) to diagram (iii) permits the emitting particle to be converted to a fermion. Internal symmetrisation within the fermion then allows the loop boson to couple to any member of the triplet at each vertex as discussed in Sec. 6: 5.2, but the resulting factors of 3 cancel with factors of $1/\sqrt{3}$ in the definitions of the fermions in Sec. 3: 3.2.1. An alternate and equivalent construction, which may also be obtained from Fig. 6.3(i)-(ii), is shown in diagrams (v)-(viii). Note that the other preons from Fig. 6.3(i)-(ii) may also optionally be reintroduced into diagrams (i)-(ii) or (v)-(vi), where they comprise one free preon with arrow oriented downwards, and either two more free preons (one up, one down) or a closed loop which is eliminated by vacuum normalisation. Their reintroduction introduces no further factors into the multiplicative constant associated with the loop correction.

mation on either set yields diagram (iii) up to a sign corresponding to the preon crossing. It is then convenient to introduce a further two preon lines which have the same A -charge as the interacting preon, and with colours chosen to yield overall colour neutrality. If these are balanced by a numerical factor of $\mathcal{N}^{-1} = (N_0 + 1)^{-2}$ then this leaves the value of the diagram unchanged. The resulting diagram has definite colour on each preon, and a specific pair of preons of definite colour engage in the gluon interaction. However, if the diagram is averaged over the locations of the preons,² and these are assumed subject to random redistribution as they propagate, for independence of arrangement at upper and lower vertices, then this gives three configurations at each loop vertex, each accompanied by a factor of $1/3$. This has no effect on the vertex factors (see Sec. 3:3.5.8.e), but completes the mapping of the preon diagram in Fig. 6.4(i) to the fermion diagram of Fig. 6.4(ii). The loops in the two diagrams are numerically equivalent up to a factor of -1 for the crossing in Fig. 6.3(ii) or (vi), and a factor of 2 for the symmetry present in Fig. 6.4(i) [and made explicit in Fig. 6.4(iii)] which gives rise to the two choices of Figs. 6.3(i) and (v).

It is convenient to have a systematic means of presenting the factors associated with the many loop diagrams encountered in this chapter. Therefore let the overall correction to the original vertex be written in terms of the following factors:

- A combined vertex and structural factor,
- A mass-related factor, and
- A common factor of $(4\pi)^{-1}$ written separately for clarity.

For reference, in this notation the factors associated with the one-photon-loop correction to lepton magnetic moment would be

$$2\alpha \cdot \mathbf{f}\left(\frac{m_\ell^2}{m_A^2}\right) \cdot \frac{1}{4\pi} \quad (6.11)$$

and those for the one- W -loop correction to lepton magnetic moment would be [26]

$$-\frac{10\alpha}{3} [1 + \mathcal{O}(\alpha)] \cdot \mathbf{f}\left(\frac{m_\ell^2}{m_W^2}\right) \cdot \frac{1}{4\pi}. \quad (6.12)$$

Where the loop boson is a foreground field, the mass dependency $\mathbf{f}(\cdot)$ evaluates as

$$\mathbf{f}\left(\frac{m_\ell^2}{m_b^2}\right) \longrightarrow \begin{cases} 1 & \text{if } m_b^2 = 0 \\ \frac{m_\ell^2}{4\pi m_b^2} & \text{if } m_b^2 \gg m_\ell^2. \end{cases} \quad (6.13)$$

(Note that this expression attracts a modification for background fields, discussed in Appendix 6: A.)

From the above breakdown of factors associated with vector boson loop corrections to vector boson emission, it is readily seen that the off-diagonal gluon attracts a structure factor of $-10\alpha/3$, supplemented by a factor of 2 from the two ways which Fig. 6.4(i) may be mapped to Fig. 6.4(ii), and a factor of -1 for the crossing in Figs. 6.5(ii) and (vi) respectively. The mass factor vanishes

²This averaging takes place with respect to the preons of Fig. 6.5(iv), which are a numerical convenience—it has no bearing on the sum over the six different loop positions available in Fig. 6.1(ii) or the three different pseudovacuum expansions apiece, and the calculation thus far is still only for a single one of these six diagrams and three expansions.

because the gluon is massless over scale \mathcal{L}_ψ . Finally, multiplying by three for the three different pseudovacuum expansions and six for the six numerically equivalent diagrams yields

$$3 \cdot 6 \cdot \frac{20\alpha}{3} [1 + \mathcal{O}(\alpha)] \cdot 1 \cdot \frac{1}{4\pi} = \frac{60\alpha}{2\pi} [1 + \mathcal{O}(\alpha)]. \quad (6.14)$$

These loop corrections apply identically to the diagrams in which the W boson interacts with background lepton fields (“ W /lepton diagrams”) and the diagrams in which the W boson interacts with background quark fields (“ W /quark diagrams”) as the colour structure of both diagrams is the same, and the gluons are agnostic of A -charge.

6:4.1.3 Photon, W , and Z boson loops

Calculation of the contribution of gluon loops is relatively straightforward because the W boson is colour-agnostic, having trivial representation on the C sector. However, more caution is required on the A sector, as the W boson is not agnostic of A -charges.

For the photon, proceed as with the gluons by enumerating all the interactions at the preon level. Begin with the W /lepton diagrams. In contrast with the preceding calculation there are only three such interactions, as the photon may only couple to the charged preons in the e_L side of the loop. However, there are still three pseudovacuum expansions per diagram. Next, as per Sec. 3:3.5.8, note that lepton couplings to photons arise in equal measure from all three preons. *Within a fermion*, the coupling of a single preon to a photon carries an effective coefficient of $\sqrt{\alpha}/3$ due to the normalisation factor in Eq. (3.28). This may be contrasted with gluon couplings which are always mediated by the single preon carrying the appropriate charge to participate in the interaction—but for which there is then a sum over three different positions for that colour of preon. For the photon the net EM vertex factor per preon is therefore $\sqrt{\alpha}/3$, in contrast with $\sqrt{2\alpha}[1 + \mathcal{O}(\alpha)]$ for gluons. Equivalently, emission by a fermion of a specific gluon is a single-preon process, whereas emission by a fermion of a photon is a collective process.

For the rest of the structure factor, the diagram this time is a simple photon loop correction to a boson emission vertex, for a factor of $1/(2\pi)$, and has no hidden crossings. Mapping to a standard photon loop correction to an emission vertex (Fig. 6.6) involves reversing the time orientation of one of the preon limbs, but also reversal of charge and parity at its source and sink operators, for a sign of $+1$. Both diagrams have equivalent symmetry factors from vertex exchange. The boson is diagonal, so the total structure factor is $2\alpha/9$. The net correction is therefore

$$3 \cdot 3 \cdot \frac{2\alpha}{9} \cdot 1 \cdot \frac{1}{4\pi} = \frac{\alpha}{2\pi}. \quad (6.15)$$

Next, the photon loop corrections to the W /quark diagrams of Eq. (5.6). For these it is helpful to compare the photon/preon interactions involved with those encountered in the photon loop correction to the W /lepton vertex just completed. There are numerous ways to count the interactions; one of the simplest is as follows: First, recognise that to host a diagram having the form of Fig. 6.1(ii), a group of three preons or antipreons must include two charged constituents. This restricts such diagrams to the up quark limb, and for a given configuration of preons there is only one such pair, in contrast with three choices in the W /lepton diagram. However, even while remaining colour-agnostic, there are now three different configurations of preons available, corresponding to the choice of which preon is uncharged. Overall, the photon loop may therefore once again be in any of three different positions (one for each of the three configurations). The remainder of the calculation proceeds identically, and the electromagnetic loop factor for the W /quark mass vertex is therefore equivalent to that for the W /lepton mass vertex.

For Z boson loop corrections, a little more caution is needed. When computing photon loop corrections, all photon emission processes are additive. However, when emitting the bosons for

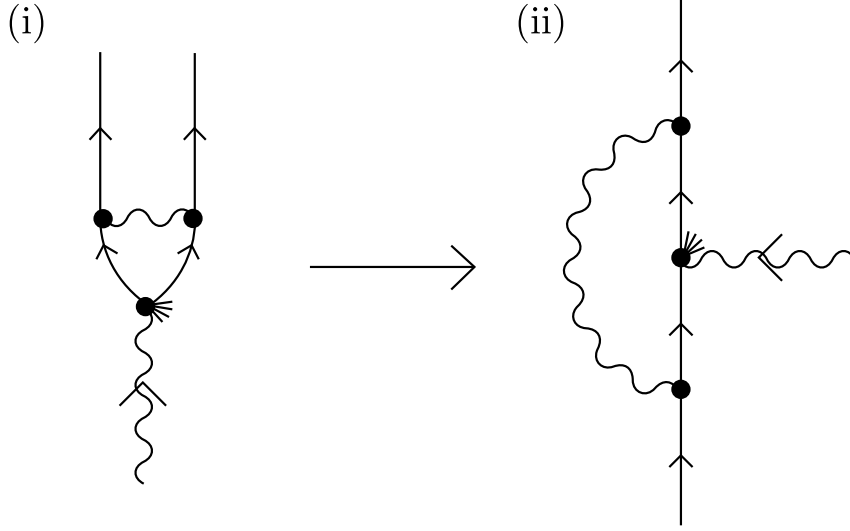


Figure 6.6: Mapping of (i) a photon-mediated preon-preon interaction in Fig. 6.1(ii) to (ii) an emission vertex interaction exploits colour agnosticism, and involves both time reversal and charge and parity inversion for no net change of sign. The other four preons at the vertex are uninvolved, and are shown as truncated stubs.

Z loops, some destructive interference takes place. Recognise that there are two vertices which may contribute to the sign of Z emission—the coupling between the W boson and the background preon fields, which gives rise to different preon and antipreon triplets with varying weights, and the coupling between these triplets and the emitted Z field which goes on to form the loop correction. When looking for cancellations it is convenient to treat the preon triplet collectively as a fermion, and the same with the antipreon triplet. However, once cancellations have been identified, it is then necessary to return to a preon picture to evaluate the surviving loops. In the present context the W boson couples to $e_L \bar{\nu}_e$ and $d_L \bar{u}_L$ with equal vertex weight, and these constituents then couple to the Z field with the strengths shown in Table 6.2. Comparison of coefficients reveals that the different Z emission processes on the preon lines cancel, as do the couplings of the individual preons within u_L , and only emission from the antineutrino sector of the antipreon line persists.

The Z loops on the antineutrino preon triplet may then be mapped to an effective overall vertex correction exactly as was done for the photon loops. To evaluate this loop correction by reduction to a previously solved problem, recognise that the relative strengths of the one-photon and one- Z boson loop corrections to lepton magnetic moment are

$$2\alpha \cdot 1 \cdot \frac{1}{4\pi} \quad \text{and} \quad -f_Z \alpha \cdot \mathbf{f} \left(\frac{m_\ell^2}{m_W^2} \right) \cdot \frac{1}{4\pi} \quad (6.16)$$

Table 6.2: When a W boson couples to the background fields, it does so to multiple particle species. This table summarises the weights of the W /preon couplings (vertex weight), the coefficients of these species' couplings to the Z boson field, and the relative contributions of each choice of fermion species to diagram Fig. 6.1(i) as a whole (loop weight). FSF factors are omitted for brevity. Species e_L and d_L are seen to occur with equal vertex weights, and have opposite coupling coefficients to the Z field, indicating that their contributions to Z emission cancel. There is no residual Z emission on the preon lines, only the antipreon lines.

Preon lines			
Species	Vertex weight	Z coefficient	Loop weight
e_L	f	$\frac{2f}{\sqrt{6}} \cdot \frac{1}{2}$	$\frac{1}{2}$
d_L	f	$\frac{2f}{\sqrt{6}} \cdot -\frac{1}{2}$	$\frac{1}{2}$
Antipreon lines			
Species	Vertex weight	Z coefficient	Loop weight
$\bar{\nu}_e$	f	$\frac{2f}{\sqrt{6}} \cdot -1$	$\frac{1}{2}$
\bar{u}_L	f	0	$\frac{1}{2}$

where f_Z is the Z boson loop structural factor

$$f_Z := \frac{1}{3} \left[(4 \sin^2 \theta_W - 1)^2 - 5 \right] \quad (6.17)$$

$$= \frac{1}{3} \left(4 - 24 \frac{m_W^2}{m_Z^2} + 16 \frac{m_W^4}{m_Z^4} \right)$$

$$\sin^2 \theta_W = 1 - \frac{m_W^2}{m_Z^2}. \quad (6.18)$$

In the present context

1. the W boson is effectively massless, eliminating $\mathbf{f}(\cdot)$, and
2. the average vertex factors are -1 (for neutrinos) instead of $1/2$ (for electrons), for a relative factor of 4.

The one- Z -loop correction term arising from the $e_L \bar{e}_L$ base diagram after eliminating cancelled terms may thus obtained by taking the one-photon-loop correction to the lepton magnetic moment, multiplying by the above two factors, and then further multiplying by the ratio of the structure coefficients for the one- Z -loop and one-photon-loop corrections to the lepton magnetic moment. This gives

$$\frac{\alpha}{2\pi} \cdot 4 \cdot -\frac{f_Z \alpha}{2\alpha} = -\frac{f_Z \alpha}{\pi} \quad (6.19)$$

which is positive as $f_Z < 0$.

This is the correction term arising from the $e_L \bar{e}_L$ loop after eliminating cancelled terms, whereas the correction term arising from the $d_L \bar{u}_L$ loop after eliminating cancellations is zero. The relative contributions of each type of loop to the overall mass process are given by squaring the vertex weights and normalising so that they sum to 1, to obtain the loop weights. In this

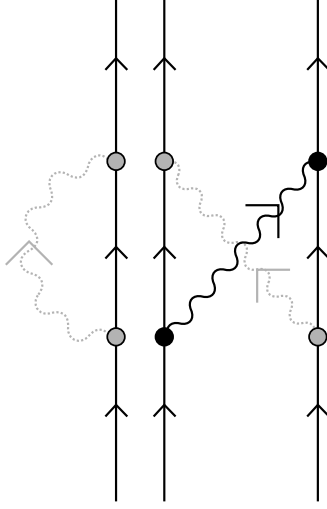


Figure 6.7: Prototype of the boson exchange process involved in a W loop correction to Fig. 6.1(i), with co-ordinate transformations represented as pale dotted bosons carrying off-diagonal A -sector representations but zero momentum.

instance these correspond to equal contributions, and the average correction factor is thus

$$-\frac{f_Z \alpha}{\pi} \cdot \frac{1}{2} + 0 \cdot \frac{1}{2} = -\frac{f_Z \alpha}{2\pi}. \quad (6.20)$$

Finally, for W boson loop corrections, recognise that for fermions, $W^{(\dagger)}$ emission is a species-changing activity accompanied by a change of co-ordinates on the A sector (see Sec. 3:3.5.4). Collectively the preon limb may convert from e_L to ν_e or from d_L to u_L with emission of W , followed shortly by reabsorption of the same, with conjugate processes on the antipreon limb.

However, now consider the accompanying co-ordinate changes which maintain the fermion as a valid species in accordance with the gauge choices of Sec. 3:3.3.6 and their implications for supported fermions (Sec. 3:3.4.1). These changes are conjugate, and may be represented as exchange of a boson in the e_{ij}^A basis with zero momentum but appropriate A -charges. The W boson must be emitted and absorbed on different preons, and thus the prototype for such diagrams is as per Fig. 6.7. This diagram is the same for leptons and quarks:

- For leptons, the interaction may be with any preon, but diagrams yielding preon PSE terms do not contribute to the vertex correction.
- For quarks, the interaction must be with the unique preon, but that preon may do so from one of three different positions:
 - On average, as noted in Sec. 4:3.2.2, each A -sector interaction is accompanied by one C -sector interaction. Over the course of a loop correction involving two preons, labelled 1 and 2, and not involving preon 3, the two associated C -sector interactions may realise any two of the following with equal likelihood:
 - * preon 1 may interact with preon 3,
 - * preon 2 may interact with preon 3, and
 - * preon 1 may interact with preon 2.

- Any of these interactions may freely transfer any amount of the foreground momentum being carried as fluctuations by the preons involved, and any colour rearrangement over the three preons may be realised. In a context where position is integrated over, this arbitrary rearrangement of all properties except A -charge is equivalent to an arbitrary repositioning of the unique A -charge between the two vertices. Thus the position of the interacting preon is independent at source and sink.

Now recognise that as per Appendix 6:A, the massless foreground W correction reduces to an interaction at a spatial point. Similarly, the co-ordinate change boson connecting the participating preons is a W boson exchange which is restricted to an interaction at a single point in momentum space. The resulting correction factors are equivalent under fourier transform, implying equivalent boson emission strengths, and the bosons have opposed orientations. The result is net zero W field at the point of emission, indicating that the contribution from the W loop must vanish.

6:4.1.4 Scalar boson loops

For scalar bosons the overall approach is similar to that taken for vector bosons, though the diagrams are different, being shown in Fig. 6.8. The preons within a scalar boson may be crossed or uncrossed.

Considering first Fig. 6.8(i), for a given set of preons in the fermion fields this diagram yields one of nine terms in the sum making up the scalar boson. Recalling the factor of $O(N_0^{-2})$ attracted by any scalar boson propagating to the far field, this term is dominated by the contribution when the two vertices coincide as shown in Fig. 6.9(i). As per Sec. 3:3.5.5, terms where the source and sink are separate then correct this diagram by at most $O(N_0^{-4})$. Further, now consider colour consistency and recognise that at either of the loop vertices in Fig. 6.8(i), both preons in the fermion must be of different colour while both preons in the scalar boson must be the same. This can only be reconciled if the two vertices are collocated, and thus may be rewritten as a single colour-conserving vertex. Any diagrams where the termini of the scalar boson loop do not coincide—written as $O(N_0^{-4})$ above—must therefore vanish. (This collocation is relaxed very slightly on noting that colour may be borrowed from the background field, but only over \mathcal{L}_ψ , assumed to be the smallest scale of the model. Similar considerations are applicable to all fermion/ \mathbf{H} interactions of the sort shown in Fig. 3.6.) Note that the factor associated with the effective colour-conserving vertex is determined by its construction from two disparate vertices (and integrating out their accessory degrees of freedom)—there is no need to assign an additional factor of two due to on-vertex symmetries.

It is now useful to compare this scenario with the vector boson loop correction of Fig. 6.1(ii):

- For the vector boson loop, the contribution is determined by the contribution when the loop vertices coincide, as discussed in the Appendix 6:A.
- For the scalar boson loop, the contribution is determined by the contribution when the loop vertices coincide, as discussed for Fig. 6.9 above.
- For the vector boson loop, this is equivalent to contracting the boson loop into either the upper or the lower vertex.
- For the scalar boson loop, writing the correction as a numerical multiplier on the original diagram is likewise equivalent to contracting the boson loop into either the upper or the lower vertex.

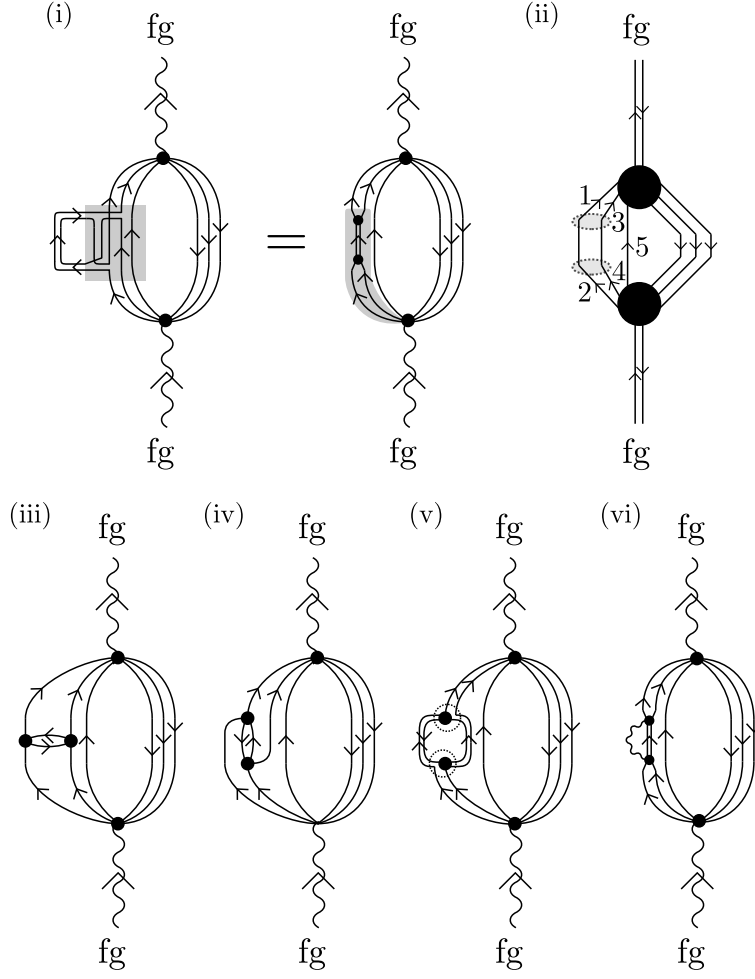


Figure 6.8: Structures of loop corrections to W /fermion vertices involving scalar bosons. Diagram (i) shows the simplest scalar boson loop correction—in the first form, the shaded area corresponds to scalar boson emission as per Fig. 3.6. In the second form this is simplified by diagrammatic isotopy. The shaded region of the second form comprises the correction loop, which may be contracted into a numerical correction to the lower vertex (or into the upper vertex if preferred, though this represents two ways to evaluate the same diagram, not a twofold degeneracy). Within the scalar boson, the preons may be crossed or uncrossed, though only uncrossed is shown. Colour inconsistency within the scalar boson is addressed in the main text, by reduction to Fig. 6.9. Diagram (ii) shows the preon expansion for the uncrossed configuration, and labels the preons which may participate in the pseudovacuum expansion. The different labellings are enumerated in Table 6.3. Diagrams (iii)-(vi) construct a further scalar boson loop correction: Begin with Fig. 6.1(ii) and first (iii) redraw the vector boson as a pair of preons. Then (iv) use diagrammatic isotopy to rotate the resulting loop. (v) Group the preons as shown, and introduce effective vertices at the top and bottom of the loop which encompass both the existing vertices (factor of f apiece) and the preon redistribution operations (factor of 1 apiece). The end result is diagram (vi), which is equivalent to diagram (i) supplemented by a further massless vector boson loop with effective vertex factors of 1. This must be considered in addition to Fig. 6.1(ii) as the mass shell of the resultant foreground scalar boson is distinct from that of the vector boson in Fig. 6.1(ii) so it is treated as a separate effective excitation.

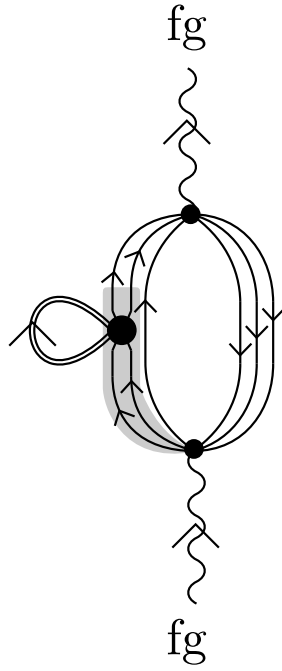


Figure 6.9: The contribution of Fig. 6.8(i) to W boson mass is dominated by contributions made when the two interaction vertices coincide, as shown here. However, given the underlying structure of Fig. 6.8(i) this should not be mistaken for a loop correction to the propagator. As a loop correction to Fig. 6.1(i), the resulting factor is still absorbed into either the upper or the lower vertex, with the latter being indicated by the shading.

- In both cases, the choice of contracting into the upper or lower vertex is a descriptive one. Although it represents a symmetry in the calculation such that there are two equivalent ways of *evaluating* the associated Feynman diagrams, these do not correspond to different diagrams, and hence there is no factor of 2 associated with this.

To evaluate Fig. 6.8(i), first recognise that with the preons crossed, the resulting preon diagram has the same preon structure as Fig. 6.3(ii)—the colour sector is summed (corresponding to the sum over terms in the scalar boson) rather than averaged, but the net result is the same up to an overall multiplier. Further, both of these diagrams are dominated by contributions in which the separation of the boson vertices approaches zero. This diagram will consequently evaluate equivalent to the photon loop of Fig. 6.3(i) up to an overall multiplier to be determined explicitly now. Whereas the photon loop accrues an overall factor of $2 \cdot (4\pi)^{-1}$, for the scalar boson take note of the following:

- For coupling coefficients,
 - the raw vertex coefficient is f in place of $f/\sqrt{2}$,
 - Each preon/scalar boson coupling should be understood in the context of a fermion/scalar boson coupling and thus attracts a factor of $\frac{1}{3}$ per vertex from the definition of the fermion (3.28). As with the photon, the total net coupling is averaged across the three preons by this factor.

The coupling coefficient is consequently $(2\alpha/9)[1 + O(\alpha)]$.

- Also contributing to the structure factor,
 - there is no symmetry under exchange of boson source/sink (factor 1), and
 - unlike the photon the complex scalar boson is not written in terms of $\sigma^\mu \sigma_\mu$ (factor $-\frac{1}{2}$).

The structure factor, incorporating the vertex coefficient, is consequently $-(\alpha/9)[1 + O(\alpha)]$ compared with the photon's $2\alpha/9$.

- Regarding the pseudovacuum expansion and crossed and uncrossed preon lines,
 - the crossed preon configuration admits three pseudovacuum expansions, directly equivalent to those of Fig. 6.1(ii), while
 - the uncrossed preon configuration admits four pseudovacuum expansions, elaborated below. These have one less crossing and are therefore of opposite sign.

The net factor arising from pseudovacuum expansions and preon crossings in combination is therefore -1 .

- For other factors:
 - Three choices of preon pairs in the ascending limb, three choices in the descending limb, yield six diagrams.
 - The above evaluates the contribution of one of nine terms in the scalar boson sum. All terms contribute, as excitation of any one leads to excitation of all by unbroken $SU(3)_C \otimes GL(1, \mathbb{R})_N$ symmetry, for a further factor of 9.

Table 6.3: List of labellings of preon lines in Fig. 6.8(ii). For brevity, labellings in which preon 5 is foreground have been omitted as these are always “connected” so never contribute to the mass correction.

Option	Background	Foreground	Status
1	1,2,5	3,4	Connected
2	1,3,5	2,4	Valid
3	1,4,5	2,3	Valid
4	2,3,5	1,4	Valid
5	2,4,5	1,3	Valid
6	3,4,5	1,2	Connected

To evaluate pseudovacuum expansions for Fig. 6.8(i) with the preon lines in the scalar boson uncrossed, label as per Fig. 6.8(ii) and expand as per Table 6.3. Following the same arguments employed to identify connected diagrams in Sec. 6:4.1.1 above, only one option out of each pair (1,3) and (4,6) need be retained, and this should be the one in which there is no foreground connection between upper and lower vertices.

It is also worth noting the caution required around the sign of scalar boson contributions to pseudovacuum expansions. In identifying the crossed preon configuration with the preon expansion of Fig. 6.1(ii), these diagrams are seen to have equivalent sign, and the uncrossed configurations to have the opposite sign. However, without making the pseudovacuum expansion explicit, it would have been easy to assume that all scalar boson loop terms had a minus sign relative to the vector boson terms due to the presence of an additional fermion loop in Fig. 6.1(i). It is always advisable to perform explicit preon expansions to check signs of terms in diagrams involving both scalar bosons and loops.

Putting together the above, the net factor associated with Fig. 6.8(i) [with terms ordered as per Eq. (6.14), and the extra factor from the nine terms in the scalar boson at the end] is

$$-1 \cdot 6 \cdot -\frac{\alpha}{9}[1 + O(\alpha)] \cdot 1 \cdot \frac{1}{4\pi} \cdot 9 = \frac{3\alpha}{2\pi}[1 + O(\alpha)]. \quad (6.21)$$

Next, consider Fig. 6.8(vi). This diagram is obtained by transforming the photon loop correction of Fig. 6.1(ii), but must be considered a separate figure as it involves the scalar boson, which propagates as a distinct entity under the Lagrangian on $\mathbb{R}^{1,3}$. The pair of loops may be decomposed into two independent multiplicative factors, one corresponding to a scalar boson and directly equivalent to Fig. 6.8(i), and another arising from the massless vector boson with interaction vertices of value 1. Note that as with Fig. 6.8(i) reducing to Fig. 6.9, the vertices of the scalar boson in Fig. 6.8(vi) must likewise be brought to coincide. The resulting scenario is very similar to that encountered in Sec. 5:3.3—compared with a photon loop, relative factors are as follows:

- The boson loop contains only the appropriate preons, so there is no factor of $1/\sqrt{2}$ associated with the vertex. The coupling would consequently be $2\alpha[1 + O(\alpha)]$ in place of α . However, this is then replaced with 1 as there are no factors of f associated with the vector boson loop. Net relative factor: α^{-1} .
- No extra symmetry factor for on-vertex interchange of boson ends where compatible, as the effective vertex has been synthesised from two subvertices and not drawn down from the generator \mathcal{Z} .

The vector boson loop on diagram (iv) therefore contributes an additional multiplier of $2 \cdot (4\pi)^{-1}$ for a total factor from Fig. 6.8(vi) of

$$\frac{3\alpha}{2\pi} \cdot \frac{1}{2\pi}. \quad (6.22)$$

Combining with Fig. 6.8(i) yields a net scalar boson loop correction factor of

$$\frac{3\alpha}{2\pi} \left(1 + \frac{1}{2\pi} \right). \quad (6.23)$$

6:4.1.5 Net effect of all boson loops

The net effect of the boson loop corrections is therefore to amend the W boson mass equation to

$$m_W^2 = 9f^2 [k_1]^4 \omega_0^2 N_0^{12} S_{6,13} \times \left[1 + \left(64 + \frac{3}{2\pi} - f_Z \right) \frac{\alpha}{2\pi} + O[(k_1 N_0)^{-4}] + O(\alpha^2) \right] \quad (6.24)$$

$$S_{6,13} := N_0^{-4} (N_0 + 2)^2 (N_0 + 1)^2 = 1 + 6N_0^{-1} + 13N_0^{-2} + \dots \quad (6.25)$$

$$f_Z = \frac{1}{3} \left(4 - 24 \frac{m_W^2}{m_Z^2} + 16 \frac{m_W^4}{m_Z^4} \right) \quad (6.26)$$

where $S_{6,13}$ was previously introduced in Eqs. (3.79), (4.10) and (5.7), and the next-most-relevant members of the correction series are those due to the coupling of the W boson to the background photon and scalar fields {which are smaller by a factor of $[k_1 N_0]^{-4}$ }, the second-order electromagnetic corrections [with leading contribution being of $O(\alpha^2)$], and the various factors of $[1 + O(\alpha)]$ in the above calculations which correct terms already containing α and thus are also of $O(\alpha^2)$.

6:4.1.6 Species dependence of k_1

Regarding the factor of k_1 in the above:

- When particle masses are evaluated beyond tree level, the mass matrices incorporate higher-order corrections which are themselves dependent on the particle masses (as seen, for example, in the f_Z dependence of m_W^2). Similar corrections will also apply in fermion mass calculations.
- It immediately follows that the mass eigenvalues k_i are thus dependent on particle species.

For fermion masses:

- At a fermion mass vertex, the only participating fermion is the foreground fermion, and thus the eigenvalues are calculated with respect to the foreground fermion.
- In fermion mass calculations, therefore replace k_i with $k_i^{(f)}$ where f is a representative member of the fermion family. For example, $k_i^{(e)}$ is mass eigenvalue i for the family $\{e, \mu, \tau\}$.

For boson masses:

- At a boson mass vertex, the boson interacts with the background fields of the pseudovacuum, which may be viewed as containing a multiplicity of fermions (and bosons).
- Attention may be restricted to the fields appearing within a region of dimension $O(\mathcal{L}_0)$. By construction of the pseudovacuum, this collection is (on average) colour-neutral and uncharged.
- Colour interactions within this region emulate the exchange of gluons between $O(N_0)$ preons. In lieu of the three-preon K -matrix of Sec. 4:3.2.2, the background field theoretically attracts a K -matrix acting on all $O(N_0)$ preons simultaneously.
- However, it is almost universally possible to identify colour-neutral triplets of identical A -charge within this region. Although such triplets are not necessarily as tightly bound as the foreground triplets of Sec. 4:3, they are nevertheless within a common correlation region and thus their exchange of coloured bosons is non-negligible and also generates a reduced K -matrix for the triplet.
- By randomness (and thus cancellation) of the interactions outside the triplet, on average such triplets are necessarily also eigenstates of this reduced K -matrix, K_ℓ , with eigenvalues in $\{k_i^{(\ell)}\}$, $\ell \in \{e, \nu\}$.
- Next, recognise that although Fig. 6.1(i) is an interaction with the collection of background fields as a whole, the normalisation of Sec. 1:3.8.6 eliminates all background-field-related terms except for the fields at the interaction vertices, and associated with these, up to four instances of eigenvalues to be denoted $k_i^{(\ell)}$.
- However, the colour interactions generating these K_ℓ -matrix eigenvalues are not constrained to act on the same preons as the A -sector interactions of Fig. 6.1(i). Further, the preon triplets interact with both C -sector and A -sector bosons from the background field and although only the effect on the K_ℓ matrix is retained, the dominant interaction types are interactions with the pseudovacuum photon and gluon fields, which are equivalent to the lepton mass interactions described in Sec. 6:5. It is therefore these interactions which determine the values of the eigenvalues $k_i^{(\ell)}$, and these are identical to those computed when determining the lepton masses in Sec. 6:5.3. Recognising that factors of $O(N_0)$ are accounted for elsewhere, the outcome is a sum over all admissible choices of eigenvalues $k_i^{(\ell)}$.
- It is seen in Sec. 6:5.3.9.a that contributions from the electron sector render the neutrino sector negligible, and thus these eigenvalues take the form $k_i^{(e)}$.
- All fermions acted on by a single K_ℓ -matrix acquire the same generation label i .
- Particle generations within the pseudovacuum are only consistent if both K_ℓ -matrices involved in the evaluation of Fig. 6.1(i) (one introduced in association with the upper vertex and one introduced in association with the lower vertex) yield eigenvalues of the same generation.
- Thus there exist three sets of mass eigenvalues for Fig. 6.1(i), corresponding to K_ℓ -matrix eigenvalues $k_i^{(e)}$, $i \in \{1, 2, 3\}$.

In Sec. 6:5.3 it is subsequently also seen that the K_ℓ -matrix eigenvalues $k_i^{(f)}$ exhibit dependency on an energy scale. Identification of this energy scale is addressed in Sec. 6:5.3.9.b, in which it

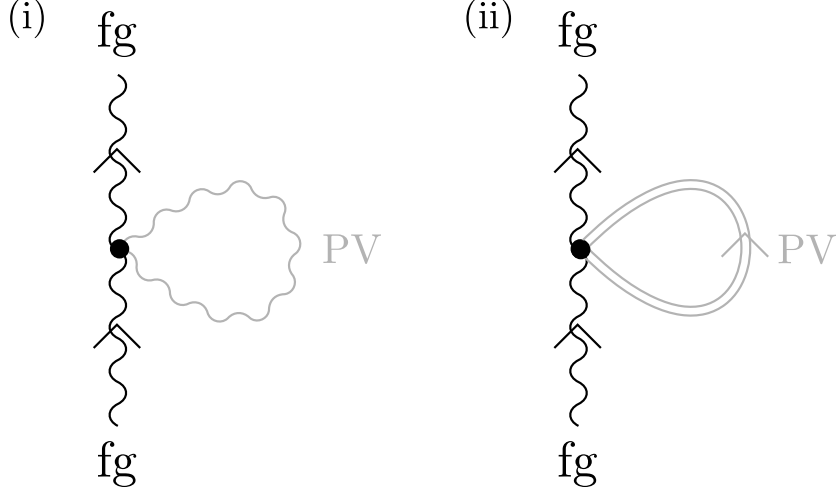


Figure 6.10: (i) Coupling between W boson and background photon field. (ii) Coupling between W boson and background scalar field. For the scalar boson there is no need to separately consider crossed and uncrossed configurations or FSF exchange in the absence of foreground fields, as all such symmetry factors are incorporated into the mean-squared background field value.

is seen that the eigenvalues appearing in the boson mass vertices are always evaluated at energy scale \mathcal{E}_{e_i} , $e_i \in \{e, \mu, \tau\}$, where the generation of the lepton label e_i matches the generation of the massive boson. For the present, this energy dependency of $k_i^{(f)}(\mathcal{E})$ is left implicit until it is demonstrated in Sec. 6:5.3.

Later evaluation of $k_1^{(e)}$ (6.166) shows the term $O[(k_1 N_0)^{-4}]$ in Eq. (6.24), which is now understood to be $O\{[k_1^{(e)} N_0]^{-4}\}$, to be between $\alpha/(4\pi)$ and $\alpha^2/(4\pi)^2$ in magnitude. This correction is evaluated shortly.

6:4.1.7 Background photon and scalar interactions

Another potentially relevant correction is the W /background photon coupling, Fig. 6.10(i). At tree level this readily evaluates to

$$\frac{f^2}{2} N_0^8 S_{6,13} \quad (6.27)$$

where a symmetry factor of 2 arises from the presence of two identical photon operators on the interaction vertex, but is cancelled by the diagrammatic equivalence of exchanging the connected photon lines/sources/sinks. This gives a net expression

$$\begin{aligned} m_W^2 = & 9f^2 \left[k_1^{(e)} \right]^4 \omega_0^2 N_0^{12} S_{6,13} \\ & \times \left\{ 1 + \left(64 + \frac{3}{2\pi} - f_Z \right) \frac{\alpha}{2\pi} \right. \\ & \left. + \frac{1}{18 \left[k_1^{(e)} N_0 \right]^4} [1 + O(\alpha)] + \dots + O(\alpha^2) \right\}. \end{aligned} \quad (6.28)$$

The composite pseudovacuum scalar boson field yields a similar contribution, represented by “...” in the above. In comparison with the photon term:

- In contrast with $A^\mu A_\mu$, the complex scalar boson operators \mathbf{H} and \mathbf{H}^* are no longer interchangeable. However, each vertex may be either an \mathbf{H} vertex or an \mathbf{H}^* vertex. The resulting factors of 2 and $\frac{1}{2}$ cancel, for no net change in on-vertex symmetry.
- Because scalar boson source and sink are located on the same vertex, the loop may be contracted to a point and as discussed in Sec. 3:3.5.5 there is therefore no factor of $2[k_1^{(e)} N_0]^{-4}$ for taking the scalar bosons to the far field.
- The vertex coupling factor is obtained from the Lagrangian. It includes evaluation of $(i/2)^2 \Upsilon^\mu \bar{\Upsilon}_\mu$, and recognition that the pair may be constructed either as $\mathbf{H}\mathbf{H}^*$ or $\mathbf{H}^*\mathbf{H}$. It evaluates as $-2f^2$. This is compared with $f^2/2$ for the photon, for a relative factor of -4 . (It is interesting to compare this with the approach taken for the scalar boson loops of Sec. 6:4.1.4, in which loops were evaluated by reduction to a previously solved problem rather than direct construction from the Lagrangian. The minus sign seen here corresponds to the one obtained in Sec. 6:4.1.4 from sigma matrices, which was included in the loop structure factor.)
- Comparing Eqs. (6.4) and (6.9), the mean field value for $[\mathbf{H}\mathbf{H}^*]_{\text{bg}}$ attracts a factor of $-9/2$ relative to that for $[A^\mu A_\mu]_{\text{bg}}$.

The scalar boson term is consequently larger than the photon term by a factor of

$$1 \cdot -4 \cdot -\frac{9}{2} = 18. \quad (6.29)$$

Incorporating the background scalar boson contribution to m_W^2 therefore yields

$$\begin{aligned} m_W^2 = & 9f^2 \left[k_1^{(e)} \right]^4 \omega_0^2 N_0^{12} S_{6,13} \\ & \times \left\{ 1 + \left(64 + \frac{3}{2\pi} - f_Z \right) \frac{\alpha}{2\pi} \right. \\ & \left. + \frac{19}{18 \left[k_1^{(e)} N_0 \right]^4} [1 + O(\alpha)] + O(\alpha^2) \right\}. \end{aligned} \quad (6.30)$$

There is no equivalent gluon coupling as the W boson is colourless. Any attempts to construct a coupling to the C sector background will vanish on summation over emission coefficients, similar to the cancellation seen while evaluating the Z coupling in Sec. 6:4.1.3 above.

6:4.1.8 Universality of loop corrections

Up to now, the photon in Fig. 6.10 has been treated as a fundamental particle. However, in principle any occurrence of a fundamental boson may be re-expressed as a pair of preons using the identity

$$\varphi_\mu^{\dot{a}\dot{c}ac} = \bar{\partial}^{\dot{a}\dot{c}} \bar{\sigma}_\mu^{\dot{a}\dot{c}} \partial^{ac} \varphi \approx f \bar{\partial}^{\dot{a}\dot{c}} \varphi \bar{\sigma}_\mu^{\dot{a}\dot{c}} \partial^{ac} \varphi = f \bar{\psi}^{\dot{a}\dot{c}} \bar{\sigma}_\mu^{\dot{a}\dot{c}} \psi^{ac} \quad (6.31)$$

derived from Eqs. (1.134) and (1.196). Such pairs are bound by the colour interaction with a characteristic separation of $O(\mathcal{L}_\psi)$, but this is also the preon separation observed at the vertices of the W /lepton diagrams such as Fig. 6.1(i).

With this in mind, consider again the preon-mediated boson mass vertex of Fig. 6.1(i). In Sec. 5:3.1 the interaction between the vector boson and the preon fields was taken to involve all three preons, collected as a composite fermion, leading to the introduction of K matrices on two of the preon lines at each vertex. Although integration reduced two preon lines and two antipreon lines to a numerical factor using Eq. (6.7), these lines still interacted with the foreground field, permitting them to acquire FSF symmetry factors (which may be understood as corresponding to a choice over which preon lines the K matrices are applied to).

An alternative approach to the evaluation of Fig. 6.1(i) is to interpret the six preons as three vector bosons. This construction has no K matrices, and corresponds to the diagrams without K matrices discussed in Sec. 5:3.1.5. After integrating out four of the lines, the remaining lines are collected as emission and absorption of vector bosons from the background field. This requires that each boson constructed involves a preon from one vertex and an antipreon from the other vertex. (Choosing both from the same vertex just yields a propagator of the foreground boson over the intervening space.) In contrast with the background fermion diagrams, since there are no K matrices associated with boson-boson interactions, the normalisation convention of Sec. 1:3.8.6 requires that the eliminated lines yield a net factor of 1.

If the residual background bosons are conjugate, then this constitutes a reduction of Fig. 6.1(i) to a diagram having the general form of Fig. 6.10(i). However, the species involved may be unexpected, and this may represent an additional channel of interaction between the foreground boson and the background boson fields which must also be taken into account. For the W boson this contribution vanishes, however, as the resulting background bosons are associated with orthogonal representation matrices on the A sector (e_{22}^A and e_{33}^A) and therefore have a vanishing mean product on the pseudovacuum.

Now consider diagrams having the form of Fig. 6.1(ii) which contain loop corrections. The preons persisting after integration no longer necessarily arise from the same vertices, but this is unimportant as they are still within \mathcal{L}_ψ of one another and can therefore once again be considered to make up composite vector bosons, again yielding a coupling to the boson sector of the pseudovacuum. (Again these vanish for the W boson.)

Crucially, however, the converse process may be applied to any boson loop diagram such as Fig. 6.10(i), recruiting an additional two bosons (two preon lines and two antipreon lines) from the pseudovacuum. Choice of gauge ensuring that this recruitment yields triplets consistent with fermions. The recruited preons permit reconstruction of a diagram having the form of Fig. 6.1(i), without K matrices. Such a reconstructed six-preon-line diagram then admits all of the loop corrections identified for Fig. 6.1 above. This mapping therefore identifies a set of nontrivial higher-order correction to the boson loop diagram of Fig. 6.10(i) which can *only* be obtained by mapping the interacting bosons into preon constituents and recruiting additional preons from the pseudovacuum to make up preon vertices before integrating them out again. [Note that this recruitment (i) is always possible due to the homogeneity of the pseudovacuum and the large number of background particles within autocorrelation length \mathcal{L}_0 , and (ii) is obligatory as it provides additional channels for interaction between a propagating boson and the background fields.] Further recalling that the scalar boson loop in Sec. 6:4.1.4 was evaluated by mapping to a vector boson loop, equivalent corrections also apply to the scalar boson loop diagram of Fig. 6.10(ii).

The net outcome is that every term in Eq. (6.24) has a counterpart on the boson loops of

Fig. 6.10. The W boson mass may then concisely be written as

$$\begin{aligned}
m_W^2 = & 9f^2 \left[k_1^{(e)} \right]^4 \omega_0^2 N_0^{12} S_{6,13} \\
& \times \left[1 + \left(64 + \frac{3}{2\pi} - f_Z \right) \frac{\alpha}{2\pi} + O(\alpha^2) \right] \\
& \times \left\{ 1 + \frac{19}{18 \left[k_1^{(e)} N_0 \right]^4} [1 + O(\alpha)] \right\}.
\end{aligned} \tag{6.32}$$

Later evaluation of $k_1^{(e)}$ (6.166) shows the term in $\left[k_1^{(e)} N_0 \right]^{-4}$ to be between $\alpha/(4\pi)$ and $\alpha^2/(4\pi^2)$ in magnitude, and the factor $[1 + O(\alpha)]$ on this term therefore introduces corrections which are small compared with $O(\alpha^2)$. However, pending demonstration of this, Eq. (6.32) may be written

$$\begin{aligned}
m_W^2 = & 9f^2 \left[k_1^{(e)} \right]^4 \omega_0^2 N_0^{12} S_{6,13} \left[1 + \left(64 + \frac{3}{2\pi} - f_Z \right) \frac{\alpha}{2\pi} \right] \\
& \times \left\{ 1 + \frac{19}{18 \left[k_1^{(e)} N_0 \right]^4} \right\} \\
& \times \left(1 + O \left\{ \alpha \left[k_1^{(e)} N_0 \right]^{-4} \right\} + O(\alpha^2) \right).
\end{aligned} \tag{6.33}$$

This universality of the preon-level loop corrections to all interactions—boson and fermion—and the involvement of both boson and fermion terms in the calculation of boson masses—even where, as for the W boson, these disappear—has the important implication that corrections to the Weinberg angle θ_W are likewise universally applied, regardless of whether θ_W is expressed in terms of boson masses or interaction strengths. Thus the mass ratio expression for θ_W in the definition of f_Z (6.17) is consistent with the interaction ratio expression $\tan \theta_W = g'_{\text{eff}}/g_{\text{eff}}$ once all corrections to interaction strengths with no counterparts in the Standard Model have been taken into account.

This completes calculation of W boson mass to the level of precision employed in this paper.

6:4.2 Z mass

Higher order corrections to the Z boson mass are also required, and their calculation is similar to that for the W boson.

6:4.2.1 Boson loops

6:4.2.1.a Gluon loops: The calculation is analogous to that performed for the W boson. However, introduction of an off-diagonal gluon coupling rearranges colour and so eliminates the end-to-end symmetry of the Z boson mass-squared interaction, resulting in the loss of a symmetry factor of 2 relative to the original diagram. There are no diagonal gluon couplings consistent with Fig. 6.1(ii), so this reduction applies to all gluon loop corrections. The net gluon contribution is therefore

$$\frac{30\alpha}{2\pi}. \tag{6.34}$$

An alternative explanation of this reduction in factors is given by noting that the original background fields are summed over connection to the source and sink in two different orientations

Table 6.4: List of channels contributing to the preon limb of the leading order Z boson mass diagram, the Z /preon couplings (vertex weights), coefficients of coupling to the (loop) Z boson field, and the relative contributions of each choice of fermion species to the leading-order mass as a whole (loop weight). Terms for the antipreon limb are identical up to a sign on both vertex weight and Z coefficient representing the selection of the CP -conjugate at the boson/fermion vertex, and the opposite sign of interaction of this conjugate with the Z boson.

Preon lines			
Species	Vertex weight	Z coefficient	Loop weight
e_L	$\frac{2f}{\sqrt{6}} \cdot \frac{1}{2}$	$\frac{2f}{\sqrt{6}} \cdot \frac{1}{2}$	$\frac{1}{8}$
\bar{e}_R	$\frac{2f}{\sqrt{6}} \cdot \frac{1}{2}$	$\frac{2f}{\sqrt{6}} \cdot \frac{1}{2}$	$\frac{1}{8}$
ν_e	$\frac{2f}{\sqrt{6}} \cdot -1$	$\frac{2f}{\sqrt{6}} \cdot -1$	$\frac{1}{2}$
d_L	$\frac{2f}{\sqrt{6}} \cdot -\frac{1}{2}$	$-\frac{2f}{\sqrt{6}} \cdot -\frac{1}{2}$	$\frac{1}{8}$
\bar{d}_R	$\frac{2f}{\sqrt{6}} \cdot -\frac{1}{2}$	$-\frac{2f}{\sqrt{6}} \cdot -\frac{1}{2}$	$\frac{1}{8}$

(corresponding to the symmetry factor of two). When the same exchange is applied to a diagram with a loop correction in the preon limb, this maps to a loop correction in the antipreon limb. Counting all six positions for loop corrections is therefore double counting, and again the contribution must be reduced by a factor of two.

6:4.2.1.b Photon, W , and Z boson loops: These calculations follow the approach described in Sec. 6:4.1.3. The photon and W boson are readily dismissed:

- The Z boson has no electromagnetic charge, so on constructing a photon-loop coupling table all terms are immediately seen to vanish.
- The W boson loop correction vanishes by the same argument as Sec. 6:4.1.3 above.

For Z loops, however, the coupling table does not sum to zero and so is computed here. Consider the relative contributions of the different fermions which contribute to the leading order diagram [analogous to Fig. 6.1(i)]. At tree level the Z boson couples only to electrons, neutrinos, and the down quarks. The relative contribution of each line to the Z field of the loop boson is the product of the vertex weights and the Z coefficients, given for the preon limb in Table 6.4. All such terms are of identical sign so no cancellation takes place.

Each choice of fermions in the loop then acquires corrections from all uncanceled terms (i.e. all terms, in this context). These must be evaluated at the preon level, but a shortcut is possible on recognising that:

- In the leptons,
 - the three preons are identical, and after incorporating the fermion normalisation, each contributes an effective Z coupling $\frac{1}{3}$ that of the corresponding fermion as per Sec. 3:3.5.8.
 - The sum over three loop positions and three pseudovacuum expansions per loop cancels with resulting the factor of $\frac{1}{9}$.

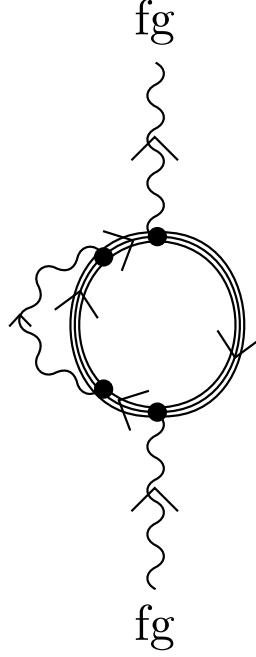


Figure 6.11: A boson loop coupling a fermion to itself as shown may be expanded to yield preon proper self-energy terms and three preon-preon couplings between members of the fermion triplet.

- In the quarks,
 - as discussed in Sec. 6:4.1.3, each A -sector interaction is accompanied by one C -sector interaction. Collectively these interactions have the effect of arbitrarily rearranging the preons between the two vertices, so the sum over position of the interacting preon proceeds independently at source and sink.
 - If source and sink are time-ordered this yields six loop diagrams; they are not time-ordered, so this reduces to three.
 - Again, each diagram has three different pseudovacuum expansions.
 - Again this cancels a factor of $\frac{1}{9}$ from fermion normalisation.

The net result is that for both leptons and quarks, the numerical factor associated with all preon/ Z /preon loops within a given fermion is precisely the same as the factor associated with a Z loop coupled at each end to that fermion, as shown in Fig. 6.11, if one ignores that such a term would normally be absorbed in to the fermion PSE. Indeed, expanding each vertex in terms of the three possible preon couplings yields nine diagrams, of which three couple a preon to itself so are not loop corrections to the vertex, but the other six are precisely those diagrams which provide the loop corrections. (More generally, Fig. 6.11 is used to describe both a PSE correction to the fermion propagator *and* the loop corrections to a boson/fermion vertex, being normalised away in the former, and yielding a numerical factor in the latter.)

In light of the above, the mean Z loop coefficient on the preon limb, after summing over preon diagrams and pseudovacuum expansions, may be calculated as the square of the Z /fermion coefficient (the vertex factor in Table 6.4) multiplied by the loop weight. This evaluates as $5f^2/12$.

The calculation is the same on the antipreon limb, so the mean value is the same across all species and diagrams. It will be corrected to $O(\alpha)$ by higher-order terms not explicitly evaluated.

Compare this with the photon loop correction to the W boson mass, where the equivalent mean factor across all species and diagrams is $f^2/2$, corrected by higher-order terms corresponding to $(1 + a_e)$. For the photon, the loop correction factor is $\alpha/(2\pi)$. On naïve inspection the Z boson loop correction to Z mass has twice as many loop diagrams as the photon correction to W mass (as the former includes both preon and antipreon terms, but the latter acquires loops only on the preon limb). Recalling that the Z boson is also effectively massless in this context, this would yield a net factor of

$$2 \cdot \frac{5f^2}{12} \cdot \left(\frac{f^2}{2}\right)^{-1} \cdot \frac{\alpha}{2\pi} \cdot \frac{1 + O(\alpha)}{1 + a_e} = \frac{5}{3} \cdot \frac{\alpha}{2\pi} [1 + O(\alpha)]. \quad (6.35)$$

However, this calculation overlooks additional symmetries present in the Z boson diagrams:

- For the photon loop corrections to the W mass:
 - With the exception of interchange of the loop vertices, which is accounted for in the structure factor, there are no other vertex interchange symmetries.
- For the Z loop corrections to the Z mass:
 - There are four identical Z /fermion vertices, which admit 24 permutations. One such permutation suffices to generate all preon diagrams associated with a given position of the fermion vertices, so this appears to be a 24-fold overcounting.
 - However, symmetry under exchange of the two inner loop vertices is also present in the W /fermion reference diagram and its associated factor of $\alpha/(2\pi)$, so factor this out and divide the count by two.
 - Similarly, symmetry under exchange of the two external loop vertices is included in the leading-order diagram of Fig. 6.1(i) which these figures correct, so again divide the overcount by a factor of two.
 - Now consider a nonvanishing loop correction diagram.
 - * To yield a nonvanishing correction the inner loop must have the form shown in Fig. 6.1(ii), and not that of Fig. 6.1(iii) which is instead a preon PSE diagram. However, the positions of the outer loop vertices are not similarly constrained.
 - * All remaining vertex exchange operations swap at least one vertex from the inner loop with a vertex from the outer loop.
 - * There is therefore a one-in-three chance that the diagram resulting from a vertex exchange will have vanishing contribution to the loop correction.

This reduces the count by a factor of $\frac{2}{3}$, for a final net overcount by a factor of 4.

To compensate for this overcount on mapping to fermions, introduce a complementary factor of $\frac{1}{4}$. The factor associated with the Z loop corrections to Z boson mass therefore becomes

$$\frac{1}{4} \cdot 2 \cdot \frac{5f^2}{12} \cdot \left(\frac{f^2}{2}\right)^{-1} \cdot \frac{\alpha}{2\pi} \cdot \frac{1 + O(\alpha)}{1 + a_e} = \frac{5}{12} \cdot \frac{\alpha}{2\pi} [1 + O(\alpha)]. \quad (6.36)$$

6:4.2.1.c Scalar boson loop: The scalar boson loop calculation is identical to that for the W boson, yielding a correction of

$$\frac{3\alpha}{2\pi} \left(1 + \frac{1}{2\pi}\right). \quad (6.37)$$

6:4.2.1.d Net effect of all boson loops: The net effect of the boson loop corrections is therefore to amend the Z boson mass equation to

$$m_Z^2 = 12f^2 \left[k_1^{(e)} \right]^4 \omega_0^2 N_0^{12} S_{6,13} \times \left[1 + \left(\frac{401}{12} + \frac{3}{2\pi} \right) \frac{\alpha}{2\pi} + O(N_0^{-4}) + O(\alpha^2) \right] \quad (6.38)$$

where the next-most-relevant corrections are those due to the coupling of the Z boson to the pseudovacuum scalar field, and the second-order electromagnetic corrections.

6:4.2.2 Background photon and scalar interactions

6:4.2.2.a Direct coupling: As the Z boson is uncharged, it acquires no mass through direct coupling to the background photon field. However, it still interacts with the background scalar boson field. Following a similar calculation to Sec. 6:4.1.7 and separating the series as per Sec. 6:4.1.8 yields

$$m_Z^2 = 12f^2 \left[k_1^{(e)} \right]^4 \omega_0^2 N_0^{12} S_{6,13} \left[1 + \left(\frac{401}{12} + \frac{3}{2\pi} \right) \frac{\alpha}{2\pi} \right] \times \left\{ 1 + \frac{1}{\left[k_1^{(e)} N_0 \right]^4} \right\} \times \left(1 + O \left\{ \alpha \left[k_1^{(e)} N_0 \right]^{-4} \right\} + O(\alpha^2) \right). \quad (6.39)$$

6:4.2.2.b Indirect (universality) coupling: Rather surprisingly, however, there does exist a mechanism whereby the Z boson may acquire mass from the background photon field. Consider again the mechanism behind the universal applicability of boson mass-squared vertex loop corrections described in Sec. 6:4.1.8. When the Z boson is interacting with the preons of the pseudovacuum, this attracts the obvious leading-order term associated with the fermion interpretation of Fig. 6.1(i). However, for the Z boson it is also possible to construct nonvanishing diagrams from the three-boson interpretation discussed in Sec. 6:4.1.8. Since the A -sector representation matrix associated with the Z boson is diagonal, the background bosons constructed from the residual preons are identical and self-conjugate, generating a diagram having the form of Fig. 6.10(ii).

A basis of diagonal bosons may be chosen consisting of the photon, Z boson, and N boson from which it is possible to construct any given composite vector boson with representation matrix e_{ii} . However, given the gauge choices of Sec. 3:3.3.6, any mass arising from this sector must always be attributed to the contributions of the background photon field. Consequently it is only necessary to consider triplets involving charged preons.

First, consider the lepton channels. When the preons are electron-type preons ($a \in \{1, 2\}$) there are three choices of charged preon and three choices of charged antipreon, and freedom to choose which preons to integrate out gives nine ways to make a composite vector boson whose a -charges indicate it relates to the photon. When the preons are neutrino-type preons ($a = 3$), these have no overlap with the photon and so can be ignored. The lepton sector thus offers a total of 18 channels (nine from e_L and nine from \bar{e}_R).

Next, consider the quark channels. Again, only diagonal contributions from electron-type preons are nonvanishing and thus each down quark contributes only one channel. The up quark does not couple to the Z boson.

For these twenty channels (nine each from the e_L and \bar{e}_R channels and two from d_L), now determine the weight of each channel when compared with the $WW^\dagger AA$ vertex of Fig. 6.10(i):

- On the electron diagrams:
 - The background preon line retained at the upper vertex may be any one of three available.
 - To construct a photon, the preon line at the lower vertex must be of matching colour. However, this may be in any of the three positions for a further factor of three (either from a sum over positions of an explicit label, or if colour labelling is suppressed, then from freedom to choose among three identical preons).
 - After integrating out the eliminated preons, the upper and lower vertex act as a single composite vertex which exhibits two photon couplings. In scenarios where the preons *become* photons, as opposed to *emit* photons, there is consequently no cancellation between photon interactions arising from the e_L and \bar{e}_R sectors of the pseudovacuum.

Preon configurations consistent with background fermions e_L and \bar{e}_R therefore contribute nine figures apiece.

- On the down quark diagrams:
 - The upper preon must be the unique preon. Its colour is whatever it is.
 - The lower preon must likewise be the unique preon. Its colour matches.

Preon configurations consistent with background quarks d_L and \bar{d}_R therefore contribute one figure apiece.

- In each of these twenty figures, there are three choices for colour of the retained preons, for a factor of 3.
- Vertex factors yield $f^2/6 = (\alpha/3)[1 + O(\alpha)]$.
- Symmetry under interchange of the Z boson source and sink is also present in the diagram which this figure corrects, so must be factored out—multiply by $\frac{1}{2}$.

Compared with the factor of $\frac{1}{2}f^2 N_0^8 S_{6,13}$ for the W/A coupling (6.27), this yields $\frac{5}{2}f^2 N_0^8 S_{6,13}$ for a net correction weight of

$$\frac{5}{18 \left[k_1^{(e)} N_0 \right]^4} [1 + O(\alpha)], \quad (6.40)$$

increasing the Z boson mass to

$$\begin{aligned} m_Z^2 = & 12f^2 \left[k_1^{(e)} \right]^4 \omega_0^2 N_0^{12} S_{6,13} \left[1 + \left(\frac{401}{12} + \frac{3}{2\pi} \right) \frac{\alpha}{2\pi} \right] \\ & \times \left\{ 1 + \frac{23}{18 \left[k_1^{(e)} N_0 \right]^4} \right\} \\ & \times \left(1 + O \left\{ \alpha \left[k_1^{(e)} N_0 \right]^{-4} \right\} + O(\alpha^2) \right). \end{aligned} \quad (6.41)$$

It should be noted that when evaluating universality couplings, a choice must be made to work on either the $SU(3)_A$ or the $SU(3)_C$ sector. As the Z boson is associated with a nontrivial representation on $SU(3)_A$ but a trivial representation on $SU(3)_C$, it is necessary to work in the $SU(3)_A$ sector. Construction of colour-agnostic composite bosons then implicitly spans all valid preon pairs and hence colour choices, making it unnecessary to independently consider the gluon sector.

6:4.2.2.c Gluon sector: There is no gluon coupling equivalent to the scalar coupling of Sec. 6:4.2.2.a, as the Z boson is colourless. Any attempts to construct a coupling to the C sector background will vanish on summation over emission coefficients. The universality coupling also cannot contribute a coupling to the gluon sector, as already discussed.

This completes calculation of Z boson mass to the level of precision employed in this paper.

6:4.3 Weak mixing angle

If the weak mixing angle is defined in terms of W and Z boson mass, the above results for m_W^2 and m_Z^2 imply a weak mixing angle

$$\sin^2 \theta_W = 1 - \frac{m_W^2}{m_Z^2} \quad (6.42)$$

$$\begin{aligned} &= 1 - \frac{3 \left[1 + \left(64 + \frac{3}{2\pi} - f_Z \right) \frac{\alpha}{2\pi} \right] \left\{ 1 + \frac{19}{18 [k_1^{(e)}]^4 N_0^4} \right\}}{4 \left[1 + \left(\frac{401}{12} + \frac{3}{2\pi} \right) \frac{\alpha}{2\pi} \right] \left\{ 1 + \frac{23}{18 [k_1^{(e)}]^4 N_0^4} \right\}} \\ &\quad \times \left(1 + O \left\{ \alpha \left[k_1^{(e)} N_0 \right]^{-4} \right\} + O(\alpha^2) \right) \end{aligned} \quad (6.43)$$

where f_Z in turn depends on $\sin^2 \theta_W$ (6.17) and it is necessary to solve for consistency. It is worth noting that the corrections described above for the W and Z boson mass diagrams also apply to foreground fermion/weak boson interaction vertices. However, note that for the Z boson, the magnitude of the corrections show some variation between different species, with (for example) the electrons attracting EM loop corrections which are not present for the neutrino. The value obtained for the weak mixing angle will consequently depend on the different weightings given to the various species which may be involved, and thus on the details of individual experiments to measure this parameter. For this reason, the present chapter concentrates on particle mass rather than seeking to reproduce experimentally determined values of $\sin^2 \theta_W$.

6:4.4 Gluon masses

By the unbroken $GL(3, \mathbb{R})$ symmetry of the colour sector, in the e_{ij} basis all gluons have identical mass, and it suffices to calculate the mass of one off-diagonal gluon [though remaining aware that FSF symmetry factors must be computed using a basis of $SU(3)_C \otimes GL(1, \mathbb{R})_N$]. Evaluation of the gluon mass is therefore similar to evaluation of W boson mass, and indeed the lepton/fermion contribution of the leading order diagram and the preon-to-preon gluon loop corrections to this diagram proceed equivalently. Where the W and gluon mass calculations diverge is in the contribution from interactions with the pseudovacuum boson fields. For the W boson this contribution arose from the pseudovacuum photon and scalar boson fields. For the gluons, there are couplings to the pseudovacuum gluon and scalar boson fields.

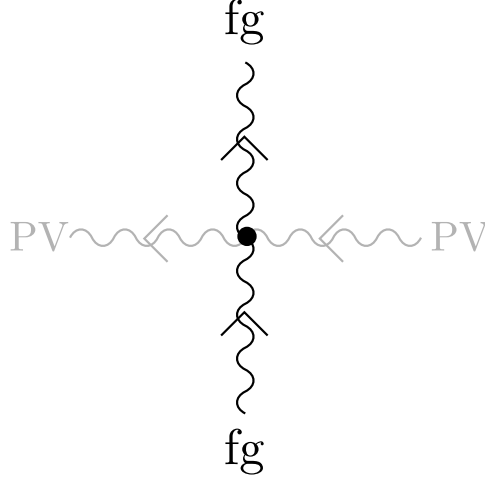


Figure 6.12: As the gluon interaction with the background gluon field need not conserve colour on a per-interaction basis, foreground gluons may interact with a pair of background gluons having non-complementary charges.

To evaluate the gluon contribution to the $O(N_0^{-4})$ term, recognise that the preservation of colour cycle invariance across the entirety of the $\mathbb{C}^{\wedge 18}$ analogue model guarantees that all gluons always appear in the context of a superposition of all nine possible species. Interactions with the pseudovacuum need not therefore conserve colour charge on an individual gluon on a term-by-term basis provided colour charge is collectively conserved across the superposition. (Individual gluon colour will, however, be preserved on average over length or time scales sufficiently large compared with \mathcal{L}_0 as the pseudovacuum has net trivial colour.) For mass interactions, the consequence of this is that rather than interacting with a single looped boson as per Fig. 6.10(i), a gluon can interact with a pair of different gluons from the pseudovacuum as per Fig. 6.12. Furthermore, as noted in Sec. 3:3.3.7, unbroken $GL(3, \mathbb{R})$ symmetry implies that background gluon correlators are on average nonvanishing even when different gluons are involved: The gluon field interacts collectively as a single, $GL(3, \mathbb{R})$ -valued species of boson.

To evaluate the background gluon contribution, note:

- This interaction has coefficient f^2 , compared with $f^2/2$ for the photon.
- A diagram in which the two background gluons have different field operators on the vertex, $\varphi^{c_1 \dot{c}_1} \varphi^{c_2 \dot{c}_2}$, receives a factor of $\frac{1}{2}$ relative to the photon term due to loss of vertex symmetry, but a factor of two as these fields may be pulled down from the generator \mathcal{Z} in either order. A diagram in which the two background gluons have the same field operator attracts neither of these factors.
- Regardless of how the vertex operators are pulled from \mathcal{Z} , each background boson independently ranges over all nine possible species for a factor of 81.

The net contribution to gluon mass from the background gluon field is therefore 81 times larger than the contribution to W boson mass from the background photon field, while the scalar contribution is unchanged. To the same order as used in Eq. (6.33) above, the gluon mass is

therefore given by

$$\begin{aligned}
m_c^2 = & 9f^2 \left[k_1^{(e)} \right]^4 \omega_0^2 N_0^{12} S_{6,13} \left[1 + \left(64 + \frac{3}{2\pi} - f_Z \right) \frac{\alpha}{2\pi} \right] \\
& \times \left\{ 1 + \frac{99}{18 \left[k_1^{(e)} N_0 \right]^4} \right\} \\
& \times \left(1 + \mathcal{O} \left\{ \alpha \left[k_1^{(e)} N_0 \right]^{-4} \right\} + \mathcal{O}(\alpha^2) \right).
\end{aligned} \tag{6.44}$$

As noted in Chapter 5, this mass is unobservable under normal circumstances as the gluon is confined on a length scale which is small compared with the scale of the mass interaction, $\mathcal{L}_\psi \ll \mathcal{L}_0$. However, as discussed briefly in Appendix 6:E.1, mass interactions themselves are an exception to this rule and contain gluon loops dominated by intermediate-scale contributions $\mathcal{L}_\psi < \mathcal{L} < \mathcal{L}_0$ for which the gluon demonstrates an effective mass m_c^2 . (This is further corrected to an energy-dependent value denoted $[m_c^*(\mathcal{E})]^2$ in Sec. 6:5.1.4.)

With regards to additional interaction channels acquired through the universality coupling of Sec. 6:4.1.8, the gluons have nontrivial representation on $SU(3)_C$ and thus this coupling must also be evaluated in the $SU(3)_C$ sector. However, all gluons already couple to all background boson members of this sector, and thus there are no missing couplings to be recovered using this technique. Any attempt to do so would result in double counting, so no further terms are acquired.

This completes calculation of gluon mass to the level of precision employed in this paper.

6:4.5 Scalar boson mass

As with the W and Z bosons and the gluon, some higher-order corrections to gluon mass are computed here. Recall from Chapter 5 that there are two leading terms in the scalar boson mass interaction, as shown in Fig. 6.13(i) and (ii), and that these carry relative weights of $[1 - 1/(9N_0)]^2$ and $1/(2\pi)$ respectively.

6:4.5.1 Boson loops

6:4.5.1.a Gluon loops: Begin with evaluation of gluon loop corrections to Fig. 6.13(ii). Recognise that the vertex configuration is identical to that of the Z boson, up to some A -sector labelling. Evaluation of loop corrections proceeds equivalently, including a factor of $\frac{1}{2}$ because interchangeability of boson/pseudovacuum vertices exchanging the preon and antipreon limb of the diagram. The resulting factor is

$$\frac{30\alpha}{2\pi}. \tag{6.45}$$

For Fig. 6.13(i), recognise that as discussed in Sec. 5:3.3 the pseudovacuum elements being interacted with are still fermions, even though the correlation of background fields over ranges of $\mathcal{O}(\mathcal{L}_0)$ permit some of these interactions to take place remotely, creating the appearance of a redistribution of the fermion components. It is the scalar bosons which interact at a distance, as the components of each fermion continue to be bound by colour interactions, and so are separated by at most \mathcal{L}_ψ . (Although the normalisation of Sec. 1:3.8.6 eliminates these interactions from numerical results, to the extent that the background fields may be represented as particles within their local correlation region it happens that the emergent Lagrangian favours configurations consistent with the same processes as observed in the foreground fields. The constituents of

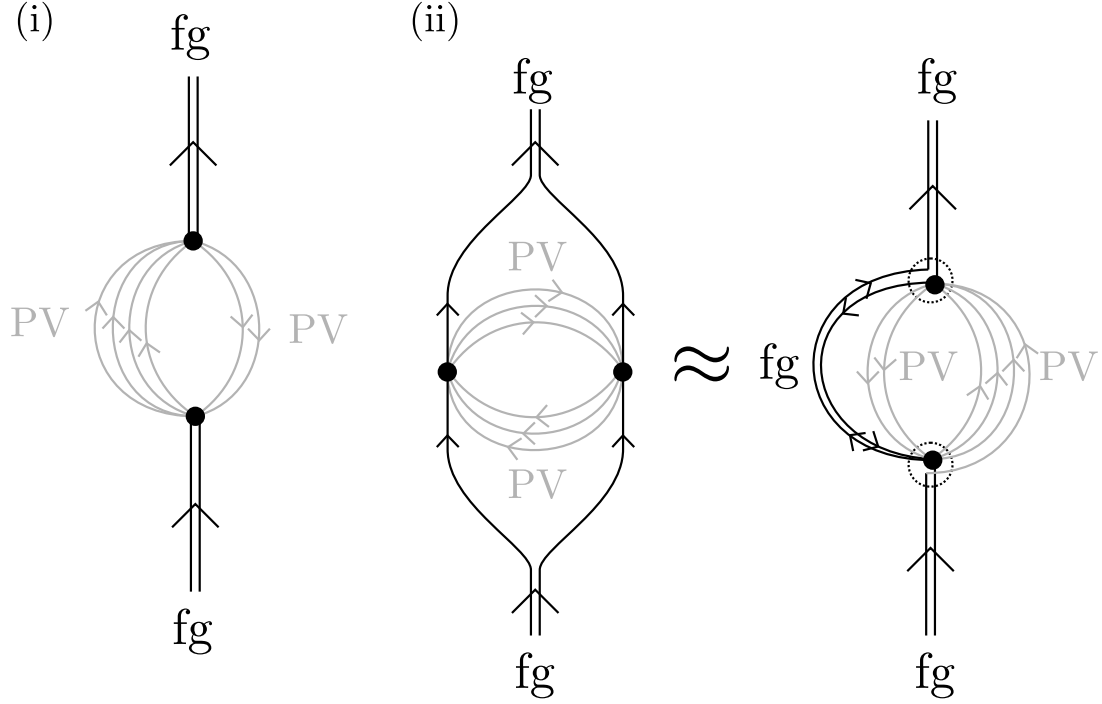


Figure 6.13: (i) Leading diagram contributing to scalar boson mass. (ii) First correction.

background fermions are consequently still represented as bound species. It is only on leaving the local correlation region that this illusion breaks down due to non-normalisation of the background fields, but can be ignored as this is also the regime in which these uncorrelated fields are cancelled out both among themselves and by other fields also in their far field regime.)

Since the loop corrections take place over distances of $O(\mathcal{L}_\psi)$, at which the loop bosons are massless, these continue to see the preons as being grouped 3+3 rather than 4+2. However, the gluon correction factor *is* reduced somewhat from $30\alpha/(2\pi)$ because the colour agnosticism of Fig. 6.13(ii), in which any preon can carry any colour label, is reduced. Two preons in the group of four must necessarily be of the same colour, and as seen in Fig. 5.5, looking inside the scalar boson/background preons interaction vertex reveals which two preons this is. While the specific colour of the pair is not fixed, the fact that the colours of these two preons are required to be the same reduces the number of degrees of freedom by a factor of 3 per outer vertex compared with Fig. 6.13(ii). (Or equivalently, only one colour labelling in nine is compatible with the interaction diagram under evaluation.) Diagram (i) therefore only attracts a correction of

$$\frac{30\alpha}{9 \cdot 2\pi}. \quad (6.46)$$

6:4.5.1.b Photon, W , and Z boson loops: Since the scalar boson field couples identically with \bar{e}_R , e_L , and ν_e , the preon limb of the loop couples to the photon and Z boson fields as per the trace of their representation matrices, which vanish. The contribution of the W boson loop also vanishes as per Sec. 6:4.1.3 above.

6:4.5.1.c Scalar boson loops: This time, begin with Fig. 6.13(i). As in Figs. 6.8 and 6.9, scalar boson loops may be constructed on any pair of preons within either the preon limb or the antipreon limb of the fermion loop. Let the scalar boson loop corrections having the form of Fig. 6.8(i) and Fig. 6.8(iii)-(vi) be termed scalar boson loops of the first and second kind respectively. Also let the leading-order scalar boson mass diagrams of Figs. 6.13(i)-(ii) be described as scalar boson mass term 1 and 2. Let the approximate form of term 2 given in Fig. 6.13(iii) be referred to as term 2’.

1. When a loop of the first kind is applied to term 1, this yields a correction to the mass vertex term obtained from Fig. 6.13(i). Let this correction be referred to as “item 1”.
2. When a loop of the first kind is applied to term 2, this yields a correction to the mass vertex term obtained from Fig. 6.13(ii). Let this correction be referred to as “item 2”.
3. When a loop of the second kind is applied to term 1, the result is equivalent to a loop of the first kind applied to term 2’. In particular, note that through the use of preon decomposition, Fierz identities, and F moves [29, 30] the accessory vector boson’s vertices (associated with factors of 1) may be taken out to the vertices of Fig. 6.13(i) permitting transformation from the form of term 2’ to that of term 2. There are nine possibilities for the accessory boson, fully offsetting the factor of $\frac{1}{9}$ from loss of colour agnosticism. This diagram is therefore largely equivalent to item 2 (above), though not quite all terms are duplicated due to the factor of $[1 - 1/(9N_0)]^2$ on term 1 from the regrouping of preon lines. Thus this diagram multiplies item 2 by $2[1 - 1/(9N_0)]^2$.
4. When a loop of the second kind is applied to term 2, if the sense of the rotation applied to the loop gluon is chosen counter to that applied in going from term 2 to term 2’ then it follows immediately that the induced vector bosons cancel (on appropriate summing across colour labels on both internal and external lines) to yield a loop of the first kind applied to term 1, up to a factor of $2[1 - 1/(9N_0)]^{-2}$ which arises because term 2 has a higher FSF symmetry factor than term 1. Alternatively, if the rotation is chosen such that the rotations do not directly cancel then the same result still follows, essentially from the same isotopy properties as Fig. 16 of Ref. [29].

It therefore suffices to consider only loops of the first kind applied to both diagrams and then multiply by the requisite factors. These loops act on preons in the form of background fermions, and thus it is simplest to evaluate first for Fig. 6.13(ii) and then apply the same factor to Fig. 6.13(i) modulo a factor of $\frac{1}{9}$ for colour knowledge on preon lines as before.

Next, note that the vertices between scalar bosons and fermions, and the vertices between scalar bosons and preons, are all interchangeable (because a coupling with a preon may be written as an average over three couplings with the constituent preons). Not all resulting diagrams yield colour consistency when the scalar boson vertices are combined as per Fig. 6.9, but for those which do, the resulting symmetry factors are in 1:1 correspondence with the induced overcounting. To obtain the vertex correction factor, it is either necessary to exploit that all diagrams make equal contributions, and offset the average per-diagram overcounting by dividing by the effective vertex interchange symmetry factor, or more simply just to recognise that the resulting cancellation makes it possible to ignore the symmetry factor altogether.

Now proceed to evaluate the scalar boson loop correction to Fig. 6.13(ii). Apply a loop correction of the first kind as per Fig. 6.8(i) and combine the vertices as per Fig. 6.9. Now recognise that at the cost of a braiding factor of -1 , diagrammatic isotopy permits reversal of the inner line of the loop. The resulting vector loop is summed over all A - and C -charges. The nine-element C -sector admits a basis with diagonal elements e_{ii}^C , each of which is averaged over

A-charge, so the sum over terms arising from the scalar boson diagram may be rewritten as a sum over gluons.

Evaluating this rewriting:

- Braid factor: -1
- Synthesis of $\sigma^\mu \sigma_\mu$: $-\frac{1}{2}$
- One \mathbf{HH}^* loop yields 81 vector boson terms:

$$\overline{\partial\partial}\varphi\partial\partial\varphi \rightarrow -\frac{1}{2} \sum_{\dot{a},\dot{c},a,c} \overline{\partial}^{\dot{a}\dot{c}}\overline{\sigma}_\mu\partial^{ac}\varphi\overline{\partial}^{\dot{a}\dot{c}}\overline{\sigma}^\mu\partial^{ac}\varphi. \quad (6.47)$$

- However, the scalar boson acts on a single diagram corresponding to an average over colour labelling. A given boson acts on a specific colour labelling, of which there are nine. Thus there is a one in nine chance of any generated gluon being compatible in any given term: $\frac{1}{9}$.
- The gluon correction in Sec. 6:4.5.1.a was evaluated on preons-in-fermions. To raise the current calculation to the fermion level introduces a factor of $\frac{1}{9}$ as each preon/boson vertex is acknowledged to occur only one third of the time in any given fermion vertex, by normalisation of the fermion field (3.28).
- Despite the appearance of Fig. 6.9, the scalar boson loop does not attract a factor of two for on-vertex symmetry as the underlying construction is as per Fig. 6.8(i) and coincidence of the vertices only occurs through emergent constraints. It is not a natural single vertex pulled down as one piece from the generator \mathcal{Z} .
- Note that neither the scalar boson in Fig. 6.8(i) nor the off-diagonal gluon in Fig. 6.1(ii) have end-to-end symmetry so there is no need to consider factors of 2 associated with vertex exchange.

Each scalar boson loop correction of the first type therefore maps (numerically) to a gluon loop correction on the same preon pair. It remains a separate correction, as the foreground boson making the loop exists relative to a distinct mass shell solution.³ The numerical coefficient associated with this mapping is

$$-1 \cdot -\frac{1}{2} \cdot 81 \cdot \frac{1}{9} \cdot \frac{1}{9} = \frac{1}{2}. \quad (6.48)$$

Then there is the factor of $2[1 - 1/(9N_0)]^2$ from also considering loops of the second kind applied to Fig. 6.13(i). This yields

$$\frac{30\alpha}{2\pi} \left(1 - \frac{1}{9N_0}\right)^2. \quad (6.49)$$

Proceeding similarly for loops of the first kind on Fig. 6.13(i) and loops of the second kind on Fig. 6.13(ii) yields

$$\frac{30\alpha}{9 \cdot 2\pi} \left(1 - \frac{1}{9N_0}\right)^{-2}. \quad (6.50)$$

³It is interesting that in the $\mathbb{C}^{\wedge 18}$ model, all on-shell solutions apply to the same underlying preon fields. Thus there exists one set of fields with multiple on-shell solutions, rather than multiple fields with one mass shell apiece. For simplicity all mass shells are treated as independent, which introduces negligible error for sufficiently distinct masses, but is quite readily apparent when different rearrangements of the same preons must be treated as loops constructed on independent foreground fields, as seen here.

6:4.5.1.d Net effect of all boson loops: Incorporating all of the above corrections yields a net mass

$$m_{\mathbf{H}}^2 = 20f^2 \left[k_1^{(e)} \right]^4 \omega_0^2 N_0^{12} S_{6,13} \times \left\{ \left(1 - \frac{1}{9N_0} \right)^2 \left[1 + \frac{30\alpha}{9\pi} \left(1 + \frac{1}{9N_0} \right) \right] + \frac{1}{2\pi} \left[1 + \frac{30\alpha}{\pi} \left(1 - \frac{1}{9N_0} \right) \right] \right\} \times \left[1 + O(N_0^{-4}) + O(\alpha N_0^{-2}) + O(\alpha^2) \right]. \quad (6.51)$$

By Eq. (5.15) the term in $O(\alpha N_0^{-2})$ is small compared with $O(\alpha^2)$ and so may be dropped.

6:4.5.2 Background photon and scalar interactions

6:4.5.2.a Direct coupling: All direct boson/boson couplings require nonvanishing matrix commutators on evaluating the boson term of Lagrangian (3.20). However, the scalar boson is associated with the identity matrix on all sectors, and thus any such term must vanish. There are therefore no direct couplings between the complex scalar boson and the background vector or scalar boson fields.

6:4.5.2.b Indirect (universality) coupling: Evaluation of this contribution proceeds as in Sec. 6:4.2.2.b. The contributions from e_L and \bar{e}_R have weight 3×3 , those from u_L and \bar{u}_R have weight 2×2 , and those from d_L and \bar{d}_R have weight 1×1 , for a total count of twenty-eight channels. As before, each channel is associated with a relative factor of $[72k_1^{(e)}N_0]^{-4}$ for a net factor of

$$\left\{ 1 + \frac{7}{18 [k_1^{(e)}N_0]^4} \right\} [1 + O(\alpha)] \quad (6.52)$$

correcting the complex scalar boson mass to

$$m_{\mathbf{H}}^2 = 20f^2 \left[k_1^{(e)} \right]^4 \omega_0^2 N_0^{12} S_{6,13} \times \left\{ \left(1 - \frac{1}{9N_0} \right)^2 \left[1 + \frac{30\alpha}{9\pi} \left(1 + \frac{1}{9N_0} \right) \right] + \frac{1}{2\pi} \left[1 + \frac{30\alpha}{\pi} \left(1 - \frac{1}{9N_0} \right) \right] \right\} \times \left\{ 1 + \frac{7}{18 [k_1^{(e)}N_0]^4} \right\} \left(1 + O \left\{ \alpha [k_1^{(e)}N_0]^{-4} \right\} + O(\alpha^2) \right). \quad (6.53)$$

This completes calculation of \mathbf{H} boson mass to the level of precision employed in this paper.

6:4.6 Neutral boson gravitation

One final note regarding the universality coupling described in Secs. 6:4.2.2.b and 6:4.2.2.b which anticipates the mechanism for $G^{(\dagger)}$ boson elimination in Sec. 7:3.4.2. Although the Z boson is uncharged, through this process it acquires a means of coupling to the photon *pair* field. This gives the Z boson a means of influencing space-time curvature when the target manifold is made non-flat in Chapter 7, and thus an emergent gravitational mass (though not necessarily one equal to its inertial mass).

The foreground gluons (including the N boson) couple to the colour charges on both the pseudovacuum preon and gluon fields, and application of the universality coupling allows the pseudovacuum preon fields to be reduced to composite vector bosons in 1:1 correspondence with the gluons, so integrating down from background fermions to background bosons does not reveal any new couplings. However, the inclusion of all possible colour couplings implies that a subset of the composite vector boson fields may also be rewritten to correspond to the two-photon coupling (carrying the photon \tilde{a} -charge, and being summed over all possible neutral colour combinations). As this coupling is constructed from the same composite vector boson fields already accounted for, it makes no additional contribution to inertial mass. However, as it is a coupling to the photon pair field it does also grant gravitational mass to the nine gluon fields. Most notably, this interaction imparts gravitational mass to the N boson, which behaves as a colourless neutral gluon with inertial mass on the electroweak scale. This is therefore a potential dark matter candidate.

6:5 Lepton Mass Interaction

6:5.1 Leading order

The fundamental interaction giving rise to lepton mass is a double scattering of the preon triplet off the vector boson component of the pseudovacuum (Fig. 6.14). Both of these diagrams may be considered mean field theory expansions of a loop correction to the fermion propagator in the presence of the pseudovacuum, but it is more convenient to refer to these as “leading order” diagrams, and to count the number of (foreground) loop corrections to these leading order diagrams, e.g. 1-loop corrections to the leading order diagram, etc. Henceforth such corrections will be termed simply “1-loop corrections”.

Figure 6.14 yields a nonvanishing pseudovacuum contribution to fermion mass only when these boson fields are both the boson field or both gluons, as per Eqs. (6.4–6.5), and the resulting interactions may each involve any of the three preons making up the lepton. By Eq. (1.169), for the mass contribution to be nonvanishing, the separation of the two boson source/sinks is of order \mathcal{L}_0 .

To evaluate the contribution of the pseudovacuum fields to lepton mass, it is helpful to separate the consequences of these boson interactions into two parts as previously discussed in Sec. 4:3 and demonstrated in Secs. 4:3.2.1–4:3.2.2. First, there is the action of the representation matrices of $SU(3)_C$ on the preon fields, and second, there is the numerical mass term arising from the mean square value of the pseudovacuum boson field.

6:5.1.1 Action on colour sector

To begin with the action of the colour sector, note that over the course of a propagator of length $\mathcal{L} \gg \mathcal{L}_0$, a lepton will engage in a near-arbitrarily large number of interactions with the background fields. Each interaction will apply a $\mathfrak{gl}(3, \mathbb{R})_C$ representation matrix from $\{\lambda_i | i \in 1, \dots, 9\}$ depending on the boson species with which the lepton interacts. In the absence of foreground W or Z bosons, the pseudovacuum is made up entirely of photons and gluons.

Given a preon of colour c_1 , this may have nonvanishing interaction with the photon or any of three gluons in the elementary basis e_{ij} . For example, if $c_1 = r$ then admissible gluons are c^{rr} , c^{gr} , and c^{br} . Heuristically, their action on the colour space may be represented as

$$c^{rr}|r\rangle \rightarrow |r\rangle \quad c^{gr}|r\rangle \rightarrow |g\rangle \quad c^{br}|r\rangle \rightarrow |b\rangle \quad (6.54)$$

where all associated numerical factors have been ignored for illustrative purposes.

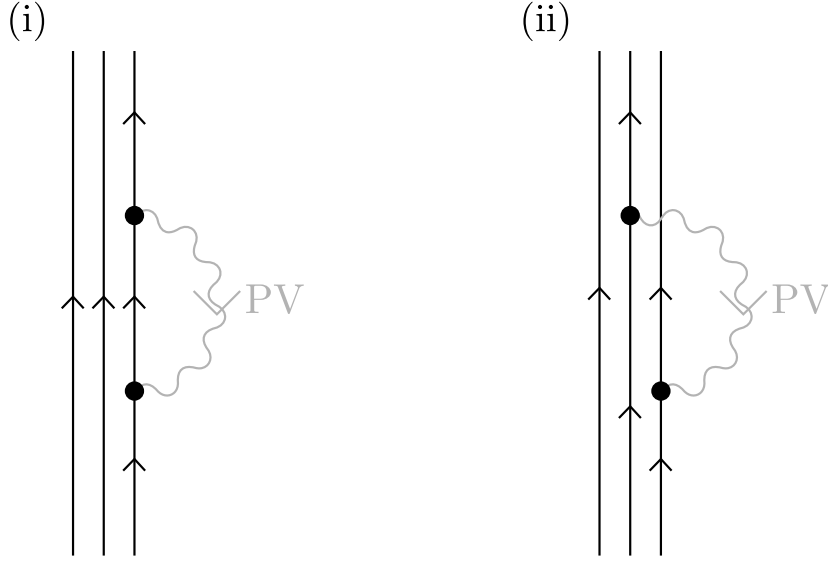


Figure 6.14: The fundamental interaction giving rise to lepton mass: The triplet of preons scatters twice off the bosonic component of the background quantum liquid. Either (i) the same, or (ii) different preons may be involved on each occasion, with the upper and lower vertices independently each connecting to any of the three preons. This results in a total of nine diagrams, three having the form of diagram (i) and six having the form of diagram (ii). These nine diagrams are then summed.

More generally, the family of gluons acts on a vector of preon colours as indicated by

$$\begin{pmatrix} c^{rr} & c^{rg} & c^{rb} \\ c^{gr} & c^{gg} & c^{gb} \\ c^{br} & c^{bg} & c^{bb} \end{pmatrix} \begin{pmatrix} |r\rangle \\ |g\rangle \\ |b\rangle \end{pmatrix}. \quad (6.55)$$

It is worth noting that there is no fixed reference point on the colour sector as the $GL(3, \mathbb{R})_C$ symmetry is unbroken, so there exists a freedom of basis corresponding to an arbitrary global transformation in $SU(3)_C$. Any coloured fundamental or composite particle may be put into an arbitrary superposition of colours using such a transformation, though relative colour charges of different particles remain unchanged, as does the magnitude of the overall colour charge of a composite particle.

Recognise now that Fig. 6.14 contains contributions to two mass vertices. Although their contributions to fermion mass are nonvanishing only when they appear pairwise, there is no requirement for this pair to be consecutive. It suffices that each vertex be paired with a conjugate vertex separated by distance and time no greater than \mathcal{L}_0 in the isotropy frame of the pseudovacuum. Indeed, these vertices are connected by a foreground fermion propagator which in general also undergoes further interactions with the pseudovacuum, represented by using a massive propagator for this fermion and requiring consistency with the outcome of the mass vertex calculation. In general a foreground fermion exhibiting a net propagation over distance or time of $O(\mathcal{L}_0)$ in the isotropy frame of the pseudovacuum will scatter back and forth multiple times in this process such that the number of unpaired vertices is assumed negligible. Furthermore, where unpaired vertices do exist, their net effect vanishes on average over probe length or time

scales larger than \mathcal{L}_0 . It is therefore reasonable to assume during evaluation that each vertex belongs to a pair.

Counting vertices arising from Fig. 6.14, for every photon vertex there is also on average one vertex for each of the nine gluons. Across macroscopic length scales, deviations from this average relative frequency will be negligible.

Consider now the specific case of interactions between a propagating lepton and the bosons of the pseudovacuum. Each preon may interact either with a photon or with any of the nine gluons, and the action of the photon on the space of preon colours is trivial, so it is convenient to ignore the photon for now and reintroduce it later.

As already noted, paired interactions with the pseudovacuum gluon field conserve the net colour-neutrality of a leptonic preon triplet. However, overlapping and intercalation of multiple interaction pairs implies that this property only holds on average, as any colour measurement will interrupt a finite number of mass interactions and thus summation to yield no net colour charge on the preon triplet cannot be assured. It is desirable that any measurement of lepton colour should be null, not just the average, and thus a local change of co-ordinates on $SU(3)_C$ must be performed on a co-ordinate patch encompassing the non-interacting preons such that changes in their colours track those of the interacting preon. This change of co-ordinates is not part of the choice of gauge on $SU(3)_C$, and thus is in principle associated with construction of some synthetic boson interactions where it intersects with particle worldlines. As described in Sec. 4:3, the vertex factors associated with these interactions arise from the representation matrices of $SU(3)_C$ given as λ_i in Eqs. (2.39–2.40). By construction these bosons are constrained to have no effect beyond the colour shifts associated with the boundary of the patch, and to leading order this effect is parameterless. In the leading order diagram these bosons consequently have no degrees of freedom, carry no momentum, and are associated with a numeric factor of 1. Consequently they are not drawn. Only the factors arising from the representation matrices persist, acting on the colour vector of an individual preon as the matrix

$$K_\ell = \begin{pmatrix} 1 & A & A^\dagger \\ A^\dagger & 1 & A \\ A & A^\dagger & 1 \end{pmatrix}, \quad A = \pm \frac{1 \pm i}{2}. \quad (6.56)$$

The sign on i is free to be chosen by convention, while the overall sign on A is fixed by noting that cyclic permutation of colours, which is in $(K_\ell)^3$, is required to leave the sign of an eigenstate of K_ℓ unchanged. The eigenvalues of K_ℓ must therefore be non-negative, setting

$$A = -\frac{1 \pm i}{2}. \quad (6.57)$$

Choosing a sign for i , the mixing matrix K_ℓ may then be written

$$K_\ell(\theta_\ell) = \begin{pmatrix} 1 & \frac{e^{i\theta_\ell}}{\sqrt{2}} & \frac{e^{-i\theta_\ell}}{\sqrt{2}} \\ \frac{e^{-i\theta_\ell}}{\sqrt{2}} & 1 & \frac{e^{i\theta_\ell}}{\sqrt{2}} \\ \frac{e^{i\theta_\ell}}{\sqrt{2}} & \frac{e^{-i\theta_\ell}}{\sqrt{2}} & 1 \end{pmatrix} \quad \theta_\ell = -\frac{3\pi}{4}. \quad (6.58)$$

As noted in Sec. 4:3, this matrix bears a strong resemblance to Koide's K matrix for leptons [24]. The minus sign on Koide's off-diagonal component $S(\theta_f)$ has been absorbed into the phase θ_ℓ , and the free parameters a_f , b_f , and θ_f are fixed by the geometry of the model, in keeping with the predictive capacity of the $\mathbb{C}^{\wedge 18}$ model.

Recognising that on average all pseudovacuum gluons act identically and with equal frequency, it is convenient to collect these together into a single $\mathfrak{gl}(3, \mathbb{R})$ -valued gluon associated with two applications of matrix K_ℓ to the non-interacting preons, as shown in Fig. 6.15.

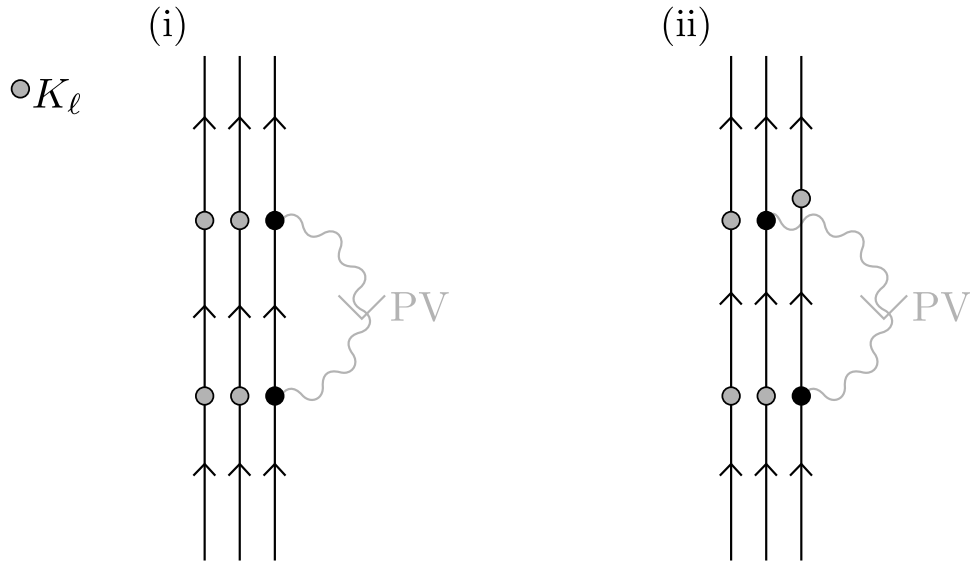


Figure 6.15: When a composite fermion interacts with the gluons from the pseudovacuum, represented as a single $\mathfrak{gl}(3, \mathbb{R})$ -valued boson, the colour mixing process represented by matrix K_ℓ acts on all preons not coupling to the boson at any given vertex. Diagrams (i) and (ii) correspond to Figs. 6.14(i)-(ii) respectively. Once again these are just two representative diagrams from a family of nine, as the upper and lower vertices may independently each be connected to any of the three preons. This results in a total of nine diagrams, three having the form of diagram (i) and six having the form of diagram (ii).

Now recognise that since the gluons of the $\mathbb{C}^{\wedge 18}$ model are massive, and since the fundamental mass interactions take the form of loop diagrams with respect to the lepton propagator (Fig. 6.14), these will be suppressed by a factor of $O(m_\ell^2/m_c^2)$ relative to the photon contribution. [In practice no single gluon will propagate a distance of $O(\mathcal{L}_0)$ due to confinement binding it tightly to the emitting lepton, but it is also unnecessary that any single gluon should do so—instead, for gluons the line in Fig. 6.14 represents the propagation of momentum carried in a distributed fashion within the gluon cloud accompanying the lepton. This propagating momentum carried in the gluon sector then necessarily displays an effective mass shell behaviour consistent with m_c^2 .] With each gluon interacting, on average, once for every photon interaction, it is convenient to write the direct contributions of the gluon terms to particle mass as corrections to the larger photon term and to associate copies of the matrix K_ℓ with the photon vertices in a manner equivalent to that shown in Fig. 6.15 and discussed in Sec. 4:3.2.2.

Next, consider that the preons on which matrix K_ℓ are acting are just two of three preons in a colour-neutral triplet. For leptons, all three a -charges are identical and thus over macroscopic scales, where chance fluctuations become negligible, matrix K_ℓ will act identically on each member of the triplet. This symmetry is convenient, as it allows the study of an individual preon prior to the reconstruction of the triplet as a whole.

As per Eq. (6.6), the preons making up observable leptons are now eigenstates of this matrix K_ℓ , corresponding to the eigenvectors

$$v_1 = \frac{1}{\sqrt{3}} \begin{pmatrix} 1 \\ 1 \\ 1 \end{pmatrix} \quad (6.59)$$

$$v_2 = \frac{1}{\sqrt{3}} \begin{pmatrix} e^{\frac{\pi i}{3}} \\ e^{-\frac{\pi i}{3}} \\ -1 \end{pmatrix} \quad (6.60)$$

$$v_3 = \frac{1}{\sqrt{3}} \begin{pmatrix} e^{\frac{2\pi i}{3}} \\ e^{-\frac{2\pi i}{3}} \\ 1 \end{pmatrix} \quad (6.61)$$

which are independent of θ_ℓ and have eigenvalues $\{k_i^{(\ell)} | i \in \{1, 2, 3\}\}$ given by

$$k_n^{(\ell)} = 1 + \sqrt{2} \cos \left[\theta_\ell - \frac{2\pi(n-1)}{3} \right]. \quad (6.62)$$

To reconstruct the lepton as a whole, recognise that for three preons at $\{x_i | i \in \{1, 2, 3\}\}$, with corresponding colours c_i , and with the preon at x_1 having a well-defined color, say $c_1 = r$, colour neutrality and colour cycle invariance imply that a choice $c_2 = g$, $c_3 = b$ is equal up to a sign to the alternative choice $c_2 = b$, $c_3 = g$ (as this exchange corresponds to spatial exchange of two fermions), and thus it suffices to consider only one such colour assignment (say $c_2 = g$, $c_3 = b$) along with spatial permutations. Putting preon 1 into a superposition of colour states then corresponds to a superposition of cyclic spatial rearrangements of the members of the triplet, with colours $c_1 = r$, $c_1 = g$, and $c_1 = b$ corresponding to colour assignments *with respect to spatial co-ordinate x* of rgb , gbr , and brg respectively. It follows that for leptons, the different spatial configurations of colours on the preon triplet are eigenvectors of a matrix $K_\ell^{(3)}$ with eigenvalues identical to those of K_ℓ .

Having established through colour cycle invariance that the matrix K_ℓ acts identically on all constituents of a lepton, and through Fig. 6.15 that two copies of K_ℓ act per pseudovacuum photon interaction, it follows that the effect of matrix K_ℓ is to contribute a factor of $[k_i^{(\ell)}]^2$ to the mass of a lepton of generation i . It might seem problematic that for $\theta_\ell = -3\pi/4$, $k_1^{(\ell)} = 0$, but it will be seen in Sec. 6:5.3 that θ_ℓ acquires corrections from higher-order diagrams, resulting in $k_i > 0 \forall i$, so $k_1^{(\ell)}$ may be assumed real and positive, and this concern may be disregarded.

6:5.1.2 Mass from photon and gluon components of the pseudovacuum

The zeroth-order electromagnetic term is readily evaluated by making a mean-field substitution (6.4) for $[A^\mu(x)A_\mu(y)]_{\text{bg}}$. For a charged lepton ℓ_i of generation i , this initial approximation may be written

$$m_{\ell_i}^2 = \frac{f^2}{2} [k_i^{(\ell)}]^4 \omega_0^2 N_0^8 S_{18,147} [1 + \mathcal{O}(\alpha)] \quad (6.63)$$

as seen in Sec. 4:3.2.2, Eq. (4.34). Note that this expression incorporates a symmetry factor of two corresponding to exchange of the two pseudovacuum interactions. This may be understood by recognising that each term corresponds to a mass vertex and has its external legs truncated independently. These two vertices are then interchangeable for a symmetry factor of 2. Alternatively, for any diagram, including ones which do not separate, recognise that the mass-squared is always applied in the context of an untruncated fermion propagator, say from x to y . In this context, all fermion connections to the interaction vertices are again untruncated. (Optionally, the full expression for propagation from x to y is then used to infer an equivalent mass term, and the diagram may then be replaced by one in which this mass term is inserted into the propagator twice.) Applying either form of this approach to Fig. 6.14, the diagram for propagation between two points is again seen to attract a symmetry factor of 2.

Now consider interactions between a foreground fermion and the pseudovacuum gluon fields. As with the photon, these interactions take the form of loop diagrams evaluated in the mean-field regime for the pseudovacuum, and as noted in Sec. 4:3.2.1, the fermion may transiently surrender momentum to or borrow momentum from the background fields. However, in contrast with the photon loop evaluated to obtain Eq. (6.63), the gluon field is massive, and when a foreground particle transfers momentum to a gluon field, this results in a massive excitation of that gluon field. Consequently both limbs of the loop must be considered massive. For a general boson b this gives rise to a loop-associated factor of $\mathbf{f}(m_{\ell_i}^2/m_b^2)$. This factor goes to 1 for the photon, as it is massless, but not for interactions with the background gluon field. It is interesting to compare this situation with the loop corrections to boson mass discussed in Sec. 6:4. In the context of boson mass interactions, the correction loop is constructed on a section of preon line which is *a priori* of dimension \mathcal{L}_ψ and consequently the loop boson appears massless. In the context of fermion mass interactions, the correction loop is constructed on a section of fermion line which is of nontrivial extent and consequently the loop boson is able to propagate over arbitrary length scales and (for loop bosons other than the photon) must therefore be considered massive.

For both the photon loop and the gluon loop, evaluation of momentum flux around the loop may be taken to yield a factor of

$$\frac{\Xi}{4\pi} \mathbf{f}\left(\frac{m_{\ell_i}^2}{m_b^2}\right), \quad b \in \{A, c\} \quad (6.64)$$

for some structure factor Ξ , where $\mathbf{f}(n)$ behaves as described in Appendix 6:A. For the photon $\Xi = 2\alpha$ and the factor $\mathbf{f}(\cdot)$ reduces to 1, and the resulting coefficient of $\alpha/(2\pi)$ is absorbed into the pseudovacuum mean-field term by choice of definition. For gluons, dependence on the same

energy scale \mathcal{E}_0 indicates that an identical factor of $\alpha/(2\pi)$ is absorbed into the mean field term, while the mass dependence of $\mathbf{f}(\cdot)$ reveals that the gluon terms are suppressed by a factor of $m_{\ell_i}^2/m_c^2$ relative to the photon term. [Although the transmission of the foreground momentum around the gluon loop is massive, the factor arising from $\mathbf{f}(\cdot)$ is $m_{\ell_i}^2/m_c^2$ and not $m_{\ell_i}^2/(4\pi m_c^2)$ as the value of the gluon loop diagram is dominated by the background terms. This is discussed further in Appendix 6:A.]

To determine the structure factor of the gluon diagram, work in the e_{ij}^C basis, and consider first a specific off-diagonal gluon. As discussed in Sec. 3:3.5.8 and Sec. 6:4.1.2 above, mapping to the one- W -loop correction to lepton magnetic moment (6.12) permits the magnitude of the structure factor to be evaluated as $\frac{10\alpha}{3} [1 + \mathcal{O}(\alpha)]$. In comparison with the reference process, however, there is no emitted boson in Fig. 6.15. The sign of the structure factor may then be easily determined by recognising that on mapping Fig. 6.15 to a tensor network [32–34] the resulting network is a perfect square and thus the structure factor must be real and positive. For a diagonal gluon e_{ii}^C the calculation is modified as there is only one possible colour, not two, on the target preon (it is the same as the source preon) but this is offset by a factor of two for vertex interchange symmetry so the result is the same.

There is, however, a further correction to the above. In Sec. 6:4.1.2, gluon exchange was restricted by the requirement of colour neutrality on the inbound and outbound triplets. In the present situation the gluon at each vertex represents the c_μ^{ij} component of the colour mixing operator \hat{K}_μ (4.25), and overall colour neutrality is conserved by the requirement that free fermions be colour-neutral eigenstates of the matrix $K_e(\mathcal{E})$. Further, since the gluons at the vertices arise from the background fields, by Eq. (6.5) they need not be conjugate to yield a non-vanishing diagram. Momentum transfer through the background field channel may still take place, due to the on-average independent separate conservation of foreground and background momenta, and may be assumed to do so through implicit scattering processes in the background fields. (As noted previously, although the normalisation of Sec. 1:3.8.6 eliminates contributions of these interactions to numerical results, they may still be considered to occur within the local correlation region.) This lack of conjugacy corresponds to reopening the loop of Fig. 6.15 to recover a diagram more akin to Fig. 4.1, much as Fig. 6.12 is an opening of the loop on Fig. 6.10(i), and increases the number of admissible gluon colours by a factor of 3. Overall, the resulting structure factor is

$$\frac{10\alpha}{3} [1 + \mathcal{O}(\alpha)] \cdot 3 \cdot \mathbf{f}\left(\frac{m_{\ell_i}^2}{m_c^2}\right) \cdot \frac{1}{4\pi}, \quad (6.65)$$

and for background gluon fields

$$\mathbf{f}\left(\frac{m_{\ell_i}^2}{m_c^2}\right) \longrightarrow \frac{m_{\ell_i}^2}{m_c^2}, \quad (6.66)$$

giving a net relative factor of

$$\frac{5m_{\ell_i}^2}{m_c^2} [1 + \mathcal{O}(\alpha)]. \quad (6.67)$$

The terms denoted $\mathcal{O}(\alpha)$ reflect potential discrepancies in the one-photon-loop corrections to the photon and gluon leading-order diagrams. However, with these corrections not yet having been calculated for either diagram it is convenient to write just the leading global correction to $m_{\ell_i}^2$ as a whole. Taking both photon and gluon terms into account (but not yet including the scalar boson contribution, denoted \dots), the leading-order expression for lepton mass is therefore given

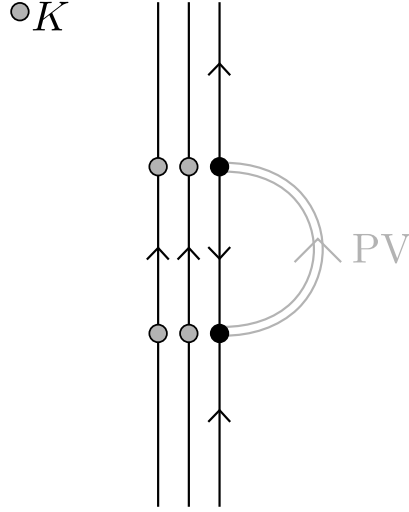


Figure 6.16: Leading-order contribution to fermion mass from the background scalar field. Grey circles represent the action of the K_ℓ -matrix.

by

$$m_{\ell_i}^2 = \frac{f^2}{2} \left[k_i^{(\ell)} \right]^4 \omega_0^2 N_0^8 S_{18,147} \times \left\{ \frac{q_\ell^2}{e^2} + \frac{5m_{\ell_i}^2}{m_c^2} + \dots \right\} [1 + O(\alpha)] \quad (6.68)$$

where q_ℓ is the charge of lepton ℓ_i .

As an aside, note that for the fermions there is no equivalent to the bosonic universality coupling explored in Sec. 6:4.2.2.b. For the Z boson, this coupling arises as the basic Z mass diagram [equivalent to Fig. 6.1(i)] intrinsically incorporates six background preon lines, and two co-ordinates to integrate over, permitting reduction to two preon lines when one of these integrals is performed. In contrast, the basic fermion mass diagram (Fig. 6.15) contains no intrinsic mechanism for adding extra preon lines. Although extra preons may be recruited from the pseudovacuum, consistent normalisation (Sec. 1:3.8.6) requires that integrating over the additional co-ordinate thus introduced will inevitably eliminate them again.

6:5.1.3 Mass from scalar component of the pseudovacuum

Next to be considered is the interaction between the composite lepton and the pseudovacuum complex scalar boson field shown in Fig. 6.16. Again it is desirable to write this term as a correction to the photon term. As per Eq. (6.7) the pseudovacuum expectation value of the complex scalar boson field is nonvanishing, and evaluation of the associated loop factor is most readily performed by determining its weight relative to the photon diagram.

To achieve this, let the $SU(3)_A$ sector be supplemented by the N boson to obtain the Lie algebra $\mathfrak{gl}(3, \mathbb{R})_A$ of an effective symmetry group $GL(3, \mathbb{R})_A$. Adopt a basis e_{ij}^A . Decomposing the scalar boson into its terms, the loop associated with each term will now be mapped to an equivalent loop involving a vector boson e_{ij}^A . Note, however, that this is just a numerical equivalence used to determine relative loop weights. The actual evaluation of the pseudovacuum

term is performed on the complex scalar boson itself, which has trivial C -sector and A -sector representation and as discussed in Sec. 3:3.3.7 this is consequently unaffected by the $SU(3)_A$ and $SU(3)_C$ gauge choices presented in Sec. 3:3.3.6.

To determine the loop weight, first recognise that each basis element in e_{ij}^A is averaged over colour. The terms in $\mathbf{H}\mathbf{H}^*$ are summed over A -charge and colour, with the result that the terms are equivalent (up to factors to be determined) to a sum over the diagonal bosons e_{ii}^A , each multiplied by three to go from an average over colour to a sum.

Now exploit the $GL(3, \mathbb{R})$ -invariance of the e_{ij}^A representation of $gl(3, \mathbb{R})_A$ by noting that the structure factor associated with an diagonal element e_{ii}^A will be the same as that associated with an off-diagonal element $e_{ij}^A|_{i \neq j}$. Therefore begin from the structure factor for the W boson, and multiply by appropriate coefficients to construct the relevant factor for the complex scalar boson. Relevant factors are as follows:

- Structure factor: $-\frac{10}{3} [1 + O(\alpha)]$ for W , 2 for photon. Relative factor: $-\frac{5}{3} [1 + O(\alpha)]$.
- Elimination of sigma matrices from W diagram when mapping to a scalar boson term: -2 .
- The W boson diagram maps to $\frac{1}{9}$ of the \mathbf{H} diagram: $\frac{1}{9}$.
- There are nine such terms: 9
- As described in Sec. 3:3.5.5 the \mathbf{H} and \mathbf{H}^* vertices are effectively constructed as if in the “far field” (in this context, relative to \mathcal{L}_Ω) and thus their emission from the fermion attracts a factor of $2[k_1^{(e)}N_0]^{-2} [1 + O(N_0^{-1})]$ apiece.
- The two interaction vertices are within $O(\mathcal{L}_0)$ of one another and thus attract K_ℓ -matrices as per Figs. 5.4 and 5.5.
- As per the caption of Fig. 3.6, there are two different ways to assemble the complex scalar boson and conjugate from constituent preons, but these are subsumed into a definition of the complex scalar boson field and thus do not introduce any factors.
- The complex scalar boson is massive, for a factor of $\mathbf{f}(m_{\ell_i}^2/m_{\mathbf{H}}^2)$.

On comparing the scalar boson diagram with the vector boson diagram, the net relative factor is thus

$$\begin{aligned} & -\frac{5}{3} [1 + O(\alpha)] \cdot -2 \cdot \frac{1}{9} \cdot 9 \cdot \left[\frac{2}{[k_1^{(e)}N_0]^2} \right]^2 [1 + O(N_0^{-1})] \mathbf{f}\left(\frac{m_{\ell_i}^2}{m_{\mathbf{H}}^2}\right) \\ & = \frac{40m_{\ell_i}^2}{3m_{\mathbf{H}}^2[k_1^{(e)}N_0]^4} [1 + O(N_0^{-1}) + O(\alpha)] \end{aligned}$$

for a total lepton mass

$$\begin{aligned} m_{\ell_i}^2 &= \frac{f^2}{2} [k_i^{(\ell)}]^4 \omega_0^2 N_0^8 S_{18,147} \\ &\times \left\{ \frac{q_\ell^2}{e^2} + \frac{5m_{\ell_i}^2}{m_c^2} + \frac{40m_{\ell_i}^2}{3m_{\mathbf{H}}^2[k_1^{(e)}N_0]^4} [1 + O(N_0^{-1})] \right\} \\ &\times [1 + O(\alpha)]. \end{aligned} \tag{6.69}$$

6:5.1.4 Gluon and scalar field mass deficits

Conservation of energy/momentum implies that the rest mass imparted to the fermion must be compensated by a reduction in the zeroth component of 4-momentum of some of the pseudovacuum fields. Likelihood of contribution from any given pseudovacuum sector will be governed by availability of zeroth-component energy within that sector, i.e. the rest mass of the associated species, and the strength of coupling to that sector. It therefore follows that this borrowing of rest mass occurs with equal likelihood from each of the nine gluon channels of the pseudovacuum, with much lower likelihood from the scalar boson channel (due to a much weaker coupling), and not at all from the photon channel (due to zero rest mass). For a first approximation, consider only the gluon channel. Borrowing a mass of m_*^2 from a background gluon field takes place at the first of the existing gluon/fermion interaction vertices of Fig. 6.14, and corresponds to deletion of a gluon of mass m_* from the pseudovacuum. This hole then propagates as a quasiparticle, and is filled by the conjugate interaction at the second vertex.

More generally, with multiple overlapping pairs of background gluon field interactions occurring along a fermion propagator, there is a consistent propagating hole in the pseudovacuum gluon sector corresponding to an energy deficit of m_*c^2 , and individual vertices may cause transient fluctuations and may change which specific gluon fields (with respect to some arbitrary choice of colour basis) are involved in propagating this hole, but in general it may be in any of the nine gluon channels at any time. This hole is in addition to the effect discussed in Sec. 6:5.1.2 where fermions may surrender momentum to or borrow momentum from the pseudovacuum, and thus gives an additional correction factor not yet discussed.

This hole propagates as a quasiparticle accompanying the lepton. Any time that a fermion interacts with the pseudovacuum gluon sector this hole is necessarily also present, and may occupy any of nine channels.

For simplicity, further consider the case when the hole occupies an off-diagonal channel. It would be convenient to write the effect of this hole as a correction to the mass of gluon,

$$m_c^2 \longrightarrow m_c^2 - km_*^2 =: (m_c^*)^2 \quad (6.70)$$

for some factor k . Recognising that the co-propagating hole's interaction with the fermion is trivial (it is only required to be present), with any local energy/momentum transfer to or from the pseudovacuum being mediated by the fermion/gluon coupling of Fig. 6.14(i), the hole's interactions attract no structural vertex factor and thus where the direct gluon interactions of Fig. 6.14(i) acquire a factor of 5/3 apiece, the hole does not, for an effective relative factor of 3/5 on the hole's interactions. Further, the presence of the hole breaks the time reversal symmetry of a portion of the pseudovacuum and this gives rise to a symmetry factor of $\frac{1}{2}$ relative to the original gluon interaction in which the pseudovacuum was assumed time-reversal-invariant. Finally, there are nine gluons, and by $GL(3, \mathbb{R})$ symmetry the mass deficit may propagate via any of them with equal likelihood and equivalent consequence. The multiplicative factor obtained assuming a single channel of propagation for the mass deficit is therefore increased ninefold. The net outcome is to correct the gluon mass to an effective mass of

$$\begin{aligned} (m_c^*)^2 &= m_c^2 - \frac{3}{5} \cdot \frac{1}{2} \cdot 9 \cdot m_*^2 \\ &= m_c^2 \left(1 - \frac{27}{10} \frac{m_*^2}{m_c^2} \right). \end{aligned} \quad (6.71)$$

Note that m_c^* is a function of m_* , but for a lepton ℓ_i which is on-shell and at (or close to) rest in the isotropy frame of the pseudovacuum this admits the convenient replacement $m_*^2 \rightarrow m_{\ell_i}^2$. Also note that the gluon mass deficit effect is a whole-field effect, acting on both the foreground

and background gluon fields. The corrected gluon mass m_c^* should be used anywhere a particle interacts with a gluon field in the presence of a lepton.

Similarly, the foreground lepton may also borrow its mass from the scalar boson field. However, coupling between leptons and scalar bosons is weaker than that between leptons and gluons. Much as the gluon deficit corrects m_c^2 by $O(m_{\ell_i}^2/m_c^2)$ in expressions for particle rest mass, the scalar mass deficit corrects $m_{\mathbf{H}}^2$ by $O(m_{\ell_i}^2/m_{\mathbf{H}}^2)$. Including this as an unevaluated higher-order term, the lepton mass equation is amended to

$$m_{\ell_i}^2 = \frac{f^2}{2} \left[k_1^{(\ell)} \right]^4 \omega_0^2 N_0^8 S_{18,147} \times \left\{ \frac{q_\ell^2}{e^2} + \frac{5m_{\ell_i}^2}{(m_c^*)^2} + \frac{40m_{\ell_i}^2}{3m_{\mathbf{H}}^2 \left[k_1^{(e)} N_0 \right]^4} \left[1 + O(N_0^{-1}) + O\left(\frac{m_{\ell_i}^2}{m_{\mathbf{H}}^2}\right) \right] \right\} \quad (6.72)$$

$$\times [1 + O(\alpha)]$$

$$(m_c^*)^2 = m_c^2 \left(1 - \frac{27m_{\ell_i}^2}{10m_c^2} \right). \quad (6.73)$$

6:5.2 Foreground loop corrections

Now consider the effects of foreground loop corrections on the leading-order diagrams of Figs. 6.14 and 6.16. Note that since momentum is continually redistributed among the constituent preons by means of gluon-mediated interactions even over length scale \mathcal{L}_ψ , a boson need not start and finish its trajectory on the same preon in order to be considered a loop correction to an emission vertex. Further note that the massive nature of the loop boson does not disrupt the pseudovacuum correlators in these diagrams, as these are brought together through the use of spinor identities at the vertices making these diagrams more robust against interference from intermediate particles propagating outside the autocorrelation region than the boson mass diagrams of Sec. 6:4.

6:5.2.1 1-loop EM corrections

The $O(\alpha)$ EM loop corrections to the lepton mass interaction are shown in Fig. 6.17. These should be compared with their Standard Model counterparts in Fig. 6.18.

As in Sec. 6:4.1.1, the only corrections which need to be incorporated into the electron mass vertex are those which do not also appear in the Standard Model. Further, as per Sec. 4:3.1 all PSE terms may be absorbed into the fundamental vertex prior to applying non-PSE corrections. Begin with the diagrams of Fig. 6.17(i), which have the Standard Model counterparts shown in Fig. 6.18. Evaluation of symmetry factors is described in Appendix 6:B and reveals these to be directly equivalent. The diagrams of Fig. 6.17(i) therefore correspond to PSE vertex corrections in the Standard Model. Provided the mass vertex after all non-PSE corrections is identified with the observable mass, in keeping with emulation of the $\overline{\text{MS}}$ renormalisation scheme, the diagrams of Fig. 6.17(i) therefore make no contribution to $m_{\ell_i}^2$.

It is complementary to note that when multiple photon loops exist, the summation over different pseudovacuum expansions of a diagram is equivalent to treating the background photon loop as being of a unique species distinguishable from any foreground photon loops, then summing over the contributions of the resulting effectively topologically distinct diagrams. Since the background loop thus behaves as a distinct species, the EM loop corrections to the background photon interaction are identical to the EM corrections to the background gluon interaction and do not

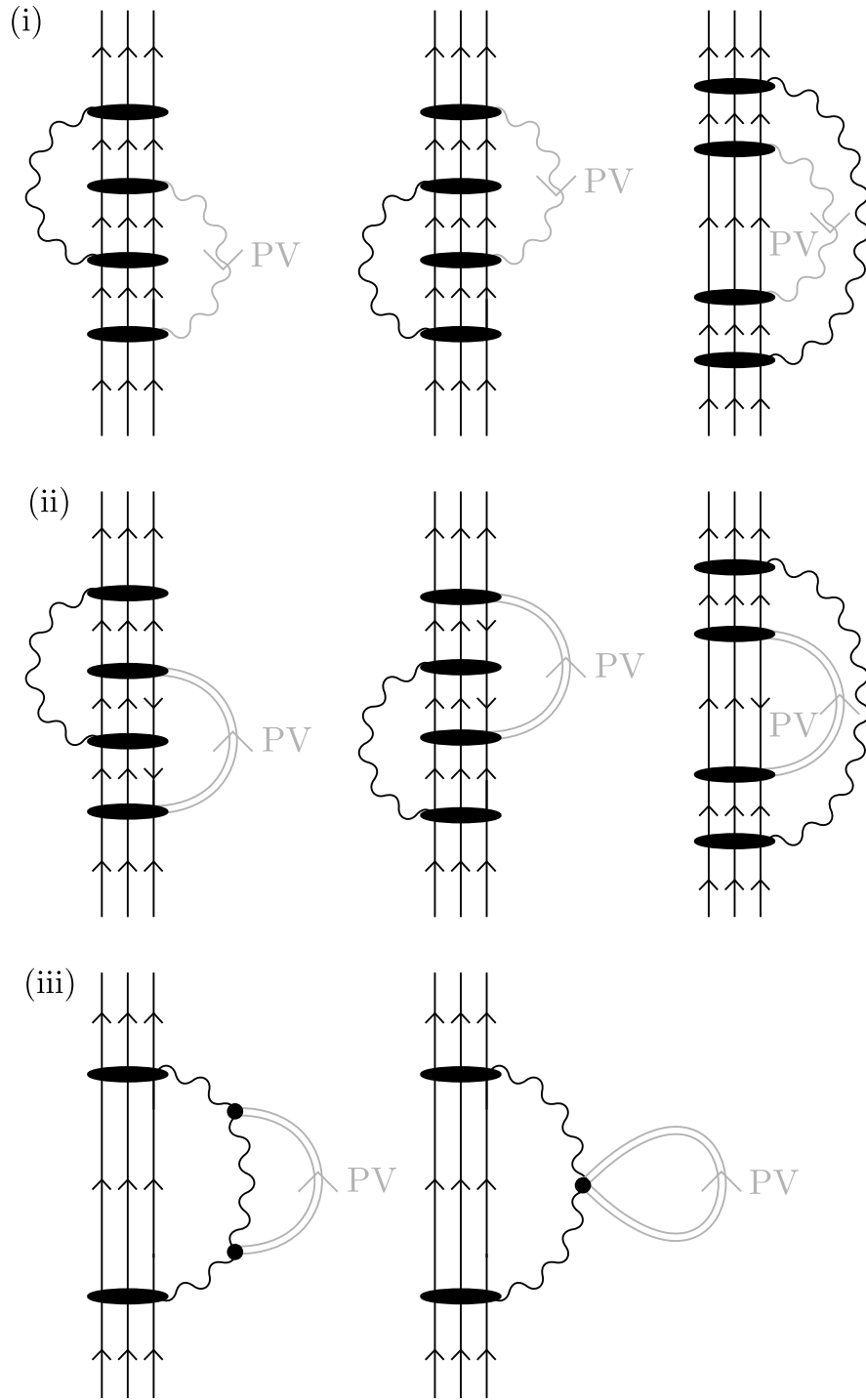


Figure 6.17: One-foreground-loop EM corrections to (i) vector boson and (ii)-(iii) scalar boson lepton mass interactions. The broad oval interaction vertices indicate that the boson may interact with any of the three preons, and all configurations should be summed over.

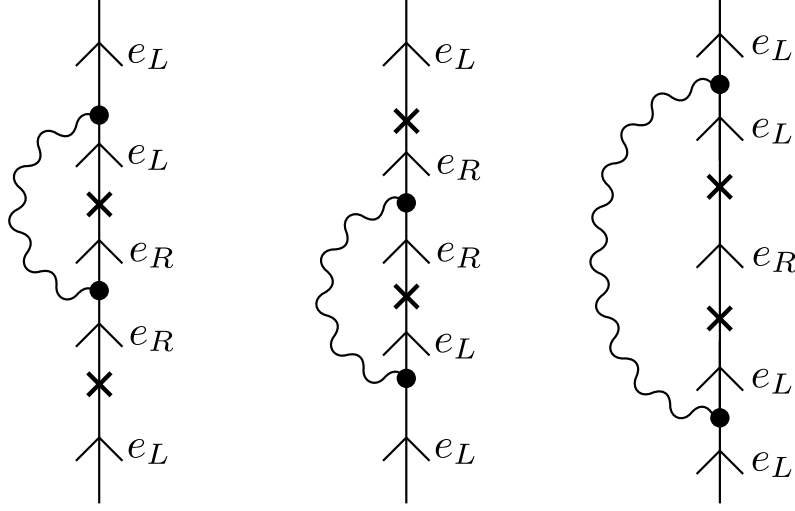


Figure 6.18: Standard Model one-foreground-loop EM corrections to the electron mass vertex. The example shown is for the left-helicity electron Weyl spinor; equivalent diagrams for the right-helicity spinor exchange L and R .

attract additional symmetry factors on account of the foreground and background interactions both being photon interactions. Thus there are no relative terms of $O(\alpha)$ on $5m_{\ell_i}^2/(m_c^*)^2$.

Next, consider the scalar boson loops of Fig. 6.17(ii). In these diagrams the intermediate lepton has one preon reversed, inverting its electromagnetic charge, and the first two diagrams therefore yield factors of $\alpha/(6\pi)$ rather than $\alpha/(2\pi)$. In conjunction with negation of the Standard Model corrections, they therefore yield a net correction to the background scalar term with weight

$$-\frac{2\alpha q_\ell^2}{3\pi e^2}. \quad (6.74)$$

The third diagram is consistent with the Standard Model equivalent and so once again does not contribute to m_{ℓ_i} .

Finally, there are two more diagrams from the scalar boson sector to consider. Moving a single scalar boson vertex onto the photon loop is prohibited as the diagram as a whole does not then leave the preon triplet unchanged (one preon gets replaced by an antipreon), but moving both vertices onto the loop is admissible. This results in the diagrams shown in Fig. 6.17(iii). However, these loops contribute to the mass of the loop photon (which vanishes by gauge), and thus will necessarily cancel with other terms in which the loop photon couples to the background fields. They may therefore be disregarded. The net expression for lepton mass thus far derived is therefore

$$m_{\ell_i}^2 = \frac{f^2}{2} \left[k_1^{(\ell)} \right]^4 \omega_0^2 N_0^8 S_{18,147} \quad (6.75)$$

$$\times \left\{ \frac{q_\ell^2}{e^2} + \frac{5m_{\ell_i}^2}{(m_c^*)^2} + \frac{40m_{\ell_i}^2}{3m_{\mathbf{H}}^2 \left[k_1^{(e)} N_0 \right]^4} \left(1 - \frac{2\alpha q_\ell^2}{3\pi e^2} \right) \left[1 + O(N_0^{-1}) + O\left(\frac{m_{\ell_i}^2}{m_{\mathbf{H}}^2} \right) + O(\alpha^2) \right] \right\}$$

$$\times (1 + \dots)$$

where “...” represents massive loop corrections of order α which are derived starting in Sec. 6:5.2.3.

For a further amendment to this expression, also note that the extra photon making up the loop may potentially comprise some of the same preons as are involved in interactions elsewhere within the local correlation region, with effect on the FSF symmetry factors associated with the loop photon vertices. The resulting corrections comprise both massless and massive terms. All relevant boson masses are of comparable magnitude, $m_c^2 \sim m_W^2 \sim m_Z^2 \sim m_H^2$, and gluon terms will be seen to outweigh weak sector terms, therefore write the leading elements of each term correcting m_{e_i} as $O(\alpha N_0^{-1})$ and $O[\alpha N_0^{-1} m_{e_i}^2 / (m_c^*)^2]$ respectively. Neither of these corrections have counterparts in the Standard Model. It is convenient to insert them into the final bracket of the above expression,

$$(1 + \dots) \longrightarrow \left\{ 1 + O\left(\frac{\alpha}{N_0}\right) + O\left[\frac{\alpha m_{\ell_i}^2}{N_0 (m_c^*)^2}\right] + \dots \right\} \quad (6.76)$$

6:5.2.2 $O(N_0^{-1})$ correction to 1-loop EM corrections

It is relatively straightforward to calculate the $O(N_0^{-1})$ corrections to the 1-loop EM corrections. First, recognise that these corrections only apply when a loop vertex is within the same correlation region as another vertex. If not, then only the usual EM symmetry factor of S_α applies, which is incorporated within the coefficient α associated with the loop vertices.

However, consider the first diagram of Fig. 6.17(i), in which the lower vertex on the foreground photon is bracketed by two correlated couplings to the pseudovacuum. Assuming the window approximation (1.169), in the isotropy frame of the pseudovacuum these bracketing vertices must lie within the autocorrelation distance and time of one another. In the dominant (on-shell) contribution, propagation from one background interaction vertex to the other is linear and hence the lower vertex of the foreground photon also lies within the same correlation region. However, as discussed in Appendix 6:B, in the dominant contribution to the loop correction the upper vertex does not.

Next, recognise that corrections of this form apply whenever the loop boson vertex in the autocorrelation region contains preons matching those present at the pseudovacuum vertices, regardless of the boson species involved. Consequently to overall order $O(\alpha/N_0)$ these $O(N_0^{-1})$ corrections arise as amendments to the EM loop corrections to background photon interactions, and to order $O(\alpha m_{\ell_i}^2/N_0)$ they arise as amendments to (ii) EM loop corrections to background gluon interactions, (iii) gluon loop corrections to background photon interactions, and (iv) weak boson loop corrections to background photon interactions. Terms (i) and (ii) are evaluated here, and terms (iii)-(iv) in Secs. 6:5.2.3.b and 6:5.2.4.d respectively.

6:5.2.2.a $O(N_0^{-1})$ correction to EM loop correction to background photon coupling:

To evaluate term (i), the $O(N_0^{-1})$ corrections arising due to FSF interchange when a photon loop corrects the coupling to the background photon field, first recognise that within a given foreground vertex there are two inbound preon lines and two outbound preon lines. It suffices to consider each separately.

Recognising that all preon lines undergo interactions with the background fields which may cause them to change colour, and that colour is only conserved separately within the foreground and background fields on average over scales large compared with \mathcal{L}_0 , the colour of each inbound or outbound line both in this vertex and in the background field interaction vertices may be considered independently random. Thus there is a chance of $\frac{1}{3}$ that the colour of a given line at the foreground vertex will match the equivalent line at a given background field vertex.

In contrast, A -charge is guaranteed to match as all photons arise from the same fermion, which contains only one type of preon carrying a well-defined A -charge. However, these fermions

emit bosons associated with representations containing both $\delta_{\dot{c}c}\bar{\psi}^{1\dot{c}}\bar{\sigma}^\mu\psi^{1c} - \delta_{\dot{c}'c'}\bar{\psi}^{2\dot{c}'}\bar{\sigma}^\mu\psi^{2c'}$ and $\delta_{\dot{c}c}\bar{\psi}^{1\dot{c}}\bar{\sigma}^\mu\psi^{1c} + \delta_{\dot{c}'c'}\bar{\psi}^{2\dot{c}'}\bar{\sigma}^\mu\psi^{2c'}$, with the former corresponding to photons and the latter to Z and N bosons. By conservation of charge at vertices, and the requirement that the fermion line carries a well-defined A -charge, these two groups are emitted with equal weight. Consequently, when there is a match of A -charges at two vertices, there is only a 50% chance that the line being matched in the e_{ij} basis corresponds to a photon. Thus the A sector provides a further factor of $\frac{1}{2}$.

There are four lines at the foreground (loop) vertex which is in the correlated region, and there are two background vertices from the leading-order diagram with which to seek symmetry matches, for factors of 4 and 2 respectively. However, the requirement that preons at a vertex exhibit appropriate correlations (i.e. preons in photons must be pairwise correlated, those in fermions must form correlated triplets, etc.) implies that:

- A preon in a photon can only be matched with a preon in a photon, and a preon in a fermion can only be matched with a preon in a fermion.
- Similarly, the orientations of preons at a vertex (inbound/outbound) must also match.
- When the FSF associated with one preon in a photon is exchanged with that of a preon in a different photon, *both* FSFs associated with those photons must (i) carry matching charges, and (ii) be exchanged. This halves the number of independent matches, but doubles the increment in FSF symmetry factor associated with a match. This effect may therefore be ignored.
- A similar consideration applies for fermions, with all three FSFs being exchanged. However, for the FSFs of non-vertex fermions this is trivial and has no bearing on the calculation.

A given preon in the foreground (loop) vertex may therefore be characterised as (for example) “photon, inbound to vertex” and only yields an $O(N_0^{-1})$ increment of the $O(\alpha)$ symmetry factor if it matches a “photon, inbound to vertex” preon on a background vertex (from the leading-order diagram).

Putting this all together, there are four preon lines in the foreground (loop) vertex, each of which may match one preon line in each of the two background (leading-order diagram) vertices, with a chance of $\frac{1}{6}$. When they match, this increments an FSF symmetry factor from $N_0 + k$ to $N_0 + (k + 1)$, and this is equivalent to multiplying by a correction factor of $[1 + N_0^{-1} + O(N_0^{-2})]$. Thus the overall net multiplicative factor arising from all lines in all vertices is

$$\left[1 + \frac{4}{3N_0} + O(N_0^{-2})\right]. \quad (6.77)$$

A similar analysis applies to the second diagram of Fig. 6.17(i) but not to the third, yielding an overall loop correction factor to the tree level vertex, accurate to $O(\alpha N_0^{-1})$, of

$$\begin{aligned} & \left[1 + \frac{\alpha}{2\pi} \left(1 + \frac{4}{3N_0}\right) + \frac{\alpha}{2\pi} \left(1 + \frac{4}{3N_0}\right) + \frac{\alpha}{2\pi} + O\left(\frac{\alpha}{N_0^2}\right) + O(\alpha^2)\right] \\ &= \left[1 + \frac{3\alpha}{2\pi} \left(1 + \frac{8}{9N_0}\right) + O\left(\frac{\alpha}{N_0^2}\right) + O(\alpha^2)\right]. \end{aligned} \quad (6.78)$$

This is compared with the Standard Model factor of $3\alpha/(2\pi) + O(\alpha^2)$ to yield a correction factor accurate to $O(N_0^{-1})$ and $O(\alpha)$ of $(1 + c_{\alpha/N_0})$ where

$$c_{\alpha/N_0} := \frac{1 + \frac{3\alpha}{2\pi} \left(1 + \frac{8}{9N_0}\right)}{1 + \frac{3\alpha}{2\pi}} - 1 = \frac{8\alpha}{3N_0(3\alpha + 2\pi)}, \quad (6.79)$$

and a net expression for electron mass

$$\begin{aligned}
m_{\ell_i}^2 = & \frac{f^2}{2} \left[k_1^{(\ell)} \right]^4 \omega_0^2 N_0^8 S_{18,147} \\
& \times \left\{ \frac{q_\ell^2 (1 + c_{\alpha/N_0})}{e^2} + \frac{5m_{\ell_i}^2}{(m_c^*)^2} \right. \\
& \quad \left. + \frac{40m_{\ell_i}^2}{3m_{\mathbf{H}}^2 \left[k_1^{(e)} N_0 \right]^4} \left(1 - \frac{2\alpha q_\ell^2}{3\pi e^2} \right) \left[1 + \mathcal{O}(N_0^{-1}) + \mathcal{O}\left(\frac{m_{\ell_i}^2}{m_{\mathbf{H}}^2}\right) + \mathcal{O}(\alpha^2) \right] \right\} \\
& \times \left\{ 1 + \mathcal{O}\left(\frac{\alpha}{N_0^2}\right) + \mathcal{O}\left(\frac{\alpha^2}{N_0}\right) + \mathcal{O}\left[\frac{\alpha m_{\ell_i}^2}{N_0(m_c^*)^2}\right] + \dots \right\}
\end{aligned} \tag{6.80}$$

where the correction of $\mathcal{O}(\alpha/N_0)$ in Eq. (6.76) has been evaluated to yield c_{α/N_0} , and the next-highest unevaluated contributions are $\mathcal{O}(\alpha/N_0^2) + \mathcal{O}(\alpha^2/N_0)$. [As with corrections of $\mathcal{O}(\alpha)$, corrections of $\mathcal{O}(\alpha^2)$ are common to both the $\mathbb{C}^{\wedge 18}$ model and the Standard Model and thus do not need to be incorporated into the expression for the mass vertex.]

6:5.2.2.b $\mathcal{O}(N_0^{-1})$ correction to EM loop correction to background gluon coupling:

The next corrections to be considered are the $\mathcal{O}(N_0^{-1})$ corrections arising due to FSF interchange when a photon loop corrects the coupling to the background gluon field. The principle is the same as for the photon loop, and calculation of the correction broadly follows Sec. 6:5.2.2.a. Again, one vertex from the loop correction lies between the two background field couplings, and on-shell, will be within the same correlation region. However:

- The preons in the background fields may each carry any of the three colour charges and any of the three A -charges. The chance of them matching a given preon in the loop photon is thus $\frac{1}{9}$, in contrast with $\frac{1}{6}$ in Sec. 6:5.2.2.a (where the A -charge of the background preons can only be 1 or 2).
- In the background gluons, both preons carry the same A -charge but their C -charges may vary independently. However, the sum over two (non-identical) preons, each of which may potentially match the background preon, yields a factor of two. In contrast, in Sec. 6:5.2.2.a the preons in the loop photon both carry the same C -charge as well as A -charge; either both match or both do not. However, matching two preons again results in a factor of two. The independence of the C -charges in the background gluons therefore does not further change the correction factor.

The resulting correction is thus

$$\frac{5m_{\ell_i}^2}{(m_c^*)^2} \longrightarrow \frac{5m_{\ell_i}^2}{(m_c^*)^2} \left[1 + \frac{2c_{\alpha/N_0}}{3} + \mathcal{O}(N_0^{-2}) \right] \tag{6.81}$$

which may be conveniently realised by redefining c_{α/N_0} in Eq. (6.80) as

$$c_{\alpha/N_0} := \frac{8\alpha}{3N_0(3\alpha + 2\pi)} \left[1 + \frac{10m_{\ell_i}^2}{3(m_c^*)^2} \right]. \tag{6.82}$$

The error terms in Eq. (6.80) remain unchanged, as this correction does not exhaust the terms of $\mathcal{O}\{\alpha m_{\ell_i}^2/[N_0(m_c^*)^2]\}$. For further terms of this order, see Secs. 6:5.2.3.b and 6:5.2.4.d.

6:5.2.3 1-loop gluon corrections

The next loop corrections to consider are those arising from gluon loops, analogous to the diagrams of Fig. 6.17. These gluons are confined, so cannot escape to the far field but must remain within the local autocorrelation region (within which the pseudovacuum is permitted to appear transiently colour-inhomogeneous). They are foreground particles existing over scales of $O(\mathcal{L}_0)$, which corresponds to the interaction scale for boson mass, and hence are massive. Over these scales gluon which form local closed loops are effectively shielded by the inhomogeneities in the pseudovacuum and exhibit at most only the bare gluon mass (including the gluon deficit correction). Only loop corrections to the background photon and background gluon interactions need be considered in the present chapter; corrections to the background scalar boson interaction are of $O[\alpha m_{\ell_i}^2/(m_c^*)^2]$ and thus are smaller than the terms of $O(m_{\ell_i}^2/m_H^2)$ in Eq. (6.75). First the corrections are calculated while neglecting preon degeneracy, and then the $O(N_0^{-1})$ corrections to the corrections are computed similarly to those previously seen in Secs. 6:5.2.2.a–6:5.2.2.b.

6:5.2.3.a Main correction: Consider the gluon loop counterparts to Fig. 6.17(i). Where the fermion interacts with the background photon field, these corrections take on the form of Fig. 6.19(i). For interactions between the fermion and the background gluon fields they may take on the form of either Fig. 6.19(i) or (ii), and conservation of colour charge indicates that when these couplings are summed, this is equal to the coupling of the background gluon to the fermion in the original leading-order diagram [Fig. 6.19(iii)]. Further, when the loop correction is evaluated, this collapses to a numerical multiplier on the original background interaction vertex and the customary application of spinor identities (4.6–4.7) yields a non-vanishing contribution to $m_{\ell_i}^2$. It then suffices to consider an example where the coupling of the background gluon and loop gluon vanishes, making it equivalent to the background photon case, evaluate the correction to the interaction vertex, and extrapolate this across all gluon colour combinations by $GL(3, \mathbb{R})$ symmetry.

Figure 6.19(iv) shows a further diagram which may be constructed using gluon loop corrections. This is a counterpart to the gluon version of the third diagram of Fig. 6.17(i), again with vertices moved onto the loop boson, and also contributes to the mass of the loop gluon.

Note that in contrast to the photon terms, where the third diagram of Fig. 6.17(i) was accounted for in the Standard Model, for preon/gluon interactions all loop corrections must be evaluated as there are no corresponding Standard Model terms.

To evaluate these corrections begin with Fig. 6.19(i), which is the gluon loop counterpart to Fig. 6.17(i). Start with the fermion coupling to the background photon field, and a specific choice of off-diagonal gluon. Compare with the equivalent EM loop figure and note the following changes:

- The vertex factors increase from $f^2/2$ to f^2 , for a relative factor of 2.
- The boson is off-diagonal, for a relative structural factor of $\frac{5}{3}$.
- The photon source may be any of three charged preons, but the gluon may only be emitted by a preon of appropriate colour. However, any of the three preons may be the preon of that colour, for a net factor of one.
- Emission of the off-diagonal gluon changes the colour of the emitting preon. There are then two preons of that colour which are capable of absorbing the loop gluon, and both of the resulting diagrams count as loop corrections due to the implicit exchange (not shown) of further gluons as a binding interaction sharing momentum between all members of the preon triplet. The choice of absorbing preons gives a factor of 2.

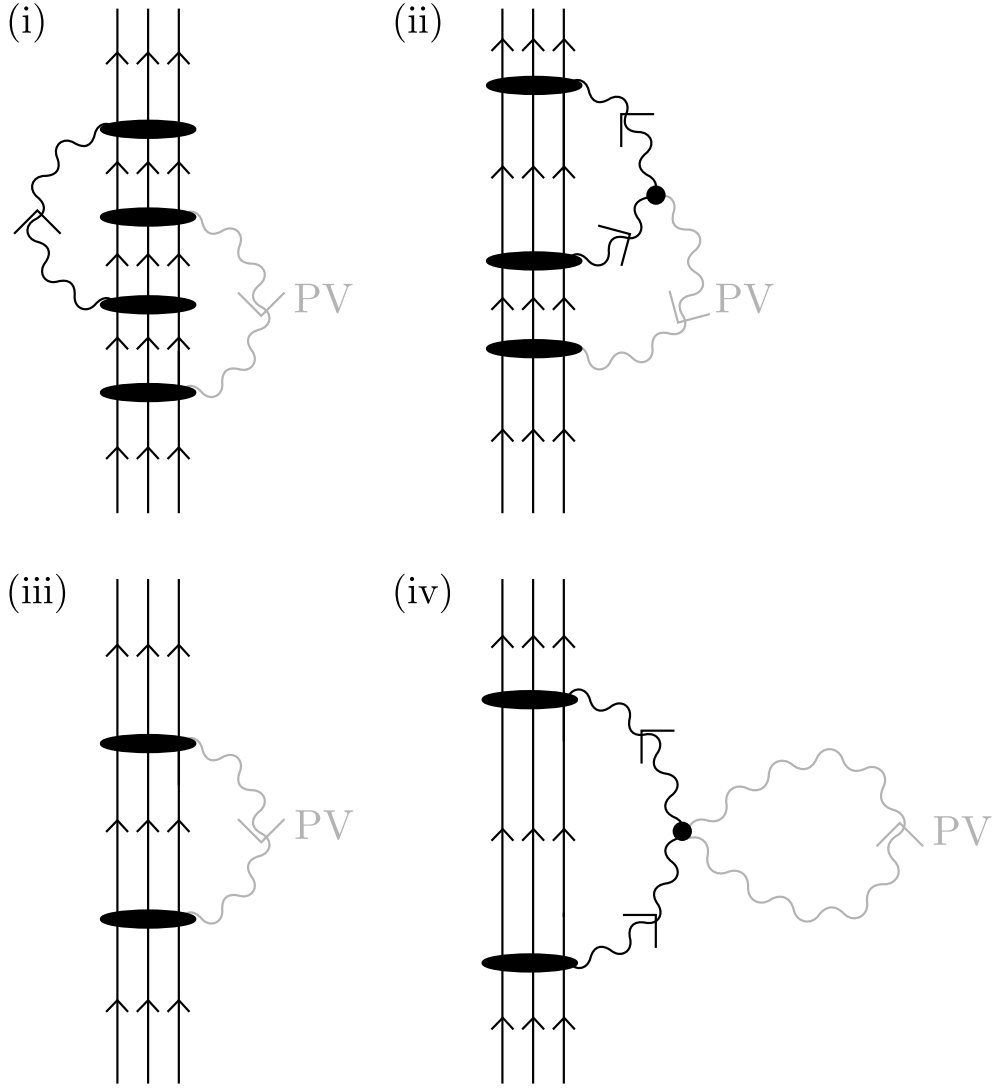


Figure 6.19: (i)-(ii) Gluon loop equivalents to the first diagram of Fig. 6.17(i). When the fermion couples to the background photon field, only diagram (i) may be constructed as the gluon does not carry an electromagnetic charge. When the fermion couples to the background gluon field, both diagram (i) and diagram (ii) may be constructed. Conservation of colour charge indicates that on summing the coupling of the background gluon to the fermion and the background gluon to the loop gluon, this is equal to the coupling of the background gluon to the fermion in the original leading-order diagram (iii). Similarly, diagram (iv) is the counterpart to the third diagram of Fig. 6.17(i). This diagram is especially interesting as it contributes both to the fermion mass and to the mass of the loop gluon. Note that the two background gluons must couple with the loop gluon at a single vertex, as discussed in Sec. 5:3.1.

- The loop gluon is massive, and is in the presence of a foreground fermion so experiences a gluon field mass deficit giving a loop factor of $m_{\ell_i}^2/(m_c^*)^2$.
- These factors multiply the equivalent photon loop factor, which is $\alpha/(2\pi)$.

The per-gluon correction weight from this diagram is therefore

$$\frac{10\alpha}{3\pi} \frac{m_{\ell_i}^2}{(m_c^*)^2}. \quad (6.83)$$

This calculation is repeated for the gluon counterparts to the other two figures of Fig. 6.17(i), and each of these figures may involve any of nine gluons, for a total weight of

$$\frac{90\alpha}{\pi} \frac{m_{\ell_i}^2}{(m_c^*)^2}. \quad (6.84)$$

Correction of the background gluon interactions proceeds equivalently, and as noted above the correction to the scalar boson may be ignored at current precision, for a net lepton mass so far of

$$\begin{aligned} m_{\ell_i}^2 = & \frac{f^2}{2} [k_1^{(\ell)}]^4 \omega_0^2 N_0^8 S_{18,147} \\ & \times \left\{ \frac{q_\ell^2}{e^2} \left[1 + c_{\alpha/N_0} + \frac{90\alpha m_{\ell_i}^2}{\pi(m_c^*)^2} \right] + \frac{5m_{\ell_i}^2}{(m_c^*)^2} \left[1 + \frac{90\alpha m_{\ell_i}^2}{\pi(m_c^*)^2} \right] \right. \\ & \quad \left. + \frac{40m_{\ell_i}^2}{3m_{\mathbf{H}}^2 [k_1^{(e)} N_0]^4} \left(1 - \frac{2\alpha q_\ell^2}{3\pi e^2} \right) \left[1 + O(N_0^{-1}) + O\left(\frac{m_{\ell_i}^2}{m_{\mathbf{H}}^2}\right) + O(\alpha^2) \right] \right\} \\ & \times \left\{ 1 + O\left(\frac{\alpha}{N_0^2}\right) + O\left(\frac{\alpha^2}{N_0}\right) + O\left[\frac{\alpha m_{\ell_i}^2}{N_0(m_c^*)^2}\right] + \dots \right\} \end{aligned} \quad (6.85)$$

where the next major terms to be determined are the one-loop weak boson corrections.

6:5.2.3.b $O(N_0^{-1})$ correction to gluon loop correction to background photon coupling: The next corrections to be considered are the $O(N_0^{-1})$ corrections arising due to FSF interchange when a gluon loop corrects the coupling to the background photon field. The principle is the same as for the photon loop, and calculation of the correction broadly follows Secs. 6:5.2.2.a–6:5.2.2.b. Again, one vertex from the loop correction lies between the two background field couplings, and on-shell, will be within the same correlation region. Again, matching is now between preons from a gluon and a photon, reducing the correction by a factor of $\frac{2}{3}$ relative to Sec. 6:5.2.2.a. The resulting correction is thus

$$\frac{q_\ell^2}{e^2} \frac{90\alpha m_{\ell_i}^2}{\pi(m_c^*)^2} \rightarrow \frac{q_\ell^2}{e^2} \frac{90\alpha m_{\ell_i}^2}{\pi(m_c^*)^2} \left[1 + \frac{2c_{\alpha/N_0}}{3} + O(N_0^{-2}) \right] \quad (6.86)$$

which may be conveniently realised by redefining c_{α/N_0} in Eq. (6.85) as

$$\begin{aligned} c_{\alpha/N_0} &:= \frac{8\alpha}{3N_0(3\alpha + 2\pi)} \left[1 + \frac{10m_{\ell_i}^2}{3(m_c^*)^2} + \frac{60\alpha m_{\ell_i}^2}{\pi(m_c^*)^2} \right] \\ &= \frac{8\alpha}{3N_0(3\alpha + 2\pi)} \left[1 + \frac{(10\pi + 180\alpha)m_{\ell_i}^2}{3\pi(m_c^*)^2} \right]. \end{aligned} \quad (6.87)$$

The error terms in Eq. (6.85) remain unchanged, as this correction does not exhaust the terms of $O\{\alpha m_{\ell_i}^2/[N_0(m_c^*)^2]\}$. For further terms of this order, see Sec. 6:5.2.4.d.

6:5.2.4 1-loop weak force corrections

In the interest of brevity, this Section and those which follow specialise to the charged leptons only, denoted e_i in lieu of ℓ_i .

6:5.2.4.a Background photon interaction: When the fermion interacts with the background photon field, W boson loops may correct this interaction as shown in Fig. 6.20. As with the gluon loops in Sec. 6:5.2.3, the boson loops may be collapsed to numerical factors on the vertices of the corresponding leading-order diagram, and the background field terms contracted using spinor/sigma matrix identities.

Some caution is required with sign—first consider diagram (iii). Evaluating this diagram as a tensor network in the manner of Ref. [32–34], it is readily seen to be an absolute square and therefore yields a contribution to $m_{e_i}^2$ which is additive to the leading order term. Diagrams (i) and (ii) contain as a subdiagram a correction to the EM emission process which is usually associated with the opposite sign to direct emission by the fermion; however, compared with diagram (iii) they have also acquired an additional fermion propagator segment which offsets this, so they are also additive. Relative to the leading-order diagram, Figs. 6.20(i)-(ii) acquire factors

- $(10/3)(m_{e_i}^2/m_W^2)$, being the usual (absolute) factor for a W loop correction to an EM vertex,
- $1/2$ due to loss of exchange symmetry for the two background photon/composite fermion interactions. (Even with a composite fermion, an effective vertex is defined on summing over all possible preon/photon pairings and when identical, these effective vertices may still be exchanged for a symmetry factor of 2.)

Diagram (iii) retains the exchange symmetry, this time on the two copies of the photon operator at the vertex, so attracts the factor of $(10/3)(m_{e_i}^2/m_W^2)$ only. These three diagrams sum to yield a net factor

$$\frac{\alpha}{2\pi} \frac{20m_{e_i}^2}{3m_W^2}. \quad (6.88)$$

Finally, consider the Standard Model counterpart: The charged lepton Proper Self-Energy (PSE) terms in the Standard Model give rise to the W /neutrino loop shown in Fig. 6.20(iv). This gives rise to a term analogous to Fig. 6.20(iii), but has no counterpart to the symmetry factor associated with the pair of identical photon operators on the pseudovacuum interaction vertex. Its associated factor is therefore $(5/3)(m_{e_i}^2/m_W^2)$. The loop corrections to the mass vertex in the Standard Model appear in the denominator, corresponding to an overall multiplicative factor on the expression for $m_{e_i}^2$ of

$$\left(1 + \dots + \frac{\alpha}{2\pi} \frac{5m_{e_i}^2}{3m_W^2} + \dots\right)^{-1}. \quad (6.89)$$

This term in particular may conveniently be approximated by subtracting $[5/(6\pi)](m_{e_i}^2/m_W^2)$ from the other terms described above, with the introduced error being no worse than $O[\alpha^2 m_{e_i}^2/(m_c^*)^2]$. The net weight of the W boson loop corrections is thus

$$\frac{\alpha}{2\pi} \left(\frac{20m_{e_i}^2}{3m_W^2} - \frac{5m_{e_i}^2}{3m_W^2} \right) = \frac{5\alpha m_{e_i}^2}{2\pi m_W^2}. \quad (6.90)$$

Next considering the Z boson loops, these take form directly analogous to Fig. 6.17, and by arguments similar to the above are also seen to all be additive. Noting that the Z boson

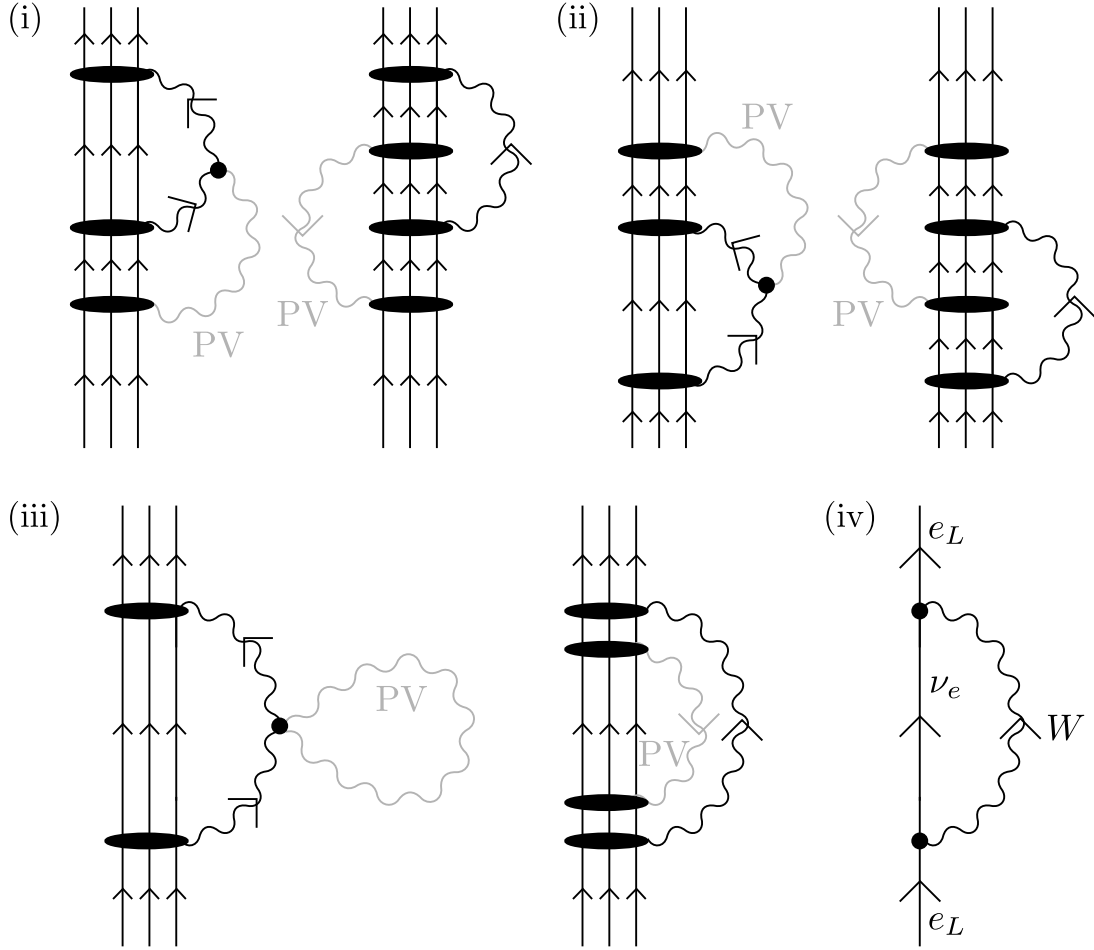


Figure 6.20: (i)-(iii) W boson loop corrections to the background vector boson interactions. Equivalent background photon and background gluon terms are grouped together; photon terms have no orientation arrows on the background boson lines. Note that background gluons do not couple to the W boson as the latter contains preons in a colour/anti-colour pair whose net gluon coupling therefore vanishes. (iv) Loop involving a W boson and a neutrino, appearing in the proper self-energy corrections of the Standard Model.

couples with opposite sign to e_L and e_R , and that mass vertices in the Standard Model reverse electron spin whereas the pseudovacuum couplings do not, the Z boson equivalents to the first two diagrams of Fig. 6.17(i) are therefore of opposite sign to their Standard Model counterparts and hence attract a factor of two, to first offset the Standard Model-derived term in the PSE, and then implement the actual correction. The third diagram of Fig. 6.17(i), on the other hand, has the same sign as its Standard Model counterpart and thus yields no net contribution to $m_{e_i}^2$. The net outcome from Z boson loops is a term with weight

$$-\frac{4f_Z\alpha m_{e_i}^2}{2\pi m_W^2} \quad (6.91)$$

where f_Z is as defined in Eq. (6.17). Overall, the weight of the weak boson corrections to the background photon interaction is seen to be

$$\frac{(5 - 4f_Z)\alpha m_{e_i}^2}{2\pi m_W^2}. \quad (6.92)$$

6:5.2.4.b Background gluon interactions: This term is readily obtained as the calculation proceeds similarly to Sec. 6:5.2.4.a, and it is found to be right at the threshold of relevance at the precision employed the current chapter.

As usual, start with the fermion interaction with a single off-diagonal background gluon channel and then use $GL(3, \mathbb{R})$ symmetry to multiply by nine for the contributions of the other eight gluons. For the gluon channels, the background gluons continue to couple to the fermion and not the looping W boson, so when evaluating the equivalents of Figs. 6.20(i)-(ii) there is no factor of $\frac{1}{2}$ for lost symmetry. The calculation is otherwise equivalent, for net W and Z corrections of

$$\frac{(25 - 12f_Z)\alpha m_{e_i}^2}{6\pi m_W^2}. \quad (6.93)$$

Note that deductions are once again made for the Standard Model counterpart terms, as corrections to mass vertices in the Standard Model correspond to corrections to both the photon and gluon terms in the present model.

6:5.2.4.c Background scalar boson interaction: These terms fall below the threshold of relevance, being smaller by a factor of $O(\alpha)$ than the unevaluated correction of $O(m_{e_i}^2/m_{\mathbf{H}}^2)$.

The cumulative expression for charged lepton mass incorporating weak boson corrections is therefore

$$\begin{aligned} m_{e_i}^2 = & \frac{f^2}{2} \left[k_i^{(e)} \right]^4 \omega_0^2 N_0^8 S_{18,147} \\ & \times \left\{ \left[1 + c_{\alpha/N_0} + \frac{90\alpha m_{e_i}^2}{\pi(m_c^*)^2} + \frac{(5 - 4f_Z)\alpha m_{e_i}^2}{2\pi m_W^2} \right] + \frac{5m_{e_i}^2}{(m_c^*)^2} \left[1 + \frac{90\alpha m_{e_i}^2}{\pi(m_c^*)^2} + \frac{(25 - 12f_Z)\alpha m_{e_i}^2}{6\pi m_W^2} \right] \right. \\ & \left. + \frac{40m_{e_i}^2}{3m_{\mathbf{H}}^2 \left[k_1^{(e)} N_0 \right]^4} \left(1 - \frac{2\alpha}{3\pi} \right) \left[1 + O(N_0^{-1}) + O\left(\frac{m_{e_i}^2}{m_{\mathbf{H}}^2} \right) + O(\alpha^2) \right] \right\} \\ & \times \left\{ 1 + O\left(\frac{\alpha}{N_0^2} \right) + O\left(\frac{\alpha^2}{N_0} \right) + O\left[\frac{\alpha m_{e_i}^2}{N_0(m_c^*)^2} \right] + \dots \right\} \end{aligned} \quad (6.94)$$

6:5.2.4.d $O(N_0^{-1})$ correction to weak loop corrections to background photon coupling: The next corrections to be considered are the $O(N_0^{-1})$ corrections arising due to FSF interchange when a W or Z boson loop corrects the coupling to the background photon field. The principle is similar to that of Sec. 6:5.2.3.b where a gluon loop corrected the background photon interaction, with the only numerical difference being the chance that preons at the participating W or Z vertex match the preons in the background photon field.

First consider the W loop and compare with the original weights in Sec. 6:5.2.2.a. If the first preon considered is the ψ^2 preon, this has a 50% chance of matching the A -charge of the relevant preon in the background photon, which is the same as in Sec. 6:5.2.2.a. However, the second preon is of type ψ^3 which does not appear in the background photon field at all. For a W loop the correction is therefore reduced by a factor of $\frac{1}{2}$. Similarly, for a Z loop each preon has a 50% chance of being of type ψ^3 at the Z vertex and a 50% chance of being in $\{\psi^1, \psi^2\}$. Thus the correction to the Z boson loop is also reduced by a factor of two,

$$\frac{(5 - 4f_Z)\alpha m_{e_i}^2}{2\pi m_W^2} \longrightarrow \frac{(5 - 4f_Z)\alpha m_{e_i}^2}{2\pi m_W^2} \left[1 + \frac{c_{\alpha/N_0}}{2} + O(N_0^{-2}) \right]. \quad (6.95)$$

This may be conveniently realised by redefining c_{α/N_0} as

$$c_{\alpha/N_0} := \frac{8\alpha}{3N_0(3\alpha + 2\pi)} \left[1 + \frac{(10\pi + 180\alpha)m_{e_i}^2}{3\pi(m_c^*)^2} + \frac{(5 - 4f_Z)\alpha m_{e_i}^2}{4\pi m_W^2} \right]. \quad (6.96)$$

This exhausts the corrections of $O\{\alpha m_{e_i}^2/[N_0(m_c^*)^2]\}$, with Eq. (6.94) becoming

$$\begin{aligned} m_{e_i}^2 = & \frac{f^2}{2} \left[k_i^{(e)} \right]^4 \omega_0^2 N_0^8 S_{18,147} \\ & \times \left\{ \left[1 + c_{\alpha/N_0} + \frac{90\alpha m_{e_i}^2}{\pi(m_c^*)^2} + \frac{(5 - 4f_Z)\alpha m_{e_i}^2}{2\pi m_W^2} \right] + \frac{5m_{e_i}^2}{(m_c^*)^2} \left[1 + \frac{90\alpha m_{e_i}^2}{\pi(m_c^*)^2} + \frac{(25 - 12f_Z)\alpha m_{e_i}^2}{6\pi m_W^2} \right] \right. \\ & \left. + \frac{40m_{e_i}^2}{3m_{\mathbf{H}}^2 \left[k_1^{(e)} N_0 \right]^4} \left(1 - \frac{2\alpha}{3\pi} \right) \left[1 + O(N_0^{-1}) + O\left(\frac{m_{e_i}^2}{m_{\mathbf{H}}^2} \right) + O(\alpha^2) \right] \right\} \\ & \times \left\{ 1 + O\left(\frac{\alpha}{N_0^2} \right) + O\left(\frac{\alpha^2}{N_0} \right) + O\left[\frac{\alpha m_{e_i}^4}{N_0(m_c^*)^4} \right] + \dots \right\}. \end{aligned} \quad (6.97)$$

Note that terms of $O\{\alpha^2 m_{e_i}^2/[N_0(m_c^*)^2]\}$ and $O\{\alpha m_{e_i}^2/[N_0^2(m_c^*)^2]\}$ also exist but are small compared with those of $O(\alpha^2/N_0)$ and $O(\alpha/N_0^2)$ already appearing in Eq. (6.97). The term $O\{\alpha m_{e_i}^4/[N_0(m_c^*)^4]\}$ arises from $O(N_0^{-1})$ corrections to the gluon loop correction to the gluon mass interaction.

6:5.2.5 1-loop scalar corrections

The largest of these terms are the scalar loop corrections to the background photon interaction. These are of comparable magnitude to the photon loop corrections to the background scalar interaction. Leaving these terms unevaluated replaces the factor of $[1 - 2\alpha/(3\pi)]$ on the scalar interaction term with an unspecified correction of $[1 + O(\alpha)]$.

6:5.2.6 2-loop EM corrections

By the same arguments as Sec. 6:5.2.1, the massless $O(\alpha^2)$ corrections are identical for the background photon and gluon interactions and coincide with their Standard Model counterparts.

The massless 2-loop EM corrections therefore yield at most a correction of $O(\alpha^2)$ to the scalar term, which is smaller than the $O(\alpha)$ term from Sec. 6:5.2.5.

The next term which may differentially affect the photon and gluon terms, and which exhibits dependency on particle generation, is a two-loop massive contribution. All relevant masses are of comparable magnitude, $m_c^2 \sim m_W^2 \sim m_Z^2 \sim m_H^2$, and gluon terms have thus far outweighed weak sector terms, therefore write this correction in terms of the gluon mass. It is also useful to pull all higher-order corrections out into the final term, and the cumulative expression for charged lepton mass incorporating all loop corrections evaluated in this paper is thus

$$\begin{aligned}
m_{e_i}^2 = & \frac{f^2}{2} \left[k_i^{(e)} \right]^4 \omega_0^2 N_0^8 S_{18,147} \\
& \times \left\{ \left[1 + c_{\alpha/N_0} + \frac{90\alpha m_{e_i}^2}{\pi(m_c^*)^2} + \frac{(5-4f_Z)\alpha m_{e_i}^2}{2\pi m_W^2} \right] \right. \\
& \quad \left. + \frac{5m_{e_i}^2}{(m_c^*)^2} \left[1 + \frac{90\alpha m_{e_i}^2}{\pi(m_c^*)^2} + \frac{(25-12f_Z)\alpha m_{e_i}^2}{6\pi m_W^2} \right] + \frac{40m_{e_i}^2}{3m_H^2 \left[k_1^{(e)} N_0 \right]^4} \right\} \\
& \times \left(1 + O\left(\frac{\alpha}{N_0^2}\right) + O\left(\frac{\alpha^2}{N_0}\right) + O\left[\frac{\alpha m_{e_i}^4}{N_0(m_c^*)^4}\right] + O\left[\frac{\alpha^2 m_{e_i}^2}{(m_c^*)^2}\right] \right. \\
& \quad \left. + O\left\{\frac{\alpha m_{e_i}^2}{m_H^2 \left[k_1^{(e)} N_0 \right]^4}\right\} + O\left\{\frac{m_{e_i}^2}{m_H^2 \left[k_1^{(e)} \right]^4 N_0^5}\right\} + O\left\{\frac{m_{e_i}^4}{m_H^4 \left[k_1^{(e)} N_0 \right]^4}\right\} \right).
\end{aligned} \tag{6.98}$$

6:5.3 Corrections to the lepton mass angle

6:5.3.1 Origin of corrections

There remains one more substantial correction to evaluate. The leading-order contributions to the lepton mass vertices and the preon colour mixing matrix were evaluated in Sec. 6:5.1. Loop corrections to the mass vertices were evaluated in Sec. 6:5.2. It remains now to determine how these loop corrections impact the preon colour mixing matrix K_ℓ .

When this matrix was constructed in Sec. 6:5.1.1 there was an implicit assumption that all eigenvectors experience equal couplings to the background fields. The eigenvalues of matrix K_ℓ then imparted different masses to the three eigenvectors, corresponding to the three members of a given fermion family. However, from Eq. (6.98) it is apparent that the higher-order corrections to the pseudovacuum coupling themselves depend on particle mass, leading to differential augmentation of the three eigenvectors (mass channels). As these eigenvectors correspond to different vectors in colour space, imparting different relative phases to the gluon couplings between the preon triplets, a change in the relative pseudovacuum couplings for the different eigenvectors will impact the colour mixing process. Conveniently, it proves possible to represent this modification by a correction to the value of θ_ℓ .

Recognising that the fermion masses vary between different particle families, it is necessary to specify the family for which the corrected value of θ_ℓ is being evaluated. This is done by replacing ℓ with a member of the particle family in question, e.g. e , μ , or τ for the electron family.

6:5.3.2 Preamble

To obtain a corrected expression for the electron mass angle at some energy scale \mathcal{E} , first recall that the eigenvectors $\{v_i | i \in \{1, 2, 3\}\}$ of K_ℓ (6.59–6.61) are independent of the value of θ_ℓ . For the electron family, matrix K_ℓ therefore always admits the decomposition

$$K_\ell = \sum_{i=1}^3 k_i^{(\ell)} v_i v_i^\dagger \quad (6.99)$$

where

$$v_1 v_1^\dagger = \frac{1}{3} \begin{pmatrix} 1 & 1 & 1 \\ 1 & 1 & 1 \\ 1 & 1 & 1 \end{pmatrix} \quad (6.100)$$

$$v_2 v_2^\dagger = \frac{1}{3} \begin{pmatrix} 1 & e^{\frac{2\pi i}{3}} & e^{-\frac{2\pi i}{3}} \\ e^{-\frac{2\pi i}{3}} & 1 & e^{\frac{2\pi i}{3}} \\ e^{\frac{2\pi i}{3}} & e^{-\frac{2\pi i}{3}} & 1 \end{pmatrix} \quad (6.101)$$

$$v_3 v_3^\dagger = \frac{1}{3} \begin{pmatrix} 1 & e^{-\frac{2\pi i}{3}} & e^{\frac{2\pi i}{3}} \\ e^{\frac{2\pi i}{3}} & 1 & e^{-\frac{2\pi i}{3}} \\ e^{-\frac{2\pi i}{3}} & e^{\frac{2\pi i}{3}} & 1 \end{pmatrix}. \quad (6.102)$$

Then note that the imaginary components of the off-diagonal matrix elements arise from components 2 and 3 only (6.101–6.102), with an increase in component 2 (corresponding, for charged leptons, to the muon) making a positive-signed contribution to the imaginary component in $[K_\ell]_{12}$, $[K_\ell]_{23}$, and $[K_\ell]_{31}$. Examining the vectors on the complex plane associated with $\exp(\theta_e) = \exp(-3\pi i/4)$ and a small correction proportional to $\exp(2\pi i/3)$, it is seen that the action of this correction is to increase the magnitude of θ_ℓ (making it more negative). Similarly, an isolated increase in component 3 (the tau) decreases the magnitude of θ_ℓ . Finally, an isolated increase in component 1 (the electron) affects only the real component of an entry such as $[K_\ell]_{12}$ and thus when $[K_\ell]_{12}$ is complex, once again affects the value of θ_ℓ . When θ_ℓ is no longer fixed to be $-3\pi/4$, it is labelled by the relevant particle family, e.g. θ_e , and it becomes necessary to specify K_ℓ as $K_\ell(\theta_\ell)$ for some family ℓ .

Next, recognise that it is convenient to write the mass interaction as a leading-order term derived from the background photon field (and associated with colour mixing matrix K_ℓ as derived Sec. 6:5.1.1) plus corrections. For the charged lepton masses, and expanding c_{α/N_0} as per Eq. (6.96), this corresponds to rewriting Eq. (6.98) as

$$m_{e_i}^2 = \frac{f^2}{2} \left[k_i^{(e)} \right]^4 \omega_0^2 N_0^8 S_{18,147} [1 + \Delta_e(m_{e_i})] [1 + \mathcal{O}_e(m_{e_i})] \quad (6.103)$$

$$= \left[m_{e_i}^{(0)} \right]^2 [1 + \Delta_e(m_{e_i})] [1 + \mathcal{O}_e(m_{e_i})] \quad (6.104)$$

$$\begin{aligned}\Delta_e(m_{e_i}) = & \frac{8\alpha}{3N_0(3\alpha + 2\pi)} \left[1 + \frac{(10\pi + 180\alpha)m_{e_i}^2}{3\pi(m_c^*)^2} + \frac{(5 - 4f_Z)\alpha m_{e_i}^2}{4\pi m_W^2} \right] + \frac{90\alpha m_{e_i}^2}{\pi(m_c^*)^2} \\ & + \frac{(5 - 4f_Z)\alpha m_{e_i}^2}{2\pi m_W^2} + \frac{5m_{e_i}^2}{(m_c^*)^2} \left[1 + \frac{90\alpha m_{e_i}^2}{\pi(m_c^*)^2} + \frac{(25 - 12f_Z)\alpha m_{e_i}^2}{6\pi m_W^2} \right] \\ & + \frac{40m_{e_i}^2}{3m_{\mathbf{H}}^2 [k_1^{(e)} N_0]^4}\end{aligned}\quad (6.105)$$

$$\begin{aligned}\mathcal{O}_e(m_{e_i}) = & \mathcal{O}\left(\frac{\alpha}{N_0^2}\right) + \mathcal{O}\left(\frac{\alpha^2}{N_0}\right) + \mathcal{O}\left[\frac{\alpha m_{e_i}^4}{N_0(m_c^*)^4}\right] + \mathcal{O}\left[\frac{\alpha^2 m_{e_i}^2}{(m_c^*)^2}\right] \\ & + \mathcal{O}\left\{\frac{\alpha m_{e_i}^2}{m_{\mathbf{H}}^2 [k_1^{(e)} N_0]^4}\right\} + \mathcal{O}\left\{\frac{m_{e_i}^2}{m_{\mathbf{H}}^2 [k_1^{(e)}]^4 N_0^5}\right\} + \mathcal{O}\left\{\frac{m_{e_i}^4}{m_{\mathbf{H}}^4 [k_1^{(e)} N_0]^4}\right\}\end{aligned}\quad (6.106)$$

where $\{e_1, e_2, e_3\} = \{e, \mu, \tau\}$ and the subscript e on Δ_e indicates the family $\{e, \mu, \tau\}$ rather than the electron in particular. As can be readily seen from Eq. (6.105), the amplitudes of these corrections to particle mass are dependent upon the squared lepton masses $m_{e_i}^2$, with the largest corrections being those associated with the tau. The charged lepton mixing matrix $K_e(\theta_e)$ is implicitly dependent on the same corrections, as changes to the particle mass ratios affect colour mixing, and hence the co-ordinate transformation required to restore colour neutrality. Allowing the corrections to augment mass and also to adjust $K_e(\theta_e)$ is not double-counting, as the mass correction *induces* the corresponding adjustment in the co-ordinate transformation implemented by $K_e(\theta_e)$. The co-ordinate transformation does, however, have an effect on the magnitude of the mass correction term, and this effect must be compensated for—see Sec. 6:5.3.5.

Note that Δ_e and \mathcal{O}_e are also dependent on $k_i^{(e)}$ which in turn is dependent on $K_e(\theta_e)$ which is dependent on θ_e which is dependent on Δ_e which is dependent on m_{e_i} . No attempt is made to express full dependencies of parameters save through the equations defining them, and going forward, notation such as $\Delta_e(m_{e_i})$ or $\Delta_e(\mathcal{E})$ is merely a heuristic to remind the reader of a parameter's dependency on some stated energy scale. Similarly, for $K_e(\theta_e)$, dependency on θ_e is shown to clearly distinguish the mass-dependent $K_e(\theta_e)$ from the mass-independent K_ℓ .

6:5.3.3 First-order correction to K_ℓ^4 from the tau channel

To understand how these corrections to lepton masses affect the matrices K_ℓ , consider the leading order term $[m_{e_i}^{(0)}]^2$ which arises from the set of nine diagrams described in the caption of Fig. 6.15, and may be thought of as the action of an operator $[\hat{m}^{(0)}]^2$ on the preon triplet comprising a sum over nine terms. The action of this operator on the colour space of the preon triplet breaks colour neutrality, but this is then corrected by application term-by-term of four matrices (or operators) K_ℓ , heuristically K_ℓ^4 (with implicit action of each operator on the appropriate Hilbert space as per the appropriate diagram of Fig. 6.15), such that $K_\ell^4 [\hat{m}^{(0)}]^2$ as a whole leaves the colour of the preon triplet unchanged up to a sum over cycles $r \rightarrow g \rightarrow b \rightarrow r$.

As seen in Eq. (6.104), higher-order corrections enhance the action of $[\hat{m}^{(0)}]^2$ on eigenstate e_i by a factor of $[1 + \Delta_e(m_{e_i})]$. If colour neutrality is to be conserved, then for colour-changing diagrams [including those which would mix colours under some global $SU(3)_C$ transformation, such as interaction with the diagonal gluons of $SU(3)_C$] there must be an equivalent enhancement of the matrices K_ℓ ,

$$K_\ell \rightarrow K_e(\theta_e) \quad (6.107)$$

[where dependence on $\theta_e(\{m_{e_i}|i \in \{1, 2, 3\}\})$ is assumed but will subsequently be shown] such

that the action of $[K_e(\theta_e)]^4$ on lepton e_i is equivalent to the action of

$$K_\ell^4 [1 + \Delta_e(m_{e_i})]. \quad (6.108)$$

As the largest such correction arises from the most massive particle, begin by considering e_3 , the tau. First note that introduction of a mass dependency for the matrices $K_e(\theta_e)$ implies that the bosons associated with the colour-neutrality-preserving co-ordinate transformation are no longer parameterless, and may therefore carry momentum in the higher-order diagrams. They must therefore be represented explicitly as per Fig. 6.21. By construction these bosons only interact at the boundary of the transformed co-ordinate patch, and are consequently both foreground and massless. Let the diagrams of Fig. 6.21(i)-(iii), having two co-ordinate transformation bosons, be termed “first order”, and for now ignore diagrams having four co-ordinate transformation bosons (“second order”) or more.

Regarding the two co-ordinate transformation bosons of Fig. 6.21(i)-(ii), their vertex factors are incorporated into the leading order matrix K_ℓ . Integration over their degrees of freedom then yields a factor per diagram of $(4\pi)^{-2}$ [not $(2\pi)^{-2}$, as they are not self-dual and thus their loop is less symmetric than that for the photon]. Note that Fig. 6.21(ii) counts as a loop diagram as there are implicit gluon-mediated couplings between the preonic constituents of the lepton, which are massless over the length-scale involved $[O(\mathcal{L}_0)]$ and complete closure of the loop.

Recognising that the leading term calculation does not perform any net colour mixing beyond the unmodified, constant factors of K_ℓ^4 , the resulting factor of $2 \cdot (4\pi)^{-2}$ does not appear in the leading term calculation. Its effect is seen only on the diagrams in $\Delta_e(m_\tau)$, where it represents variations in colour mixing relative to K_ℓ^4 , and multiplies any correction to K_ℓ^4 by a factor of $2 \cdot (4\pi)^{-2}$.

Next, recognise that the components of each matrix $K_e(\theta_e)$ which perform rotations on $SU(3)_C$ are composed from a weighted superposition of some set of representation matrices λ'_i [possibly, but not necessarily the rescaled Gell-Mann matrices λ_i in Eqs. (2.39–2.40)], of which there are eight. (The ninth basis element is associated with the N boson and the trivial representation, but does not change colour and is independent of θ_e so is not yet of interest here.) An appropriate choice of basis permits every off-diagonal element in $K_e(\theta_e)$ to be associated with a single basis element {for example, in K_ℓ , entry $[K_\ell]_{12}$ is associated with $(\lambda_1 + \lambda_2)/\sqrt{2}$ }. A change to θ_e may correspond to a change in choice of representation matrices [e.g. to $\lambda_1 \cos \beta + \lambda_2 \sin \beta$ for some angle β] but this ability to construct a single basis element corresponding to a particular entry in $K_e(\theta_e)$ persists for any reasonably small perturbation around $\theta_e = -3\pi/4$.

Now consider a preon in Fig. 6.15(i) or (ii) which has two matrices $K_e(\theta_e)$ acting on it, and recognise that if the portion of $K_e(\theta_e)$ which performs colour transformations is decomposed into these eight components, then if a given component λ'_i acts on the preon in the lower position, then its conjugate must act in the upper position for the foreground preon colour to be left invariant overall.⁴ The action of the *pair* of matrices $K_e(\theta_e)$ on this boson consequently admits decomposition into eight channels, enumerated by the family of orthogonal representation matrices λ'_i appearing at the lower matrix $K_e(\theta_e)$.

Next, consider the remaining two matrices $K_e(\theta_e)$ when these are not on the same preon. In this situation the representation matrices present will be conjugate up to a colour cycle

⁴Note that if one diagram family as per Fig. 6.15 can be made to have no net effect on colour, then all paired background bosons have no net effect on colour. Further, as unpaired bosons (as well as being exceedingly rare) have on average no net effect on colour, these may also be grouped into clusters having zero net colour effect overall, and an analogous co-ordinate transformation performed such that their effect on colour vanishes instant-by-instant as well as on average, with the associated bosons vanishing over distances large compared with \mathcal{L}_0 . Thus no error is made in requiring that colour is left unchanged on a per-diagram basis. Also note that once the mechanism for corrections to θ_e is fully elucidated, the co-ordinate transformations arising from the unpaired bosons yield no systematic effect on θ_e and thus their effect may be ignored over macroscopic scales.

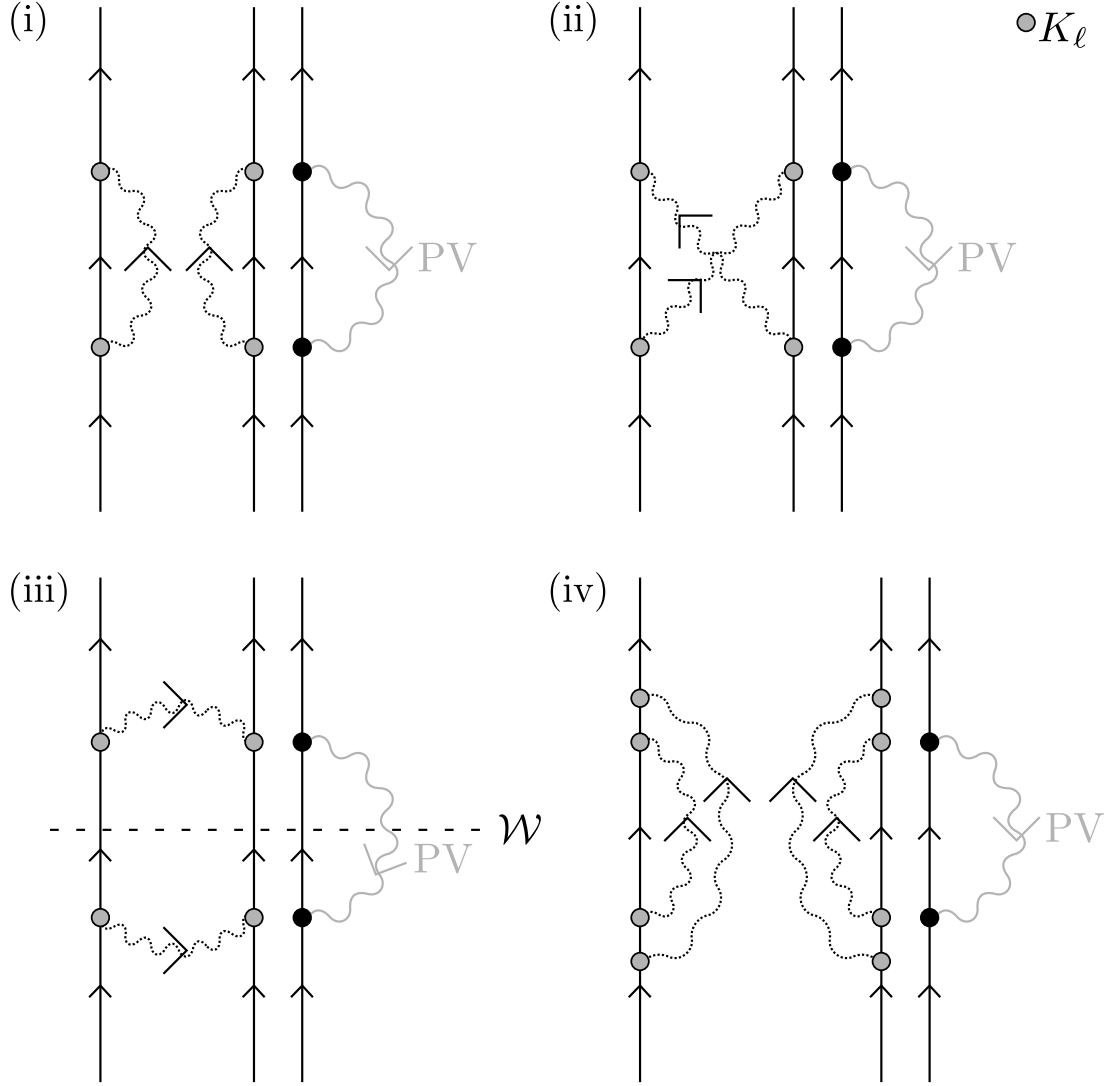


Figure 6.21: When the matrices K_ℓ are replaced by $K_e(\theta_e)$, which depends on energy scale, this induces a pair of gauge bosons which may in principle connect the four matrices $K_e(\theta_e)$ in any of three ways [shown for Fig. 6.15(i) in diagrams (i)-(iii)]. In diagram (i), the bosons each connect to two matrices $K_e(\theta_e)$ on the same preon and thus enact a co-ordinate transformation followed by its inverse. In diagram (ii), where the bosons are crossed, there may be a permutation of the preon colour labels but overall colour neutrality is nevertheless conserved. Diagram (iii) contrasts with the other two in that the boson trajectories are orthogonal to the preon trajectories. For a worldsheet such as that shown (labelled \mathcal{W}), which is equidistant between the boson vertices and isochronous in the rest frame of the particle, the total number of oriented crossings for each of the bosons in diagram (iii) is zero regardless of the trajectory followed. This implies that these bosons do not describe a co-ordinate transformation extant at this worldsheet, and thus this diagram does not contribute to $K_e(\theta_e)$. Diagram (iv) is an example second-order diagram having four bosons arising from the co-ordinate transformation and spanning from the lower to the upper collection of matrices $K_e(\theta_e)$. This diagram represents the consecutive application of two (possibly different) transformations in $SU(3)_C$ to each preon.

$r \rightarrow g \rightarrow b \rightarrow r$ or its inverse. As the only colour-changing bosons in the pseudovacuum are gluons, and $SU(3)_C$ symmetry is preserved on the gluon sector and in the definition of the charged lepton, evaluation of any diagram where the entries from $K_e(\theta_e)$ are offset by a colour cycle is necessarily equivalent to evaluation of a diagram where they are not offset. It is therefore acceptable to evaluate entries in $K_e(\theta_e)$ under the assumption that all matrices $K_e(\theta_e)$ appear in conjugate pairs. In addition, in all diagrams all representation matrices are multiplied by their conjugate (whether independently or in conjunction with the representation matrices associated with the bosonic vertices) and thus the terms arising from all 64 channels contributing to the actions of the matrices $K_e(\theta_e)$ on the preon triplet are additive on the same (net trivial) charge sector, and therefore summed. By $SU(3)_C$ symmetry, each channel will contribute equally to the overall correction to the leading order diagram.

Now consider the single channel associated with a specific off-diagonal entry in at least one lower matrix $K_e(\theta_e)$. For definiteness, let this be $[K_e(\theta_e)]_{12}$. As there are, overall, 64 contributing channels, each channel must produce a net correction of $\Delta_e(m_\tau)/64$. However, the synthetic bosons multiply all correction diagrams by a factor of $2 \cdot (4\pi)^{-2}$ and thus $[K_e(\theta_e)]_{12}$ and $[K_e(\theta_e)]_{21}$ must satisfy

$$\begin{aligned} [K_e(\theta_e)]_{12}^2 [K_e(\theta_e)]_{21}^2 &= [K_\ell]_{12}^2 [K_\ell]_{21}^2 \left[1 + \frac{(4\pi)^2}{2 \cdot 64} \Delta_e(m_\tau) \right] \\ &= [K_\ell]_{12}^2 [K_\ell]_{21}^2 \left[1 + \frac{\pi^2}{8} \Delta_e(m_\tau) \right] \end{aligned} \quad (6.109)$$

$$\Rightarrow [K_e(\theta_e)]_{12} [K_e(\theta_e)]_{21} = [K_\ell]_{12} [K_\ell]_{21} \sqrt{1 + \frac{\pi^2}{8} \Delta_e(m_\tau)}. \quad (6.110)$$

Noting that $[K_\ell]_{12} = [K_\ell]_{21}^\dagger$, it is convenient to write

$$\delta_e(n) = \sqrt{1 + \frac{\pi^2 n}{8}} - 1 \quad (6.111)$$

$$[1 + \delta_e(n)] = [1 + i\sqrt{\delta_e(n)}][1 - i\sqrt{\delta_e(n)}] \quad (6.112)$$

and assign the corresponding off-diagonal entries of $K_e(\theta_e)$ to be

$$\begin{aligned} [K_e(\theta_e)]_{12} &= [K_\ell]_{12} [1 \pm i\sqrt{\delta_e[\Delta_e(m_\tau)]}] \\ [K_e(\theta_e)]_{21} &= [K_\ell]_{21} [1 \mp i\sqrt{\delta_e[\Delta_e(m_\tau)]}], \end{aligned} \quad (6.113)$$

preserving the hermiticity of $K_e(\theta_e)$.

By the factor of $\pm i$ on the correction term, this correction is orthogonal to the leading-order value of $[K_\ell]_{12}$. As this orthogonality is independent of the value of θ_e , this implies that for a non-infinitesimal correction, $[K_\ell]_{12} \sqrt{\delta_e[\Delta_e(m_\tau)]}$ is the length of an arc. The corresponding correction to θ_ℓ is

$$\theta_\ell \rightarrow \theta_\ell \pm \sqrt{\delta_e[\Delta_e(m_\tau)]}. \quad (6.114)$$

In the vicinity of $\theta_\ell = -3\pi/4$, this may be rewritten

$$\theta_\ell \rightarrow \theta_\ell \left\{ 1 \mp \frac{4\sqrt{\delta_e[\Delta_e(m_\tau)]}}{3\pi} \right\}. \quad (6.115)$$

As per the discussion under Eqs. (6.100–6.102), the tau correction is known to decrease the magnitude of θ_ℓ , giving

$$[K_e(\theta_e)]_{12} = \frac{e^{i\theta_e}}{\sqrt{2}} = [K_\ell]_{12} \left\{ 1 + i\sqrt{\delta_e[\Delta_e(m_\tau)]} + \dots \right\} \quad (6.116)$$

$$\theta_e = -\frac{3\pi}{4} \left\{ 1 - \frac{4\sqrt{\delta_e[\Delta_e(m_\tau)]}}{3\pi} \right\} \quad (6.117)$$

where the uncorrected value of θ_ℓ has been written explicitly as $-\frac{3\pi}{4}$.

6:5.3.4 Second-order correction to K_ℓ^4 from the tau channel

The first-order correction to K_ℓ^4 is applied to all diagrams which modify the colour mixing process, i.e. all diagrams contributing to Δ_e . For these diagrams, this correction is equivalent by construction to enacting the transformation

$$K_\ell^4 \rightarrow K_\ell^4 [1 + \Delta_e(m_\tau)], \quad (6.118)$$

resulting in a relative increase in these diagrams' contribution to particle mass equivalent to

$$\Delta_e(m_\tau) \rightarrow \Delta_e(m_\tau)[1 + \Delta_e(m_\tau)]. \quad (6.119)$$

Any species-dependent increase in mass affects colour mixing in precisely the way described above for correction $\Delta_e(m_\tau)$, regardless of whether this increase is diagrammatic (as in the first-order component) or gauge-dependent and derived from a change to θ_e (as here). This correction therefore attracts a further smaller correction to K_ℓ , enhancing the first-order correction calculated above. While this series may be continued indefinitely, it is convenient to truncate at second order for a precision of $O[\Delta_e^2(m_\tau)]$, ensuring that the error in numerical calculations is dominated by the error in $\Delta_e(m_\tau)$ itself, and not in the evaluation of $\delta_e[\Delta_e(m_\tau)]$.

To implement the corresponding adjustment to $K_e(\theta_e)$, let the $O[\Delta_e^2(m_\tau)]$ term be compensated by the second-order diagrams of which Fig. 6.21(iv) is a prototype. In these diagrams, a first-order correction [Fig. 6.21(i)-(ii)] is supplemented by a further, smaller correction.

For Figs. 6.21(i)-(ii) there is a symmetry factor of two corresponding to crossing or not crossing the bosons. For Fig. 6.21(iv),

- the inner pair may be crossed (factor of two),
- the outer pair may be crossed (factor of two),
- the inner and outer bosons on the left may be exchanged (factor of two), and
- the inner and outer bosons on the right may be exchanged (factor of two).

The factor of $2 \cdot (4\pi)^{-2}$ associated with the set of diagrams Figs. 6.21(i)-(ii) becomes a factor of $16 \cdot (4\pi)^{-4}$ for the set of diagrams derived from Fig. 6.21(iv). The expression for $[K_e(\theta_e)]_{12}^2 [K_e(\theta_e)]_{21}^2$ then becomes

$$\begin{aligned} & [K_e(\theta_e)]_{12}^2 [K_e(\theta_e)]_{21}^2 \\ &= [K_\ell]_{12}^2 [K_\ell]_{21}^2 \left[1 + \frac{(4\pi)^2}{2 \cdot 64} \Delta_e(m_\tau) + \frac{(4\pi)^4}{16 \cdot 64^2} \Delta_e^2(m_\tau) \right] \\ &= [K_\ell]_{12}^2 [K_\ell]_{21}^2 \left\{ 1 + \frac{\pi^2}{8} \Delta_e(m_\tau) \left[1 + \frac{\pi^2}{32} \Delta_e(m_\tau) \right] \right\} \end{aligned} \quad (6.120)$$

for a redefinition of $\delta_e(n)$ in Eq. (6.117) to

$$\delta_e(n) = \sqrt{1 + \frac{\pi^2 n}{8} \left(1 + \frac{\pi^2 n}{32}\right)} - 1. \quad (6.121)$$

The next order term extends $\delta_e(n)$ to

$$\delta_e(n) = \sqrt{1 + \frac{\pi^2 n}{8} \left[1 + \frac{\pi^2 n}{32} \left(1 + \frac{\pi^2 n}{72}\right)\right]} - 1 \quad (6.122)$$

but its effects are verified to fall below the threshold of relevance for the present paper when evaluated in Sec. 6:6.3.

6:5.3.5 Reparameterisation of θ_e

The above transformations have maintained colour neutrality, but at the expense of introducing an additional multiplicative factor of $[1 + \Delta_e(m_\tau)]$ on all diagrams which affect the colour mixing process [including all diagrams in $\Delta_e(m_\tau)$, by virtue of matrices K_ℓ], as per Eq. (6.108). In effect this is equivalent to replacing any instance of $\Delta_e(m_\tau)$ with $\Delta_e(m_\tau) \cdot [1 + \Delta_e(m_\tau)]$. This replacement, in turn, induces further corrections to K_ℓ , which then induces further corrections to the effective value of $\Delta_e(m_\tau)$, and so forth. The largest correction to $\Delta_e(m_\tau)$ arising from this effect is of order $m_\tau^4/(m_c^*)^4$, which is large compared with $\mathcal{O}_e(m_\tau)$. It is therefore necessary to evaluate how this series in $\Delta_e(m_\tau)$ affects m_τ^2 , but this will be done indirectly.

First, note that convergence of the series in $\Delta_e(m_\tau)$ yields a unique value of m_τ^2 with associated unique values of $\theta_e(\Delta_e)$ and $\Delta_e(m_\tau)$, and is identified by consistency of equations in $\Delta_e(m_\tau)$ (6.105), $\theta_e(\Delta_e)$ (6.117), and $k_3^{(e)}$ (6.62) [which is now a function of $\theta_e(\Delta_e)$]:

$$m_\tau^2 = \frac{f^2}{2} \left[k_3^{(e)}(\theta_e) \right]^4 \omega_0^2 N_0^8 S_{18,147} [1 + \Delta_e(m_\tau) + \dots] [1 + \mathcal{O}_e(m_\tau)] \quad (6.123)$$

$$\begin{aligned} \Delta_e(m_\tau) = & \frac{8\alpha}{3N_0(3\alpha + 2\pi)} \left[1 + \frac{(10\pi + 180\alpha)m_\tau^2}{3\pi(m_c^*)^2} + \frac{(5 - 4f_Z)\alpha m_\tau^2}{4\pi m_W^2} \right] + \frac{90\alpha m_\tau^2}{\pi(m_c^*)^2} \\ & + \frac{(5 - 4f_Z)\alpha m_\tau^2}{2\pi m_W^2} + \frac{5m_\tau^2}{(m_c^*)^2} \left[1 + \frac{90\alpha m_\tau^2}{\pi(m_c^*)^2} + \frac{(25 - 12f_Z)\alpha m_\tau^2}{6\pi m_W^2} \right] \\ & + \frac{40m_\tau^2}{3m_H^2 \left[k_1^{(e)} N_0 \right]^4} \end{aligned} \quad (6.124)$$

$$\theta_e = -\frac{3\pi}{4} \left\{ 1 - \frac{4\sqrt{\delta_e[\Delta_e(m_\tau)]}}{3\pi} \right\} \quad (6.117)$$

$$k_n^{(e)} = 1 + \sqrt{2} \cos \left[\theta_e - \frac{2\pi(n-1)}{3} \right]. \quad (6.125)$$

Given the value of m_τ and thus $\Delta_e(m_\tau)$ for which these equations are mutually consistent, now reparameterise by writing

$$\Delta_e(m_\tau) = \Delta'_e(m_\tau)[1 - \Delta'_e(m_\tau)] \quad (6.126)$$

such that prior to iterating, the tau mass equation is

$$\begin{aligned} m_\tau^2 = & \frac{f^2}{2} \left[k_i^{(e)}(\theta_e) \right]^4 \omega_0^2 N_0^8 S_{18,147} \\ & \times \{1 + \Delta'_e(m_\tau)[1 - \Delta'_e(m_\tau)]\} [1 + \mathcal{O}_e(m_\tau)]. \end{aligned} \quad (6.127)$$

On implementing the associated correction to θ_e as before, all occurrences of $\Delta_e(m_\tau)$ are incremented to $\Delta_e(m_\tau)[1 + \Delta_e(m_\tau)]$ and thus the factor of

$$\{1 + \Delta'_e(m_\tau)[1 - \Delta'_e(m_\tau)]\} \quad (6.128)$$

in m_τ^2 becomes

$$\begin{aligned} & 1 + \Delta'_e(m_\tau)[1 - \Delta'_e(m_\tau)]\{1 + \Delta'_e(m_\tau)[1 - \Delta'_e(m_\tau)]\} \\ &= 1 + \Delta'_e(m_\tau) + \mathcal{O}\{[\Delta'_e(m_\tau)]^3\}. \end{aligned} \quad (6.129)$$

Under this reparameterisation there is no $\mathcal{O}\{[\Delta'_e(m_\tau)]^2\}$ term in m_τ^2 .

But what, then, does $\theta_e(\Delta_e)$ look like when written in terms of Δ'_e ? Observe that $\theta_e(\Delta'_e)$ yields a correction to Δ_e in Eq. (6.123) of

$$\{1 + \Delta'_e(m_\tau)[1 - \Delta'_e(m_\tau)]\} \quad (6.128)$$

in place of $[1 + \Delta_e(m_\tau)]$, consistent with Eq. (6.126). However, this correction to Eq. (6.123) arises from the application of four $K_e(\theta_e)$ matrices as per Fig. 6.15, which may be thought of as two channels each containing two $K_e(\theta_e)$ matrices. In Fig. 6.15 this may nominally be identified as one channel per participating preon, though in practice an arbitrary basis may be chosen across these channels and this anyway undergoes mixing during propagation due to the preon binding couplings (not shown). Indeed, because of this mixing, Fig. 6.15 may likewise be considered to contain two such channels. In each case, the correction must be factorised across these two channels.

Within each of these channels are a further nine subchannels corresponding to the nine entries in $K_e(\theta_e)$ identified with the nine basis elements of $\text{GL}(3, \mathbb{R})$. In contrast, the calculation of θ_e is performed on a single channel of $\text{SU}(3)_C$, and thus on a single channel of $\text{GL}(3, \mathbb{R})$. It therefore follows that the calculation of θ_e must be performed with respect to only one ninth of the correction to $\Delta'_e(m_\tau)$, so as to deliver one ninth of the channel's total correction in each subchannel.

The net effect of both of these considerations is to define

$$\theta_e(\Delta'_e) = -\frac{3\pi}{4} \left(1 - \frac{4\sqrt{\delta_e\{r[\Delta'_e(m_\tau)]\}}}{3\pi} \right) \quad (6.130)$$

$$r(n) = n \cdot \sqrt{1 - \frac{n}{9}}. \quad (6.131)$$

which, taken in conjunction with Eq. (6.123) without requiring any higher-order terms, yields a particle mass accurate to a precision of $\mathcal{O}\{[\Delta_e(m_\tau)]^2\}$.

Dropping the primes, it follows that if $\theta_e(\Delta_e)$ is redefined as per Eq. (6.130) and *no* corrective terms are introduced on Eq. (6.123), the value of m_τ^2 thus obtained will be consistent to $\mathcal{O}\{[\Delta_e(m_\tau)]^2\}$ with those obtained from Eqs. (6.117, 6.123–6.125) on iteration as described earlier. Recognising that the leading order term of c_{α/N_0} is of $\mathcal{O}(\alpha/N_0)$, the next order of corrections scales as

$$\left\{ \mathcal{O}\left(\frac{\alpha}{N_0}\right) + \mathcal{O}\left[\frac{m_{e_i}^2}{(m_c^*)^2}\right] \right\}^3. \quad (6.132)$$

All terms in this expansion are dominated by terms already present in \mathcal{O}_e (6.106) with the

exception of $O[m_{e_i}^6/(m_c^*)^6]$. Incorporating this additional term into $\mathcal{O}_e(m_{e_i})$ gives

$$\begin{aligned} \mathcal{O}_e(m_{e_i}) = & O\left(\frac{\alpha}{N_0^2}\right) + O\left(\frac{\alpha^2}{N_0}\right) + O\left[\frac{\alpha m_{e_i}^4}{N_0(m_c^*)^4}\right] + O\left[\frac{\alpha^2 m_{e_i}^2}{(m_c^*)^2}\right] + O\left\{\frac{\alpha m_{e_i}^2}{m_{\mathbf{H}}^2 [k_1^{(e)} N_0]^4}\right\} \\ & + O\left[\frac{m_{e_i}^6}{(m_c^*)^6}\right] + O\left\{\frac{m_{e_i}^2}{m_{\mathbf{H}}^2 [k_1^{(e)}]^4 N_0^5}\right\} + O\left\{\frac{m_{e_i}^4}{m_{\mathbf{H}}^4 [k_1^{(e)} N_0]^4}\right\}. \end{aligned} \quad (6.133)$$

6:5.3.6 Corrections to $[K_e(\theta_e)]^4$ from the muon channel

In the above it has been assumed that $K_e(\theta_e)$ attracts corrections from the tau channel only, corresponding to projection of $K_e(\theta_e)$ onto its $v_3 v_3^\dagger$ component (6.102). However, the term $[1 + \Delta_e(m_{e_i})]$ in Eq. (6.104) corrects all masses m_{e_i} and thus also affects the $v_1 v_1^\dagger$ and $v_2 v_2^\dagger$ components.

Also note that a propagating fermion undergoes multiple scatterings off the background fields. These scatterings may impart energy to or take energy from the fermion. They are generally ignored as their average contributions vanish over length scales large compared with \mathcal{L}_0 , but at any instant they may impart energy to the fermion in the range $-\frac{1}{2}\mathcal{E}_\Omega$ to $+\frac{1}{2}\mathcal{E}_\Omega$. In conjunction with this, background field interactions may also transiently modify the relative phases and amplitudes of the fermion's three constituent preons.

In consequence, although in the low-energy (large probe) limit a fermion occupies a definite eigenstate of the net mass matrix, at any given interaction a fermion with energy small compared with $\frac{1}{2}\mathcal{E}_\Omega$ (corresponding, close to the isotropy frame, to rest mass small compared to $\frac{1}{2}\mathcal{E}_\Omega c^{-2}$) will, in general, be arbitrarily off-shell in a quasi-random superposition of eigenstates. Such a fermion therefore attracts corrections from all eigensectors of $K_e(\theta_e)$.

To evaluate the correction arising from the e_2 or muon channel, recognise from Eqs. (6.101–6.102) that the effect of this correction is in opposition to the tau correction, and increases the magnitude of θ_e . As its scale is seen from Eq. (6.105) to be small compared with the tau correction, and from the construction of Eq. (6.113) it is seen to act in direct opposition to the tau correction, its effects are conveniently represented at energy scale \mathcal{E} by subtracting the muon correction from the tau correction at the level of the interaction diagrams. This yields

$$\theta_e(\mathcal{E}) = -\frac{3\pi}{4} \left(1 - \frac{4\sqrt{\delta_e \{r[\Delta_e(m_\tau, \mathcal{E}) - \Delta_e(m_\mu, \mathcal{E})]\}}}{3\pi} \right) \quad (6.134)$$

where $\theta_e(\mathcal{E})$ is the effective value of θ_e experienced by a particle whose energy is \mathcal{E} (i.e. if at rest, a particle with rest mass $\mathcal{E}c^{-2}$), and henceforth all instances of θ_e are acknowledged to depend, either explicitly or implicitly, on a particle's energy scale \mathcal{E} .

The correction from the e_1 or electron channel is smaller, but not negligible at the level of precision employed in this paper. However, introducing this correction results in an electron rest mass which runs with energy scale, including when the electron is in motion with respect to the isotropy frame. It is desirable that the electron rest mass behave as a fixed reference point which can be calibrated against experimental observation independent of electron velocity in the isotropy frame, allowing it to be consistent with observation and to be taken as one of the input parameters of the model. Therefore, before addressing the electron channel correction to $K_e(\theta_e)$, it is first necessary to revisit the local scaling symmetry discarded in Sec. 3:3.3.1.

6:5.3.7 Local scaling symmetry

As noted above, recognise that regardless of whether the mass is evaluated through the series in $\Delta_e(m_e)$, or whether θ_e is redefined to absorb the $[\Delta_e(m_e)]^2$ term in m_τ^2 , the value of θ_e necessarily runs with energy scale, and thus so too do the values of the colour mixing matrix eigenvalues $k_i^{(e)}$, and hence all lepton masses. This is undesirable if the model is to emulate the observable universe, in which electron rest mass is frame-independent. This issue with the model may be addressed by revisiting the discussion of local scaling symmetry.

In Sec. 3:3.3.1 it was stated that global scaling symmetry was broken by the introduction of a pseudovacuum with definite energy scale \mathcal{E}_0 . However, an alternative perspective now proves more fruitful: On the introduction of any nonvanishing vacuum excitations, let the scaling degree of freedom associated with symmetry subgroup

$$\mathbf{1}_A \otimes \mathbf{1}_C \otimes \mathbb{R}^+ \quad (6.135)$$

be gauged such that on average, over regions of some length scale $O(\mathcal{L}_0)$, the electron mass is constant. Since the electron mass is a function of the background photon energy scale, this largely corresponds to requiring that the average energy scale of the pseudovacuum (\mathcal{E}_0) is constant, at least in the presence of first-generation particles close to rest in the isotropy frame of the pseudovacuum. The assumption of maximum entropy of the pseudovacuum then ensures that $\mathcal{L}_0 = \mathcal{E}_0^{-1}$, and that the net spacetime dilation factor is homogeneous and undetectable at probe scales large compared with \mathcal{L}_0 .

Relative to this fixed reference value of m_e^2 , computation of the lepton mass ratios then corresponds to computation of the ratios of the eigenvalues of the pseudovacuum mass coupling. Now that there are multiple energy scales involved, it is advisable to be more careful with notation. Noting that a lepton may be off-shell (or in motion) and thus its energy scale \mathcal{E} may not coincide with $m_{e_i}c^2$, therefore write

$$m_{e_i}^2(\mathcal{E}) = \frac{f^2}{2} \left[k_i^{(e)}(\mathcal{E}) \right]^4 \omega_0^2 N_0^8 S_{18,147} [1 + \Delta_e(m_{e_i}, \mathcal{E})] [1 + \mathcal{O}_e(m_{e_i})] \quad (6.136)$$

$$\begin{aligned} \Delta_e(m_{e_i}, \mathcal{E}) = & \frac{8\alpha}{3N_0(3\alpha + 2\pi)} \left\{ 1 + \frac{(10\pi + 180\alpha)m_{e_i}^2}{3\pi [m_c^*(\mathcal{E})]^2} + \frac{(5 - 4f_Z)\alpha m_{e_i}^2}{4\pi m_W^2} \right\} + \frac{90\alpha m_{e_i}^2}{\pi [m_c^*(\mathcal{E})]^2} \\ & + \frac{(5 - 4f_Z)\alpha m_{e_i}^2}{2\pi m_W^2} + \frac{5m_{e_i}^2}{[m_c^*(\mathcal{E})]^2} \left\{ 1 + \frac{90\alpha m_{e_i}^2}{\pi [m_c^*(\mathcal{E})]^2} + \frac{(25 - 12f_Z)\alpha m_{e_i}^2}{6\pi m_W^2} \right\} \\ & + \frac{40m_{e_i}^2}{3m_{\mathbf{H}}^2 \left[k_1^{(e)}(\mathcal{E}_e) N_0 \right]^4} \end{aligned} \quad (6.137)$$

$$[m_c^*(\mathcal{E})]^2 = m_c^2 \left(1 - \frac{27}{10} \frac{\mathcal{E}^2}{m_c^2 c^4} \right) \quad (6.138)$$

$$\theta_e(\mathcal{E}) = -\frac{3\pi}{4} \left(1 - \frac{4\sqrt{\delta_e} \{ r[\Delta_e(m_\tau, \mathcal{E}) - \Delta_e(m_\mu, \mathcal{E})] \}}{3\pi} \right) \quad (6.139)$$

$$k_n^{(e)}(\mathcal{E}) = 1 + \sqrt{2} \cos \left[\theta_e(\mathcal{E}) - \frac{2\pi(n-1)}{3} \right]. \quad (6.140)$$

where previous occurrences of these parameters in Secs. 6:5.3.3–6:5.3.5 are noted to implicitly be dependent on energy scale, e.g.

$$\Delta_e(m_\tau) \longrightarrow \Delta_e(m_\tau, m_\tau c^2) \quad (6.141)$$

for an on-shell tau close to rest in the isotropy frame. (Note also that when $k_n^{(e)}$ takes a parameter with values of energy, this is the energy of the relevant foreground particle. There is no need for a factor of two; this factor applies only when converting relating the energy scales of the foreground particles and the pseudovacuum as discussed in e.g. Sec. 1:3.6.4.)

Calculation of higher-generation masses then corresponds to identification of energy scales \mathcal{E}_{e_i} at which Eqs. (6.136–6.140) are simultaneously consistent for rest mass $m_{e_i}c^2 = \mathcal{E}_{e_i}$, taking into account the correction to $\theta_e(\mathcal{E})$ discussed in Sec. 6:5.3.5 and the running of all parameters with energy. Prior to gauging of the scaling symmetry (6.135), the electron rest mass satisfies

$$m_e^2 = \frac{f^2}{2} \left[k_1^{(e)}(\mathcal{E}) \right]^4 \omega_0^2 N_0^8 S_{18,147} \times [1 + \Delta_e(m_e, \mathcal{E}) + \dots] [1 + \mathcal{O}_e(m_e)] \quad (6.142)$$

and runs with energy, but fixing a gauge to hold m_e^2 constant then corresponds to a rescaling of ω_0 such that the product $\left[k_1^{(e)} \right]^4 \omega_0^2$ remains fixed. Denoting the scaling field $\kappa(\mathcal{E})$, the electron mass becomes

$$m_e^2 = \frac{f^2}{2} \left[k_1^{(e)}(\mathcal{E}) \right]^4 [\kappa(\mathcal{E}) \omega_0]^2 N_0^8 S_{18,147} \times [1 + \Delta_e(m_e, \mathcal{E}) + \dots] [1 + \mathcal{O}_e(m_e)]. \quad (6.143)$$

which is constant by definition of $\kappa(\mathcal{E})$. The general lepton mass at energy \mathcal{E} then becomes

$$m_{e_i}^2(\mathcal{E}) = \frac{f^2}{2} \left[k_i^{(e)}(\mathcal{E}) \right]^4 [\kappa(\mathcal{E}) \omega_0]^2 N_0^8 S_{18,147} \times [1 + \Delta_e(m_{e_i}, \mathcal{E}) + \dots] [1 + \mathcal{O}_e(m_{e_i})]. \quad (6.144)$$

Changes in energy scale modulate the ratio

$$\frac{k_i^{(e)}(\mathcal{E})}{k_1^{(e)}(\mathcal{E})} \quad (6.145)$$

and thus modulate $m_{e_i}^2/m_e^2$, while choice of gauge keeps m_e^2 unchanged. Valid ratios (6.145) directly yield consistency of Eqs. (6.137–6.140) and (6.144). For definiteness, let $\kappa(\mathcal{E}_e) = 1$.

The search for consistent ratios is much simplified by writing

$$\frac{m_{e_i}^2}{m_e^2} = \frac{\left[k_i^{(e)}(\mathcal{E}_{e_i}) \right]^4 [1 + \Delta_e(m_{e_i}, \mathcal{E}_{e_i})]}{\left[k_1^{(e)}(\mathcal{E}_{e_i}) \right]^4 [1 + \Delta_e(m_e, \mathcal{E}_{e_i})]} [1 + \mathcal{O}_e(m_{e_i})], \quad (6.146)$$

regarding which, note the following:

- Identification of a mass eigenstate corresponds to identification of an eigenvalue ratio *at a particular energy scale* which yields consistency of Eqs. (6.137–6.140) and (6.144). Thus the energy scale is \mathcal{E}_{e_i} in both the numerator and the denominator.
- The electron mass is a constant of the model, with $\kappa(\mathcal{E}_{e_i})$ offsetting the energy dependency of $k_1^{(e)}(\mathcal{E}_{e_i})$ and $\Delta_e(m_e, \mathcal{E}_{e_i})$ in Eq. (6.144).
- Conveniently, on evaluating numerator and denominator at a common energy scale, gauge parameter $\kappa(\mathcal{E}_{e_i})$ is identical in numerator and denominator and thus does not appear in Eq. (6.146).

6:5.3.8 Corrections to $[K_e(\theta_e)]^4$ from the electron channel

Having addressed frame and energy scale invariance of m_e^2 , the correction to $K_e(\theta_e)$ from the e_1 or electron channel may now be determined. This channel is seen from Eq. (6.100) to contribute purely to the real part of $[K_e(\theta_e)]_{12}$. For the imaginary part, all positive contributions to the imaginary portion of $[K_e(\theta_e)]_{12}$ arise from the muon channel and all negative contrinutions from the tau channel, enabling the relatively simple form of Eq. (6.134). In contrast, while the electron channel contributes to the real part of $[K_e(\theta_e)]_{12}$ the bulk of the real part arises instead from the muon and tau channels. (Indeed, for $\theta_\ell := -3\pi/4$ the entirety of the real part arises from the muon and tau channels, though the corrections from the tau and mu sectors already discussed ensure that this particular situation is avoided.)

To evaluate the electron-mass-induced corrections to the electron mass, consider first an electron mass not incorporating these effects,

$$m_e^2 = [m_e^{(0)}]^2 [1 + \Delta_e(0, \mathcal{E})] \quad (6.147)$$

for some $m_e^{(0)}$. Turning on these effects causes the electron mass to undergo a rescaling

$$m_e^2 \rightarrow m_e^2 \left[\frac{1 + \Delta_e(m_e, \mathcal{E})}{1 + \Delta_e(0, \mathcal{E})} \right] \quad (6.148)$$

which may be rewritten as

$$m_e^2 = m_e^2 [1 + \underline{\Delta}_e(m_e, \mathcal{E})] \quad (6.149)$$

$$\underline{\Delta}_e(m_e, \mathcal{E}) := \left[\frac{1 + \Delta_e(m_e, \mathcal{E})}{1 + \Delta_e(0, \mathcal{E})} \right] - 1. \quad (6.150)$$

This rescaling of electron mass results in turn in some rescaling $(1 + \varepsilon)$ of $k_1^{(e)}(\mathcal{E})$. As the real and imaginary components of $\exp(i\theta_\ell)$ are both negative, the increase in the real component of $[v_1 v_1^\dagger]_{12}$ associated with this correction will decrease the magnitude of θ_ℓ . However, by choice of gauge in Sec. 6:5.3.7 the electron mass is one of the fixed input parameters to the model, and consequently this rescaling (and its associated effect on θ_ℓ) must be offset by a decrease in magnitude of the associated energy scale \mathcal{E}_0 {and thus of $[m_e^{(0)}]^2$ } corresponding to multiplication by $(1 + \varepsilon)^{-1}$. If this value is pulled out as an independent factor, in the electron mass diagram it cancels with the $(1 + \varepsilon)$ arising from the electron mass rescaling, leaving m_e and $k_1^{(e)}(\mathcal{E})$ unchanged (and eliminating any need to evaluate colour effects from this sector). However, for the muon and the tau it may be seen as a rescaling of $k_2^{(e)}(\mathcal{E})$ or $k_3^{(e)}(\mathcal{E})$ respectively by a factor of $(1 + \varepsilon)^{-1}$. To elucidate the effect of this scaling factor on θ_ℓ , restore colour neutrality by likewise holding the muon and tau masses fixed, corresponding to enacting a transformation

$$k_i^{(e)}(\mathcal{E}) \rightarrow k_i^{(e)}(\mathcal{E}) (1 + \varepsilon) \quad | \quad i \in \{2, 3\}. \quad (6.151)$$

The leading colour effect arising from this transformation is equivalent to a rescaling of $k_3^{(e)}(\mathcal{E})$ (which generates the leading correction to θ_ℓ) by $(1 + \varepsilon)$ and is therefore associated with an *increase* in the magnitude of θ_ℓ . The rescaling of the muon term is by the same factor. This multiplier is independent of the existing muon and tau corrections, having its origins on the real rather than the imaginary portion of $[K_e(\theta_e)]_{12}$, and therefore must be evaluated as a separate correction to $\theta_\ell := -3\pi/4$ rather than being conflated into a single term (as was possible for the muon and tau channels by their linearity on the imaginary component). In effect this correction

acts on both the muon and the tau channel to yield

$$\theta_e(\mathcal{E}) = -\frac{3\pi}{4} \left(1 - \frac{4\sqrt{\delta_e \{r[\Delta_e(m_\tau, \mathcal{E}) - \Delta_e(m_\mu, \mathcal{E})]\}}}{3\pi} \right) \times \left(1 + \frac{4\sqrt{\delta_e \{r[\Delta_e(m_e, \mathcal{E})]\}}}{3\pi} \right). \quad (6.152)$$

This completes corrections to $\theta_e(\mathcal{E})$ at the level of precision employed in the present paper, with the form of $\theta_e(\mathcal{E})$ chosen to avoid the need for corrections to Eq. (6.136) at $\mathcal{O}\{[\Delta_e(m_{e_i}, \mathcal{E})]^2\}$.

6:5.3.9 Species and energy dependence of K_ℓ -matrix eigenvalues in boson mass interactions

6:5.3.9.a Species dependence: As noted in Sec. 6:5.1.1, corrections to θ_ℓ are dependent on the mass of the fermion, and the leading order contributions to fermion mass are charge-dependent so vanish for the neutrino. Consequently, even if massive, the neutrino would be anticipated to receive a much smaller correction to the fermion mass angle than does the electron, with consequence that $k_1^{(\nu)} \ll k_1^{(e)}$. When evaluating the generation-1 W boson mass in Sec. 6:4.1, the K_ℓ -matrix interactions may be placed either slightly to the electron side or slightly to the neutrino side of the $W\nu_e\bar{e}_L$ vertex, corresponding to the location of the implicit background photon and gluon couplings. A sum over these possibilities is overwhelmingly dominated by contributions where K_ℓ acts on the electron, for eigenvalue $k_1^{(e)}$.

For higher generations, recognise that the K_ℓ -matrices are co-ordinate transformations on a region of manifold M . They are a freedom of the model, but are fixed up to physically irrelevant perturbations by the requirement that the A -sector bosons act on fermions as a representation of $SU(3)_A$. The A -sector components of these transformations may equivalently be represented as vertices of boson field couplings whose associated numerical factor is set to 1. In the boson mass interaction, these induced bosons form additional loop corrections.

Loop corrections are always a sum of terms proportional to the ratios of the masses of two of the participating species, bounded from above by 1. In Sec. 10:2 it is shown that all neutrinos in the $\mathbb{C}^{\wedge 18}$ analogue model are massless (and Chapter 9 describes, in passing, how the W/ν coupling in the $\mathbb{C}^{\wedge 18}$ model is modified to distribute neutrinos across generations and eliminate the need for a seesaw mechanism). Consequently there are no contributions to the K_ℓ -matrix eigenvalues from the neutrino branch of the $W\nu_e\bar{e}_L$ interactions in Fig. 5.2 regardless of boson generation.

Subject to this inference of non-contribution from the neutrino sector, these masses are calculated in Sec. 10:1, with the lightest higher-generation boson being the second-generation W at 16.67130(47) TeV. When seeking evidence of this boson, it must be remembered that there is a pseudovacuum energy cutoff of $\frac{1}{2}\mathcal{E}_\Omega$ in the $\mathbb{C}^{\wedge 18}$ model (not \mathcal{E}_Ω —for a discussion of the factor of $\frac{1}{2}$ see Chapter 8), and this cutoff is seen from Appendix 6:D to be approximately 3.1 TeV. This limits the amount of energy which may be borrowed when emulating QFT effects, and thus the threshold for observation of effects attributable to second-generation W bosons in the $\mathbb{C}^{\wedge 18}$ model is anticipated to be no less than 13.5 TeV.

6:5.3.9.b Energy dependence: In evaluating the leading-order boson mass interaction of Fig. 6.1(i), the pseudovacuum is partitioned into a background lepton associated with some energy scale \mathcal{E}_ℓ and the remaining pseudovacuum, of energy $\mathcal{E}_0 - \mathcal{E}_\ell$. Recognising that this partitioning is dependent on the random fluctuations of energy distribution within the pseudovacuum, all expressions are averaged over all energies from $-\infty$ to $+\infty$ with appropriate

weighting. Under the window approximation this reduces to $[-\frac{1}{2}\mathcal{E}_0, \frac{1}{2}\mathcal{E}_0]$, though on relaxation of this approximation it is recognised that the true range of fluctuations is $[-\frac{1}{2}\mathcal{E}_\Omega, \frac{1}{2}\mathcal{E}_\Omega]$. The value of \mathcal{E}_0 is evaluated in Appendix 6:D as approximately 3.6 GeV, while \mathcal{E}_Ω evaluates to approximately 6.2 TeV. Certainly for generation one and likely for generation two it is reasonable to ignore the finite nature of this cutoff, so that the usual outcome applies where evaluation of interactions is dominated by the on-shell term. In Eqs. (6.33), (6.41), (6.44), and (6.53), $k_i^{(e)}$ is therefore evaluated at \mathcal{E}_{e_i} for $i \in \{1, 2\}$. For generation three, if comparing the tau rest mass with $\frac{1}{2}\mathcal{E}_0$ it appears possible that cancellation of contributions from $|\mathcal{E}| < \mathcal{E}_\tau$ and $|\mathcal{E}| > \mathcal{E}_\tau$ could be sufficiently incomplete as to yield a significant correction to the third-generation boson masses. This is, however, unlikely when the pseudovacuum is capable of generating energy fluctuations on scales up to and including \mathcal{E}_Ω , and the possibility is not evaluated further here.

6:6 Predictions of the $\mathbb{C}^{\wedge 18}$ analogue model

6:6.1 Mass relationships

As seen in the above exploration of the $\mathbb{C}^{\wedge 18}$ analogue model, the increased structure of the $\mathbb{C}^{\wedge 18}$ free field model as compared with the Standard Model provides for complex interrelationships between the particle masses. When these relationships are collected together, it transpires that it suffices to take three input parameters from

$$\alpha, m_e, m_\mu, m_\tau, m_W, m_Z, m_{\mathbf{H}} \quad (6.153)$$

with the remaining four parameters then being derived quantities. It is, therefore, an obvious test of the $\mathbb{C}^{\wedge 18}$ model to evaluate these derived quantities. As seen in Sec. 6:6.2, the calculated quantities are in such excellent agreement with observation that this goes beyond being a test of the reasonableness of the $\mathbb{C}^{\wedge 18}$ analogue model, and becomes an application of the model.

To obtain these predictions, combine the mass equations for the various particle species developed above, and explicitly expand $S_{6,13}$ and $S_{18,147}$ to yield the relationships

$$\frac{m_{e_i}^2}{m_e^2} = \frac{[k_1^{(e)}(\mathcal{E}_{e_i})]^4 [1 + \Delta_e(m_{e_i}, \mathcal{E}_{e_i})]}{[k_1^{(e)}(\mathcal{E}_{e_i})]^4 [1 + \Delta_e(m_e, \mathcal{E}_{e_i})]} [1 + \mathcal{O}_e(m_{e_i}, \mathcal{E}_{e_i})] \quad \left| \quad e_i \in \{e, \mu, \tau\} \right. \quad (6.146)$$

$$\frac{m_W^2}{m_e^2} = 18N_0^4 \left(1 + \frac{2}{N_0}\right)^{-4} \left(1 + \frac{1}{N_0}\right)^{-4} \frac{\left[1 + \left(64 + \frac{3}{2\pi} - f_Z\right) \frac{\alpha}{2\pi}\right] \left\{1 + \frac{19}{18[k_1^{(e)}(\mathcal{E}_e) N_0]^4}\right\}}{[1 + \Delta_e(m_e, \mathcal{E}_e)]} [1 + \mathcal{O}_b + \mathcal{O}_e(m_e, \mathcal{E}_e)] \quad (6.154)$$

$$\frac{m_W^2}{m_Z^2} = \frac{3 \left[1 + \left(64 + \frac{3}{2\pi} - f_Z\right) \frac{\alpha}{2\pi}\right] \left\{1 + \frac{19}{18[k_1^{(e)}(\mathcal{E}_e) N_0]^4}\right\}}{4 \left[1 + \left(\frac{401}{12} + \frac{3}{2\pi}\right) \frac{\alpha}{2\pi}\right] \left\{1 + \frac{23}{18[k_1^{(e)}(\mathcal{E}_e) N_0]^4}\right\}} (1 + \mathcal{O}_b) \quad \frac{m_W^2}{m_c^2} = \frac{1 + \frac{19}{18[k_1^{(e)}(\mathcal{E}_e) N_0]^4}}{1 + \frac{99}{18[k_1^{(e)}(\mathcal{E}_e) N_0]^4}} (1 + \mathcal{O}_b) \quad (6.155)$$

$$\frac{m_W^2}{m_H^2} = \frac{9 \left[1 + \left(64 + \frac{3}{2\pi} - f_Z\right) \frac{\alpha}{2\pi}\right] \left\{1 + \frac{19}{18[k_1^{(e)}(\mathcal{E}_e) N_0]^4}\right\}}{20 \left\{\left(1 - \frac{1}{9N_0}\right)^2 \left[1 + \frac{30\alpha}{9\pi} \left(1 + \frac{1}{9N_0}\right)\right] + \frac{1}{2\pi} \left[1 + \frac{30\alpha}{\pi} \left(1 - \frac{1}{9N_0}\right)\right]\right\} \left\{1 + \frac{7}{18[k_1^{(e)}(\mathcal{E}_e) N_0]^4}\right\}} (1 + \mathcal{O}_b) \quad (6.156)$$

$$\Delta_e(m_{e_i}, \mathcal{E}) = \frac{8\alpha}{3N_0(3\alpha + 2\pi)} \left\{1 + \frac{(10\pi + 180\alpha)m_{e_i}^2}{3\pi[m_c^*(\mathcal{E})]^2} + \frac{(5 - 4f_Z)\alpha m_{e_i}^2}{4\pi m_W^2}\right\} + \frac{90\alpha m_{e_i}^2}{\pi[m_c^*(\mathcal{E})]^2} + \frac{(5 - 4f_Z)\alpha m_{e_i}^2}{2\pi m_W^2} \\ + \frac{5m_{e_i}^2}{[m_c^*(\mathcal{E})]^2} \left\{1 + \frac{90\alpha m_{e_i}^2}{\pi[m_c^*(\mathcal{E})]^2} + \frac{(25 - 12f_Z)\alpha m_{e_i}^2}{6\pi m_W^2}\right\} + \frac{40m_{e_i}^2}{3m_H^2[k_1^{(e)}(\mathcal{E}_e) N_0]^4} + \mathcal{O}_e(m_{e_i}, \mathcal{E}) \quad (6.137)$$

$$\theta_e(\mathcal{E}) = -\frac{3\pi}{4} \left(1 - \frac{4\sqrt{\delta_e}\{r[\Delta_e(m_\tau, \mathcal{E}) - \Delta_e(m_\mu, \mathcal{E})]\}}{3\pi}\right) \left(1 + \frac{4}{3\pi} \sqrt{\delta_e \left\{r \left[\frac{1 + \Delta_e(m_e, \mathcal{E})}{1 + \Delta_e(0, \mathcal{E})} - 1\right]\right\}}\right) \quad (6.157)$$

$$f_Z = \frac{1}{3} \left(4 - 24 \frac{m_W^2}{m_Z^2} + 16 \frac{m_W^4}{m_Z^4}\right) \quad (6.26)$$

$$[m_c^*(\mathcal{E})]^2 = m_c^2 \left(1 - \frac{27}{10} \frac{\mathcal{E}^2}{m_c^2 c^4}\right) \quad (6.138)$$

$$\mathcal{E}_\ell = m_\ell c^2 \quad (6.158)$$

$$r(n) = n \cdot \sqrt{1 - \frac{n}{9}} \quad (6.131)$$

$$k_n^{(\ell)}(\mathcal{E}) = 1 + \sqrt{2} \cos \left[\theta_\ell(\mathcal{E}) - \frac{2\pi(n-1)}{3}\right] \quad (6.159)$$

$$\delta_e(n) = \sqrt{1 + \frac{\pi^2 n}{8} \left[1 + \frac{\pi^2 n}{32}\right]} + \mathcal{O}(n^3) - 1 \quad (6.160)$$

$$\mathcal{O}_b = \mathcal{O} \left\{ \frac{\alpha}{\pi} [k_1^{(e)}(\mathcal{E}_e) N_0]^{-4} \right\} + \mathcal{O} \left(\frac{\alpha^2}{\pi^2} \right) \quad (6.161)$$

$$\mathcal{O}_e(m_{e_i}, \mathcal{E}) = \mathcal{O} \left(\frac{\alpha}{\pi N_0^2} \right) + \mathcal{O} \left(\frac{\alpha^2}{\pi^2 N_0} \right) + \mathcal{O} \left[\frac{\alpha m_{e_i}^4}{\pi N_0 [m_c^*(\mathcal{E})]^4} \right] + \mathcal{O} \left\{ \frac{\alpha^2 m_{e_i}^2}{\pi^2 [m_c^*(\mathcal{E})]^2} \right\} + \mathcal{O} \left\{ \frac{\alpha m_{e_i}^2}{\pi m_H^2 [k_1^{(e)}(\mathcal{E}_e) N_0]^4} \right\} \\ + \mathcal{O} \left\{ \frac{m_{e_i}^6}{[m_c^*(\mathcal{E})]^6} \right\} + \mathcal{O} \left\{ \frac{m_{e_i}^2}{m_H^2 [k_1^{(e)}(\mathcal{E}_e)]^4 N_0^5} \right\} + \mathcal{O} \left\{ \frac{m_{e_i}^4}{m_H^4 [k_1^{(e)}(\mathcal{E}_e) N_0]^4} \right\}. \quad (6.162)$$

Note that $r(n)$ is taken to be exact by definition. The finite length of the series in n is associated with an error in the lepton masses, but this is incorporated into $\mathcal{O}_e(m_{e_i}, \mathcal{E}_{e_i})$.

6:6.2 Results

Taking m_e , m_μ , and α as input parameters [28, 31],

$$m_e = 0.51099895000(15) \text{ MeV}/c^2 \quad (6.163)$$

$$m_\mu = 105.6583755(23) \text{ MeV}/c^2 \quad (6.164)$$

$$\alpha = 7.2973525693(11) \times 10^{-3}, \quad (6.165)$$

the relationships of Sec. 6:6.1 may be solved numerically to yield the results given in Table 6.5. The calculated values obtained for fundamental constants m_W , m_Z , $m_{\mathbf{H}}$, and m_τ are all within $0.1 \sigma_{\text{exp}}$ of the experimental results. For a discussion of the numerical methods used to solve the equations of Sec. 6:6.1, see Appendix 6:C.

For purpose of comparing the scale of terms in $\mathcal{O}_e(m_{e_i}, \mathcal{E})$, it is noted that the value of $k_1^{(e)}(\mathcal{E}_e)$ evaluates as

$$k_1^{(e)}(\mathcal{E}_e) = 0.04035007804(40). \quad (6.166)$$

For purpose of considering the breakdown scale of the $\mathbb{C}^{\wedge 18}$ analogue model, in a gauge in which $\kappa(\mathcal{E}_e) = 1$ it follows from Eqs. (5.23), (6.136), and (6.168) that

$$\frac{1}{2} \mathcal{E}_\Omega^2 \approx \frac{n^2 N_0^2 m_e^2}{2\alpha [k_1^{(e)}(\mathcal{E}_e)]^4} \quad | \quad n = 9. \quad (6.167)$$

The value of \mathcal{E}_Ω is evaluated more precisely in Appendix 6:D, and gives a UV cutoff of ± 3.1 TeV.

For completeness it is also interesting to note the value of f , which also evaluated in Appendix 6:D and is found to satisfy

$$f^2 = \frac{2\alpha}{N_0^6 S_\alpha (1 + a_e)^2} \quad (6.168)$$

$$f = 1.669540(95) \times 10^{-8}. \quad (6.169)$$

6:6.3 Sources of numerical error

The relationships between the fundamental constants presented in Sec. 6:6.1 incorporate numerous truncations. These are listed in Table 6.6, with their impacts on the numerical results being presented in Table 6.7.

Table 6.5: Calculated values of particle masses in the $\mathbb{C}^{\wedge 18}$ analogue model. Quantity m_c is the bare gluon mass, which is not observable at the confinement scale but enters some calculations in this chapter as a collective property of momentum transfer in the colour sector. The notation σ_{exp} corresponds to the uncertainty in the observed values of the particle masses.

Parameter	Calculated value (GeV/ c^2)	Observed value (GeV/ c^2) [28]	Discrepancy
m_τ	1.776867409(43)	1.77686(12)	$0.06 \sigma_{\text{exp}}$
m_W	80.3785(22)	80.377(12)	$0.13 \sigma_{\text{exp}}$
m_Z	91.1877(35)	91.1876(21)	$0.04 \sigma_{\text{exp}}$
$m_{\mathbf{H}}$	125.2501(49)	125.25(17)	$0.0003 \sigma_{\text{exp}}$
m_c	80.42812(42)	—	—

Table 6.6: List of sources of error in the results of Table 6.5. Note that coefficients of \mathcal{O}_b are assumed to vary independently in each of the boson masses, and hence in each of the listed mass ratios.

Label	Description
E1	Term 1 of \mathcal{O}_b applied to m_c^2/m_W^2
E2	Term 2 of \mathcal{O}_b applied to m_c^2/m_W^2
E3	Term 1 of \mathcal{O}_b applied to m_W^2/m_Z^2
E4	Term 2 of \mathcal{O}_b applied to m_W^2/m_Z^2
E5	Term 1 of \mathcal{O}_b applied to $m_W^2/m_{\mathbf{H}}^2$
E6	Term 2 of \mathcal{O}_b applied to $m_W^2/m_{\mathbf{H}}^2$
E7	Term 1 of \mathcal{O}_e applied to $\Delta_e(m_{e_i}, \mathcal{E})$
E8	Term 2 of \mathcal{O}_e applied to $\Delta_e(m_{e_i}, \mathcal{E})$
E9	Term 3 of \mathcal{O}_e applied to $\Delta_e(m_{e_i}, \mathcal{E})$
E10	Term 4 of \mathcal{O}_e applied to $\Delta_e(m_{e_i}, \mathcal{E})$
E11	Term 5 of \mathcal{O}_e applied to $\Delta_e(m_{e_i}, \mathcal{E})$
E12	Term 6 of \mathcal{O}_e applied to $\Delta_e(m_{e_i}, \mathcal{E})$
E13	Term 7 of \mathcal{O}_e applied to $\Delta_e(m_{e_i}, \mathcal{E})$
E14	Term 8 of \mathcal{O}_e applied to $\Delta_e(m_{e_i}, \mathcal{E})$
E15	The next term in $\delta_e(n)$
E16	Uncertainty in α
E17	Uncertainty in m_e
E18	Uncertainty in m_μ

Table 6.7: Contributions of different sources of error to the results of Table 6.5, expressed in units of energy, and relative to the experimental error. Labels are enumerated in Table 6.6. For purposes of summation, sources of error are assumed independent.

Label	Coefficient	Uncertainty in τ mass		Uncertainty in Z mass		Uncertainty in W mass		Uncertainty in H mass		Uncertainty in c mass
		eV/c^2	$10^{-4} \sigma_{\text{exp}}$	MeV/c^2	σ_{exp}	MeV/c^2	σ_{exp}	MeV/c^2	$10^{-2} \sigma_{\text{exp}}$	MeV/c^2
E1	± 10	0.0	0.00	0.29	0.14	0.26	0.02	0.40	0.24	0.00
E2	± 10	0.0	0.00	2.46	1.17	2.16	0.18	3.37	1.98	0.01
E3	± 10	0.0	0.00	0.29	0.14	0.00	0.00	0.00	0.00	0.00
E4	± 10	0.0	0.00	2.46	1.17	0.00	0.00	0.00	0.00	0.00
E5	± 10	0.0	0.00	0.00	0.00	0.00	0.00	0.40	0.24	0.00
E6	± 10	0.1	0.01	0.00	0.00	0.00	0.00	3.38	1.99	0.00
E7	± 10	1.4	0.12	0.00	0.00	0.00	0.00	0.00	0.00	0.00
E8	± 10	0.6	0.05	0.00	0.00	0.00	0.00	0.00	0.00	0.00
E9	± 10	0.0	0.00	0.00	0.00	0.00	0.00	0.00	0.00	0.00
E10	± 10	24.3	2.02	0.47	0.22	0.42	0.03	0.65	0.38	0.42
E11	± 10	2.4	0.20	0.02	0.01	0.02	0.00	0.03	0.02	0.02
E12	± 10	1.1	0.09	0.02	0.01	0.02	0.00	0.03	0.02	0.02
E13	± 10	5.4	0.45	0.05	0.02	0.05	0.00	0.07	0.04	0.05
E14	± 10	0.2	0.02	0.00	0.00	0.00	0.00	0.00	0.00	0.00
E15	1	0.0	0.00	0.00	0.00	0.00	0.00	0.00	0.00	0.00
E16	± 1	0.0	0.00	0.00	0.00	0.00	0.00	0.00	0.00	0.00
E17	± 1	0.0	0.00	0.00	0.00	0.00	0.00	0.00	0.00	0.00
E18	± 1	35.3	2.94	0.00	0.00	0.00	0.00	0.00	0.00	0.00
Total		43.3	3.61	3.53	1.68	2.22	0.18	4.85	2.85	0.42

In determining the error bars on the results of Table 6.5, all sources of error have been assumed independent. No attempt has been made to quantify exactly how large the next-order correction coefficients E1-E14 are; instead, a generous coefficient of ± 10 has been applied to each term. As an order of magnitude factor, ± 10 has been preferred over ± 1 because colour charges may introduce up to a ninefold degeneracy on some loops. Nevertheless, it is expected this will somewhat over-estimate the higher-order corrections.

6:7 Conclusion

The $\mathbb{C}^{\wedge 18}$ analogue model has many elements in common both with the Standard Model of particle physics and with the observable universe. As it has only three tunable parameters, which must be set by reference to physical constants, the $\mathbb{C}^{\wedge 18}$ analogue model may readily be tested against observation.

In the present chapter, calculation of higher-order terms in the mass relationships of the $\mathbb{C}^{\wedge 18}$ model permitted the values of four fundamental constants, the masses of the W boson, Z boson, Higgs boson, and tau particle, to be predicted with precision comparable to current experimental observation. The results were found to be in essentially perfect agreement to the limits of experimental precision (tensions $< 1\sigma$).

The conceptual underpinnings of the $\mathbb{C}^{\wedge 18}$ analogue model are radically different to those of the Standard Model, being a classical model on anticommuting co-ordinates which only emulates a quantum field theory on pseudo-Riemannian space-time in an appropriate regime. Nevertheless, this chapter provides an extremely compelling case for the utility of this analogue model.

Other predictions of the $\mathbb{C}^{\wedge 18}$ model include a “neutral gluon” N_μ , which is a dark matter candidate with a mass of $80.42812(42) \text{ GeV}/c^2$, and a second and third generation of weak bosons, with the lightest being a W -analogue at $16.61730(47) \text{ TeV}$. In view of the model’s ability to successfully derive the masses of known particles to full experimental precision, perhaps these predictions should be taken seriously.

The model also exhibits two further particles, weakly-interacting right-handed weak bosons denoted G_μ and G_μ^\dagger . However, detection of these particles should not be anticipated as they are eliminated in Chapter 7, in which the $\mathbb{C}^{\wedge 18}$ analogue model is also shown to reproduce gravitational metric consistent with General Relativity—again, in an appropriate regime.

Finally, it is exciting to ask: What *is* the domain of validity of the $\mathbb{C}^{\wedge 18}$ model? The existence of a finite ultraviolet cutoff at $\frac{1}{2}\mathcal{E}_\Omega = 3.1 \text{ TeV}$ suggests that experiments at the Large Hadron Collider have entered a regime where they may probe the limits of the model, but effects identified thus far are subtle, and discrimination between the $\mathbb{C}^{\wedge 18}$ analogue model and the Standard Model is challenging. Nevertheless, the identification of tests capable of discriminating between these two models is highly desirable, as with the elimination of the $G_\mu^{(\dagger)}$ bosons forthcoming in Chapter 7, the $\mathbb{C}^{\wedge 18}$ model has greater predictive capacity than the Standard Model, and as yet, no domains have been identified in which it is demonstrably inferior as a description of the observable universe. However, extensive further assessment is required to determine whether the $\mathbb{C}^{\wedge 18}$ model is capable of acting as a model of the observable universe in its own right, or simply an analogue model whose limitations of validity have not yet been fully determined.

Appendices

6: A Mass-related loop coefficients

In Sec. 6: 4.1.1 it was observed that the one-photon-loop correction to lepton magnetic moment is associated with a factor of

$$2\alpha \cdot \mathbf{f}\left(\frac{m_\ell^2}{m_A^2}\right) \cdot \frac{1}{4\pi} \quad (6.11)$$

while the one- W -loop correction is associated with [26]

$$-\frac{10\alpha}{3} [1 + \mathcal{O}(\alpha)] \cdot \mathbf{f}\left(\frac{m_\ell^2}{m_W^2}\right) \cdot \frac{1}{4\pi} \quad (6.12)$$

where the mass dependency $\mathbf{f}(\cdot)$ evaluates as

$$\mathbf{f}\left(\frac{m_\ell^2}{m_b^2}\right) \longrightarrow \begin{cases} 1 & \text{if } m_b^2 = 0 \\ \frac{m_\ell^2}{4\pi m_b^2} & \text{if } m_b^2 \gg m_\ell^2. \end{cases} \quad (6.170)$$

All bosons in these interactions are foreground fields.

In Sec. 6: 5.1.2 a similar situation is encountered save that the loop bosons are background fields. That is, their values are evaluated as expansions around the mean field value, with terms beyond the first making negligible numerical contribution provided the foreground fields are small compared with $\frac{1}{2}\mathcal{E}_\Omega$ (see Sec. 1: 3.6). Although not making significant contribution to the overall value of the diagram, these higher-order contributions are conceptually important, representing 4-momentum transferred to and then recovered from the background fields, analogous to the foreground loops associated with the corrections to the lepton magnetic moment.

There is, however, a critical difference in the value of $\mathbf{f}(\cdot)$ for massive foreground and background fields. For foreground fields, emission and reabsorption of a single particle forms a loop, and integration over this loop yields a factor of $(4\pi)^{-1}$. For background fields, the loop is lost and it is replaced by two randomly oriented interactions with photons from the pseudovacuum. It may be anticipated that some other factor will then replace $(4\pi)^{-1}$. The relative weights of these two distinct scenarios may be evaluated by considering the semiclassical emission and absorption process on $\mathbb{C}^{\wedge 18}$ from a geometric perspective.

First examining the massive foreground scenario, if the lepton is stationary prior to emitting the loop particle, and the emitted particle has nonzero spatial momentum, there exists a preferred direction from which to recover the loop particle. Barring external interference, preferred absorption is from the same direction that emission was towards. This yields a function in solid angle which approaches a delta function in the classical limit. Similarly, if the particle emitted is stationary in the rest frame of the lepton (this yielding a trajectory in some sense “closest to classical”, about which other trajectories form symmetric perturbations), then change frames such that both are in motion. The preferred direction of emission is along the future trajectory of the lepton, and the preferred direction for absorption is from the past trajectory of the lepton, again yielding a delta function in solid angle.

If, however, the two vertices represent interactions with the background field, then provided the foreground momentum superimposed upon this is sufficiently small, the returning boson at the inbound vertex is equally likely to come from any spatial orientation. The delta function is lost, and integration over solid angle yields a relative factor of 4π .

Finally, if the boson is massless, then regardless of whether it is foreground or background the same argument applies: There is no comoving choice of spatial momentum as the emitting leptons

are all massive (including the neutrinos—to be shown in a future paper) and the emitted particle is lightlike. The closest-to-classical trajectory is therefore that in which the loop contracts down to a point. There is no delta function over solid angle.

The corresponding values of $\mathbf{f}(\cdot)$ are thus

$$\mathbf{f}\left(\frac{m_\ell^2}{m_b^2}\right) \rightarrow \begin{cases} 1 & \text{if } m_b^2 = 0 \\ \frac{m_\ell^2}{4\pi m_b^2} & \text{if } m_b^2 \gg m_\ell^2 \text{ and } b \text{ is } [b]_{\text{fg}} \\ \frac{m_\ell^2}{m_b^2} & \text{if } m_b^2 \gg m_\ell^2 \text{ and } b \text{ is } [b]_{\text{bg}}. \end{cases} \quad (6.171)$$

It is also worth elaborating on what it means for photon loops to be contracted “down to a point”. In the limit of any loop being sufficiently large, emission and absorption approach being equally likely to be in phase or antiphase, and the long-range contribution of the loop to the vertex correction vanishes. Over distances which are sub-wavelength, however, correlated emission and absorption dominate, yielding a systematic contribution to the loop correction. Recognising that interactions with the background field emulate quantum uncertainty, for a photon with energy below $\frac{1}{2}\mathcal{E}_\Omega$ an interaction is functionally pointlike if it takes place over a distance of less than half a wavelength. Within the subset of all such contributions, other process considerations (such as the energy scale of the particles involved) will determine which dominate. If the dominant loop energy is small compared with $\frac{1}{2}\mathcal{E}_0$, then a loop contracted down “to a point” still spans a region large compared with the autocorrelation length of the pseudovacuum, \mathcal{L}_0 . This is seen to have relevance for the calculation of some symmetry factors for loop corrections in Chapter 7 and Appendix 6:B.

6:B Symmetry factors and photon loops

When evaluating $\mathcal{O}(\alpha)$ loop diagrams such as those shown in Fig. 6.17, it can be convenient to have a quick method of evaluating symmetry factors relative to the one-loop electromagnetic correction to the EM vertex of Fig. 6.22(i). To this end, consider diagram (i) as constituting an electron which, as it propagates, interacts with two correlated photons and one uncorrelated photon. The components of this interaction are shown in diagram (ii). The first interaction is with a correlated photon, with two to choose from. Next there is the interaction being corrected, which is with the uncorrelated photon, and the final interaction is with the photon correlated with the first photon, choice of one, for a relative factor of two.

This may be contrasted with diagram (ii) where the loop photon has been replaced by a W boson. The interactions of the loop correction are now with W and W^\dagger , so each attracts a factor of one, for an overall relative symmetry factor of one.

Next, consider diagram (iii). In this diagram, which corresponds to the third diagram of Fig. 6.17(i), the electron interacts with two pairs of correlated photons. However, these pairs are distinguishable by the characteristics of their correlations—for the background pair, these correlations vanish over length scales large compared with \mathcal{L}_0 , whereas for the foreground pair they do not. The diagram being constructed mandates whether each interaction is with a foreground or background boson, and thus the first interaction is with one of the two correlated foreground photons for a symmetry factor of two. This is then followed by the pair of interactions being corrected, and finally by the interaction with the second boson of the correlated foreground pair. The symmetry factor associated with the loop is thus two, and like Fig. 6.18, the diagrams of Fig. 6.17(i) attract loop correction factors of $\alpha/(2\pi)$ apiece.

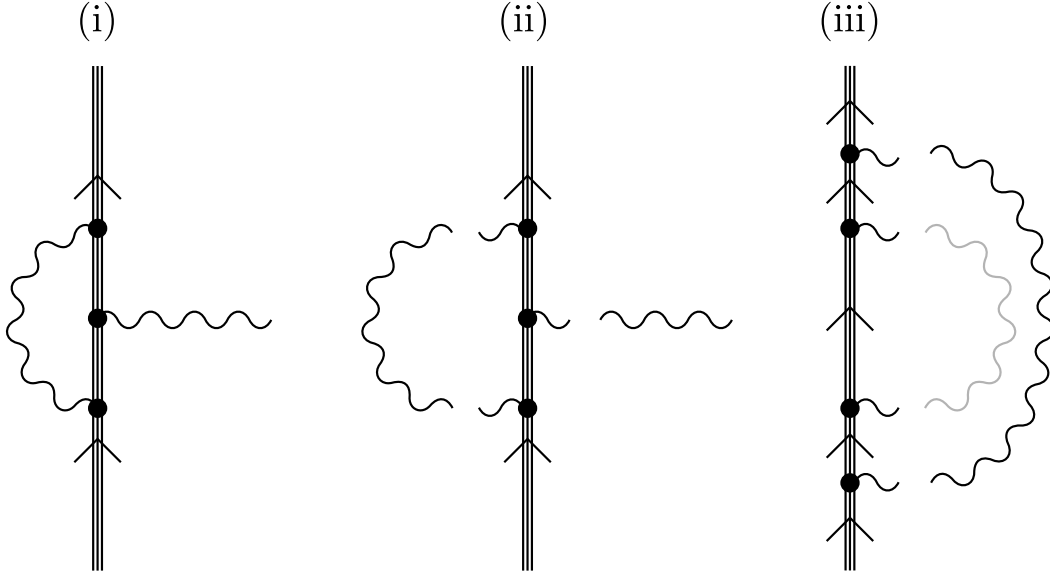


Figure 6.22: Evaluation of symmetry factors of $O(\alpha)$ loop corrections. Background (pseudovacuum) photons are shown in grey. (i) The one-loop electromagnetic correction to the EM vertex. (ii) This diagram may be decomposed as a series of interactions between a propagating electron and a set of photons in its vicinity. The arc of the loop may be understood as a correlated photon pair. (iii) A similar decomposition of the third diagram of Fig. 6.17(iii).

Although not encountered in this chapter, an example will be seen in Chapter 7 in which the loop correction boson of Fig. 6.22(iii) is also constrained to exhibit rapidly vanishing contributions over length scales large compared with \mathcal{L}_0 . In this context the two correlated pairs of Fig. 6.22(iii) become indistinguishable and the first interaction attracts a symmetry factor of four as it may be with either constituent of either pair. The next two interactions comprise the process receiving the loop correction, and the final interaction attracts a symmetry factor of one, for a total symmetry factor of four. Such a loop thus attracts a factor of α/π rather than $\alpha/(2\pi)$. As discussed in Appendix 6:A, however, most loop corrections do not exhibit such a constraint, and are dominated by terms which generate the symmetry factor of $\alpha/(2\pi)$ seen in the Standard Model.

It is also worth making an observation regarding the sign of loop corrections, and the number of fermion lines present. A loop correction to a single photon emission process, such as Fig. 6.22(i), is positive when the loop incorporates an even number of fermion lines. In contrast, the one-photon loop in the PSE expansion of the electron propagator yields a positive correction when the number of fermion lines is odd. On closing the background photon loop to obtain the parent diagram (prior to mean field expansion), the relationship between diagram (iii) and the PSE is observed. Although diagram (iii) is not part of the fermion PSE of the Standard Model, as there are no pseudovacuum photons in the Standard Model, this diagram is nevertheless seen to be positive with an odd number of fermion lines.

6:C Solving the particle mass relationships

To solve the particle mass relationships of Sec. 6:6.1, proceed as follows:

Take α , m_e , and m_μ as input parameters. To set up the initial value of m_τ , take the uncorrected angle $\theta_\ell = -3\pi/4$, construct the uncorrected K_ℓ matrix as per Eq. (6.58), and diagonalise to obtain initial values for $k_i^{(e)}$, then write the initial value of m_τ as

$$[m_\tau]_0 = \frac{[k_3^{(e)}]^2}{[k_2^{(e)}]^2} m_\mu. \quad (6.172)$$

Let the initial value of m_W be arbitrary and large, e.g. $10^4 \text{ GeV}/c^2$. Let initial values of m_c , m_H , and m_Z be computed from m_W using tree-level calculations. Determine an initial value for N_0 using Eq. (5.15). Determine also an initial value for $k_1^{(e)}(\mathcal{E}_e)$; when assigning this initial value it is convenient to neglect terms in θ_e involving $[k_1^{(e)}(\mathcal{E}_e)N_0]^{-4}$.

Expand Eq. (6.146) for $i = 2$ (muon channel, energy scale \mathcal{E}_μ) and substitute m_W^2 for $(m_c^*)^2$ using the expressions for m_W^2/m_c^2 (6.155) and $[m_c^*(\mathcal{E})]^2$ (6.138). Rewrite as

$$f_{Wc}^\ell = \frac{1 + \frac{19}{18[k_1^{(e)}(\mathcal{E}_e)N_0]^4}}{\left\{1 + \frac{99}{18[k_1^{(e)}(\mathcal{E}_e)N_0]^4}\right\} \left(1 - \frac{27m_\ell^2}{10m_c^2}\right)} \quad \tilde{f}_{Wc}^\ell = f_{Wc}^\ell \left\{1 + \frac{E1 \alpha}{\pi [k_1^{(e)}(\mathcal{E}_e)N_0]^4} + \frac{E2 \alpha^2}{\pi^2}\right\} \quad (6.173)$$

$$\begin{aligned} 0 = [m_W^4]_{n+1} & \left(\left\{ [k_1^{(e)}(\mathcal{E}_\mu)]^4 m_\mu^2 - [k_2^{(e)}(\mathcal{E}_\mu)]^4 m_e^2 \right\} \left[1 + \frac{8\alpha}{3N_0(3\alpha+2\pi)} + \frac{E7 \alpha}{\pi N_0^2} + \frac{E8 \alpha^2}{\pi^2 N_0} \right] \right. \\ & + \left\{ [k_1^{(e)}(\mathcal{E}_\mu)]^4 - [k_2^{(e)}(\mathcal{E}_\mu)]^4 \right\} \left\{ \frac{40m_e^2 m_\mu^2}{3m_H^2 [k_1^{(e)}(\mathcal{E}_e)N_0]^4} + \left(\frac{E11 \alpha}{\pi} + \frac{E13}{N_0} \right) \frac{m_e^2 m_\mu^2}{m_H^2 [k_1^{(e)}(\mathcal{E}_e)N_0]^4} \right\} \\ & + \left\{ [k_1^{(e)}(\mathcal{E}_\mu)]^4 m_e^2 - [k_2^{(e)}(\mathcal{E}_\mu)]^4 m_\mu^2 \right\} \frac{E14 m_e^2 m_\mu^2}{m_H^4 [k_1^{(e)}(\mathcal{E}_e)N_0]^4} \Bigg) \\ & + [m_W^2]_{n+1} \left(\left\{ [k_1^{(e)}(\mathcal{E}_\mu)]^4 - [k_2^{(e)}(\mathcal{E}_\mu)]^4 \right\} m_e^2 m_\mu^2 \right. \\ & \times \left\{ \frac{8\alpha}{3N_0(3\alpha+2\pi)} \left[\frac{(10\pi+180\alpha)\tilde{f}_{Wc}^\mu}{3\pi} + \frac{(5-4f_Z)\alpha}{4\pi} \right] + \frac{90\alpha\tilde{f}_{Wc}^\mu}{\pi} + \frac{(5-4f_Z)\alpha}{2\pi} + 5\tilde{f}_{Wc}^\mu + \frac{E10 \alpha^2 \tilde{f}_{Wc}^\mu}{\pi^2} \right\} \Bigg) \\ & + \left(\left\{ [k_1^{(e)}(\mathcal{E}_\mu)]^4 m_e^2 - [k_2^{(e)}(\mathcal{E}_\mu)]^4 m_\mu^2 \right\} m_e^2 m_\mu^2 \left\{ 5\tilde{f}_{Wc}^\mu \left[\frac{90\alpha\tilde{f}_{Wc}^\mu}{\pi} + \frac{(25-12f_Z)\alpha}{6\pi} \right] + \frac{E9 \alpha (\tilde{f}_{Wc}^\mu)^2}{\pi N_0} \right\} \right. \\ & \left. + \left\{ [k_1^{(e)}(\mathcal{E}_\mu)]^4 m_e^4 - [k_2^{(e)}(\mathcal{E}_\mu)]^4 m_\mu^4 \right\} \frac{E12 m_e^2 m_\mu^2 (\tilde{f}_{Wc}^\mu)^3}{[m_W^2]_n} \right) \end{aligned} \quad (6.174)$$

In correction E12 it is convenient to use the value of the W mass from the previous iteration such that the equation as a whole remains quadratic in $[m_W^2]_{n+1}$. For numerical stability, terms involving m_H^2 are only evaluated provided the working value of m_H^2 satisfies $m_H^2 > m_\mu^2$. Values on convergence are unaffected by this precaution.

To update m_W^2 , iterate across trial values of θ_e in the vicinity of $-3\pi/4$. Note that as per Sec. 6:5.3.2, the leading correction to θ_e (from the tau channel) makes it less negative so only values $\theta_e > -3\pi/4$ need be considered. For each value of θ_e , compute the associated eigenvalues of the K -matrix at energy scale \mathcal{E}_μ using Eq. (6.159), then solve Eq. (6.174) for an updated value of m_W^2 . Use this to compute associated values of m_c^2 , m_H^2 , and m_Z^2 using the mass ratios

of Eqs. (6.155–6.156), and N_0 using Eq. (6.154) rearranged to solve for N_0^4 ,

$$[N_0^4]_{n+1} = \frac{m_W^2 \left(1 + \frac{2}{[N_0]_n}\right)^4 \left(1 + \frac{1}{[N_0]_n}\right)^4 [1 + \Delta_e(m_e, \mathcal{E}_e)]}{18m_e^2 \left[1 + \left(64 + \frac{3}{2\pi} - f_Z\right) \frac{\alpha}{2\pi}\right] \left(1 + \frac{19}{18\{k_1^{(e)}(\mathcal{E}_e)[N_0]_n\}^4}\right)} (1 + \mathcal{O}_N) \quad (6.175)$$

$$\begin{aligned} \mathcal{O}_N := & \frac{E3 \alpha}{\pi \{k_1^{(e)}(\mathcal{E}_e)[N_0]_n\}^4} + \frac{E4 \alpha^2}{\pi^2} + \frac{E7 \alpha}{\pi [N_0]_n^2} + \frac{E8 \alpha^2}{\pi^2 [N_0]_n} + \left\{ \frac{E9 \alpha m_e^2}{\pi [N_0]_n [m_c^*(\mathcal{E}_e)]^2} + \frac{E10 \alpha^2}{\pi^2} \right\} \frac{m_e^2}{[m_c^*(\mathcal{E}_e)]^2} \\ & + \frac{E11 \alpha m_e^2}{\pi m_{\mathbf{H}}^2 \{k_1^{(e)}(\mathcal{E}_e)[N_0]_n\}^4} + \frac{E12 m_e^6}{[m_c^*(\mathcal{E}_e)]^6} + \frac{E13 m_e^2}{m_{\mathbf{H}}^2 [k_1^{(e)}(\mathcal{E}_e)]^4 [N_0]_n^5} + \frac{E14 m_e^4}{m_{\mathbf{H}}^4 \{k_1^{(e)}(\mathcal{E}_e)[N_0]_n\}^4} \end{aligned} \quad (6.176)$$

where $\Delta_e(m_e, \mathcal{E}_e)$ is evaluated using $[N_0]_n$, and the error terms in Eq. (6.137) are ignored when computing this value as these terms are all accounted for explicitly in Eqs. (6.175) and (6.176). Using these updated values, then attempt to recover θ_e by evaluating Eq. (6.157). If the trial value is denoted θ_e^T and the recovered value is denoted θ_e^R , then each trial value of θ_e is assigned a score based on how well θ_e^R reproduces θ_e^T . Repeat and refine the trial values of θ_e until a best fit is obtained. Update the values of m_c^2 , $m_{\mathbf{H}}^2$, m_Z^2 , and N_0 accordingly.

Since the value of m_W^2 depends on m_c^2 , $m_{\mathbf{H}}^2$, and N_0 , and the values of m_c^2 , $m_{\mathbf{H}}^2$, and N_0 depend on m_W , it is advisable to iterate between updating m_W^2 and updating m_c^2 , $m_{\mathbf{H}}^2$, m_Z^2 , and N_0 until these parameters are satisfactorily converged. In practice, performing one further update to m_W^2 and one further update to m_c^2 , $m_{\mathbf{H}}^2$, m_Z^2 , and N_0 suffices.

Next, expand Eq. (6.146) for $i = 3$ (tau channel, energy scale \mathcal{E}_τ) and rewrite as

$$\begin{aligned} 0 = & [m_\tau^4]_{n+1} \left\{ \frac{450\alpha}{\pi [m_c^*(\mathcal{E}_\tau)]^4} + \frac{5(25 - 12f_Z)\alpha}{6\pi [m_c^*(\mathcal{E}_\tau)]^2 m_W^2} + \frac{E9 \alpha}{\pi N_0 [m_c^*(\mathcal{E}_\tau)]^4} + \frac{E12 [m_\tau^2]_n}{[m_c^*(\mathcal{E}_\tau)]^6} + \frac{E14}{m_{\mathbf{H}}^4 [k_1^{(e)}(\mathcal{E}_e)N_0]^4} \right\} \\ & + [m_\tau^2]_{n+1} \left(\frac{90\alpha}{\pi [m_c^*(\mathcal{E}_\tau)]^2} + \frac{(5 - 4f_Z)\alpha}{2\pi m_W^2} + \frac{5}{[m_c^*(\mathcal{E}_\tau)]^2} + \frac{40}{3m_{\mathbf{H}}^2 [k_1^{(e)}(\mathcal{E}_e)N_0]^4} - \frac{[k_1^{(e)}(\mathcal{E}_\tau)]^4 [1 + \Delta_e(m_e, \mathcal{E}_\tau)]}{[k_3^{(e)}(\mathcal{E}_\tau)]^4 m_e^2} \right. \\ & \quad + \frac{8\alpha}{3N_0(3\alpha + 2\pi)} \left\{ \frac{10\pi + 180\alpha}{3\pi [m_c^*(\mathcal{E}_\tau)]^2} + \frac{(5 - 4f_Z)\alpha}{4\pi m_W^2} \right\} - \left(\frac{E7 \alpha}{\pi N_0^2 m_e^2} + \frac{E8 \alpha^2}{\pi^2 N_0 m_e^2} \right) \left[\frac{k_1^{(e)}(\mathcal{E}_\tau)}{k_3^{(e)}(\mathcal{E}_\tau)} \right]^4 \\ & \quad - \left\{ \frac{E9 \alpha}{\pi N_0 [m_c^*(\mathcal{E}_\tau)]^4} + \frac{E12 m_e^2}{[m_c^*(\mathcal{E}_\tau)]^6} + \frac{E14}{m_{\mathbf{H}}^4 [k_1^{(e)}(\mathcal{E}_e)N_0]^4} \right\} m_e^2 \left[\frac{k_1^{(e)}(\mathcal{E}_\tau)}{k_3^{(e)}(\mathcal{E}_\tau)} \right]^4 \\ & \quad + \left\{ \frac{E10 \alpha^2}{\pi^2 [m_c^*(\mathcal{E}_\tau)]^2} + \frac{E11 \alpha}{\pi m_{\mathbf{H}}^2 [k_1^{(e)}(\mathcal{E}_e)N_0]^4} + \frac{E13}{m_{\mathbf{H}}^2 [k_1^{(e)}(\mathcal{E}_e)]^4 N_0^5} \right\} \left\{ 1 - \left[\frac{k_1^{(e)}(\mathcal{E}_\tau)}{k_3^{(e)}(\mathcal{E}_\tau)} \right]^4 \right\} \Bigg) \\ & + 1 + \frac{8\alpha}{3N_0(3\alpha + 2\pi)} + \frac{E7 \alpha}{\pi N_0^2} + \frac{E8 \alpha^2}{\pi^2 N_0}. \end{aligned} \quad (6.177)$$

The value of \mathcal{E}_τ is evaluated using $[m_\tau^2]_n$, and correction E12 is likewise partially evaluated using $[m_\tau^2]_n$, such that this expression is quadratic in $[m_\tau^2]_{n+1}$. Again, iterate over trial values of θ_e , denoted θ_e^T , this time solving for $[m_\tau^2]_{n+1}$ and again computing the recovered value θ_e^R using Eq. (6.157). Again refine and reiterate until the optimal value of θ_e is identified, this time with all other parameters held constant except m_τ^2 .

Repeatedly alternate between updating m_W^2 (and other boson masses and N_0) and m_τ^2 until convergence.

As a couple of practical notes:

- Close to $\theta_e = -3\pi/4$, $k_1^{(e)}(\mathcal{E}_e)$ as obtained from Eq. (6.159) becomes very small and it may be preferable to write

$$\left[k_1^{(e)}(\mathcal{E}_e)\right]^2 \approx \frac{m_e^2}{m_\mu^2} \left[k_2^{(e)}(\mathcal{E}_e)\right]^2, \quad (6.178)$$

this approximation being accurate to $O[\alpha m_{e_i}^2/(m_c^*)^2]$. This approximation should not be employed close to convergence.

- On the first pass for updating m_W^2 , it may be convenient to suppress terms in $[k_1^{(e)}(\mathcal{E}_e) N_0]^4$. If omitted, these terms can be incorporated for a small correction from the second pass onward, once initial updates to m_W^2 and N_0 have been obtained.
- Negative solutions for m_W^2 or m_τ^2 may be discarded.
- The algorithm presented here is vulnerable to becoming trapped in pseudominima. These can be recognised by inspecting the value of $\|\theta_e^T - \theta_e^R\|$, which converges to far smaller values at a true minimum (always under 10^{-11} and generally under 10^{-13} in the reference implementation). Pseudominima may be avoided by changing the sampling density over θ_e .

Octave/C++ code implementing the above algorithm may be found accompanying this volume [35]. It has been tested under macOS 11.5.1 in Octave 6.2.0 with symbolic package 2.9.0, Clang 11.0.0, and Python 3.9.4.

6:D Evaluation of accessory results

Although not yet determined to be directly observable, it is also useful to evaluate the values of the model parameters N_0 , f , ω_0 , \mathcal{E}_0 , and \mathcal{E}_Ω . Allowing the coefficients E1-E18 to range as per Table 6.7 and assuming that all error terms are independent, solving Eq. (6.175) yields

$$N_0 = 191.9703(37). \quad (6.179)$$

Rearranging Eq. (3.83) gives

$$f^2 = \frac{2\alpha}{N_0^6 S_\alpha (1 + a_e)^2} \quad (6.168)$$

where

$$S_\alpha := N_0^{-6} (N_0 + \frac{5}{4}) (N_0 + 1)^3 (N_0 + 2)^2. \quad (3.84)$$

Now note the equivalence of a_e in the Standard Model and in the $\mathbb{C}^{\wedge 18}$ model, valid at least up to the mass-independent terms of $O(\alpha^2/\pi^2)$, and the existence of an uncertainty of $O(\alpha^2/\pi^2)$ in the calculation of N_0 (6.175). The magnitude of this uncertainty justifies the use of either the observed or the Standard Model value of a_e when evaluating Eq. (6.168)—if there is any error associated with doing so, it is below the threshold of relevance for the calculation. To minimise the number of measured parameters in the software, the reference implementation takes

$$\begin{aligned} a_e &= \frac{\alpha}{2\pi} + \left\{ \frac{197}{144} + \frac{\pi^2[1 - 6\ln(2)]}{12} + \frac{3\zeta(3)}{4} \right\} \frac{\alpha^2}{\pi^2} \\ &\quad + O\left(\frac{\alpha^2 m_e^2}{m_\mu^2}\right) \\ &\approx \frac{\alpha}{2\pi} - 0.328478965579193 \frac{\alpha^2}{\pi^2} + O\left(\frac{\alpha^2 m_e^2}{m_\mu^2}\right) \end{aligned} \quad (6.180)$$

where the numeric coefficient on α^2/π^2 is as per Refs. [36–38], and the uncertainty term, designated E19, is evaluated as

$$\left. \frac{\text{E19 } \alpha^2 m_e^2}{\pi^2 m_\mu^2} \right| \quad \text{E19} = \pm 10 \quad (6.181)$$

in keeping with the approach employed for other unevaluated higher-order terms in the present paper. For a_e this is an extremely conservative approach, with the Standard Model value of E19 being approximately 0.022220 [38]. Directly evaluating the effect of each error term on the computed value of f yields

$$f = 1.669540(95) \times 10^{-8} \quad (6.169)$$

where independence of sources of uncertainty E1-E19 has been assumed.

The value of ω_0 is given by rearranging Eq. (6.136) and substituting Eq. (6.168),

$$\omega_0 = \left\{ \frac{m_e^2 S_\alpha (1 + a_e)^2}{\alpha \left[k_1^{(e)}(\mathcal{E}_e) \right]^4 N_0^2 S_{18,147} [1 + \Delta_e(m_e, \mathcal{E}_e)]} \right\}^{\frac{1}{2}} \times [1 + \frac{1}{4} \mathcal{O}_N + \frac{1}{2} \mathcal{O}_e(m_e, \mathcal{E}_e)] \quad (6.182)$$

$$S_{18,147} := N_0^{-12} (N_0 + 2)^6 (N_0 + 1)^6 \quad (6.183)$$

where the definition of $S_{18,147}$ agrees with Eq. (4.32), while

$$\mathcal{E}_0 := N_0 \omega_0 (1 - \frac{1}{4} \mathcal{O}_N) \quad (6.184)$$

$$\mathcal{E}_\Omega := \mathbf{n} N_0 (N_0 - \frac{1}{2}) \omega_0 \quad | \quad \mathbf{n} = 9 \quad (5.23)$$

where the coefficients on \mathcal{O}_e and \mathcal{O}_N reflect rescalings of the range of the error coefficients E1-E18 relative to their original appearances in Eqs. (6.146–6.162). Once again allow the coefficients E1-E18 to range as per Table 6.7 prior to this rescaling, and E19 as per Eq. (6.181). The errors associated with each of E1-E19 are again evaluated directly, then combined under the assumption of independence.

Note that the terms in \mathcal{O}_N disappear on \mathcal{E}_0 . However, \mathcal{O}_e contains corrections of $\mathcal{O}[\alpha/(\pi N_0)]$ which are large enough to permit the use of Eq. (6.180) for a_e in Eq. (6.182) without discernible error.

On evaluation these equations yield

$$\omega_0 = 18.68257(35) \text{ MeV} \quad (6.185)$$

$$\mathcal{E}_0 = 3.5864993(17) \text{ GeV} \quad (6.186)$$

$$\mathcal{E}_\Omega = 6.18037(12) \text{ TeV}. \quad (6.187)$$

6: E Further notes on the colour sector

6: E.1 Gluon masses

All bosons in the $\mathbb{C}^{\wedge 18}$ Classical Analogue to the Standard Model exhibit a scale-dependent mass interaction. However, for A -sector bosons this phenomenon is obscured by the fact that A -sector phenomena are customarily observed over length scales large compared with the largest length scale of the model, \mathcal{L}_0 . In contrast, gluon-related phenomena occur over a range of length scales. The critical scales are as follows:

$\mathcal{L} < \mathcal{L}_\psi$: Gluon exchange binds preons into triplets or preon/antipreon doublets. On this length scale, which is much smaller than the length scale of the mass interaction, the gluon is massless.

$\mathcal{L}_\psi < \mathcal{L} < \mathcal{L}_0$: On this length scale, the pseudovacuum is inhomogeneous. Under appropriate conditions, colour shielding effects may permit the gluon to propagate as a free massive particle (see Chapter 8 for more details). Loop corrections to particle masses involve composite quasi-particles and thus implicitly occur at length scales large compared with \mathcal{L}_ψ , but occur over length scales associated with the mass interaction so are bounded from above by \mathcal{L}_0 . Loop corrections to particle masses therefore involve gluons with masses of order m_c^2 . A small correction described in Sec. 6:5.1.4 introduces an energy dependency denoted by the replacement $m_c^2 \rightarrow [m_c^*(\mathcal{E})]^2$.

$\mathcal{L} > \mathcal{L}_0$: Due to confinement, free gluons are not observed at these length scales—with the exception of the stabilised gluon holes in the pseudovacuum described in Sec. 6:5.1.4, which again exhibit an effective mass $(m_c^*)^2$.

6:E.2 Separability of A and C charge sectors

In Sec. 3:3.1, the $SU(9)_{\mathbf{80}} \oplus GL(1, \mathbb{R})_1$ local symmetry of the $\mathbb{C}^{\wedge 18}$ model was factorised to yield $\{[SU(3)_A]_{\mathbf{8}} \oplus [GL(1, \mathbb{R})_A]_1\} \otimes \{[SU(3)_C]_{\mathbf{8}} \oplus [GL(1, \mathbb{R})_C]_1\}$, reducing the pre-gauging number of bosons from 81 to 18. In the context of a classical model this decomposition is wholly satisfactory, as any boson field in $SU(9)_{\mathbf{80}} \oplus GL(1, \mathbb{R})_1$ may be reconstructed as the product of a field from $\{[SU(3)_A]_{\mathbf{8}} \oplus [GL(1, \mathbb{R})_A]_1\}$ and a field from $\{[SU(3)_C]_{\mathbf{8}} \oplus [GL(1, \mathbb{R})_C]_1\}$. However, in the quantised effective description which emerges from the $\mathbb{C}^{\wedge 18}$ model, the local symmetry group $SU(9)_{\mathbf{80}} \oplus GL(1, \mathbb{R})_1$ permits a single boson to carry both an A -sector and a C -sector charge whereas symmetry groups $\{[SU(3)_A]_{\mathbf{8}} \oplus [GL(1, \mathbb{R})_A]_1\} \otimes \{[SU(3)_C]_{\mathbf{8}} \oplus [GL(1, \mathbb{R})_C]_1\}$ require the exchange of two quanta (one carrying an A -sector charge and one carrying a C -sector charge) to achieve the same effect.

This distinction may be overlooked in situations where one or both of the charge sectors interacts in a manner approaching the continuum. Thus, for example, during tree-level lepton mass interactions (Secs. 4:3 and 6:5.1), while the A -sector interactions are discrete, the C -sector interactions are represented cumulatively by the K_ℓ -matrices. Similarly, during loop corrections to these interactions (Sec. 6:5.2), all particles are assumed massive (with solution by consistency) and thus both A and C sector interactions occur continuously in the vicinity of the explicit loop corrections. Thus electroweak sector loop corrections may be considered without attaching C -sector charges (due to the rescaling of the fermion fields described in Appendix 4:A and the presence of C -sector K_ℓ -matrices in the implicit mass vertices of all propagators). Effective separability of the A -sector charges also necessarily implies effective separability of the C -sector charges.

For boson mass interactions, in the dominant (pseudovacuum fermion) terms the A -sector interactions are discrete and the C -sector interactions are represented cumulatively by the K_ℓ -matrices. The pseudovacuum boson terms vary depending on the charges of the boson whose mass is being determined, and in principle it is necessary to take the product rather than the sum of A - and C -sector contributions. The current paper addresses only the masses of bosons carrying A -sector *or* C -sector charges, not both, but nevertheless, bosons carrying both A -sector and C -sector charges do exist in the $\mathbb{C}^{\wedge 18}$ model, and may be observed as distinct entities in processes involving a single quantum in an environment which permits a coloured species to survive long enough for its unique properties to be determined. In Chapter 8 it is discussed that single-boson decay events occurring at energies between $\mathcal{E}_0/2$ and $\mathcal{E}_\psi/2$, i.e. $1.79\text{GeV} <$

$E < 3.09$ TeV, experience an inhomogeneity of the pseudovacuum which stabilises free colour charges and favours channels involving coloured W and Z bosons over their usual non-coloured counterparts. This augments their masses by $50 \text{ MeV}/c^2$ and $57 \text{ MeV}/c^2$ respectively. The $\mathbb{C}^{\wedge 18}$ model consequently predicts observation of W -like bosons with masses of $80.4287(22) \text{ GeV}/c^2$ in the CDF II experiment at Tevatron (see Chapter 8). This prediction is consistent with the observed value of $80.4335(94) \text{ GeV}/c^2$ with tension 0.49σ . In comparison, the Standard Model has a tension with this result of 6.9σ [28, 39–41]. Similarly, a Z -like resonance with energy $91.2446(35) \text{ GeV}/c^2$ is predicted in high-energy-initial-state-radiation (high-ISR) decays such as those studied by L3 in the LEP [42]. However, existing experiments have lacked the sensitivity to discriminate between the coloured and neutral Z boson (L3, ALEPH, DELPHI $q\bar{q}$), and in some cases (OPAL, DELPHI $\mu\bar{\mu}$) the data analysis specifically excludes detection of these events (see discussion in Chapter 8 and Refs. [42–45]).

Chapter 7

Curved space-times from $\mathbb{C}^{\wedge 18}$

Abstract

The $\mathbb{C}^{\wedge 18}$ analogue model is a classical model of free fields on a manifold with anticommuting co-ordinates which emulates the quantum field theory of the Standard Model. In some ways this emulation is remarkably accurate, predicting masses for the weak bosons and the tau which are in precise agreement with observation. However, the model also predicts a right-handed weak interaction which has not been observed. In this chapter the final ungauged freedom of the $\mathbb{C}^{\wedge 18}$ analogue model is used to eliminate the right-handed weak interaction, while simultaneously introducing space-time curvature, and a gravitational interaction which emulates general relativity in experimentally observed regimes. The model is predictive of the value of Newton's constant, yielding $G_N = 6.67430(230) \times 10^{-11} \text{ m}^3 \text{kg}^{-1} \text{s}^{-2}$. Although the error bars on this calculated value are quite large, the central value is in agreement with the observed value of $G_N = 6.67430(15) \times 10^{-11} \text{ m}^3 \text{kg}^{-1} \text{s}^{-2}$ to a precision of $0.03 \sigma_{\text{exp}}$.

7:1 Introduction

Introduced in Chapters 1–6, the $\mathbb{C}^{\wedge 18}$ analogue model is a classical model on a manifold with anticommuting co-ordinates which is capable of supporting a quasiparticle spectrum analogous to the Standard Model. Manifold $\mathbb{C}^{\wedge 18}$ is taken to support an infinite number of scalar fields, and on mapping a subspace $M \subset \mathbb{C}^{\wedge 18}$ onto $\mathbb{R}^{1,3}$,

$$\mathcal{G}(M) \cong \mathbb{R}^{1,3}, \quad (7.1)$$

the product of these fields behaves (in appropriate limits) as a pseudovacuum. Solitonic excitations about the pseudovacuum state then behave as preonic quasiparticles from which the species of the Standard Model are constructed. These are necessarily supplemented by a weakly-interacting massive vector boson denoted N_μ , higher-generation counterparts to the weak sector bosons (starting with W_2 at $16.61730(47) \text{ TeV}/c^2$), and an attenuated right-handed weak interaction mediated by a pair of bosons denoted G_μ and G_μ^\dagger .

An essential part of relating the $\mathbb{C}^{\wedge 18}$ analogue model to the Standard Model is the choice of a gauge on the local symmetry of the analogue model, described in Sec. 3:3.3.6. The local symmetries which are gauged are an emergent property of the model arising in the limit of low quasiparticle energy, and originate in the freedom to choose an arbitrary co-ordinate frame on manifold $\mathbb{C}^{\wedge 18}$. Of the gaugeable degrees of freedom described in Sec. 3:3.3.1, the vast majority are fixed in Chapters 3 and 6 on physically motivated grounds. The sole exception is the gauging

of the $\mathbf{1}_A \otimes \mathbf{1}_C \otimes \text{SL}(2, \mathbb{C})$ subgroup associated with the space–time connections on $\mathcal{G}(M)$. These connections are fixed (up to a change of co-ordinates on a fixed manifold) by requiring, arbitrarily, that the target of mapping \mathcal{G} in Chapter 3 be flat.

In the present chapter it is seen that relaxation of this requirement, such that the target of mapping \mathcal{G} need only be locally Minkowski, permits a choice of gauge on $\mathbf{1}_A \otimes \mathbf{1}_C \otimes \text{SL}(2, \mathbb{C})$ which eliminates the $G_\mu^{(\dagger)}$ bosons (and also some other beyond-Standard-Model effects). Adopting this gauge uniquely fixes the geometry of $\mathcal{G}(M)$, and in the vicinity (but outside the Schwarzschild radius) of a nonrotating electrically neutral massive body this geometry is seen to correspond to the Schwarzschild metric. The Kerr metric for a rotating source is anticipated to follow in a similar regime from the usual classical arguments [46]. Further, the effective value of Newton’s constant in this gravitational analogue is uniquely determined by the structure of the $\mathbb{C}^{\wedge 18}$ model and is found to be $G_N = 6.67430(230) \times 10^{-11} \text{ m}^3\text{kg}^{-1}\text{s}^{-2}$, in excellent agreement with observation.

This is not the first attempt to calculate of the value of Newton’s constant. Acknowledgement must be made of the efforts of [Di Mario](#) in a series of articles made available online from 2003 [47], whose equations reduce to the relationship

$$G_N = \frac{\alpha^2 h^3 \omega_1^2}{4\pi c^3 m_e^4} [1 + \text{O}(\alpha)]. \quad (7.2)$$

However, the parameter ω_1 in Eq. (7.2) is a unitful constant taking the value of exactly 1 s^{-1} , and the origin of this constant is never satisfactorily explained. This leaves the uncomfortable inference that the universe might have some special relationship with our arbitrarily-chosen unit of time, and this equation must therefore be considered a coincidence. The present paper make no use of any such factor of ω_1 .

The structure of this chapter is as follows: Section 7:2.1 recaps and references the conventions of notation and terminology employed in this chapter. Section 7:2.2 then introduces a convenient relationship between Feynman diagrams and classical fields termed a *quantum/classical correspondence*. Sections 7:3.1 and 7:3.2 begin the mapping of beyond-Standard-Model effects to space–time curvature. The most ubiquitous interaction involving $G^{(\dagger)}$ bosons is identified as involving a spin-2 pair $G_\mu G_\nu^\dagger$, and elimination of this process (and other related beyond-Standard-Model processes) is compared with choosing a gauge in the low-energy regime. Calculation of the resulting metric is performed in Sec. 7:3.3, and is shown to be predictive of the value of Newton’s constant. Section 7:3.4 extends this treatment to include all sources of $G^{(\dagger)}$ bosons, including single-boson (spin-1) interactions. Numerical results are presented in Sec. 7:4.1, with some discussion of implications in Sec. 7:4.2, and the future of the $\mathbb{C}^{\wedge 18}$ model is discussed in Sec. 7:5.

7:2 Conventions

7:2.1 Notation and terminology

This chapter follows the same conventions as Chapters 1–6. As in previous chapters, units are chosen such that $c = 1$, $\hbar = 1$. When equations and lemmas from Chapters 1–6 are referenced, they take the forms (1.1), (2.1), etc.

When referring to uncertainty in results, experimental uncertainties will be denoted σ_{exp} , and uncertainties in the theoretical calculation will be denoted σ_{th} .

In this chapter, it is generally assumed that any particle under study is at rest or near-rest with respect to the isotropy frame of the pseudovacuum.

Regarding terminology around Feynman diagrams and symmetry factors:

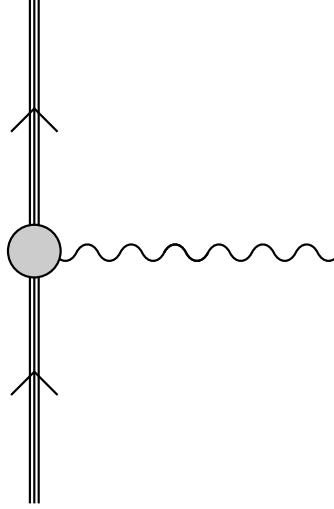


Figure 7.1: Emission of a single photon by a single electron. The grey circle is the all-orders vertex incorporating loop corrections. The triple line represents the existence of a preonic substructure, consistent with Chapters 1-6.

- Where there exist multiple ways to connect up sources, vertices, and sinks to obtain equivalent diagrams up to interchange of non-distinguishable co-ordinates, the same term is obtained from the generator \mathcal{Z} in multiple different ways and thus the diagram acquires a multiplicative factor. This is referred to in the present volume as a *symmetry factor*.
- Where integration over the parameters of a diagram (for example, over source/sink co-ordinates) yields the same diagram multiple times up to interchange of labels on these parameters, this represents a double- (or multiple-)counting of physical processes. It is then necessary to eliminate this multiple-counting by dividing by the appropriate symmetry factor. This is referred to in the present volume as *diagrammatic redundancy* or *double- (multiple-)counting*.

7:2.2 Quantum/classical correspondence

In the limit of large particle numbers it is convenient to introduce a quantum/classical correspondence which permits classical field profiles to be obtained from the Feynman diagrams describing the processes taking place within these fields. As a specific example, consider the emission of a photon by an electron as shown in Fig. 7.1. Although a classical-regime A field is assumed to be made up of many, many virtual photons, these are all emitted in accordance with Fig. 7.1 and it is customary to associate features of this diagram with elements of the classical expression

$$A = \frac{Q}{|e|} \frac{\alpha}{r} \quad (7.3)$$

(in which only the source is associated with a factor of α) or with its symmetrised form

$$A = \frac{Q}{|e|} \frac{\sqrt{\alpha}}{r} \quad (7.4)$$

in which a factor of $\sqrt{\alpha}$ appears at both source and sink. To set up the quantum/classical correspondence used in the present chapter:

- First, as is customary, associate the all-orders vertex in Fig. 7.1 with a factor of $\sqrt{\alpha}$, the classical electromagnetic field coupling. This is consistent with the quantum field theory treatment of Sec. 3:3.5.1, and in particular with Eq. (3.83). When a photon is exchanged between two charged particles, this coefficient is squared to yield α , and incorporates a factor of $1/(4\pi)$ which is associated with directionality of emission.
- Second, normalise the fermion fields such that the fermion line and associated operators (e.g. $\bar{e}_L \bar{\sigma}^\mu e_L$) may be identified as a number operator. This is to be understood in the sense that (for example) given a collection of fermions at rest, $\|\bar{e}_L \bar{\sigma}^\mu e_L\|$ counts the number of left-handed electrons per unit volume.
- Third, it is necessary to relate a single boson to a field profile. This is again a choice not just in the quantum/classical correspondence, but also in quantum field theory, and must reproduce the geometric factor of $1/r$ in Eq. (7.4). Thus the photon line emerging from the interaction vertex for a spherically symmetric point source, and hence the associated photon operator at that vertex, must be associated with a factor of r^{-1} . (It should be noted that this latter association applies only to radially propagating fields. In contrast, for example, the mean energy per effective excitation in the background field is known to be $\omega_0 = \mathcal{E}_0/N_0$ everywhere.)

Having imposed this relationship between Feynman diagrams and classical fields, which is almost trivial in the $\overline{\text{MS}}$ renormalisation scheme, it is now possible to use Feynman diagrams to calculate the profiles of classical fields in the presence of perturbing processes. The above three choices calibrate the electromagnetic 4-potential of a single electron against the emission diagram of Fig. 7.1, and application of the same calibration to the diagrams for other processes then permits determination of their effects on fields in the classical limit.

The remainder of this chapter is essentially a calculation performed using the quantum/classical correspondence specified above, taking into account additional effects due to the presence of the pseudovacuum and the fundamental scalar field (FSF) symmetry factors.

7:3 $\mathbb{C}^{\wedge 18}$ with curved space–time

7:3.1 Curvature and choice of gauge

As noted in the introduction, the choice of co-ordinate frame on the $\mathbf{1}_A \otimes \mathbf{1}_C \otimes \text{SL}(2, \mathbb{C})$ subgroup of $\text{GL}(18, \mathbb{C})$ is a freedom of the $\mathbb{C}^{\wedge 18}$ model. In choosing this frame the 4-volume form must be preserved under translations, as the scaling symmetry $\mathbf{1}_A \otimes \mathbf{1}_C \otimes \mathbb{R}^+$ is fixed in Sec. 6:5.3.7. Once a prescription has been described for choosing such a frame based on the field content of the model on $\mathbb{C}^{\wedge 18}$, the target of mapping \mathcal{G} must then be chosen to be able to support the associated metric, being the manifold on which the $\mathbb{C}^{\wedge 18}$ model emulates particle dynamics.

Recognising that all choices of gauge for local symmetries of the low-energy effective description of the $\mathbb{C}^{\wedge 18}$ model similarly correspond to choices of co-ordinate frame on $\mathbb{C}^{\wedge 18}$, it is natural to refer to this particular choice of co-ordinate frame in the same language, describing the degrees of freedom associated with this co-ordinate frame as gauge degrees of freedom, and the prescription for choosing the co-ordinate frame as being a choice of gauge.

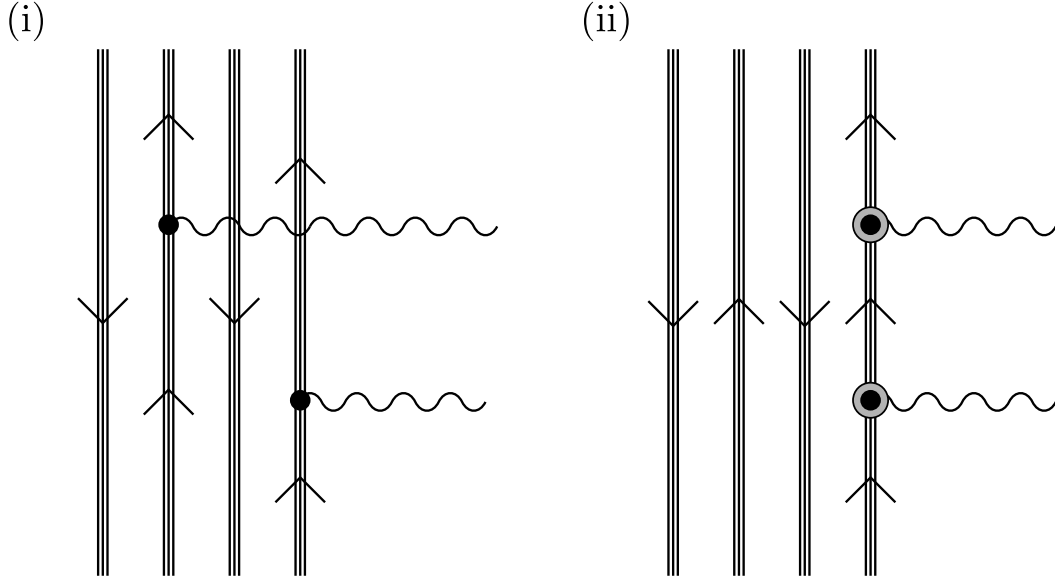


Figure 7.2: Emission of a pair of photons, (i) with standard electromagnetic vertices, and (ii) with K -augmented vertices. In diagram (i), emission may be from any fermion or pair of fermions in the matter source. In diagram (ii), for the background interactions which give rise to the K matrices to be on average nonvanishing, emission of the pair must be from the same fermion.

7:3.2 Beyond-Standard-Model processes in the photon pair field

7:3.2.1 Origin of the photon pair field

The governing principle behind the choice of co-ordinate frame on $SL(2, \mathbb{C})$ is that it should eliminate as many beyond-Standard-Model effects as possible, including the $G^{(\dagger)}$ fields, and thus the right-handed weak interaction. As a first step, it is necessary to identify the most prevalent $G^{(\dagger)}$ -boson-mediated interactions appearing in the $\mathbb{C}^{\wedge 18}$ analogue model. These interactions take place within a photon pair field having no counterpart in the Standard Model.

As a prototype for fermionic matter, consider a collection of positrons and electrons with zero net spin and zero net charge (and see Sec. 7:3.2.3 for discussion of more general matter sources). Let this source emit a pair of photons as per Fig. 7.2(i), either with both being emitted from the same fermion, or with both being emitted from different fermions. There are precisely as many diagrams for emission of pairs from sources with charges of the same sign as there are for emissions of pairs from sources with different sign, and in the far field, being the regime in which all source elements may be treated as collocated, these diagrams cancel to yield no net photon pair field $A_\mu A_\nu$.

However, in the $\mathbb{C}^{\wedge 18}$ model there is a further emission channel to consider. In addition to the simple photon pair emission channel described above, if both sources are correlated and both vertices are within \mathcal{L}_0 of one another (with these conditions in practice implying that both emission vertices are on the same fermion) there is also a process of emission augmented by background colour field interactions.

In the mass calculations of Chapters 4 and 6 it was convenient to separate the description of interactions with the background gluon fields into colourless boson couplings (implicitly exploiting symmetry of the C sector under colour mixing) and independent colour transformations

(represented by K matrices), and then to write the effectively colourless gluon contributions to particle mass as small corrections to the photon contributions. This approach is once again useful here, although it is not the emission of the gluon pairs themselves which is important this time, since the gluons are (i) massive and (ii) confined. This time, it is the effects of these gluon interactions on preon colour (as represented by the K matrices) which are of interest, as these effects may be nonvanishing over length scales of up to $O(\mathcal{L}_0)$. Physically these diagrams represent processes whereby preons scatter off background gluons one or more times to change colour, then scatter again to change back again, contemporaneous with the emission of a photon pair. The scattering process itself is absorbed into the normalisation of the fermion propagator, but the effects on preon colour provide physically distinguishable alternative channels for photon emission. The pair of background field scatterings must be correlated, and in matter of normal densities, this necessitates the involvement of the same fermion at each background interaction.

In principle these K matrices are associated with explicit gluon couplings as per Eq. (4.25), but these explicit field couplings are subsumed into the fermion propagator as indicated in Fig. 4.4, and hence into the fermion mass term. However, as per Sec. 4:3.2.2, knowing that the application of K matrices is in 1:1 correspondence with A -sector interactions permits these matrices to be equivalently associated with the non-subsumed photon interaction vertices. Proper accounting for colour effects is then obtained if up to one set of K matrices is applied for every A -sector interaction (as discussed in Sec. 4:3.3), with the matrices being applied to the same fermion as participates in the A -sector interaction. (Applying the K matrices elsewhere has no effect on the emission process.) An example diagram for the resulting process is shown in Fig. 7.2(ii). As emission is constrained to always be of two photons from the same fermion, there is no cancellation of diagrams and a nonvanishing photon pair field is supported. In flat space-time, both the intensity of the foreground photon pair field $[A_\mu A_\nu]_{fg}$ and the number of pairs traversing unit area of a spherical shell scale as r^{-2} . This is a convenient feature of the photon pair field in the position basis, and provided all subsequent processes act equivalently on all photon pairs, it allows any relative (i.e. multiplicative) attrition of the field to be understood equivalently either in terms of a relative reduction in the field amplitude, or a relative reduction in the number of participating pairs.

7:3.2.2 Interactions of the photon pair field

Once a pair of foreground photons has been emitted by a matter source, that pair may propagate radially unchanged, or may undergo interactions. To understand these processes, it is helpful to study the behaviour of a photon pair on propagation across an infinitesimal interval $[r, r + dr)$. By requirement that the photon be capable of interacting, but that an infinitesimal interval be unsubdividable, each photon undergoes one interaction within such an interval. Free propagation is represented by treating the propagator term of the Lagrangian, $\frac{1}{2}A_\mu \Delta^{\mu\nu} A_\nu$, as a vertex. This is represented diagrammatically in Fig. 7.3.

In addition to the emission of foreground photon pair fields, a charged fermion necessarily also interacts with background photon pairs to yield the mass interactions discussed in Chapters 4 and 6. Figure 7.4(i) shows a pair of photons arising from the background field at a radius between r and $r + dr$ and propagating inward to interact with a fermion in the source. In general such diagrams make vanishingly small contributions to particle mass for $r \gg \mathcal{L}_0$, but it must nevertheless be asked whether they contribute to the photon pair field at $r' < r$. This may be answered in the negative by considering emulation of foreground fields under the $\overline{\text{MS}}$ normalisation scheme, and recognising that Fig. 7.4(i) is the zeroth order term in the mean field expansion of Fig. 7.4(ii), which belongs to the Proper Self Energy (PSE) series of the source fermion. All such diagrams are accounted for in the renormalised foreground fermion propagator,

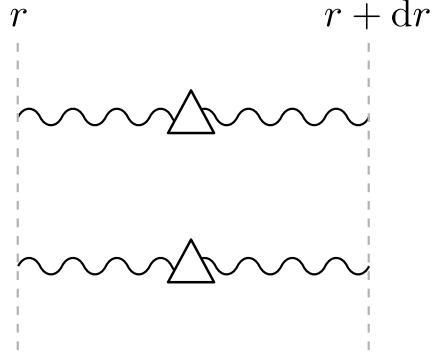


Figure 7.3: Free propagation of a pair of photons across interval $[r, r + dr]$, with the propagator term of the Lagrangian represented as an interaction vertex Δ .

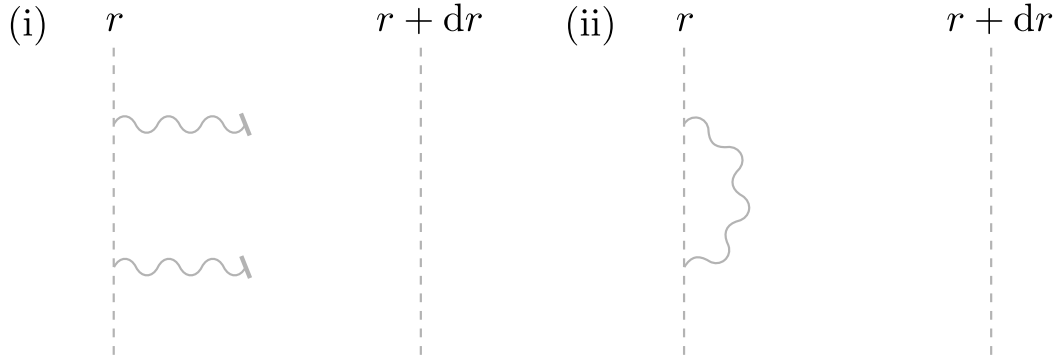


Figure 7.4: (i) A pair of photons arising from the pseudovacuum in interval $[r, r + dr]$ propagates radially inward and interacts with a fermion in the matter source of the foreground photon pair field. The symbol \backslash denotes origin within the local pseudovacuum. (ii) The parent figure for diagram (i) reveals this to be the mean field expansion of a term in the Proper Self Energy (PSE) of the source fermion. Pseudovacuum photons are shown in grey.

and so may be discounted, as per Sec. 4:3.1.

It is next necessary to understand what further processes do take place within the propagating foreground photon pair field. A great many of these processes may be discounted for a wide variety of reasons, including the following:

- As in Fig. 7.4, any diagram which is itself part of the PSE series of the source fermion, or whose parent diagram is part of the PSE series of the source fermion, may be discounted as (regardless of r) it is accounted for in the propagator of the source fermion. Further examples include Figs. 7.5(i)-(ii), (iv), and (vii)-(viii).
- Any diagram for which the only possible parent diagrams are tadpole diagrams must also vanish. An example is given by Fig. 7.5(iii).
- Any diagram in which a $G^{(\dagger)}$ boson couples to a background photon must have vanishing net effect (whether singly or pairwise) when averaged over length scales greater than \mathcal{L}_0 . Otherwise background photons could generate $G^{(\dagger)}$ boson pairs, and these in turn would necessarily have background character, in violation of gauge choice (3.56). Examples include Figs. 7.5(i) and (v)-(x).
- Diagrams involving an odd number of fermion lines may be eliminated using a generalisation of Furry's theorem. If a diagram or set of diagrams remain invariant when left- and right-handed representations are interchanged, corresponding to reversal of all arrows on the diagram and replacing

$$\bar{\psi}\bar{\sigma}^\mu\psi \rightarrow \psi\sigma^\mu\bar{\psi} = -\bar{\psi}\bar{\sigma}^\mu\psi, \quad (7.5)$$

it follows that that set of diagrams must vanish. Examples include Figs. 7.5(ii) and (ix)-(x), with diagrams (ix)-(x) forming a set which map into one another on arrow reversal, and therefore collectively cancel.

- Any diagram which gives mass to the photon may be discounted by gauge choice (3.60) (with subsequent higher-order corrections as per Sec. 5:3.1). Examples include Figs. 7.5(vii)-(viii).
- Any diagram in which pseudovacuum couplings explicitly give rise to mass for any of the constituent particles may also be ignored. Examples include Figs. 7.5(iii)-(iv), in which pseudovacuum photon coupling gives mass to the electron. [As with many of the examples in Fig. 7.5 these particular diagrams have multiple reasons to be ignored—the parent of diagram (iii) is a tadpole, and the parent of diagram (iv) belongs to the PSE expansion of the source fermion propagator.]

Regarding why diagrams containing mass interactions may be ignored, recognise that foreground species other than photons and $G^{(\dagger)}$ bosons may either acquire mass as a result of interaction with the background fields, placing them in any generation, or they may be ephemeral—generationless and massless—if they only exist over scales of $O(\mathcal{L}_0)$ or less in the isotropy frame. Both situations are in principle admissible in photon pair decay processes, and thus both massive and massless propagators must be taken into account when evaluating decay processes, unless otherwise constrained. Diagrams in which the foreground propagators are massive implicitly incorporate all diagrams in which pairs of background photon interactions behave as mass vertices as per Chapters 4–6, and thus these pseudovacuum interactions do not need to also be considered separately.

Now consider only diagrams not eliminated by the above considerations. In the large- r limit the most important diagrams in evaluation of the foreground pair field are those with the least-negative exponent in the radial co-ordinate. As examples of candidate processes, consider the

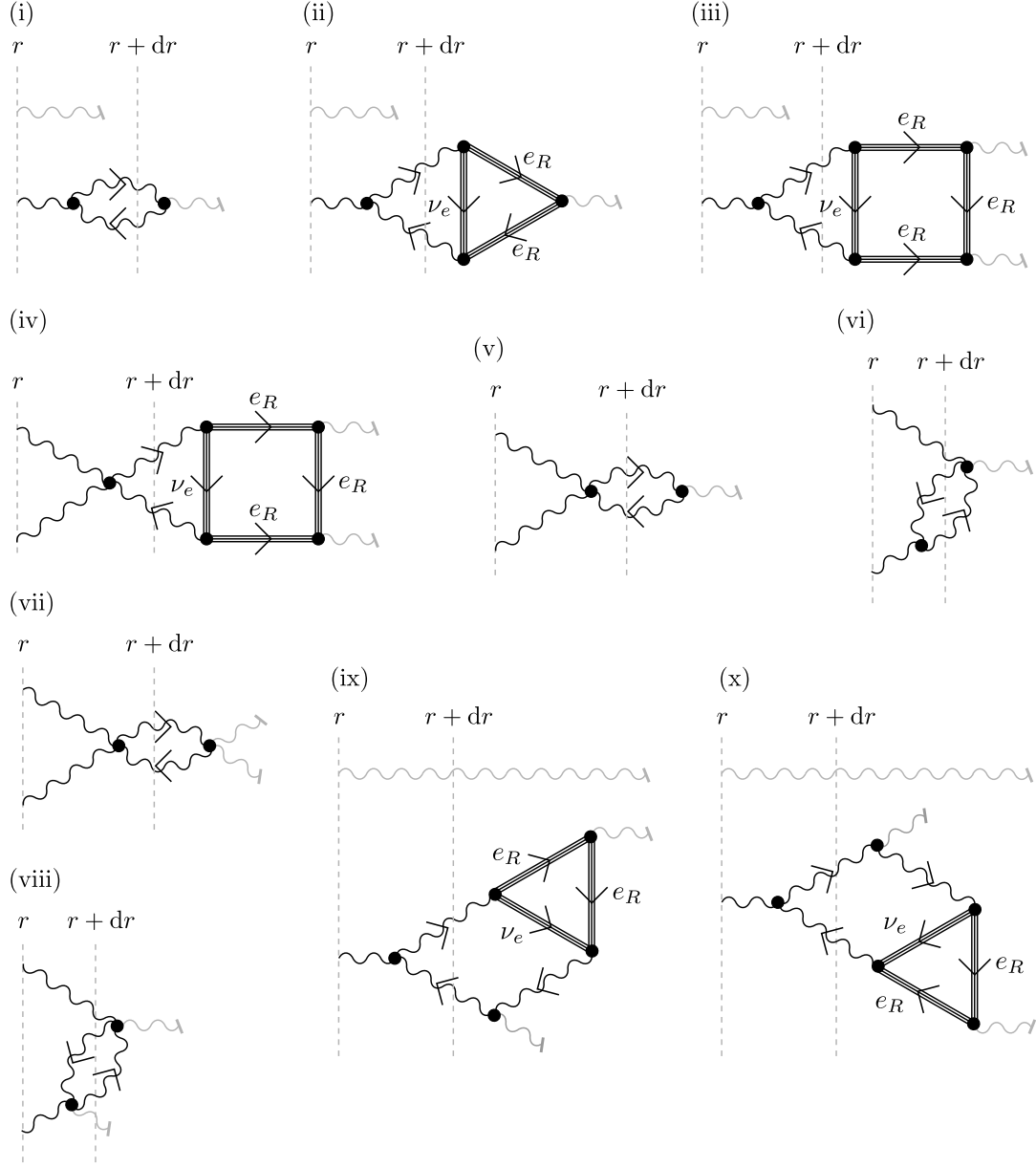


Figure 7.5: Candidate diagrams for processes occurring within the photon pair field. Boson lines without an arrow represent photons, and boson lines with an arrow represent G bosons. Disruption of the pair occurs within interval $[r, r + dr)$. Species may be massive with generations, or if existing over time and distance short compared with \mathcal{L}_0 they may lack interactions with the pseudovacuum and be massless and without generation. Note that by Sec. 1:3.8.6, all interactions involving only background fields may be ignored. Consequently, background photons attract no vertex in interval $[r, r + dr)$. When the propagation term is treated as a vertex, it is necessarily included in this treatment.

$G^{(\dagger)}$ -mediated diagrams shown in Fig. 7.6. The presence of a radially outbound photon indicates that these diagrams do not belong to the PSE of the source fermion propagator, and although neutrality of the matter source implies that the *average* value of the outbound foreground photon field must vanish, for any individual photon pair it may be non-zero. Furthermore, in contrast with Figs. 7.5(i) and (v)-(x), there is no gauge-induced requirement that this process have vanishing impact on the photon pair field as a whole. Indeed, if the source is examined fermion by fermion, these processes may be understood instead as making a fairly high-order contribution to the gyromagnetic anomaly of the electron.

Although shown as $G^{(\dagger)}$ bosons in Figs. 7.5-7.6, the circulating off-diagonal boson in these processes may in principle be any of W , G , or \mathbf{a}^{12} . The latter is functionally eliminated by extension of gauge choices (3.45) and (3.55) to all energy scales as described in Sec. 3:3.3.7, but the remaining processes—involving either G or W bosons—are potentially non-vanishing, and are all beyond-Standard-Model processes due to the presence of K -matrices in the emission vertices as per Fig. 7.2(ii).

Specialising first to the $G^{(\dagger)}$ bosons, the requirement that these bosons do not couple to the background photon field implies that all photons in Figs. 7.6(i)-(ii) are foreground, and thus the diagrams scale as r^{-3} . In contrast, although Fig. 7.6(iii) is of much higher order in the coupling constant $f = 1.669540(95) \times 10^{-8}$, it is seen in Sec. 7:3.3.1 to scale as r^{-1} and is thus of greater importance in the far field regime. Parent diagrams for Fig. 7.6(iii) prior to mean-field expansion are shown in Figs. 7.6(iv)-(v), noting that in order to affect the boson pair count in interval $[r, r + dr)$, only the initial decay of one member of the photon pair need take place within that interval; the rest of the diagram may be evaluated over any length scale. It is then convenient to evaluate the other photon of the pair by substituting the pseudovacuum term of the mean field theory expansion. Further, by overall neutrality of the matter source (which is made up of both electrons and positrons), the average onward-propagating photon field necessarily has net zero foreground component, and thus the average total photon field on the outbound leg *also* evaluates to the pseudovacuum field. Nevertheless, diagrams (iv) and (v) are distinguishable as it is possible to spatially discriminate between the mean-field term of a photon inbound from r and the nonvanishing component of a photon outbound to $r + dr$.

It may at first appear problematic that Fig. 7.6(iii) is being evaluated in a mean-field limit in which the outbound component of the foreground fields vanishes. However, recall that an inverse-square biphoton field mediates no net force transfer beyond that accounted for by its individual constituents, and it is therefore unnecessary for an interaction which reduces the photon pair field to exhibit any net (average) transfer of momentum from this pair field to elsewhere. Further, in the present context (with a net electrically neutral source) the single-photon exchange process likewise mediates no force. Thus the radially outbound single-photon field carries an average foreground momentum of zero, and reduces to the background component on average in the mean-field limit. Consequently, although Fig. 7.6(iii) has no net outbound foreground particle species, it may nevertheless result in a reduction in the *number* of photon pairs.

Ironically, on mapping negative energy outbound pairs into positive energy inbound pairs, the resulting deviation from inverse-square decay does now result in an imbalance between the outward and inward photon pair pressures (with decay occurring more rapidly in the lower- r , higher-field regime), and may be anticipated to yield a net attractive force between neutral bodies not corresponding to any process in the Standard Model. This effect is small, so there is no immediate need to engage in a perturbative calculation to evaluate second- and higher-order effects, and to present accuracy it suffices to adopt a co-ordinate frame on $\mathbb{C}^{\wedge 18}$ in which the photon pair number density obeys the expected inverse-square profile with respect to the connection on the $SL(2, \mathbb{C})$ subframe. The coupling of the photon to GG^\dagger pairs in Fig. 7.6(iii) is thus supplanted by an equivalent coupling to space-time curvature, which is by construction

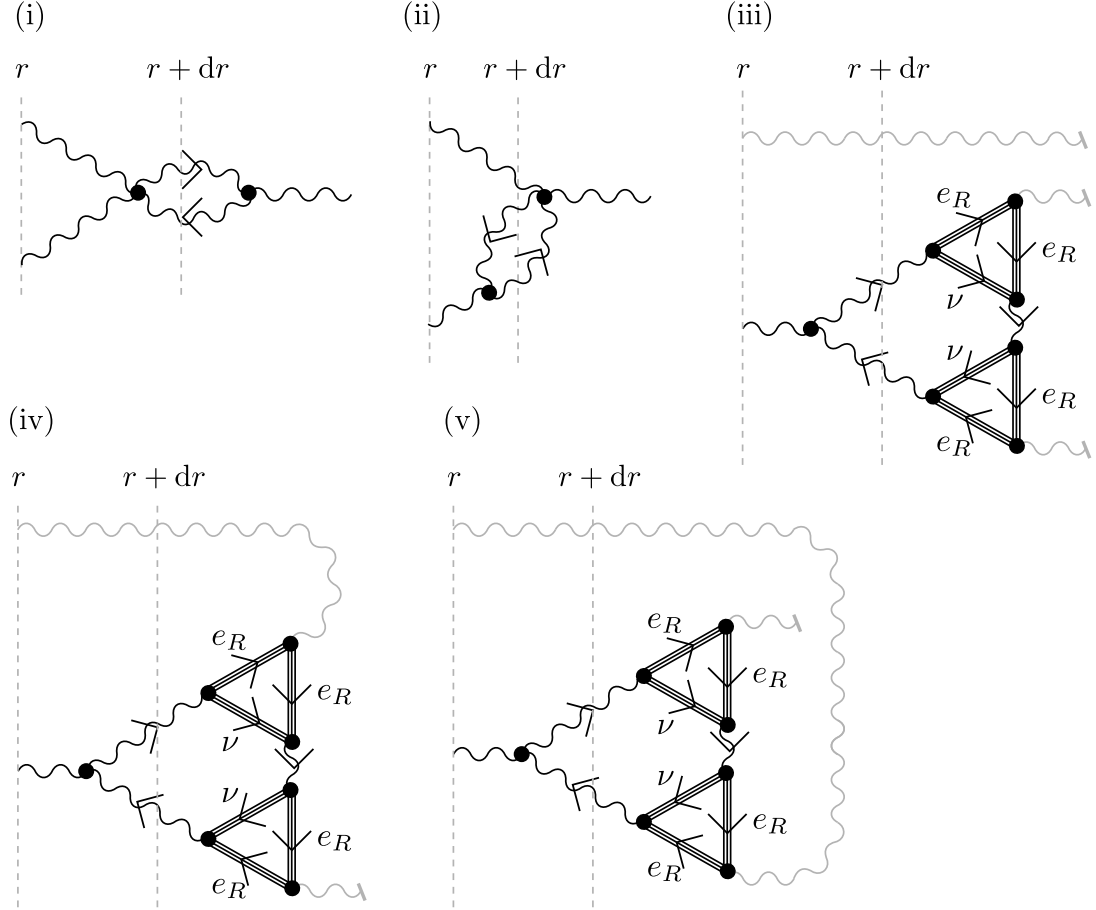


Figure 7.6: Example diagrams not eliminated by the considerations of Sec. 7:3.2.2. Bosons with no arrows are photons, and bosons with arrows are $G^{(\dagger)}$ bosons. Background bosons are shown in grey. Diagrams (i)-(ii) are $O(f^3)$ in vertex coefficients, but scale as r^{-3} so in the far field they are supplanted by diagram (iii), which is of $O(f^7)$ but is seen in Sec. 7:3.3.1 to scale as r^{-1} . Diagrams (iv)-(v) are parent diagrams for diagram (iii), meaning that they yield it as the zeroth-order term of mean-field expansion about the pseudovacuum state for the indicated photons.

a true space–time curvature on the manifold which is the target of mapping \mathcal{G} .

As noted above, every diagram in Figs. 7.5–7.6 also has a counterpart in which the $G^{(\dagger)}$ bosons are replaced by $W^{(\dagger)}$ bosons. However:

- $G^{(\dagger)}$ bosons are massless over all length and timescales, whereas $W^{(\dagger)}$ bosons are massive over scales large compared with \mathcal{L}_0 , and
- there is no requirement that the $G^{(\dagger)}$ or $W^{(\dagger)}$ loop in these figures should be small compared with \mathcal{L}_0 . (This is discussed further in Sec. 7:3.3.) Thus behaviour in the low-energy regime is dominated by $\mathcal{L} > \mathcal{L}_0$ in which the W boson is massive but the G boson is not.
- The classical limit of the photon field around a point source may be understood as a superposition of positive and negative energy massless virtual photons. Thus massive W boson loop processes in the photon pair field are heavily disfavoured relative to massless G boson loops.

Taking all of this into account, now observe that electromagnetically neutral composite bodies are ubiquitous on classical scales, and the K -augmented emission process of Fig. 7.2(ii) is thus likewise widespread. As a result, so are the $G^{(\dagger)}$ -mediated decay processes which take place throughout the supported photon pair fields. It is postulated that Fig. 7.6(iii) is the highest-weight beyond-Standard-Model diagram affecting the photon pair field in the large- r regime.

In regions where $G^{(\dagger)}$ -mediated photon pair decay is the dominant beyond-Standard-Model process, it then follows that space–time curvature in the large- r regime, and thus Newton’s Constant, may be obtained from evaluation of Figs. 7.6(iv)–(v). This calculation is performed in Sec. 7:3.3.

7:3.2.3 Principle of equivalence

The above discussion has addressed photon pair emission from a prototype source comprising left- and right-handed electrons and positrons. However, for higher-generation leptons, mass is augmented by the K matrices and these appear identically in the fermion mass interaction and in the K -augmented photon pair emission process, with net result that all leptons support the beyond-Standard-Model processes in photon pair fields of Fig. 7.6 at a rate identically proportional to their mass. Anticipating Sec. 7:3.3.3, in which these processes are mapped to space–time curvature, this equivalence of proportion implies the weak principle of equivalence for leptons (equivalence of gravitational and inertial mass).

The mass mechanism for quarks is identical to that for leptons. It may therefore be reasonably anticipated that quarks will also respect the weak principle of equivalence.

With baryons also being composite fermions, let it be assumed that the baryon mass mechanism is the natural extension of the quark mechanism, with inertial mass being determined by coupling to background boson fields and by the nine-preon/three-quark counterpart to operator $\hat{\mathcal{K}}_\mu$ (4.25). In addition to their preonic constituents, baryons also contain the gluons which bind them together—but then, so do leptons and quarks. Under the assumption that the confinement scale \mathcal{L}_ψ is much smaller than \mathcal{L}_0 , the gluons are not in general able to participate in any mass interactions over their individual lifetimes. They therefore behave as particles without inertial mass, and consequently without gravitational mass. The sole exception to this is the unconfined “neutral gluon” N_μ . However, this particle is not associated with the dimension-8 representation of $SU(3)_C$ and thus is not a participant in the preon or quark confinement interactions. With the gluons being essentially massless, any transient appearances of gluons within a baryon may simply be viewed as variety in the associations of the preon lines making up the baryon (including brief time-reversals in trajectory, and the appearance of temporary loops of characteristic scale

less than \mathcal{L}_0 , which are thus normed to 1). The net preon composition, which interacts with the nine-preon analogue of $\hat{\mathcal{K}}_\mu$, remains unchanged. It is therefore reasonable to anticipate that baryonic matter also respects the weak principle of equivalence.

Indeed, the only exception of any significant abundance is likely to be the neutral gluon, N_μ . This particle has an inertial mass of 80.42812(42) GeV/ c^2 (Table 6.5), but its coupling to the photon pair field (via the universal coupling mechanism of Sec. 6:4.2.2.b) is smaller by a factor of $99/\{18[k_1^{(e)}(\mathcal{E}_e)N_0]^4\} = 1.52774(12) \times 10^{-3}$. If the N_μ boson exists in any significant quantity, it has substantial inertial mass (making it a Weakly Interacting Massive Particle or WIMP) and also supports a photon pair field (which is the prerequisite for the gravity-like interaction of the $\mathbb{C}^{\wedge 18}$ model). It is therefore a candidate for an interesting species of dark matter which breaks the weak principle of equivalence (equivalence of gravitational and inertial mass).

7:3.3 Evaluation of space–time curvature

This Section calculates the metric in the vicinity of a nonrotating electrically neutral body, including the value of Newton’s Constant. Extension to incorporate conceptually important subleading effects is discussed in Sec. 7:3.4, though these processes are numerically irrelevant in the large- r regime at current numerical precision.

7:3.3.1 Leading-order photon pair decay profile

To evaluate the photon pair field decay profile as a function of radius, first note the following:

- As per Sec. 7:3.2.3, the photon pair field support is expected to scale identically with inertial mass for all fermionic species, so for convenience let any mass M be represented by the already-discussed prototypical chargeless, spinless neutral body made up entirely of electrons and positrons.
- Functionally the propagator term of the Lagrangian behaves as a two-particle vertex, structurally equivalent to the mass vertex but acting with the momentum operator k_μ in lieu of the rest mass operator (which takes the form $[m, 0, 0, 0]$ in the rest frame of the particle).
- On radial propagation the photon pair field supported by a mass M exhibits decay as r^{-2} , such that on propagation from r to $r + dr$ the photon pair field experiences a geometrically induced decrease according to the corresponding infinitesimal relationship

$$A_\mu A_\nu \longrightarrow A_\mu A_\nu \left(1 - \frac{2dr}{r}\right). \quad (7.6)$$

This is associated with Fig. 7.3.

- Alternatively, the photon pair may undergo decay in accordance with Figs. 7.6(iv)-(v). Normalising these diagrams with respect to the radial propagation of Fig. 7.3 introduces the quantity $I(r)$, defined in Fig. 7.7. The pair propagation of Fig. 7.3 yields a relative decay of the pair field of $-2dr/r$, as in Eq. (7.6) above, so that associated with Figs. 7.6(iv)-(v) is weighted by a further factor of $I(r)$ to yield a contribution of $-2I(r)dr/r$.
- The net relative decay of the photon pair field on propagation from r to $r + dr$ is thus given by

$$A_\mu A_\nu \longrightarrow A_\mu A_\nu \left[1 - \frac{2dr}{r} - \frac{2I(r)dr}{r}\right]. \quad (7.7)$$

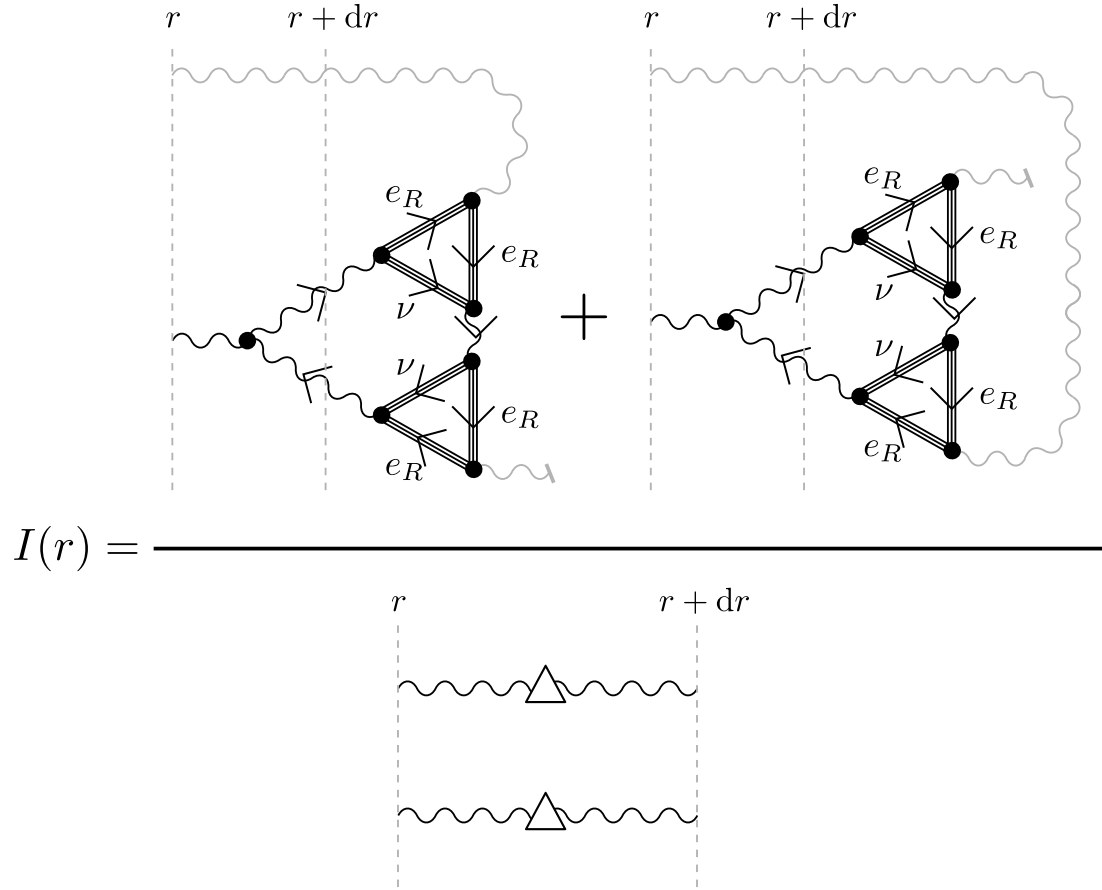


Figure 7.7: Relative weight of diagrams associated with photon pair decay, normalised with respect to photon pair propagation. If the latter is associated with a relative decay of $-2dr/r$, then the former is associated with $-2I(r)dr/r$ where $I(r)$ is defined as above.

Evaluation of ratio $I(r)$ may be broken down into a series of stages. First, recognise that the behaviour under study is the radial decay of foreground photon pairs. Consider the denominator, and recognise:

- The multiplier of $\left[k_1^{(e)}(\mathcal{E})\right]^4$ on Fig. 7.2(ii) may be interpreted as a modifier to the vertex factor which changes the rate of foreground photon pair emission. Thus each photon line inbound or outbound in the denominator of Fig. 7.7 is associated with a factor of $\left[k_1^{(e)}(\mathcal{E})\right]^2$.
- For a prototype body made up entirely of electrons and positrons, the characteristic particle energy \mathcal{E} corresponds to $\mathcal{E}_e = m_e c^2$.
- Although the objects of study are foreground fields, over an interval of width dr the foreground and background fields are not clearly distinguishable. Although the number of photon pairs in the foreground field is clearly determined, the foreground momentum is distributed across all preons with correlators consistent with photon pairs within this region. In the large- r regime the average momentum of a photon within a pair is that of the pseudovacuum, up to a small foreground perturbation. On-shell, the propagation operators thus evaluate as

$$\Delta^{\mu\nu} \rightarrow k^\mu k^\nu \rightarrow -\delta^{\mu\nu} \omega_0^2. \quad (7.8)$$

- To evaluate FSF symmetry factors:
 - Recognise that the interval $[r, r + dr)$ is small compared with \mathcal{L}_0 and there are four foreground preons inbound (two from r and two from $r+dr$) and four preons outbound, each of which may be of type $a = 1$ or $a = 2$. Colour is summed over and net neutral across the foreground fields, so may be ignored. There are also N_0 inbound and N_0 outbound background preons for any given charge labelling.
 - All inbound preons participate in equivalent interactions, so their associated FSFs are interchangeable. Likewise for all outbound preons.
 - First assume all inbound foreground preons have the same A -charge; conservation of charge requires that the outbound charges be the same. The first photon line in the diagram may incorporate any one of the $N_0 + 4$ inbound preons (or more strictly, incorporates one specific inbound preon but this may be associated with any of $N_0 + 4$ eligible FSFs), and any one of the four $N_0 + 4$ outbound preons (ditto). Up to a normalisation factor, the corresponding sources/sinks are associated with a FSF symmetry factor of $(N_0 + 4)^2$. The second photon yields $(N_0 + 3)^2$, and so on. There are two choices of the A -charge involved ($a = 1$ and $a = 2$). This yields two configurations each with a factor of $[(N_0 + 4)(N_0 + 3)(N_0 + 2)(N_0 + 1)]^2$.
 - Next, consider configurations where one inbound preon has a different charge to the others. There are eight such configurations, each yielding a factor of $[(N_0 + 3)(N_0 + 2)(N_0 + 1)^2]^2$.
 - Finally, there are six configurations in which two inbound preons have charge $a = 1$ and two have charge $a = 2$, for a factor of $[(N_0 + 2)(N_0 + 1)]^4$.
 - Normalisation with respect to background fields as per Sec. 1:3.8.6 requires that for a single background photon field source/sink the FSF symmetry factor goes to 1. That is, in the absence of foreground fields the source/sink attracts a factor of N_0^2 and this is then divided by N_0^2 .

- As all photons in the above factors are foreground, the number of background FSFs available is constant at N_0 for every term, so

$$\begin{aligned}
(N_0 + 4) &\rightarrow N_0^{-1}(N_0 + 4) \\
(N_0 + 3) &\rightarrow N_0^{-1}(N_0 + 3) \\
&\vdots
\end{aligned} \tag{7.9}$$

- For each of these configurations, the same symmetry factors apply at the propagation operators (considered collectively) as at the sources/sinks (considered collectively), though without requiring the N_0^{-1} normalisation factor. Instead, Sec. 1:3.8.6 is taken to imply that no vertex should be drawn which involves only background fields.
- The net FSF symmetry factor associated with the sources and sinks is thus

$$N_0^8 S_{\Delta\Delta} \tag{7.10}$$

where $S_{\Delta\Delta}$ is a correction of $O(1)$ given by

$$\begin{aligned}
S_{\Delta\Delta} := & \{2[(N_0 + 4)(N_0 + 3)(N_0 + 2)(N_0 + 1)]^4 \\
& + 8[(N_0 + 3)(N_0 + 2)(N_0 + 1)^2]^4 \\
& + 6[(N_0 + 2)(N_0 + 1)]^8\} / (16N_0^{16}).
\end{aligned} \tag{7.11}$$

- Following construction of the photons, their connection to the propagation vertices attracts a symmetry factor of sixteen:
 - The first photon (let this be a photon inbound from r) may be connected to any of the four connection points on the two propagation vertices: Factor 4.
 - The second photon at the same radius must be connected to one of the two connection points on the other propagation vertex: Factor 2.
 - The first of the remaining two photons may be connected to the remaining connection point on either of the propagation vertices: Factor 2.
 - The final photon has only one possible connection: Factor 1.
- The net factor associated with the denominator is thus

$$16 \left[k_1^{(e)}(\mathcal{E}_e) \right]^8 \omega_0^4 N_0^8 S_{\Delta\Delta}. \tag{7.12}$$

Now consider the numerator:

- Figures 7.6(iv)-(v) both evaluate to the same value, therefore specialise to Fig. 7.6(iv) and multiply by two.
- The lower photon in the pair inbound at r is required to be foreground as it interacts with the $G^{(\dagger)}$ fields. The upper photon may be foreground or background, and the contribution of the diagram will be dominated by the background terms at large r .
- The foreground photon decay vertex within interval $[r, r + dr)$ is associated with a factor of $f/\sqrt{2}$.

- The vertex (propagation or otherwise) within this interval which acts on the other member of the photon pair is not shown. Figure 7.6(iv) is dominated by contributions in which this member evaluates to the background term, and while a background photon may indeed undergo an interaction within interval $[r, r + dr)$, its effect on Fig. 7.6(iv) is normed away as per Sec. 1:3.8.6.
- Note that the vertex in Fig. 7.6(iv) in which this background photon does engage *may* be within interval $[r, r + dr)$ but is not required to be—the value of the diagram is independent of the radius at which this vertex is evaluated.
- Since only the lower photon inbound from r is foreground, only that photon attracts a factor of $\left[k_1^{(e)}(\mathcal{E}_e)\right]^2$. In conjunction with the quantum/classical correlation of Sec. 7:2.2, the net classical factor associated with the photon field of a single pair at the lower vertex is thus $\left[k_1^{(e)}(\mathcal{E}_e)\right]^2 / r$.
- There are M/m_e fermions capable of acting as sources of such a pair, so this factor is multiplied by M/m_e to yield $\left[k_1^{(e)}(\mathcal{E}_e)\right]^2 M/(m_e r)$.
- A momentum operator $i\partial_\mu$ also acts at this vertex.
 - It may act on the photon field, the G field, or the G^\dagger field, with the weights of the latter two processes being half that of the former.
 - As previously discussed for the denominator term, the momentum associated with the foreground photon field is distributed across all photons within the local correlation region. On average the background contribution vanishes, but *instantaneously* the action of the derivative operator on the A_μ field at this vertex is given by $N_0^2 i\omega_0$, up to an arbitrary sign and a small perturbation representing the foreground field superimposed on the pseudovacuum. The factor of N_0^2 arises from the choice of FSF fields which may be acted on by the chiral derivative operators making up the background photon whose momentum is then evaluated.
 - There is a further factor of $\frac{1}{2}$ from the structure constants of $SU(3)_A$.
 - The terms in which the derivative operator acts on G and G^\dagger may be ignored as there are no background $G^{(\dagger)}$ fields and the contributions which these terms yield are thus negligible at large r .
- The subsequent completion of the decay process, which may take place outside interval $[r, r + dr)$, contains a further six vertices which yield a factor of $f^6/2$.
- Two of these vertices involve pseudovacuum photons. As this portion of the diagram is not constrained to take place within interval $[r, r + dr)$, in order to be non-vanishing these vertices must be within the same autocorrelation region of the pseudovacuum (i.e. within distance and time \mathcal{L}_0 of one another in the isotropy frame). Up to FSF symmetry factors, they therefore evaluate to $-\omega_0^2$.
- The FSF symmetry factors associated with the interaction vertices in Fig. 7.6(iv) are illustrated in Fig. 7.8.
- There is a symmetry factor of 2 associated with the interchangeability of the two fermion triangles within the G boson loop.

- Regarding particle masses in Fig. 7.6(iv):
 - On-shell photons and $G^{(\dagger)}$ bosons are massless.
 - The neutrino-family and electron-family particles may be massive or massless, with the latter being favoured over scales small compared with \mathcal{L}_0 . With the two background photon interactions being within a single autocorrelation region, the portion of the diagram connecting these two vertices may either incorporate a path which remains within the autocorrelation region and is therefore made up of massless particles, or it may be that for any path from one vertex to the other, one or more particles ventures outside of the autocorrelation region and thus (with the exception of the G boson) may be anticipated to acquire mass. To then return to the original autocorrelation region and connect with the other background vertex then involves a significantly off-shell trajectory. Thus interactions are anticipated to be dominated by conditions in which there exists at least one series of massless propagators connecting the two background photon interactions. Thus at least one of the electron lines in each triangle is massless.
 - For Fig. 7.6(iv) it then follows directly that the closest diagrams to on-shell are those in which either
 - * all fermions are massless, or
 - * the neutrino and one electron in each triangle are massive but the location of the vertex involving both of these fermions is chosen such that the participating G boson is also off-shell, and the off-shell contribution from massive fermion propagation cancels a similar off-shell contribution from the G boson propagation.

In this latter scenario the loop as a whole couples to external fields as if all participating particles were massless. In Sec. 7:3.3.2.a it is argued that contributions dominate in which one of the fermion vertices in each triangle is outside the correlation region, favouring the massive fermion solution. However, for purposes of the present leading-order calculation, the anticipated cancellation of off-shell contributions in this scenario permits the loop as a whole to be treated as if made up of massless species.

- Examining the fermion triangles, at each vertex the interaction is averaged over three preons equivalent up to colour. The result is numerically unchanged by replacing each with a single interaction multiplied by a factor of three.
- If this is done so as to bring each vertex onto the same preon within each loop, as per Fig. 7.9(i), then two of the preons within each loop are now free loops. In the massless regime, diagrammatic isotopy techniques (or equivalently, vacuum normalisation) give that such loops evaluate to 1. This leaves four superfluous FSFs at each vertex, but these are cancelled by the factors of $f = \langle \varphi \rangle^{-1}$ appearing in the definition of the fermion operators (3.28), so may also be removed for an average factor of 1.
- Up to differences in FSF symmetry factors, the remaining unevaluated preons in the fermion loop are then seen to be equivalent to G bosons, as per Fig. 7.9(ii), permitting reduction of the loop structure of Fig. 7.6(iv) to that of Fig. 7.9(iii). Note that this reduction is only valid up to a factor of $f^4(N_0 + 2)^2(N_0 + 1)^2N_0^4$ corresponding to vertices and FSF symmetry factors present in Fig. 7.6(iv) but not in Fig. 7.9(iii).
- Selecting out a specific subdiagram as per Fig. 7.9(iv) permits evaluation of the resulting G boson loop to yield a factor of $1/(4\pi)$.

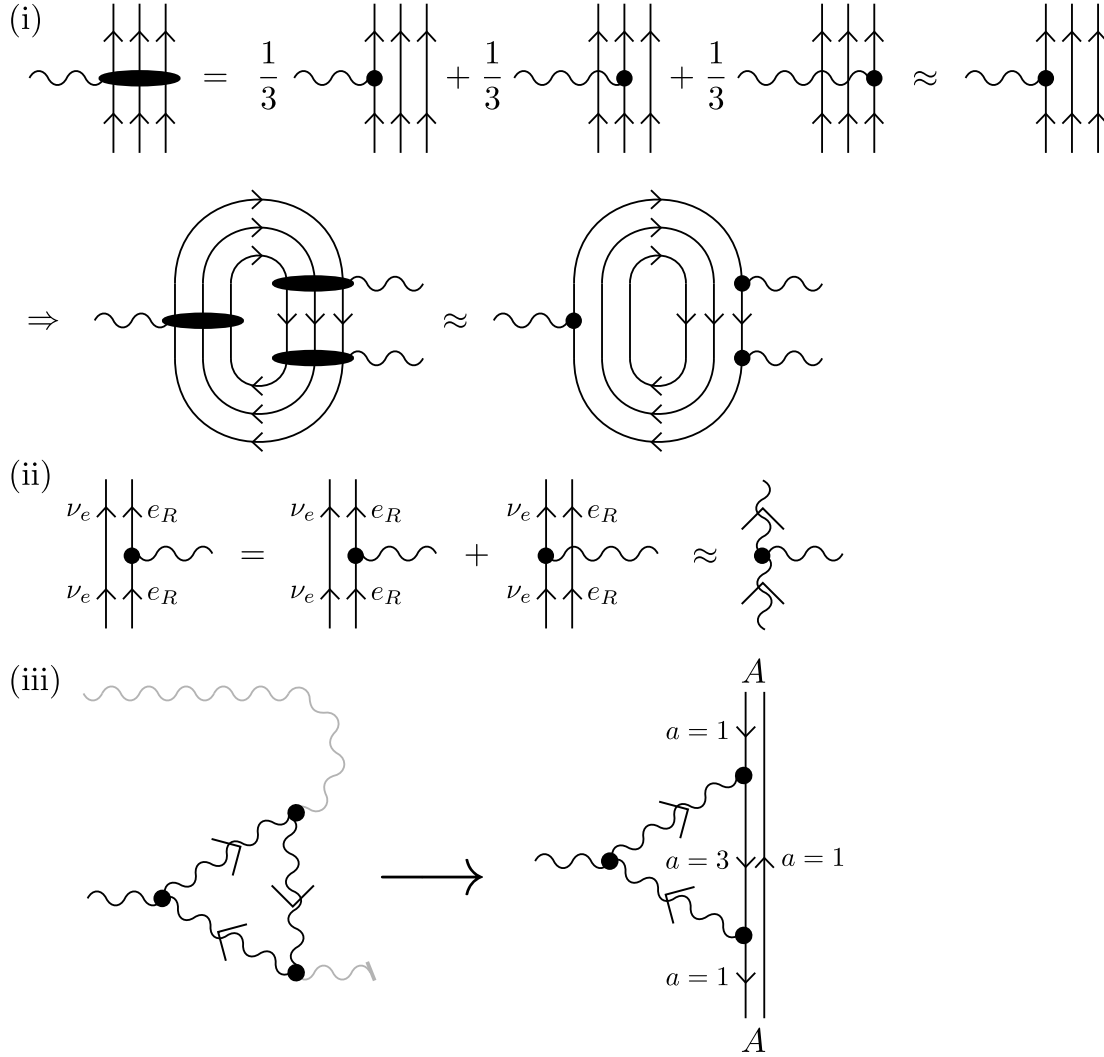


Figure 7.9: (i) Interaction vertices involving fermions are averaged over three different internal configurations. However, it is numerically equivalent to replace these interactions with a single interaction weighted by a factor of three. In the fermion loops of Fig. 7.6(iv) this permits two fermion loops to be disconnected, and thus mapped to vacuum fluctuations and evaluated to yield factors of 1. (ii) The neutrino is associated with preons having $a = 3$. Since these preons have no electric charge, the interaction of the photon with the $a = 1$ preon is equivalent to the total interaction of the photon with the entire preon pair. Up to considerations of FSF symmetry factors, this preon pair is equivalent to a G boson. The loop structure of Fig. 7.6(iv) therefore reduces to a single G boson loop as shown in diagram (iii), up to a numerical factor of $f^4(N_0+2)^2(N_0+1)^2N_0^4$ corresponding to vertices and FSF factors present in Fig. 7.6(iv) but not in this diagram. If the preon decomposition of some of the bosons in diagram (iii) is made explicit, the resulting diagram may be understood as a loop correction to photon emission/absorption by a preon with $a = 1$. (The photon also contains terms with $a = 2$ but these do not couple to the $G^{(\dagger)}$ fields, and this is accounted for in the factor of $1/\sqrt{2}$ on the A/G coupling coefficient.) The loop boson is massless but chiral, and the loop thus evaluates to a factor of $(f^2/2)(1/4\pi)$ as per Appendices 6: A-6: B, of which the vertex-related factor of $f^2/2$ has already been accounted for.

- Finally, note that Fig. 7.6(iv) incorporates the completed exchange of a foreground photon between a source at radius r (as proxy for the original neutral source) and the AGG^\dagger vertex, which attracts a factor of S_α . This is independent of, and in addition to, the other FSF symmetry factors in Fig. 7.8.

Putting this all together permits evaluation of the mean value of the numerator of $I(r)$, up to a sign arising from the derivative operator in the AGG^\dagger vertex. The mean magnitude of the numerator is given by

$$\frac{Mf^7 \left[k_1^{(e)}(\mathcal{E}_e) \right]^2 \omega_0^3 N_0^6 (N_0 + 2)^2 (N_0 + 1)^2 S_\alpha}{4\sqrt{2}\pi m_e r}. \quad (7.13)$$

Curiously, the sign of this term is unimportant. The interactions of Figs. 7.6(iv)-(v) unambiguously destroy photon pairs, whereas the ambiguity of the sign merely ensures vanishing of any emitted (net residual) species. For a neutral source this is already known. However, it is interesting to note that with a charged source, this summation over sign ensures that photon pair decay does not lead to any unexpected augmentation of the single-photon field.

The overall leading-order expression for $\langle |I(r)| \rangle$ is thus

$$\langle |I(r)| \rangle = \frac{Mf^7 N_0^2 S_G S_\alpha}{64\sqrt{2}\pi \left[k_1^{(e)}(\mathcal{E}_e) \right]^6 \omega_0 m_e r} \quad (7.14)$$

$$S_G := \frac{(N_0 + 2)^2 (N_0 + 1)^2}{N_0^4 S_{\Delta\Delta}}, \quad (7.15)$$

with the infinitesimal radial decay of the photon pair field taking the form

$$A_\mu A_\nu \longrightarrow A_\mu A_\nu \left(1 + \frac{2dr}{r} + \frac{2\langle |I(r)| \rangle dr}{r} \right). \quad (7.16)$$

7:3.3.2 Higher-order corrections

Two sources of higher-order corrections are evaluated in the present chapter. These are the $O(\alpha)$ corrections to Figs. 7.6(iv)-(v), and the $O(N_0^{-1})$ corrections associated with introducing additional bosons—initially the boson from the pair field, in Sec. 7:3.3.2.a, then also the loop boson of the $O(\alpha)$ correction in Sec. 7:3.3.2.c. Following the approach of Sec. 6:5.2.2, these are evaluated as a multiplicative corrections to the fundamental and $O(\alpha)$ terms respectively.

7:3.3.2.a The $O(N_0^{-1})$ corrections to the fundamental diagrams of Figs. 7.6(iv)-(v) are corrections which arise due to more than two vertices inhabiting the same correlation region. Regarding this:

- It is immediate that the two background field interactions must inhabit the same correlation region, in order that the mean field term does not vanish.
- These vertices are connected by a series of other species, which may be massless over scales small compared with \mathcal{L}_0 or massive over scales large compared with \mathcal{L}_0 .
- As the separation of the background vertices is at most $O(\mathcal{L}_0)$, the dominant contributions (being those closest to on-shell propagation) necessarily involve massless particles not leaving the correlation region.

- There therefore exists a chain of in-zone vertices connecting the two background field interactions.

Next, posit a minimal chain comprising the two background field vertices and two additional vertices. For the moment, ignore the AGG^\dagger vertex. For the remaining two vertices, being fermion/ $G^{(\dagger)}$ vertices, recognise that these two vertices are free to be in or out of the correlation region. However, deleting the correlation region from the path integral approximates eliding only a very small region from the manifold. The perturbations to push the vertex away from that near-pointlike region introduce infinitesimal corrections to particle paths, say with amplitude correction $O(\epsilon)$, and these corrections are symmetric in space and time and may therefore be anticipated to cancel. Overall, evaluation of the diagram is dominated by contributions where these vertices are *not* in the correlation region.

Finally, consider the AGG^\dagger vertex.

- When the adjacent vertices are not in the correlation region, nor is this vertex by the same argument about infinitesimal perturbations.
- When they *are* in the correlation region, then they are part of the chain connecting the background field interaction vertices. By the assumption that the diagram is dominated by terms close to on-shell, species in this chain are required to be massless, and the close-to-shell requirement then ensures that the AGG^\dagger vertex also lies within the correlation region.

As the diagram is symmetric under interchange of which G boson couples to the photon, these two scenarios carry equal weight, and thus there are on average 4.5 vertices within the correlation region, compared with two in the mass interactions of Chapters 4 and 5.

There are, however, no factors of $O(N_0^{-1})$ due to these additional vertices:

- The preons bringing in the foreground photon momentum must be foreground in character, and so can only arise from the scalar fields external to the region whose gradients correlate with those within the region, being in external momentum. At this order, this choice is unique.
- The $e_R \nu_e G^\dagger$ and $\bar{e}_R \bar{\nu}_e G$ vertices are not background, but do not bring external foreground momentum into the correlation region.
 - They form part of the loop circulating the introduced (net zero) foreground momentum, from the inbound preon within the inbound photon to the outbound preon within the inbound photon (up to beyond-mean-field interactions with the background field which do not need to be explicitly evaluated in the far field of the source).
 - By gauge they receive no background contribution as they involve $G^{(\dagger)}$ bosons.
 - Their momentum is thus not carried in a distributed fashion across all local FSFs, but rather the preons are in 1:1 correspondence with the FSFs from which they are constructed. If a preon which would have been inbound into the upper such vertex is interchanged with a preon inbound into the lower vertex, this results in a preon tadpole diagram on one of the two vertices. Interchange of their FSFs is therefore not permitted within the lowest-order diagrams of Figs. 7.6(iv)-(v).
 - The preons in the background interaction vertices are capable of participating in FSF exchange, but have no species left to exchange FSFs with other than each other, and this is already accounted for in the mean field term. There is therefore no further factor of $O(N_0^{-1})$ arising from these fields.

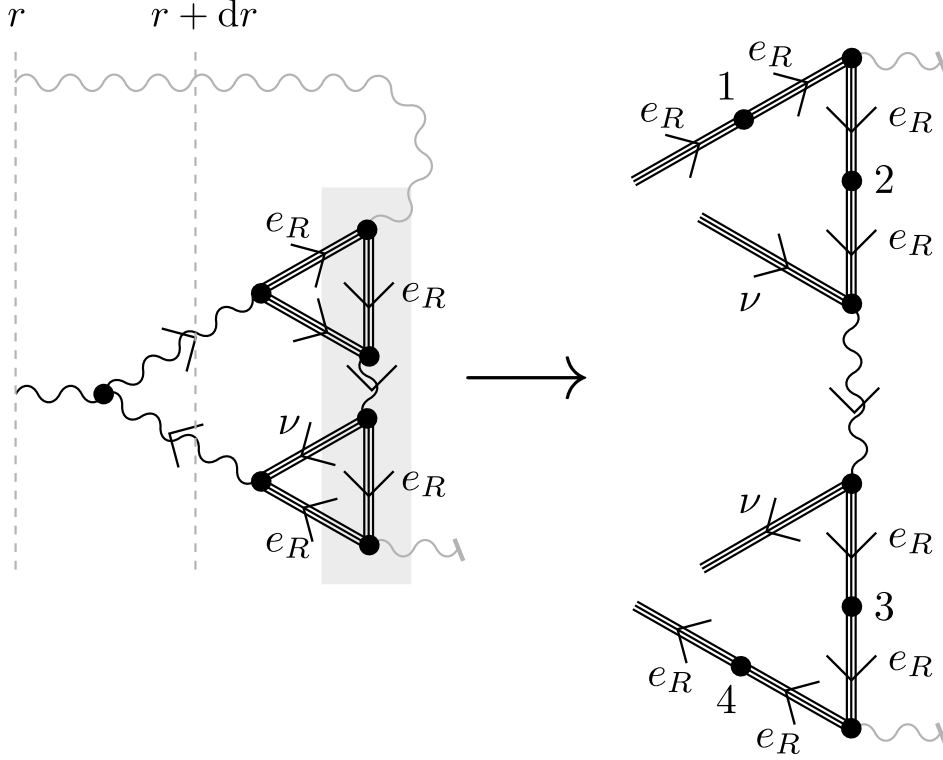


Figure 7.10: Six diagrams give rise to $O(\alpha)$ corrections to each of Figs. 7.6(iv)-(v). Considering Fig. 7.6(iv) and magnifying the area of interest as shown, these corrections are constructed by pairwise connecting the points marked 1-4. Diagram (i) corresponds to connection of points 1 and 2, diagram (ii) to connection of 1 and 3, diagram (iii) to connection of 2 and 4, diagram (iv) to connection of 3 and 4, diagram (v) to connection of 2 and 3, and diagram (vi) to connection of 1 and 4. These diagrams are readily visualised from the above Figure and thus are not drawn explicitly. An equivalent set of diagrams exists for Fig. 7.6(v). Note that although the G bosons carry an electromagnetic charge, their coupling is heavily suppressed due to the lack of a background G field and thus loop corrections with vertices on the G bosons may be ignored.

The resulting factor of $[1 + O(N_0^{-1})]$ due to additional vertices within the correlation region in Figs. 7.6(iv)-(v) therefore reduces to 1.

7:3.3.2.b The $O(\alpha)$ corrections to Fig. 7.6(iv) are given by Fig. 7.10, where the photon loops may be viewed as generating gyromagnetic anomaly-like corrections to the interactions with background fields and/or neutrino emission processes. Those for Fig. 7.6(v) are equivalent. The first step in evaluating these diagrams is to determine which loop vertices are within the same correlation region as the two interactions with the photons from the pseudovacuum. As observed in Sec. 7:3.3.1, at least one of the electron-family lines associated with the pseudovacuum interaction must be massless. However, the other is massive as per Sec. 7:3.3.2.a.

As also noted in Sec. 7:3.3.2.a, there are two possible choices regarding which vertices lie within a common correlation region; reading from top to bottom in Fig. 7.10, these are the

vertices lying along the particle chains

$$\begin{aligned} [A]_{\text{bg}} &\rightarrow e_R \rightarrow G \rightarrow e_R \rightarrow [A]_{\text{bg}} \\ [A]_{\text{bg}} &\rightarrow \bar{e}_R \rightarrow G^\dagger \rightarrow G^\dagger \rightarrow \bar{e}_R \rightarrow [A]_{\text{bg}}. \end{aligned} \quad (7.17)$$

Considering Fig. 7.10 diagram (i), one of the two ends of the loop correction photon is therefore on a massless electron within the correlation region, and the other connects to a massive electron, doing so either within or outside the local correlation region. For a loop correction of energy \mathcal{E}_ℓ , contributions are dominated by diagrams with loop vertex separation of $(2\mathcal{E}_\ell)^{-1}$ or less, as per Appendix 6: A. This may be substantially larger than \mathcal{L}_0 at low \mathcal{E}_ℓ , and the second vertex of the photon thus almost universally lies outside the local correlation region.

As in Fig. 7.9 it is recognised that with the neutrino being chargeless, couplings between the loop photon and an electron commute with couplings between the electron and a neutrino, up to any change in FSF symmetry factors. Thus, for example, the correction associated with Fig. 7.10 diagram (ii) is numerically equivalent to that associated with Fig. 7.10 diagram (i).

With only one end of the loop photon lying within the same local correlation region as the two pseudovacuum couplings, evaluation of Figs. 7.10 diagrams (i)-(iv) is without surprises and it follows immediately that each of is associated with a correction factor $\alpha/(2\pi)$, for a subtotal over these four diagrams of $2\alpha/\pi$. Similarly, both loop vertices in Fig. 7.10 diagram (vi) are outside the region and thus this diagram yields a further contribution of $\alpha/(2\pi)$. In contrast, however, both vertices of the loop correction in Fig. 7.10 diagram (v) are within the same correlation region as both pseudovacuum vertices. Following the approach described in Appendix 6: B, this diagram yields a symmetry-augmented contribution with weight α/π . The total corrections due to photon loops to $\mathcal{O}(\alpha)$ thus multiply Eq. (7.14) by a factor of

$$\left(1 + \frac{7\alpha}{2\pi}\right). \quad (7.18)$$

7:3.3.2.c The $\mathcal{O}(N_0^{-1})$ corrections to the $\mathcal{O}(\alpha)$ corrections are conceptually similar to those of Sec. 6:5.2.2. As already discussed, the loop corrections to Fig. 7.6(iv) presented in Fig. 7.10 may have between zero and two vertices within the same correlation region as the two background photons, and the same is true for the equivalent corrections to Fig. 7.6(v). The key question, however, is how many vertices exist within the same correlation region, and whether the preons in these vertices are capable of exchanging FSFs with the loop photon. In Sec. 7:3.3.2.a it was established that there are on average 4.5 vertices from the original diagram within the correlation region, but for the leading-order diagram the additional 2.5 vertices were not free to participate in exchange of FSFs, so no additional factor was gained. However, this restriction no longer applies at $\mathcal{O}(\alpha N_0^{-1})$:

- For the inbound photon from the photon pair, this is foreground in character so the FSFs from which its preons are constructed must be external to the correlation region, corresponding to arrival of an external foreground photon. The foreground loop photon extends outside the correlation region, so its associated FSFs also meet this criterion. Exchange of these FSFs is therefore permitted.
- Note, however, that exchanging an FSF with one of the FSFs associated with the foreground loop correction also results in some of the circulating momentum entering the diagram at a different location. If this is interpreted as preon interchange, it does not yield a transformation to a different QFT diagram at the composite particle level; indeed it cannot be understood at the composite particle level unless it is reinterpreted as fluctuations in the

foreground momentum. Such fluctuations are already incorporated into the emulated QFT [see Sec. 1:3.8.5; on dropping the window approximation (1.169) this argument extends to scales below \mathcal{L}_0]. Contributions arising from this interchange are therefore well-represented as corrections to Fig. 7.10(i).

- For the fermion vertices in the G boson loop, interchange of a preon with the loop correction photon does not generate tadpole diagrams, so this also is permitted, with similar considerations regarding momentum fluctuations.
- For the background fields, this interchange is also permitted since the momentum of a foreground photon (as opposed to a $G^{(\dagger)}$ boson) is carried in a distributed fashion across all FSFs in the correlation region.

Thus there are on average 4.5 vertices from the leading-order diagram which are within the local correlation region and able to participate in FSF exchange. However, two of these vertices have $G^{(\dagger)}$ bosons in place of photons. Regarding these vertices:

- One preon in the $G^{(\dagger)}$ boson has A -charge $a = 3$ (or equivalently, its associated FSF has a long-range correlation on its gradient in the $a = 3$ sector). This is not compatible with photon construction, so it may be ignored.
- The other preon has a fixed A -charge of 2. However, the A -charge of a preon in the loop photon may be 1 or 2 so the odds of matching A -charge are $\frac{1}{2}$. This is the same as when both bosons are photons.
- Thus in terms of symmetry factors at $O(\alpha N_0^{-1})$, a $G^{(\dagger)}$ vertex behaves as half a photon vertex.

This yields 3.5 as the effective number of participating photon-like vertices from the leading-order diagram, compared with two in Sec. 6:5.2.2. It is also useful to recap that when a loop photon has a single vertex in the correlation region, there is a correction factor of

$$\left[1 + \frac{2}{3N_0} + O(N_0^{-2}) \right] \quad (7.19)$$

per vertex from the leading-order diagram which is within the correlation region, which corresponds to

- a factor of four for the four preon lines at the vertex from the leading-order diagram,
- weighted by the $1/6$ chance of any two preons (from photons) matching A -charge, C -charge, and species ($A/N/Z$),
- yielding a probability of performing a single increment of an FSF count.
- A single increment is realised through multiplication by $[1 + N_0^{-1} + O(N_0^{-2})]$, and the probability weighting on the increment is realised through weighting of the N_0^{-1} term.

Consider first Figs. 7.10(i)-(iv), which are associated with $O(\alpha)$ correction terms of weight $\alpha/(2\pi)$. The correlation region in these diagrams contains one vertex from the photon loop, and on average 3.5 vertices from the leading-order diagram. The resulting correction from each of these four diagrams is therefore

$$\frac{\alpha}{2\pi} \longrightarrow \frac{\alpha}{2\pi} \left[1 + \frac{7}{2} \cdot \frac{2}{3N_0} + O(N_0^{-2}) \right]. \quad (7.20)$$

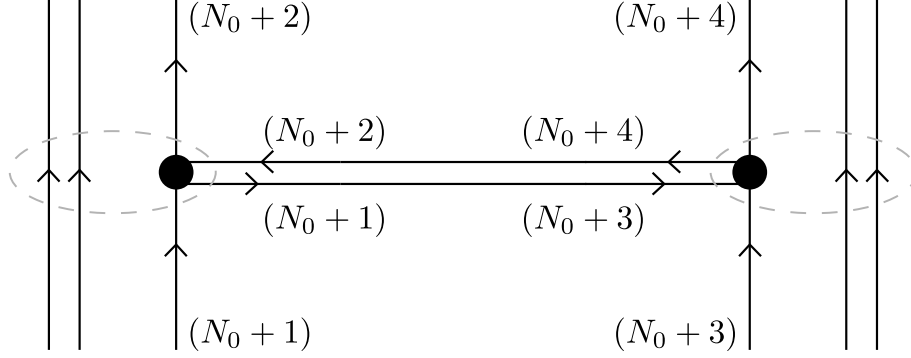


Figure 7.11: FSF symmetry factors associated with photon emission and absorption when the entire process is contained within a single correlation region.

Next, consider Fig. 7.10(v), which is associated with an $O(\alpha)$ correction term of weight α/π . In this diagram there are two added vertices within the correlation region, which both belong to the same photon. Each of these vertices contains preons which may match those in the (on average) 3.5 vertices from the leading-order diagram present within the correlation region. Consider, therefore, the correction arising from matches between the vertex labelled 2 and the vertices from the leading-order diagram, ignoring the presence of vertex 3. Evaluation is as for Figs. 7.10(i)-(iv), this time yielding a correction

$$\frac{\alpha}{\pi} \longrightarrow \frac{\alpha}{\pi} \left[1 + \frac{7}{2} \cdot \frac{2}{3N_0} + O(N_0^{-2}) \right]. \quad (7.21)$$

An identical factor arises from matches between vertex 3 and the vertices from the leading-order diagram.

Finally, consider matches between vertices 2 and 3. In treating this as a standard electromagnetic loop correction, it has implicitly been assumed that the FSF symmetry factors on the preons of these vertices are as shown in Fig. 3.3,

$$(N_0 + 2)^2 (N_0 + 1)^5 (N_0 + \frac{5}{4}). \quad (7.22)$$

This is further multiplied by a factor of $(N_0 + 1)^{-2}$ which arises from ensuring connection of the external photon lines in diagrams (i) and (ii), as described in Sec. 3:3.5.1.b. However, this factor is only correct when the two vertices are separated by a distance or time large compared with \mathcal{L}_0 . In the present context, the correct factors are shown in Fig. 7.11 with the factor of $(N_0 + 1)^{-2}$ remaining unchanged. The resulting FSFs differ by a factor of

$$\left(1 + \frac{20 - 10\frac{1}{4}}{N_0} \right), \quad (7.23)$$

again applied to the $O(\alpha)$ term of α/π arising from Fig. 7.10(v). Putting together all effects arising from Fig. 7.10(v) yields

$$\begin{aligned} \frac{\alpha}{\pi} &\longrightarrow \frac{\alpha}{\pi} \left[1 + 2 \cdot \frac{7}{2} \cdot \frac{2}{3N_0} + \frac{39}{4N_0} + O(N_0^{-2}) \right] \\ &= \frac{\alpha}{\pi} \left[1 + \frac{173}{12N_0} + O(N_0^{-2}) \right]. \end{aligned} \quad (7.24)$$

There are no $O(N_0^{-1})$ corrections to Fig. 7.10(vi).

Finally, putting together all six $O(\alpha)$ corrections and the $O(N_0^{-1})$ corrections to these corrections yields the amendment

$$\left(1 + \frac{7\alpha}{2\pi}\right) \longrightarrow \left[1 + \frac{7\alpha}{2\pi} + \frac{229\alpha}{12\pi N_0} + O\left(\frac{\alpha}{\pi N_0^2}\right)\right]. \quad (7.25)$$

7:3.3.3 Elimination of GG^\dagger pairs

To eliminate the formation of GG^\dagger pairs, it suffices to identify a choice of co-ordinate frame for which the radial profile of the photon pair field is returned to inverse-square. This replaces couplings between the AA and GG^\dagger fields with interactions between the photon pair field and space-time curvature. As the photon pair field has recovered an inverse-square profile, it becomes undetectable (as it no longer mediates any direct force transfer) and the resulting space-time curvature may be associated with the neutral body which acts as the source of the field. Under mapping \mathcal{G} from $M \subset \mathbb{C}^{\wedge 18}$ to a manifold $\mathcal{G}(M)$ which is locally Minkowski, this is a true curvature on the target manifold, and the $SL(2, \mathbb{C})$ connection on $\mathbb{C}^{\wedge 18}$ maps to the space-time connection on $\mathcal{G}(M)$, appearing appropriately in the covariant derivative operator and thus acting on all (quasi)particles appearing on $\mathcal{G}(M)$.

Note that with the resultant AA field exhibiting inverse-square propagation, although the AA fields prior to gauging determine the curvature of the resulting space-time, after gauging they do not couple to it. Thus the implied graviton is massless.

To realise the requisite co-ordinate frame, and thus identify the target space-time of mapping $\mathcal{G}(M)$, recognise that the total decay process of Eq. (7.16) resembles that of Eq. (7.6) with the radial propagation interval rescaled as

$$dr \longrightarrow dr [1 + \langle |I(r)| \rangle]. \quad (7.26)$$

As this effect affects *only* radial propagation, it is akin to evaluating purely geometric propagation on the space-time whose metric is obtained from that of Minkowski space-time by substituting

$$dr^2 \longrightarrow dr^2 [1 + 2\langle |I(r)| \rangle]. \quad (7.27)$$

Recalling that the \mathbb{R}^+ component of the $GL(18, \mathbb{C})$ symmetry of the $\mathbb{C}^{\wedge 18}$ model was gauged in Sec. 6:5.3.7, the volume form must be conserved, giving

$$dt^2 \longrightarrow dt^2 \{1 - 2\langle |I(r)| \rangle + O[\langle |I(r)|^2 \rangle]\}. \quad (7.28)$$

and this serves to uniquely identify the target space-time as one which supports the Schwarzschild metric,

$$ds^2 = - \left(1 + \frac{2G_N M}{r}\right)^{-1} dt^2 + \left(1 + \frac{2G_N M}{r}\right) dr^2 + r^2 d\Omega, \quad (7.29)$$

with

$$\begin{aligned} G_N := & \frac{f^7 N_0^2 S_G S_\alpha}{64\sqrt{2}\pi [k_1^{(e)}(\mathcal{E}_e)]^6 \omega_0 m_e} \left(1 + \frac{7\alpha}{2\pi} + \frac{229\alpha}{12\pi N_0}\right) \\ & \times \left[1 + O\left(\frac{\alpha}{\pi N_0^2}\right) + O\left(\frac{\alpha^2}{\pi^2}\right)\right]. \end{aligned} \quad (7.30)$$

Taking into account the definitions of N_0 , f , and ω_0 as per Eqs. (6.175), (6.168), and (6.182) this may be solved alongside Eqs. (6.146–6.162) (Sec. 6:6.1) to yield

$$G_N = 6.67430(230) \times 10^{-11} \text{ m}^3\text{kg}^{-1}\text{s}^{-2}, \quad (7.31)$$

with the central value differing from observation at the level of $< 0.1 \sigma_{\text{exp}}$.

7:3.3.4 Rotating source

Extension to a rotating source is not considered explicitly in terms of photon pair decay in this chapter. However, noting that the argument deriving the Kerr metric is a classical one [46], requiring only the Schwarzschild metric and a rotating frame of reference, its extension to the $\mathbb{C}^{\wedge 18}$ model is expected to be immediate within the regime of validity of Eq. (7.29), this corresponding to the classical regime and a source sufficiently close to rest in the isotropy frame of the $\mathbb{C}^{\wedge 18}$ model, and excluding high-curvature regimes in which it would be necessary to also take into account corrections of higher order in r such as Figs. 7.6(i)–(ii), or in which the assumption that the foreground field is small is anticipated to break down.

7:3.4 Beyond the dominant process

7:3.4.1 Other spin-2 processes

The above discussion has centred around Fig. 7.6(iii) and its $O(\alpha)$ corrections. However, it extends directly to other beyond-Standard-Model spin-2 interactions, in which the relevant spin-2 boson field is mapped to a further correction to curvature such that the effect of the beyond-Standard-Model effect vanishes on the foreground field counterparts of the Standard Model and is replaced by the effect of a curved space–time.

Understanding how all spin-2 beyond-Standard-Model processes correct photon pair propagation in the flat-space gauge thus permits more precise calculation of the geometry of space–time in the curved-space (physical) gauge, with photon pair propagation then being purely geometric on that curved space–time in keeping with the expectations of the Standard Model (supplemented by dark processes involving boson N_μ).

The further extension to absorb beyond-Standard-Model spin-1 processes into the space–time curvature is discussed in Sec. 7:3.4.2.

7:3.4.2 The right weak interaction and other spin-1 effects

While the above process may readily be extended to eliminate all spin-2 beyond-Standard-Model processes, further detail is required regarding spin-1 processes such as the right-handed weak interaction. Processes such as

$$\nu_e \longrightarrow \bar{e}_R + G \quad (7.32)$$

may create single $G^{(\dagger)}$ bosons, which does not immediately admit a mapping to space–time curvature.

The solution is a technique previously encountered in Sec. 3:3.5.4 and Sec. 4:3.2.2 in which a process serves as a point of reference for charge on a sector. In Sec. 4:3.2.2, the identification of preon triplets in fermions as being the reference point for colour neutrality induced an active co-ordinate transformation which gave rise to the K matrices. Similarly, now let it be a point of definition that all $G^{(\dagger)}$ bosons appear in GG^\dagger pairs. The only other comparable imposition of an active co-ordinate transformation on the A sector is the introduction of co-ordinate sleeves in Sec. 3:3.5.4, and the processes which give rise to these transformations are independent and may

both be applied as required without conflict. Every G boson emission is thus accompanied by a G^\dagger boson emission, and the resulting pair may be immediately mapped to space–time curvature, completing the elimination of $G^{(\dagger)}$ bosons from the $\mathbb{C}^{\wedge 18}$ model.

It is tempting—but inappropriate—to attempt to also apply this process to the neutral N boson. In contrast with the $G^{(\dagger)}$ bosons, the N boson does not change the species of particles it interacts with, and it is also not a significant force mediator in its own right. Its largest physical effect is as a gravitational source. The $W^{(\dagger)}$ and $G^{(\dagger)}$ bosons do also gravitate, and thus there will be corrections of $\mathcal{O}(99/\{18[k_1^{(e)}(\mathcal{E}_e)N_0]^4\})$ to the massive versions of Fig. 7.6(iii) arising via the universal coupling mechanism (Sec. 6:4.2.2.b), but for the N boson (which has a near-totally-eliminated coupling on the A sector) there is no significant leading-order effect to correct. Further, as a weakly-interacting species it is relatively stable, and thus the primary effect of its massive nature is anticipated to be as a gravitational source in its own right, not as a correction to its (negligible) effects on photon pair decay. A co-ordinate sleeve cannot be applied to such a process. For this reason, the N boson is assumed not to be mapped to space–time curvature, and is predicted to be discoverable with an inertial mass of $80.42812(42) \text{ GeV}/c^2$ and a gravitational mass of $240.457(18) m_e$.

7:4 Results

7:4.1 Value of Newton’s constant

As noted in Sec. 7:3.3, elimination of the $G^{(\dagger)}$ bosons from the $\mathbb{C}^{\wedge 18}$ model induces the Schwarzschild metric

$$ds^2 = - \left(1 + \frac{2G_N M}{c^2 r}\right)^{-1} dt^2 + \left(1 + \frac{2G_N M}{c^2 r}\right) dr^2 + r^2 d\Omega \quad (7.29)$$

on the target manifold of mapping \mathcal{G} which acts on $M \subset \mathbb{C}^{\wedge 18}$. Further, the value of G_N is fixed to be

$$G_N := \frac{f^7 N_0^2 S_G S_\alpha}{64\sqrt{2}\pi [k_1^{(e)}(\mathcal{E}_e)]^6 \omega_0 m_e} \left(1 + \frac{7\alpha}{2\pi} + \frac{229\alpha}{12\pi N_0}\right) \times \left[1 + \mathcal{O}\left(\frac{\alpha}{\pi N_0^2}\right) + \mathcal{O}\left(\frac{\alpha^2}{\pi^2}\right)\right]. \quad (7.30)$$

Substituting as per Eqs. (6.175), (6.168), and (6.182) and making factors of c and h explicit yields

$$G_N = \frac{\alpha^4 h c [1 + \Delta_e(m_e, \mathcal{E}_e)]^{\frac{1}{2}} S_{18,147}^{\frac{1}{2}} S_G}{8\pi N_0^{18} [k_1^{(e)}(\mathcal{E}_e)]^4 m_e^2 (1 + a_e)^8 S_\alpha^3} \times \left(1 + \frac{7\alpha}{2\pi} + \frac{229\alpha}{12\pi N_0}\right) \times \left[1 + \mathcal{O}_b + \mathcal{O}_e(m_e, \mathcal{E}_e) + \mathcal{O}\left(\frac{\alpha^2 m_e^2}{m_\mu^2}\right)\right] \quad (7.33)$$

$$S_{18,147} := N_0^{-12} (N_0 + 2)^6 (N_0 + 1)^6 \quad (6.183)$$

$$S_\alpha := N_0^{-6} (N_0 + \frac{5}{4}) (N_0 + 1)^3 (N_0 + 2)^2 \quad (3.84)$$

Table 7.1: List of supplementary sources of uncertainty in the calculation of G_N (7.33).

Label	Description
E20	$O[\alpha/(\pi N_0^2)]$ term in Eq. (7.30)
E21	$O(\alpha^2/\pi^2)$ term in Eq. (7.30)

$$\begin{aligned}
S_G := & 16(N_0 + 2)^2(N_0 + 1)^2 N_0^{12} \\
& \times \{2[(N_0 + 4)(N_0 + 3)(N_0 + 2)(N_0 + 1)]^4 \\
& + 8[(N_0 + 3)(N_0 + 2)(N_0 + 1)^2]^4 \\
& + 6[(N_0 + 2)(N_0 + 1)]^8\}^{-1}
\end{aligned} \tag{7.34}$$

where a_e is the gyromagnetic anomaly of the electron in the Standard Model, evaluated here to $O(\alpha^2)$ [36–38]:

$$\begin{aligned}
a_e = & \frac{\alpha}{2\pi} + \left\{ \frac{197}{144} + \frac{\pi^2[1 - 6\ln(2)]}{12} + \frac{3\zeta(3)}{4} \right\} \frac{\alpha^2}{\pi^2} \\
& + O\left(\frac{\alpha^2 m_e^2}{m_\mu^2}\right) \\
\approx & \frac{\alpha}{2\pi} - 0.328478965579193 \frac{\alpha^2}{\pi^2} + O\left(\frac{\alpha^2 m_e^2}{m_\mu^2}\right).
\end{aligned} \tag{6.180}$$

The above equations fully define G_N in terms of the parameterisation of Eqs. (6.146–6.162). Note that the error terms \mathcal{O}_b and $\mathcal{O}_e(m_e, \mathcal{E}_e)$ incorporate error terms E1–E15 of Chapter 6, and also the error terms appearing in Eq. (7.30) in the present chapter, which are designated E20 and E21 respectively. The remaining term $O(\alpha^2 m_e^2/m_\mu^2)$ corresponds to error term E19 in Appendix 6:D, and arises from truncation of a_e as per Eq. (6.180). This term need not be written explicitly, as it is small compared with term $O(\alpha^2/\pi^2)$ in \mathcal{O}_b , but retaining it ensures that it will not be overlooked when subsequent higher-order calculations reduce the magnitude of the error terms in \mathcal{O}_b .

Evaluating Eq. (7.33) simultaneously with Eqs. (6.146–6.162) yields

$$G_N = 6.67430(230) \times 10^{-11} \text{ m}^3 \text{ kg}^{-1} \text{ s}^{-2}. \tag{7.31}$$

The sources of uncertainty in this result include all those listed in Table 6.6, E19 from Appendix 6:D, plus also those listed in Table 7.1 of the present chapter. Their magnitudes are tabulated in Table 7.2. As in Sec. 6:6.3, rather than attempting to quantify the magnitudes of the higher-order corrections these have been given a generous coefficient of ± 10 with the intent of allowing for up-to-ninefold colour-related degeneracies, thus avoiding underestimation of uncertainty in the resulting figure. The largest terms in the uncertainty results from contributions E2 and E4, which correspond to two-loop corrections to the boson mass diagrams of Chapters 5 and 6.

The value of Newton’s constant thus obtained is presently less precise than experimental results, but the central calculated value is nevertheless in agreement with observation at the level of $0.03 \sigma_{\text{exp}}$.

Table 7.2: Contributions of different sources of error to the value of G_N , expressed both in units of $\text{m}^3\text{kg}^{-1}\text{s}^{-2}$ and relative to the experimental error. Labels are enumerated in Table 7.1, and in Table 6.6 and Appendix 6:D. For purposes of summation, sources of error are assumed independent.

Label	Coefficient	Uncertainty in G_N	
		$10^{-14} \text{ m}^3\text{kg}^{-1}\text{s}^{-2}$	σ_{exp}
E1	± 10	0.19	1.26
E2	± 10	1.58	10.51
E3	± 10	0.19	1.26
E4	± 10	1.58	10.54
E5	± 10	0.00	0.00
E6	± 10	0.00	0.00
E7	± 10	0.02	0.12
E8	± 10	0.01	0.05
E9	± 10	0.00	0.00
E10	± 10	0.30	2.02
E11	± 10	0.01	0.10
E12	± 10	0.01	0.09
E13	± 10	0.03	0.22
E14	± 10	0.00	0.01
E15	1	0.00	0.00
E16	± 1	0.00	0.00
E17	± 1	0.00	0.00
E18	± 1	0.00	0.01
E19	± 10	0.00	0.00
E20	± 10	0.00	0.03
E21	± 10	0.36	2.38
Total		2.30	15.31

7:4.2 Qualitative implications

It is interesting to examine some key qualitative properties of the gravitational mechanism of the $\mathbb{C}^{\wedge 18}$ model. First, the extent to which the model truly realises a space–time curvature. The underlying $\mathbb{C}^{\wedge 18}$ manifold remains flat, but the emulated manifold with real co-ordinates, $\mathcal{G}(M)$, has a true curvature as reflected by metric (7.29). This is the same curvature as is exhibited by the $\text{SL}(2, \mathbb{C})$ subgroup of the physically motivated co-ordinate frame on $\mathbb{C}^{\wedge 18}$. In one sense it might therefore be argued that the underlying manifold is flat, with metric $\varepsilon^{\alpha\beta}$. In another, to the extent that there exists a space–time inhabited by the particles of the Standard Model, this space–time is curved. This is conceptually not dissimilar to the widely-used technique of treating the metric or vierbein/vielbein as a field over a Minkowski space–time, with the particles inhabiting that space–time then coupling to the indices of the metric/vielbein rather than that of the Minkowski space–time itself. The only significant difference here is in the choice of underlying manifold (and hence the construction consequently required to generate emergent normalisable quasiparticles on that manifold).

Given this fairly robust footing for interpreting the $\text{SL}(2, \mathbb{C})$ co-ordinate frame in the physical gauge as a true curvature of the emergent space–time, at a minimum up to energy scales of $\frac{1}{2}\mathcal{E}_\Omega \sim 3.1$ TeV and potentially beyond, the gravitational interaction of bosons is of particular interest. All species of boson in the $\mathbb{C}^{\wedge 18}$ model break the weak principle of equivalence, which may variously be stated as the bosons having different value(s) of Newton’s constant to the fermions, or the bosons having discrepancies between their gravitational and inertial masses. This is of particular significance given the existence of the neutral vector boson N_μ , which is colourless, and chargeless with respect to both electromagnetic and weak interactions, but is nevertheless capable of participating in gravitational interactions, albeit with an effective gravitational mass substantially smaller than its inertial mass. With an inertial mass of $80.42812(42)$ GeV/ c^2 (see Table 6.5) and a gravitational mass only $240.457(18) m_e$ (where m_e is the gravitational mass of the electron), it is a candidate for an unusual form of WIMP dark matter.

7:5 Conclusion

This chapter has provided a further demonstration of the predictive capability of the $\mathbb{C}^{\wedge 18}$ model, this time permitting calculation of the value of Newton’s constant from first principles. This comes in addition to the previous derivation of the masses of the tau particle and the W , Z , and Higgs bosons presented in Chapter 6. In both calculations, the only input parameters are the fine structure constant and the masses of the electron and muon, and the model is completely without any other tuning parameters.

The $\mathbb{C}^{\wedge 18}$ model was originally introduced as an analogue model, emulating the Standard Model within an appropriate energy regime. However, with elimination of the G and G^\dagger bosons, and the nonvanishing photon pair field rendered physically irrelevant, there are now no known points of tension remaining between the $\mathbb{C}^{\wedge 18}$ model and experimental observation. Of course, the $\mathbb{C}^{\wedge 18}$ model is much newer than the Standard Model and has not been subjected to anything like as exhaustive a search for incongruencies with physical reality.

Further testing of the $\mathbb{C}^{\wedge 18}$ model may comprise further detailed numerical predictions for parameters already observed, and also for parameters and particle species not yet observed, such as the mass of the second generation W boson anticipated to appear at $16.61730(47)$ TeV/ c^2 (and, indeed, its heavy Z and Higgs boson companions at $18.85138(74)$ TeV/ c^2 and $25.8963(10)$ TeV/ c^2 respectively). The calculation of known parameters will allow further elucidation of the regime of validity of the model, while the calculation of as-yet-unknown physical parameters (such as the mass of the W_2 boson) will provide for direct experimental tests of its predictive power in

previously unexplored domains.

It should be noted that the lack of any tuning parameters indicates that these predictions are already implicit in the model to arbitrarily high precision, and it is now merely necessary to perform the requisite calculations to obtain high-accuracy concrete numerical predictions.

Having come thus far, and calculated the value of so many fundamental constants, it is apposite to come full circle to the opening paragraphs of Chapter 1 and speculate whether *all* of physics is in fact the study of quasiparticles.

Acknowledgements

In addition to the usual financial acknowledgements, the author would particularly like to thank the following individuals, without whom this work would have been far more difficult: Prof. Y. Koide for recognising a relationship between the lepton masses, and exploring the mechanisms which underly this remarkable property. Dr. A. N. Chantler for the confidence to believe that a better model could be achieved. And finally, D. Di Mario for another remarkable numerical relationship which is probably coincidental, but which nevertheless served as a beacon along the way.

This research was supported in part by the Perimeter Institute for Theoretical Physics. Research at the Perimeter Institute is supported by the Government of Canada through Industry Canada and by the Province of Ontario through the Ministry of Research and Innovation. The author thanks the Ontario Ministry of Research and Innovation Early Researcher Awards (ER09-06-073) for financial support. This project was supported in part through the Macquarie University Research Fellowship scheme. This research was supported in part by the ARC Centre of Excellence in Engineered Quantum Systems (EQuS), Project No. CE110001013.

Chapter 8

Calculations beyond the Standard Model: W mass in CDF II, and Muon $g - 2$

See [arXiv:2212.01255](#) [48].

Chapter 9

Leptoquarks and LHCb

Abstract

The Classical Analogue to the Standard Model (CASM) is an analogue model which reproduces the quantum field theory of the Standard Model, and the curved space-time of general relativity, in appropriate limits. It has a strong beyond-Standard-Model track record, predicting the anomalous value of the W boson mass measured by CDF II, and the value of the muon gyromagnetic anomaly measured at Fermilab Muon $g - 2$, with tensions 0.49σ and 0.20σ respectively (Chapter 8). This chapter applies the CASM to beauty quark decay in LHCb. The CASM predicts the existence of leptoquarks with lifetimes small compared to $[3.09 \text{ TeV}]^{-1}$. These leptoquarks yield a muon to electron pair production ratio $R_K = 0.857 \dots$, in agreement with the observed value of $R_K = 0.846^{+0.044}_{-0.041}$ at the level of 0.25σ .

9:1 Introduction

The Classical Analogue to the Standard Model (CASM) [49–52] is an analogue model which reproduces the quantum field theory of the Standard Model, and the curved space-time of general relativity, in appropriate limits. It correctly predicts the anomalous value of the W boson mass measured by CDF II, and the value of the muon gyromagnetic anomaly measured at Fermilab Muon $g - 2$, with tensions 0.49σ and 0.20σ respectively (compared with the Standard Model tensions of 6.9σ and 4.2σ respectively). With these encouraging results, and with suggestions of a deviation from the Standard Model in recent results from LHCb [53], it is natural to ask whether the CASM may also be productively applied to the analysis of beauty quark decay.

In the Standard Model the nonresonant decay of the B^+ meson to the K^+ meson (i.e. excluding $B^+ \rightarrow J/\psi K^+$) is prohibited at tree level by symmetry constraints, re-emerging only at the 1-loop level as shown in Fig. 9.1(i). This process respects lepton universality, such that electron and muon pairs from non- J/ψ decay processes are produced in equal numbers (if muon and electron masses are assumed vanishingly small compared with the mass of the beauty quark). In contrast, extensions to the Standard Model may break lepton universality and result in pair production rates with ratios other than unity. Leptoquarks are one such proposal, and introduce a tree-level diagram mediating $B^+ \rightarrow K^+$ decay as shown in Fig. 9.1(ii). For appropriate coupling coefficients, this diagram may dominate over Fig. 9.1(i) and may yield pair production ratios dependent on the ratio of the leptoquark:muon and leptoquark:electron couplings, which are not *a priori* required to coincide.

In this paper, the high-energy regime of the CASM is shown to include leptoquarks with lifetimes small compared with $[3.09 \text{ TeV}]^{-1}$. The interactions mediated by these leptoquarks are

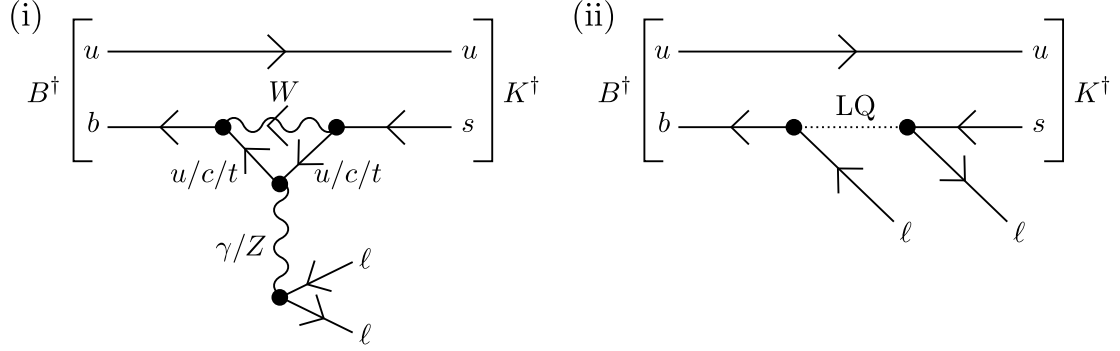


Figure 9.1: (i) Dominant Standard Model process for decay of B^+ mesons to K^+ mesons by lepton pair emission. The Standard Model does not predict deviation from lepton universality. (b) Proposed tree-level leptoquark channel for $B^+ \rightarrow K^+$ decay. If different generations of leptons exhibit different coupling constants to the leptoquark, this breaks lepton universality, allowing for different rates of electron and muon pair production.

generation-dependent, and cause the pair production ratios to deviate from unity. Comparing non- J/ψ production of muon and electron pairs the model predicts a ratio

$$R_K = 0.857 \dots \quad (9.1)$$

in regimes where corrections due to electron and muon masses are negligible. This is in agreement with the observed value of $R_K = 0.846^{+0.044}_{-0.041}$ at the level of 0.25σ , in contrast with the Standard Model which predicts R_K to be consistent with unity to $O(1\%)$ and displays a tension with experiment of 3.1σ [53–57].

In what follows, references to $B^+ \rightarrow K^+$ decay are implicitly taken to exclude the $B^+ \rightarrow J/\psi K^+$ channel.

9:2 $B^+ \rightarrow K^+$ decay in the CASM

9:2.1 Fermions in $B^+ \rightarrow K^+$ decay

In the CASM, fermions and bosons are constructed from spin- $\frac{1}{2}$ preon with dimension $L^{-\frac{1}{2}}$. Fermions comprise three such preons, and bosons two, with allowed combinations being restricted by specifying characteristics of preferred co-ordinate frames on the underlying model—these map into symmetry-breaking choices of gauge on the effective field theory of the intermediate regime, yielding the particle spectrum of the Standard Model in the low-energy regime [51]. The assumption that phenomena at higher-energy regimes may be explained in terms of the species observed at low-energy regimes then extends the emergent Standard Model particle spectrum to all length scales.

Preons carry charges with respect to two copies of $SU(3)$ in the intermediate regime, denoted $SU(3)_A$ and $SU(3)_C$. Triplets of preons with identical A -charge and distinct C -charges make up the leptons, with relative phases determining the particle generation. Left-handed preon triplets $\psi^{ar} \psi^{ag} \psi^{ab}$ having a first-generation relative phase configuration are identified with the left-handed Weyl spinors $[\bar{e}_R, e_L, \nu_e]$ for a taking values $[1, 2, 3]$ respectively, transforming in the usual way under hermitian conjugation. It is therefore convenient to denote the left-handed

preons by $[\bar{e}_R^c, e_L^c, \nu_e^c]$ reflecting the lowest-generation lepton they may construct when assembled in groupings homogeneous in A -charge.

Quarks are similarly constructed from triplets of preons, this time inhomogeneous in A -charge. A quark continues to contain one preon of each colour, with its constituents being bound by the colour interaction, but the differing mass interaction of ν_e^c compared with e_L^c and \bar{e}_R^c results in ν_e^c preons being less tightly bound than their e_X^c counterparts and exhibiting a wider distribution around their common centre of mass. In conjunction with colour shielding this results in an effective residual colour charge when the quark is observed from a distance large compared with the preon binding scale.

This paper explicitly addresses $B^+ \rightarrow K^+$ decay where the B^+ meson contains an anti-[left-handed beauty quark] denoted \bar{b}_L , but generalises immediately to \bar{b}_R with no change to numerical results.

The preon structures associated with the anti-[left-handed beauty/strange quarks], henceforth \bar{b}_L and \bar{s}_L , are

$$\bar{\nu}_e^{c_1} \bar{\nu}_e^{c_2} \bar{e}_L^{c_3}, \quad \{c_1, c_2, c_3\} \in P\{r, g, b\}. \quad (9.2)$$

The quarks d_L , s_L , and b_L form a generation triplet, with the three preons occupying an eigenstate of the colour-mediated binding interaction. These eigenstates correspond to eigenvectors of a matrix K_{d_L} which mediates the binding interaction, with eigenvalues $k_1^{(d_L)}$, $k_2^{(d_L)}$, $k_3^{(d_L)}$ in ascending order. Up to a global phase and a freedom of sign on i these eigenstates may be denoted

$$\frac{1}{\sqrt{3}} \begin{pmatrix} 1 \\ 1 \\ 1 \end{pmatrix}, \quad \frac{1}{\sqrt{3}} \begin{pmatrix} e^{\frac{\pi i}{3}} \\ e^{-\frac{\pi i}{3}} \\ 1 \end{pmatrix}, \quad \frac{1}{\sqrt{3}} \begin{pmatrix} 1 \\ e^{\frac{2\pi i}{3}} \\ e^{-\frac{2\pi i}{3}} \end{pmatrix}. \quad (9.3)$$

9.2.2 Leptoquark processes in $B^+ \rightarrow K^+$ decay

The preon-level description of $B^+ \rightarrow K^+$ contains three distinct processes which are illustrated in Fig. 9.2. In each, a W boson is exchanged between two fermion triplets. As per Sec. 3:3.5.4 of Ref. [51], W boson exchange is obligatorily accompanied by a local change in co-ordinate frame on the underlying model selected by the requirement that the charges of the $SU(3)_A$ sector are conserved by fermion/boson interactions. Specifying the species entering and leaving the interaction suffices to uniquely constrain this transformation (up to physically meaningless perturbations). As discussed in Sec. 6:5.3.3 of Ref. [52], where this passive transformation results in a change in charge labelling across the boundary of the transformed region, it may equivalently be represented as an active transformation described by a boson interacting only where species lines traverse this boundary. However, in contrast with Sec. 6:5.3.3 this process is not energy-dependent and thus the equivalent bosons (or co-ordinate sleeves as per Sec. 3:3.5.4) are necessarily trivial aside from the net transfer of A -sector charges. They are represented in pale grey in Fig. 9.2, and interact with an effective coupling constant of 1.

It is reasonable to assign the induced (grey) vertices to occur simultaneous (in the isotropy frame of the CASM pseudovacuum) with the foreground (black) W /preon interactions which induce them. It is then convenient to connect these vertices, for example as shown in Fig. 9.2, as a reflection of local conservation of A -sector charge. In order that the co-ordinate transformations may be considered a part of a propagating leptoquark, it is appropriate that they be represented by bosons co-propagating with the boson which induces them. Thus in Fig. 9.2 the connections of the induced boson vertices are chosen so as to always span from one fermion to the other. Where a co-ordinate transformation admits multiple equivalent boson arrangements, these form an equivalence class from which only one need be considered.

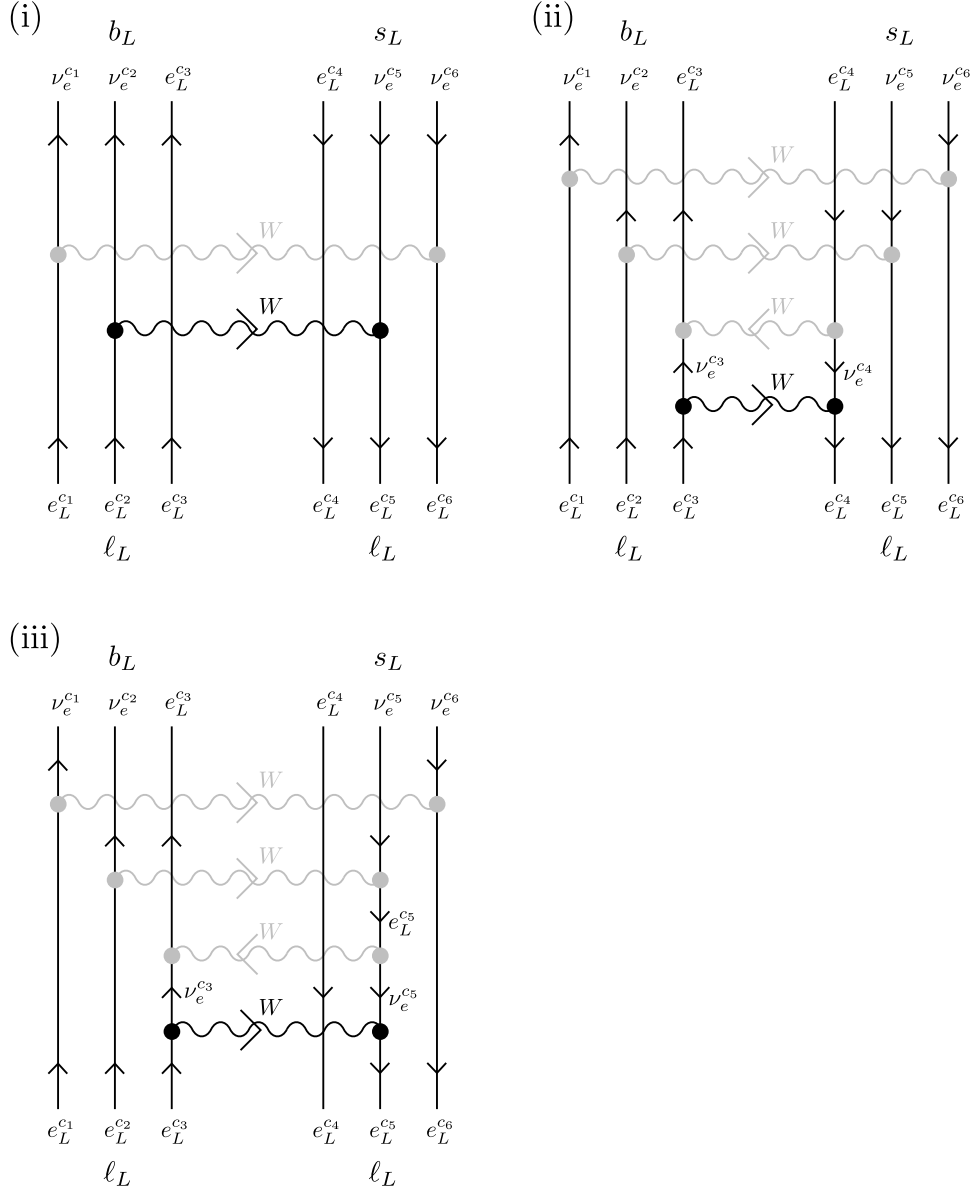


Figure 9.2: Three example composite-leptoquark processes mediating $b \rightarrow \ell \bar{\ell}$ decay in the CSM. Grey lines represent local co-ordinate transforms on the gauge group, consistent with the gauge choices of Chapter 3, which act on the preon A -sector charges in a manner equivalent to the exchange of a massless W boson. In the sub-preon scalar field model these transforms correspond to induced choices of co-ordinate frame on $\mathbb{C}^{\wedge 18}$. Labels (i), (ii), and (iii) permit identification of individual diagrams in the main text.

Next, observe that the quarks of Fig. 9.2 are required to be bound within B^+ and K^+ mesons and thus the process as a whole takes place on the order of the colour confinement scale which is $\mathcal{L}_\psi \sim [3.09 \text{ TeV}]^{-1}$ [48]. Over this scale, the foreground W boson does not acquire mass through interactions with the CASM pseudovacuum.

Putting this all together, a leptoquark in the CASM comprises an exchanged foreground boson accompanied by one or more induced co-ordinate transforms as required by the species labelling of the diagram lines, and ultimately by the far-field process (or term of said process) being described. Over the timescales of the leptoquark-mediated interactions, the foreground boson, and thus the leptoquark as a whole, is massless.

In evaluating the diagrams of Fig. 9.2, a further property of the CASM must be kept in mind.

- First, consider a pair of vertices which are topologically equivalent to each other but not to any other vertices in a diagram. As in QFT, the freedom to connect up either vertex in either location yields a multiplicative factor of two on the process being described. When a diagram exists as part of a set summed over colour perturbations, it suffices that the set be invariant under vertex exchange and thus that an individual diagram be invariant up to a colour perturbation mapping it onto another member of the set. An example of such a pair of vertices is the pair of preon vertices in the left fermion/leptoquark interaction of Fig. 9.2(i).
- In the CASM, however, a further factor arises in processes dominated by contributions arising over length scales small compared with $\mathcal{L}_0 \approx [1.79 \text{ GeV}]^{-1}$. All preon fields in the CASM correspond to gradients of Fundamental Scalar Fields (FSFs) taken with respect to directions on the underlying \mathbb{C}^{18} manifold, and these fields are in general correlated over length scales of order \mathcal{L}_0 or less. Two of these correlated fields carry perturbations in their (Grassmann-valued) gradients corresponding to preons $\{\nu_e^{c_1}, \nu_e^{c_2}\}$ for some colours $\{c_1, c_2\}$, and since the FSFs are common to all members of the sum over colour, the FSFs on which these derivatives act may be interchanged. The FSFs associated with the preons $\{e_L^{c_1}, e_L^{c_2}\}$ may be likewise interchanged, but interchanging both sets is equivalent to interchanging the vertex to which the W bosons connect, and thus is double counting. The preonic constituents of the boson are contiguous with the preons, so no further factors arise from the boson. The vertices acquire an additional factor of two from the FSFs, but only because they are within a common FSF autocorrelation region.
- Note this exchange of the FSFs on which the anticommuting derivatives act is independent of an exchange of the order of the derivative operators themselves. It is thus in addition to, not instead of, fermion exchange symmetries at the level of the QFT diagram.

The same argument also applies to the right-hand fermion/leptoquark vertex of Fig. 9.2(i).

Next, consider how W boson interactions may mediate generation changes in the CASM. Critical to this ability is the recognition that the W boson is a complex boson. When a preon couples to a W boson, this coupling may impart an arbitrary phase to the preon provided the conjugate phase is applied to the W boson, from where it may be factored out into a global phase acting on the diagram as a whole. Thus, in the A sector, *only* W bosons may participate in generation-nonconserving interaction vertices.¹ Generation changes may be mediated by real W bosons and also by the pale grey frame bosons when these have W character in the A -sector.

Now consider each of the above diagrams in turn. All have the same basic weight from species and vertices. For descriptive purposes, each diagram is considered to comprise two composite fermion/leptoquark vertices regardless of the number of additional bosons induced.

¹In the C sector it is anticipated that gluons are also prohibited from participating in net generation-nonconserving processes, due to the combination of unbroken $SU(3)_C$ and phase symmetry.

- (i) This diagram belongs to the simplest class of processes. The conventional W boson connects to two preons which are changing flavour. Four such diagrams are possible. There is also an additional factor of two at each fermion vertex arising from the FSFs as described above. With four diagrams and a factor of four from FSF interchange, this class of processes has a relative weight of 16.
- (ii) This diagram belongs to a class in which the W boson connects the two non-flavour-changing preons. This class contains only the diagram shown in Fig. 9.2(ii). FSF symmetry factors on the $e_L^c \bar{\nu}_e^c W^\dagger|_{\dot{c}=c}$ vertices and their conjugates yield a factor of 4. Note that even though no numerical factor is obtained from exchange of W boson connections, a factor is still acquired from interchange of the associated FSFs. The total weight of this class of processes is 4.
- (iii) This diagram belongs to a class in which the W boson couples a flavour-changing preon to a preon which does not change flavour. There are four configurations of the foreground boson (the conventional W may couple to the non-flavour-changing preon in either the left or the right vertex, and then to either flavour-changing preon in the other vertex). The vertices on the two flavour-changing preons of the left side of Fig. 9.2(iii) are topologically equivalent for an FSF factor of two, and the net weight of this class of processes is 8.

There is one further caveat which applies to Fig. 9.2(ii). When the input and output fermion at a vertex are of the same generation (for example when the rightmost vertex is $s_L \bar{\mu}_L W$) then there is no phase applied to the W boson. One of the induced co-ordinate transformation bosons follows exactly the same trajectory as the absorbed W , and the two may be combined to yield a real superposition of the photon, Z boson, and the dark matter N boson. As this superposition is real, it may not engage in a phase-transferring interaction at the $\mu_L \bar{b}_L W^\dagger$ vertex and this diagram consequently vanishes when there is a generation match at either vertex (i.e. during muon or tau pair production).

The relative weights of the leptoquark-mediated muon and electron pair production processes are therefore 24 and 28 respectively, yielding

$$R_K^{\text{th}} = \frac{6}{7} \approx 0.857 \dots \quad (9.4)$$

up to corrections due to the lepton masses being non-negligible with respect to the beauty quark mass of $4.18 \text{ GeV}/c^2$. A factor of $(1 + m_\mu^2/m_b^2)$ corrects R_K by 5.41×10^{-4} , which is on the order of 1% of the standard error of the experimental result

$$R_K^{\text{exp}} = 0.846^{+0.044}_{-0.041}. \quad (9.5)$$

This mass correction is consequently ignored.

9:3 Conclusion

Making extensive use of the microscopic properties of the CASM, and calculation techniques developed in Refs. [49–52], it is relatively straightforward to obtain a prediction from the CASM for the relative rates of non- J/ψ -mediated muon pair and electron pair production during beauty quark decay. The pair production process is dominated by leptoquark-mediated interactions, and the predicted ratio is

$$R_K = 0.857 \dots \quad (9.6)$$

Tension with experiment is 0.25σ .

For comparison, the Standard Model predicts R_K equal to unity, up to corrections of $\mathcal{O}(1\%)$ [53–57]), yielding a tension of 3.1σ .

The beyond-Standard-Model construction of the CASM consequently resolves all three primary points of tension between experiment and the Standard Model:

- CDF II measurement of W mass, SM tension 6.9σ , CASM tension 0.49σ ,
- Fermilab measurement of muon $g - 2$, SM tension 4.2σ , CASM tension 0.20σ , and
- LHCb measurement of nonresonant $b \rightarrow \ell\bar{\ell}$ pair production, SM tension 3.1σ , CASM tension 0.25σ

with tensions all less than 1σ . It further achieves this without any tuning or fitting parameters, taking only Standard Model constants as input.

Chapter 10

Additional Brief Notes

10:1 Higher-generation weak bosons in the CASM

10:1.1 Brief comments

10:1.1.1 Meaning of boson generation

In the CASM, there exist three eigenstates for each of the weak bosons (W , Z , and \mathbf{H}). These may be identified as “generations” of these bosons. However, in contrast with the charged leptons where different generations correspond to different eigenstates of a 3×3 mass matrix, for the bosons there are instead three different mass-generating processes, whose eigenstates are distinguished by rest mass alone. Thus the only prerequisite for a boson to change generations is that it should be supplied with a sufficiently large augmentation to its rest mass. (Consider the hypothetical situation of an on-shell generation-1 W boson at rest which is given additional energy while remaining at rest. The most likely outcome is that this boson will become off-shell—*unless* the additional energy imparted is of the correct amount to cause it to become an on-shell W boson of generation 2 or 3. It is readily seen that it is meaningless to talk about the generation of an off-shell W boson as the generation labels merely describe the three on-shell rest energies.)

10:1.1.2 Beyond the preon scale

The second and third generation W boson states are hard to access, as their rest masses exceed the preon scale. Typically it would be expected that at energies slightly below the rest mass of an excitation, it may make meaningful contributions as a virtual particle. However, the most energy that can be borrowed towards the construction of a virtual particle is the preon scale $E_\psi = \frac{1}{2}\mathcal{E}_\psi = 3.09 \text{ TeV}$ [48, 51]. Therefore, no hint whatsoever of these particles will be observed until at least within 3 TeV of their rest mass (and even then, processes in which they appear may be affected by local depletion of the pseudovacuum until significantly closer than 3 TeV).

10:1.2 Calculating the heavy weak boson masses

The heavy weak boson masses are given directly by replacing the generation-1 vertices in the mass interactions with their generation-2 or generation-3 counterparts. Thus

$$\frac{m_{W_i}^2}{m_W^2} = \frac{\left[k_i^{(e)}(\mathcal{E}_{e_i})\right]^4 \left\{1 + \frac{19}{18 \left[k_i^{(e)}(\mathcal{E}_{e_i})N_0\right]^4}\right\}}{\left[k_1^{(e)}(\mathcal{E}_e)\right]^4 \left\{1 + \frac{19}{18 \left[k_1^{(e)}(\mathcal{E}_e)N_0\right]^4}\right\}} \quad \frac{m_{Z_i}^2}{m_Z^2} = \frac{\left[k_i^{(e)}(\mathcal{E}_{e_i})\right]^4 \left\{1 + \frac{19}{18 \left[k_i^{(e)}(\mathcal{E}_{e_i})N_0\right]^4}\right\}}{\left[k_1^{(e)}(\mathcal{E}_e)\right]^4 \left\{1 + \frac{19}{18 \left[k_1^{(e)}(\mathcal{E}_e)N_0\right]^4}\right\}} \quad (10.1)$$

$$\frac{m_{c_i}^2}{m_c^2} = \frac{\left[k_i^{(e)}(\mathcal{E}_{e_i})\right]^4 \left\{1 + \frac{19}{18 \left[k_i^{(e)}(\mathcal{E}_{e_i})N_0\right]^4}\right\}}{\left[k_1^{(e)}(\mathcal{E}_e)\right]^4 \left\{1 + \frac{19}{18 \left[k_1^{(e)}(\mathcal{E}_e)N_0\right]^4}\right\}} \quad \frac{m_{\mathbf{H}_i}^2}{m_{\mathbf{H}}^2} = \frac{\left[k_i^{(e)}(\mathcal{E}_{e_i})\right]^4 \left\{1 + \frac{19}{18 \left[k_i^{(e)}(\mathcal{E}_{e_i})N_0\right]^4}\right\}}{\left[k_1^{(e)}(\mathcal{E}_e)\right]^4 \left\{1 + \frac{19}{18 \left[k_1^{(e)}(\mathcal{E}_e)N_0\right]^4}\right\}}. \quad (10.2)$$

Here, m_c is the effective long-range gluon mass; this parameter is not normally observable except

- (i) indirectly during the propagation of gluon field holes in the pseudovacuum, which contribute a correction to particle masses as discussed in Chapter 6 of Ref. [52], and
- (ii) as the mass of the 80.42812(42) GeV/ c^2 neutral dark matter boson denoted N_μ in Ref. [51].

Hypothetically, coloured W and Z eigenstates (here denoted $W^{\dot{c}c}$ and $Z^{\dot{c}c}$) may also be created as discussed in Ref. [48]. However, their rest masses are far outside the regime in which coloured weak bosons are supported ($1.79 \text{ GeV} < E < 3.09 \text{ TeV}$) and thus they are not expected to be observed. If colour-rich circumstances can be contrived in which to generate these bosons, they satisfy

$$\frac{m_{W_i^{\dot{c}c}}^2}{m_{W^c}^2} = \frac{\left[k_i^{(e)}(\mathcal{E}_{e_i})\right]^4 \left\{1 + \frac{19}{18 \left[k_i^{(e)}(\mathcal{E}_{e_i})N_0\right]^4}\right\}}{\left[k_1^{(e)}(\mathcal{E}_e)\right]^4 \left\{1 + \frac{19}{18 \left[k_1^{(e)}(\mathcal{E}_e)N_0\right]^4}\right\}} \quad \frac{m_{Z_i^{\dot{c}c}}^2}{m_{Z^c}^2} = \frac{\left[k_i^{(e)}(\mathcal{E}_{e_i})\right]^4 \left\{1 + \frac{19}{18 \left[k_i^{(e)}(\mathcal{E}_{e_i})N_0\right]^4}\right\}}{\left[k_1^{(e)}(\mathcal{E}_e)\right]^4 \left\{1 + \frac{19}{18 \left[k_1^{(e)}(\mathcal{E}_e)N_0\right]^4}\right\}}. \quad (10.3)$$

The calculated heavy weak boson masses (including the higher-generation dark matter boson masses m_{c_2} and m_{c_3}) are:

Boson	Mass (TeV/ c^2)	Boson	Mass (TeV/ c^2)
m_{W_2}	16.61730(47)	m_{c_2}	16.61730(10)
m_{Z_2}	18.85138(74)	$m_{W_2^{\dot{c}c}}$	16.61730(47)
$m_{\mathbf{H}_2}$	25.8963(10)	$m_{Z_2^{\dot{c}c}}$	18.85138(74)
m_{W_3}	279.4728(79)	m_{c_3}	279.4728(17)
m_{Z_3}	317.046(12)	$m_{W_3^{\dot{c}c}}$	279.4728(79)
$m_{\mathbf{H}_3}$	435.529(17)	$m_{Z_3^{\dot{c}c}}$	317.046(12)

Because the CASM exhibits a real UV cutoff, there is a minimum energy below which these species cannot be observed, even as virtual particles. For the W_2 that minimum energy is predicted to be 13.5 TeV [52].

10:2 Neutrino masses

10:2.1 No seesaw mechanism

There is no seesaw mechanism in the CASM. Instead, the W boson coupling can be generation-nonconserving at the cost of imparting a phase to the overall wavefunction as described in Chapter 9 of Ref. [52]. In contrast with the Standard Model, any W -mediated interaction yielding neutrinos therefore produces a superposition of all three generations, with wavefunctions differing by a phase. This provides an alternative resolution to the solar neutrino deficit, with the emitted neutrinos being divided between the three generations.

10:2.2 Neutrino masses

In the absence of a seesaw mechanism, there is no longer an *a priori* requirement for the neutrinos to have mass. The CASM provides a mechanism whereby neutrinos may acquire mass, and retracing the calculation of Chapter 6 of Ref. [52] but with neutrinos instead of electrons yields an expression

$$\begin{aligned}
m_{\nu_i}^2 = & \frac{f^2}{2} \left[k_i^{(\nu)}(\mathcal{E}_{\nu_i}) \right]^4 \omega_0^2 N_0^8 S_{18,147} \\
& \times \left(\frac{5m_{\nu_i}^2}{[m_c^*(\mathcal{E}_{\nu_i})]^2} \left\{ 1 + \frac{90\alpha m_{\nu_i}^2}{\pi [m_c^*(\mathcal{E}_{\nu_i})]^2} + \frac{\alpha (f_W m_{\nu_i}^2 - 48f_Z m_{\nu_i}^2 + 25 \sum_j m_{e_j}^2)}{6\pi m_W^2} \right\} + \frac{40m_{\nu_i}^2}{3m_{\mathbf{H}}^2 [k_1^{(e)}(\mathcal{E}_e) N_0]^4} \right) \\
& \times \left(1 + \mathcal{O} \left\{ \frac{\alpha m_{\nu_i}^2 \sum_j m_{e_j}^2}{N_0 [m_c^*(\mathcal{E}_{\nu_i})]^2 m_W^2} \right\} + \mathcal{O} \left(\frac{\alpha^2 \sum_j m_{e_j}^4}{m_W^4} \right) + \mathcal{O} \left\{ \frac{m_{\nu_i}^2}{m_{\mathbf{H}}^2 [k_1^{(e)}(\mathcal{E}_e)]^4 N_0^5} \right\} \right. \\
& \quad \left. + \mathcal{O} \left\{ \frac{\alpha m_{\nu_i}^2 \sum_j m_{e_j}^2}{m_{\mathbf{H}}^2 [k_1^{(e)}(\mathcal{E}_e) N_0]^4 m_W^2} \right\} + \mathcal{O} \left\{ \frac{m_{\nu_i}^4}{m_{\mathbf{H}}^4 [k_1^{(e)}(\mathcal{E}_e)]^4} \right\} + \mathcal{O} \left\{ \frac{m_{\nu_i}^6}{[m_c^*(\mathcal{E}_{\nu_i})]^6} \right\} \right)
\end{aligned} \tag{10.4}$$

where f_W comes from the $m_{\nu_i}^2/m_W^2$ component of the W loop correction. This term of the W loop correction is usually ignored as $m_{\nu_i}^2/m_W^2 \ll m_e^2/m_W^2$. While not formally evaluated here, f_W is anticipated to be around 100.

Note that the neutrino mass terms all involve massive bosons; consequently the neutrino mass interaction is dependent on the neutrino having mass, and the solution $m_{\nu_i} = 0$ is acceptable for any or all generations of neutrino.

Assuming at least one massive generation of neutrinos, and ignoring the higher-order correc-

tions, for the massive neutrinos the above may be rewritten

$$\begin{aligned}
1 = & \frac{f^2}{2} \left[k_i^{(\nu)}(\mathcal{E}_{\nu_i}) \right]^4 \omega_0^2 N_0^8 S_{18,147} \\
& \times \left(\left\{ \frac{1}{[m_c^*(\mathcal{E}_{\nu_i})]^2} + \frac{25\alpha \sum_j m_{e_j}^2}{6\pi m_W^2 [m_c^*(\mathcal{E}_{\nu_i})]^2} + \frac{40}{3m_{\mathbf{H}}^2 [k_1^{(e)}(\mathcal{E}_e)N_0]^4} \right\} \right. \\
& \left. + \left\{ \frac{450\alpha m_{\nu_i}^2}{\pi [m_c^*(\mathcal{E}_{\nu_i})]^4} + \frac{5\alpha (f_W - 48f_Z) m_{\nu_i}^2}{6\pi m_W^2 [m_c^*(\mathcal{E}_{\nu_i})]^2} \right\} \right). \tag{10.5}
\end{aligned}$$

Provided the neutrino mass is small compared to the electroweak scale (i.e. m_W^2 etc.), the second term in curly braces is a small (perturbative) correction to the first.

By the leading order terms, all $k_i^{(\nu)}$ are (approximately) equal. However, for

$$k_n^{(\nu)}(\mathcal{E}) = 1 + \sqrt{2} \cos \left[\theta_\nu(\mathcal{E}) - \frac{2\pi(n-1)}{3} \right] \tag{10.6}$$

there are no values of θ_ν for which all three eigenvalues even approximately coincide. Therefore at least one neutrino must be massless.

Further, restricting to the leading order expression

$$1 = \frac{f^2}{2} \left[k_i^{(\nu)}(\mathcal{E}_{\nu_i}) \right]^4 \omega_0^2 N_0^8 S_{18,147} \left\{ \frac{1}{[m_c^*(\mathcal{E}_{\nu_i})]^2} + \frac{25\alpha \sum_j m_{e_j}^2}{6\pi m_W^2 [m_c^*(\mathcal{E}_{\nu_i})]^2} + \frac{40}{3m_{\mathbf{H}}^2 [k_1^{(e)}(\mathcal{E}_e)N_0]^4} \right\} \tag{10.7}$$

and solving for $k_i^{(\nu)}$ yields $k_i^{(\nu)} \approx 16$. However, the maximum value of $k_i^{(\nu)}$ for any θ_ν is $\sqrt{2}$. Hence there are no nonzero solutions for neutrino masses in the regime $m_{\nu_i} \ll m_e \ll m_W$. All light neutrinos are therefore massless:

$$m_{\nu_i} = 0 \quad \forall i. \tag{10.8}$$

NOTE: This argument does not exclude the possibility of additional superheavy neutrino mass eigenstates ($m_{\nu_i} \geq m_W$), which would be beyond the scope of the present perturbative treatment.

Bibliography

- [1] L. Onsager, [Phys. Rev. **65**, 117 \(1944\)](#).
- [2] M. Suzuki, [Prog. Theor. Phys. **56**, 1454 \(1976\)](#).
- [3] G. P. Srivastava, *The Physics of Phonons* (Taylor & Francis, 1990).
- [4] P. G. Drazin and R. S. Johnson, *Solitons: An Introduction*, 2nd ed. (University Press, Cambridge, 1989).
- [5] L. N. Cooper, [Phys. Rev. **104**, 1189 \(1956\)](#).
- [6] J. Bardeen, L. N. Cooper, and J. R. Schrieffer, [Phys. Rev. **108**, 1175 \(1957\)](#).
- [7] J. D. Maynard, [Rev. Mod. Phys. **73**, 401 \(2001\)](#).
- [8] D. Dragoman and M. Dragoman, *Quantum–Classical Analogies*, The Frontiers Collection (Springer-Verlag, Berlin Heidelberg, 2004).
- [9] M. Lewenstein, A. Sanpera, V. Ahufinger, B. Damski, A. Sen(De), and U. Sen, [Adv. Phys. **56**, 243 \(2007\)](#).
- [10] M. Visser, C. Barceló, and S. Liberati, [Gen. Rel. and Grav. **34**, 1719 \(2002\)](#).
- [11] S. Liberati, F. Girelli, and L. Sindoni, Analogue models for emergent gravity, [arXiv:0909.3834v1 \[gr-qc\] \(2009\)](#).
- [12] C. Barceló, S. Liberati, and M. Visser, [Living Reviews in Relativity **14**, 3 \(2011\)](#).
- [13] W. G. Unruh, [Phys. Rev. Lett. **46**, 1351 \(1981\)](#).
- [14] L. J. Garay, J. R. Anglin, J. I. Cirac, and P. Zoller, [Phys. Rev. Lett. **85**, 4643 \(2000\)](#).
- [15] L. J. Garay, J. R. Anglin, J. I. Cirac, and P. Zoller, [Phys. Rev. A **63**, 023611 \(2001\)](#).
- [16] O. Lahav, A. Itah, A. Blumkin, C. Gordon, S. Rinott, A. Zayats, and J. Steinhauer, [Phys. Rev. Lett. **105**, 240401 \(2010\)](#).
- [17] W. Gordon, [Ann. Phys. **377**, 421 \(1923\)](#).
- [18] U. Leonhardt and P. Piwnicki, [Phys. Rev. A **60**, 4301 \(1999\)](#).
- [19] U. Leonhardt and P. Piwnicki, [Phys. Rev. Lett. **84**, 822 \(2000\)](#).
- [20] T. A. Jacobson and G. E. Volovik, [Phys. Rev. D **58**, 064021 \(1998\)](#).

- [21] B. Reznik, [Phys. Rev. D](#) **62**, 044044 (2000).
- [22] R. Schützhold and W. G. Unruh, [Phys. Rev. Lett.](#) **95**, 031301 (2005).
- [23] R. Schützhold and W. G. Unruh, [Phys. Rev. D](#) **66**, 044019 (2002).
- [24] Y. Koide, in *Proc. 30th Int. Conf. High-energy Phys., Osaka, Japan*, edited by C. S. Lim and T. Yamanaka (World Scientific, Singapore, 2001) [arXiv:hep-ph/0005137v1](#).
- [25] Y. Koide, [Phys. Lett. B](#) **120**, 161 (1983).
- [26] M. E. Peskin and D. V. Schroeder, *An Introduction to Quantum Field Theory* (Westview Press, 1995).
- [27] B. Abi *et al.* (Muon $g - 2$ Collaboration), [Phys. Rev. Lett.](#) **126**, 141801 (2021).
- [28] R. L. Workman *et al.*, [Prog. Theor. Exp. Phys.](#) **2022**, 083C01 (2022).
- [29] A. Kitaev, [Ann. Phys.](#) **321**, 2 (2006).
- [30] P. H. Bonderson, *Non-Abelian Anyons and Interferometry*, [Ph.D. thesis](#), California Institute of Technology (2007).
- [31] E. Tiesinga, P. J. Mohr, D. B. Newell, and B. N. Taylor (2018), (Web Version 8.1). Database developed by J. Baker, M. Douma, and S. Kotochigova. Available at <http://physics.nist.gov/constants>, National Institute of Standards and Technology, Gaithersburg, MD 20899.
- [32] R. Penrose, in *Combinatorial Mathematics and its Applications*, edited by D. J. A. Welsh (Academic Press, 1971) pp. 221–244.
- [33] R. N. C. Pfeifer, P. Corboz, O. Buerschaper, M. Aguado, M. Troyer, and G. Vidal, [Phys. Rev. B](#) **82**, 115126 (2010).
- [34] R. N. C. Pfeifer, *Simulation of Anyons Using Symmetric Tensor Network Algorithms*, [Ph.D. thesis](#), The University of Queensland (2011), [arXiv:1202.1522v2](#).
- [35] R. N. C. Pfeifer, Software for “A classical analogue to the Standard Model (and General Relativity)”, <https://www.academia.edu/65931512> (2022).
- [36] A. Petermann, [Nuclear Physics](#) **5**, 677 (1958).
- [37] C. M. Sommerfield, [Annals of Physics](#) **5**, 26 (1958).
- [38] T. Aoyama, T. Kinoshita, and M. Nio, [Atoms](#) **7**, 28 (2019).
- [39] M. Awramik, M. Czakon, A. Freitas, and G. Weiglein, [Phys. Rev. D](#) **69**, 053006 (2004).
- [40] J. Erler and M. Schott, [Prog. Part. Nucl. Phys.](#) **106**, 68 (2019).
- [41] T. Aaltonen *et al.* (CDF Collaboration), [Science](#) **376**, 170 (2022).
- [42] P. Achard *et al.* (L3 Collaboration), [Phys. Lett. B](#) **585**, 42 (2004).
- [43] R. Barate *et al.* (ALEPH Collaboration), [Phys. Lett. B](#) **464**, 339 (1999).
- [44] J. Abdallah *et al.* (The DELPHI Collaboration), [Eur. Phys. J. C](#) **46**, 295 (2006).

- [45] G. Abbiendi *et al.* (OPAL Collaboration), *Phys. Lett. B* **604**, 31 (2004).
- [46] R. P. Kerr, *Phys. Rev. Lett.* **11**, 237 (1963).
- [47] D. Di Mario, <http://digilander.libero.it/bubblegate/ephys.html>, *The Physics Deep*, retrieved 31st October 2007, hosting articles *Magnetic Anomaly in Black Hole Electrons* (2003), *Planck Permittivity and Electron Force* (2003), *Reality of the Planck Mass* (2003), *Electric Field as Variation of Gravity* (2005).
- [48] R. N. C. Pfeifer, *Calculations beyond the Standard Model: W mass in CDF II, and Muon $g-2$* , arXiv:2212.01255 with updates at <https://www.academia.edu/65931513> (Chapter 8) (2022).
- [49] R. N. C. Pfeifer, *A classical analogue to the Standard Model, chapter 1: Normalisable quasi-particles on a manifold with anticommuting co-ordinates*, arXiv:2106.08130 with updates at <https://www.academia.edu/65931513> (2022).
- [50] R. N. C. Pfeifer, *A classical analogue to the Standard Model, chapter 2: Colour interactions and fermions from scalar fields on \mathbb{C}^6* , arXiv:2108.07719 with updates at <https://www.academia.edu/65931513> (2022).
- [51] R. N. C. Pfeifer, *A classical analogue to the Standard Model, chapter 3: Standard Model particle spectrum from scalar fields on \mathbb{C}^{18}* , arXiv:0805.3819 with updates at <https://www.academia.edu/65931513> (2022).
- [52] R. N. C. Pfeifer, *A classical analogue to the Standard Model, chapters 4-10: Particle generations and masses, curved spacetimes and gravitation*, arXiv:2008.05893 with updates at <https://www.academia.edu/65931513> (2022).
- [53] R. Aaij *et al.* (LHCb collaboration), *Nature Physics* **18**, 277 (2022).
- [54] S. Descotes-Genon, L. Hofer, J. Matias, and J. Virto, *J. High Energ. Phys.* **2016**, 92.
- [55] C. Bobeth, G. Hiller, and G. Piranishvili, *J. High Energ. Phys.* **2007**, 12.
- [56] M. Bordone, G. Isidori, and A. Pattori, *Eur. Phys. J. C* **76**, 440 (2016).
- [57] G. Isidori, S. Nabeebaccus, and R. Zwicky, *J. High Energ. Phys.* **2020**, 104.